The effect of microstructure and fatigue on the acoustoelastic response of aerospace materials

by Robert Ellwood, MEng

Thesis submitted to The University of Nottingham for the degree of Doctor of Philosophy, December 2012

Abstract

This thesis presents work relating to the measurement of the nonlinear acoustoelastic response of several materials with respect to microstructure and fatigue life. The nonlinear acoustoelastic response measures the acoustoelastic coefficient of a material. During normal usage components are subject to stresses that while not sufficient to cause fracture cause fatigue, gradually weakening the component. Linear ultrasonic methods have been shown to be poor at detecting fatigue. However, there is evidence that the accumulation of fatigue damage gives the material a nonlinear elastic response that can be probed by ultrasound. A potential technique to monitor fatigue is produced by monitoring changes in the response of nonlinear ultrasonic techniques.

Several methods of detecting material nonlinearity using acoustic waves have been proposed. In this thesis a system using the collinear mixing of ultrasonic waves is developed. By measuring the velocity change of a probe wave due to the induced stress from a pump wave, a measure of the nonlinearity is obtained. By using laser ultrasound techniques we gain the benefits of high spatial and temporal resolution. This is important when investigating the nonlinear response of a material as there is evidence that the microstructure affects the nonlinear response of a material.

Single point measurements of the acoustoelastic coefficient are taken. In polycrystalline materials the measurement is found to vary with location. A technique is developed to measure the spatial variation of the acoustoelastic coefficient. A relationship between the acoustoelastic coefficient of a material and the underlying microstructure is found. The technique to monitor the spatial variation of the acoustoelastic coefficient is used to monitor the change in samples as they are fatigued. The acoustoelastic coefficient is found to change with fatigue by a larger proportion (9-30%) than linear velocity measurements (0.5-0.6%). Spatial variation of the acoustoelastic coefficient indicated a complex relationship between fatigue and the acoustoelastic coefficient of a material. The implications and further work required from the observed changes in the acoustoelastic coefficient with microstructure and fatigue are discussed.

Acknowledgements

I would like to thank my supervisor Professor Matt Clark for his efforts, guidance and support. His drive for excellence has improved the rigour of my work considerably. I would also like to extend my thanks to Professor Mike Somekh for his advice, guidance and sense of perspective, often dispensed with a sense of humour that was much appreciated. The assistance rendered and advice given by Dr Steve Sharples was extremely useful and very much appreciated. I am also grateful for the advice and support offered by Dr Teti Stratoudaki.

I would like to thank Dr Ian Collison for the work he conducted during his PhD that led to the initial development of the nonlinear technique that is further developed in this work. Thanks go to my colleagues, Richard, Wenqi and Jethro, for their input into discussions about my work and providing sources of further information. I would like to thank the technicians at the University of Nottingham for their timely work in constructing custom mechanical components for the system.

Thanks go to my family and friends for not only putting up with me through all this, but also their continued support and encouragement. I would also like to thank them for providing the occasional planned/ unplanned distraction and in some cases even providing a roof over my head. Thank you for understanding when I couldn't be there.

With all my heart I would like to thank Rosie for everything, which is an extremely long list.

Contents

Chapter 1

Introduction

1.1 Thesis aims and overview

This thesis presents work relating to the measurement of the nonlinear response of several materials with respect to microstructure and fatigue. The aims of the work presented in this thesis are:

- Develop an instrument and procedure for the monitoring of the nonlinear ultrasonic response of a material.
- Develop a technique to image the nonlinear ultrasonic response over the surface of a material.
- Investigate the effects of microstructure and fatigue on the nonlinear ultrasonic response of aerospace materials.

During normal usage components are subject to stresses that while not sufficient to cause fracture cause fatigue, gradually weakening the component. The failure of safety critical components due to fatigue has caused large scale loss of life and

incurred great costs. This highlights the importance of being able to monitor the progression of fatigue.

Ultrasound is a powerful tool used to probe material properties and is of interest for monitoring fatigue. There is evidence that fatigue causes changes in the third and higher order elastic constants of a material. The third-order elastic constants and the impact of fatigue are discussed in section 2. Nonlinear ultrasonic techniques are sensitive to the third and higher-order elastic constants. By monitoring the nonlinear response of a material, theoretically a measure of the fatigue can be made. Linear ultrasonic techniques have been found to be less sensitive [1–3] to the fatiguing process. A brief overview of both linear and nonlinear ultrasonics is given in chapter 2. In the literature a range of nonlinear ultrasonic techniques are discussed.

The purpose of the work conducted in this thesis is to investigate the sensitivity of a nonlinear ultrasonic technique to the fatigue process. Initially the focus of this work was to develop an industrially relevant technique. However it was found that the microstructure also affects both the nonlinear response and the fatigue process. This broadens the work carried out to a material science oriented investigation of the change in the nonlinear response with fatigue and microstructure. The effect of the microstructure on the nonlinear response is investigated. To assess the impact of fatigue, the spatial variation of the nonlinear response due to microstrucutre is monitored over several fatigue levels.

Prior to this work, Ian Collison at the University of Nottingham [4] developed a nonlinear measurement technique using an optical ultrasonic system, different from the one developed in this work. The system he built was capable of making single point nonlinear measurements. A single measurement took 40 minutes or more. Measurements were conducted on two materials, aluminium and fused silica. Two

different grades of aluminium were investigated (2024 and 6061). The focus of this work is the further development of the technique developed previously, resulting in a new system being produced. The measurement parameter is developed to be consistent with the literature. Some of the single point acoustoelastic coefficient measurements conducted by Ian are repeated in this work to calibrate the new system. The uncertainties and errors in the new system are established. The technique has been significantly increased in speed to allow imaging, it is now 60 times faster. The imaging technique is used to investigate the effect of microstucture and fatigue on the acoustoelastic coefficient.

The technique developed in this work measures the nonlinear acoustoelastic interaction between two co-propagating surface acoustic waves (SAWs). The interaction takes the form of a velocity shift in a high frequency probe wave (38–67 MHz dependent on material) due to the induced stress caused by the propagation of a low frequency pump wave (0.5–2.25 MHz). The stress dependence of the acoustic wave velocity is known as the acoustoelastic effect. By measuring the acoustoelastic effect, the acoustoelastic response of a material can be found. The acoustoelastic response of the material can be quantified in terms of the acoustoelastic coefficient for Rayleigh waves, A_R. By altering the temporal interaction point of the pump and probe waves, a range of stress levels are experienced by the probe wave. In chapter 4 this procedure is outlined, and the measurement uncertainty is determined.

Laser ultrasonic techniques are used to generate the probe wave and to detect both the pump and probe waves, a brief description of the principles of the generation and detection of ultrasonics is given in chapter 2. Imaging is made easier by using these techniques as they are non-contact so moving over the sample is simpler. Using laser ultrasound also gives the advantage of having a high spa-

tial resolution compared to contact methods. Laser ultrasonics does not require a coupling medium. It is beneficial to not use a coupling medium, as they can introduce additional nonlinear effects into measurements. A description of the instrumentation is given in chapter 3.

By capturing the data efficiently and reducing the number of interactions between the SAWs, the amount of time each measurement takes can be minimised. Reducing the amount of time each acoustoelastic measurement takes allows for the imaging of the spatial variation of the acoustoelastic coefficient of the material. The instrumentation and procedure to do this were developed side by side; for clarity they are discussed in separate chapters (3 and 4 respectively). The ability to image the variation in the acoustoelastic coefficient allows comparison between the variation in the acoustoelastic coefficient due to microstrucutre and that caused by fatigue. The experimental method developed to do this is discussed in chapter 4. Experimental results relating the microstructure and the fatigue life to the acoustoelastic coefficient are presented in chapter 5.

Fused silica was initially used, due to its isotropic nature and large acoustoelastic response, as a test sample to make measurements. Aluminium and titanium were subsequently used to investigate the relationship between fatigue and the acoustoelastic coefficient, due to their industrial relevance.

Finally chapter 6 discusses the issues derived from this work and the further work to be investigated. Chapter 7 summarises the work completed in this thesis.

1.2 Chapter summary

The following is a description of each chapter:

- Chapter 1 contains a brief introduction to the work carried out in this thesis

before outlining the structure of the thesis.

- Chapter 2 contains a review of the background information relevant to the work carried out in this thesis. This includes a review of fatigue, microstructure, the elastic constants and non-destructive testing techniques. Ultrasonic techniques are specifically focused upon, including linear and nonlinear techniques. A review of ultrasonic generation and detection techniques concludes the chapter.

- Chapter 3 discusses the instrumentation developed to take an acoustoelastic measurement on a material. This includes a laser ultrasonic system to generate the probe wave and to detect both the pump and probe waves. This instrumentation was developed in parallel with the experimental methods developed in chapter 4.

- Chapter 4 explores the experimental method developed to monitor the acoustoelastic coefficient for Rayleigh waves (A_R). This chapter discusses the measurements recorded, the uncertainty in each of these and how these are used to make the acoustoelastic measurement. The optimal configuration of the experiment to reduce the measurement uncertainty is discussed. A technique is developed to monitor the spatial variation of A_R. Finally the design and fatigue schedule of the samples is described.

- Chapter 5 presents the experimental results generated using the system developed in the previous chapters. Initially single point measurements are made on different materials and are compared to static strain acoustoelastic measurements. A_R is recorded as varying spatially. The effect of the microstructure on A_R is investigated. The spatial variation of the A_R is monitored over a range of fatigue levels for two industrially relevant materials,

aluminium and titanium. The data collected is analysed. The implications of the results are discussed.

- Chapter 6 discusses potential further work to investigate the implications of the results discussed in chapter 5.

- Chapter 7 Concludes the thesis.

1.3 Summary

The motivation behind this work was initially to develop an industrially relevant method for the monitoring of fatigue damage using nonlinear ultrasonics. The scope of the work broadened with the investigation of the effects of microstrucutre, as well as fatigue, on the nonlinear ultrasonic measurement. This thesis presents the development of a nonlinear ultrasonic technique that uses laser ultrasound techniques. The experiment monitors the change in velocity caused by an applied stress. The gradient of the velocity-stress curve is a measure of the acoustoelastic coefficient of the material. By taking multiple measurements over a sample surface the spatial variation of the acoustoelastic coefficient with microstructure and fatigue can be mapped.

The work presented in this thesis is novel as it demonstrates a new imaging technique that allows the imaging of the acoustoelastic coefficient (A_R) of a material. The effect of the microstructure of the sample on A_R is investigated. This imaging technique is used to monitor changes in A_R of a material over several stages of its fatigue life.

Chapter 2

Background

2.1 Introduction

This chapter starts with a general review of fatigue. The purpose is to highlight the importance of fatigue and the need to be able to monitor it. Two important material properties are discussed in this chapter, microstructure and the elastic constants, as they impact the formation and potential detection of fatigue.

A variety of techniques to probe material properties have been developed, some are more suited to potentially monitoring fatigue than others, these techniques are discussed. Of all these techniques, ultrasonics show the most potential as an industrially relevant, *in situ*, method of detecting fatigue. The sub-group of linear ultrasonics has been reported to be relatively insensitive to the fatigue process [5–9]. Nonlinear ultrasonic techniques have been shown by various workers [2,3,5,6,10–23] to be highly sensitive to the fatigue process. A full overview is given for these techniques along with the technique developed in this work. Finally a range of practical methods for generating and detecting ultrasound is outlined.

2.1.1 Fatigue

During normal usage components are subject to stresses that while not sufficient to cause fracture produce fatigue. Fatigue is defined as [24]:

> "the modification of the properties of materials due to the application of stress cycles whose repetition can lead to fracture."

During the process of fatigue micro-damage is formed. Eventually the micro-damage coalesces into macro-cracks [10], severely weakening the structural integrity of a component and finally causing mechanical failure.

From the beginning of the industrial revolution to the modern day a range of accidents have been attributed to mechanical failure due to the fatigue process. One of the earliest recorded instances of fatalities caused by fatigue damage was in 1842 when a train axle ruptured causing the death of 60 people in Versailles [24]. As early as 1838 the importance of microstructure on the fatigue process was understood. A thorough review of the history of fatigue is given by Schütz [25].

In recent history one of the most famous tragedies attributed to the fatigue process was the crash of two de Havilland DH 106 Comets in 1953 and 1954. Not only were these two incidents highly costly in terms of human life (78 people died [26]), but also huge economic costs were incurred in establishing the cause of the tragedies and correcting the defects [27]. As recently as 2006 a Boeing 767 had one of its engines suffer from an uncontained failure attributed to a fatigue crack [24]. Being able to monitor the accumulation of fatigue damage could potentially save lives, large sums of money, time, material waste and effort.

The fatigue process is complicated as it varies with type of material and in the case of metals, alloy type and treatment [28]. The initial phase of fatiguing in all materials is the formation of micro-defects. Micro-defects will eventually coalesce

to form the nuclei of macro-cracks. A good review of the process of high cycle fatigue in face-centred-cubic (FCC) metals with wavy dislocation slip is presented by Cantrell [10]. Micro-defects are extremely small and as such many techniques used to investigate materials cannot easily resolve them. Some authors [6, 29, 30] have shown that in some metals the formation of micro-defects occur close to the surface. By probing the sample surface a technique that is highly sensitive to the formation of these micro-defects is produced.

2.1.2 Microstructure

The long range order (>nm) of the atoms, molecules or ions making up a material is used to define different material formats known as phases. In some materials the long range order is high, giving them a highly periodic structure; these materials are known as crystals. Amorphous or non-crystalline materials may have a small scale regularity in structure but have no long range order. A phase is any part of a material with a distinct crystalline structure and/or chemical composition. A single phase polycrystalline material consists of multiple small crystals, known as grains, which are randomly orientated. The imperfections separating grains are called grain boundaries [31].

The random arrangement of the grains and phases is known as the microstructure. The microstructure of a material can strongly influence many of its physical properties such as strength, toughness, hardness, wear resistance and most importantly in the case of this work, the formation of fatigue.

Microstructure presents challenges when using material testing techniques. For instance, in ultrasonic measurements (see section 2.3) the velocity of the wave is related to the microstructure. This leads to attenuations (scattering) and aberration (change in direction) of the waves travelling in the material.

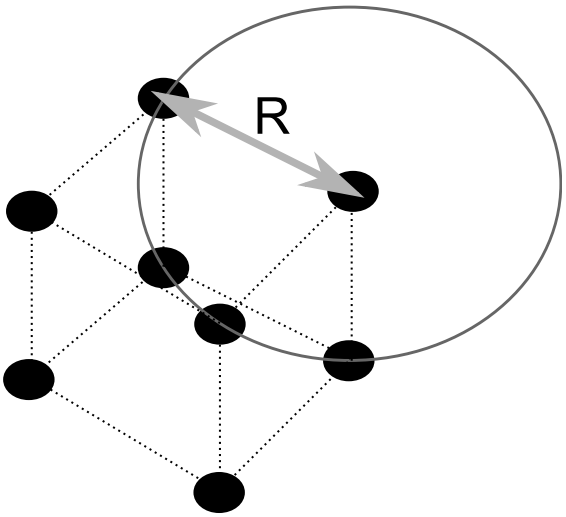

Figure 2.1: Diagram of atoms positioned at their energy equilibrium positions equally spaced apart from each other, forming a lattice. R represents the inter-atomic spacing

2.1.3 Elastic constants and fatigue

Atoms making up a solid are held in a single position by repulsive (nuclear repulsion energy) and attractive (Coulombic attraction energy) [32] forces that are in a balanced state. The inter-atomic potential energy can be expressed as a function of the inter-atomic spacing [33] R (see figure 2.1). When a particle is moved away from its equilibrium position the repulsive and attractive forces binding the molecules in place act to restore it.

This leads to the concept of elasticity where by a material returns to its original shape after external forces have been applied. The change in shape or position of the structure is known as the strain (commonly denoted by ϵ). The external influence displacing the lattice is known as stress (commonly denoted by σ). The stress can be related to the strain by means of the elastic stiffness coefficients (normally denoted by c and also often referred to as the elastic moduli), from Hooke's law:

$$\sigma = c\epsilon \tag{2.1}$$

The elastic moduli have the unit of Pascals (Pa). The elastic constants of a material vary according to the shape of the atomic lattice and with direction within the lattice. The elastic constants can be used to define the energy due to strain in a material given by [34]:

$$E = E_c + gC_{ij}\epsilon_{ij} + \frac{1}{2}C_{ijkl}\epsilon_{ij}\epsilon_{kl} + \frac{1}{3}C_{ijklmn}\epsilon_{ij}\epsilon_{kl}\epsilon_{mn} + ... \tag{2.2}$$

where ϵ_{RY} is the strain tensor expressed in terms of components RY with respect to a standard basis, E_c is the strain energy before any displacement takes place; it can be assumed that this is zero in most cases. C_{ij} are the elastic moduli that relate to static non varying strains, these are the first order elastic constants (denoted from here on as C_1), and g is a constant. C_{ijkl} represents the second order elastic constants which relate to the linear distortion of a material with a varying strain (denoted from here on as C_2), this is expressed as a fourth-rank tensor. There are a maximum of 81 independent second order elastic constants. Due to conservation of energy and the symmetry in the structure of some materials, the number of unique second order elastic constants is often reduced. C_{ijklmn} represents the third-order elastic constants, denoted from here on as C_3. C_3 is a sixth-rank tensor, which has in general, 729 components. The number of independent third-order elastic constants reduces, dependent on crystal symmetry. The C_3 elastic constants are small compared to the C_2 elastic constants.

The effects of the fatigue process on higher order elastic constants

The presence of micro-defects affects the local elastic constants. The mechanism of the change in higher order elastic constants due to the presence of a micro-defect is illustrated by considering a single crack. When the crack is forced shut the

local elastic modulus approaches that of the undamaged material. When the crack is forced open this reduces the local elastic modulus of the region. This process is known as clapping. This results in further strain dependence of the elastic constants, in addition to the existing strain dependence due to the lattice, giving rise to an increase in the higher order elastic constant. Other types of defects have a similar effect.

2.2 Non-destructive testing (NDT)

Non-destructive testing (NDT) is a wide collection of techniques which are used to probe material properties without destroying or damaging the sample. NDT is also known as non-destructive evaluation (NDE) and non-destructive inspection (NDI). NDT has a range of applications such as flaw detection, structural assessment, determination of the physical properties of a material and the detection of foreign bodies [35]. These techniques are particularly important where the cost of catastrophic failure is too high to be left to chance, such as in the aerospace or nuclear industries.

The importance of monitoring fatigue has been highlighted in the previous section. Various NDT techniques have the potential to monitor fatigue, in this section these are discussed along with their limitations. In this work an ultrasonic technique is developed. Due to the depth of description required a review of ultrasonics is reserved for the next section, though it is an NDT technique.

Techniques such as visual, liquid penetrant, magnetic particle and eddy-current inspection do not have sufficient resolution to detect the formation of micro-defects associated with the fatigue process. By the time a macro-crack of sufficient size to be detected by these techniques has formed the sample can be considered terminally

damaged.

Below, techniques that have sufficient resolution to detect changes, due to the fatigue process, are discussed.

2.2.1 Radiographic inspection

Radiographic methods involve investigating materials using high energy electromagnetic waves. X-rays or gamma rays are regularly used but some techniques use neutron radiation due to its low absorption. Because of the radiations shorter wavelength it interacts differently than normal light with materials. Depending on the thickness of the sample the radiation can pass straight through some types of material and not others. These techniques are highly accurate and allow for precise measurement of material properties. The major drawback of all radiographic methods is their relative expense.

X-ray diffraction

The X-ray diffraction technique is part of the group of techniques collectively known as radiographic inspection. As with other waveforms, X-rays demonstrate the principle of diffraction. The wavelength of X-rays is sufficiently small so that the atomic lattice that forms a material acts as a diffraction grating. By measuring the diffraction pattern of the X-rays the orientation of an atomic lattice can be found (and so crystal orientation in anisotropic materials [36]). When a material is stressed (which occurs during the process of fatiguing) it affects the atomic lattice, the localised stress effect is monitored by measuring a change in the X-ray diffraction pattern in two separate directions [37].

2.2.2 Electron Microscopes

Electron microscopes use a beam of electrons to illuminate a specimen and produce a magnified image in a similar way to a conventional optical microscope (electrons replace the photons). As electrons have a very short wavelength (compared to light) extremely high resolutions can be achieved. Several different types of electron microscope exist. Electron microscopes have been used to image micro-defects caused by fatigue [6, 19, 38].

The process of imaging a sample using an electron microscope is non-destructive, preparing a sample to be analysed is very destructive. The sample has to fit into a vacuum chamber, so most industrially relevant components have to be cut down. Producing the required surface finish is also highly destructive. This limits electron microscopes application as a method of detecting fatigue damage on real world components.

2.2.3 Positron annihilation spectroscopy

Positron annihilation spectroscopy uses a source to emit positrons into a sample [39]. The source of positron is either from the decay of a radioactive element or from the conversion of a high energy gamma-ray. When a positron and electron come into close proximity they are both annihilated, producing a gamma-ray. Highly sensitive photo-multipliers are used to detect the gamma-ray. In regions where defects and voids are present the electron density is low. The amount of time taken between the emission of a positron and the production of the annihilation gamma-rays is a function of the electron density of the material. By tracking the time between generation of a positron and the gamma-rays a measurement of the dislocation density can be made. Doppler shifts in the annihilation energy have also been used to gain information about type and number of defects.

Positron annihilation spectroscopy also requires highly sensitive, expensive instrumentation to detect the emission of annihilation gamma-rays. This limits its practical use.

2.3 Ultrasonic material testing techniques

Ultrasonics are a set of powerful techniques used to assess material properties. Ultrasonic techniques are investigated in this work due to their potential to produce a highly sensitive, industrially relevant testing technique for fatigue. In this section a brief overview of ultrasonics is given. Ultrasonic testing for both linear and nonlinear techniques is introduced. Finally a description of relevant generation and detection techniques to produce and monitor ultrasonic waves is given.

An acoustic wave is a waveform created by mechanical displacement of the particles in a medium. An acoustic or sound wave above the human audible frequency range (20Hz-22kHz dependent on age and hearing impairment) is known as an ultrasonic wave. The properties of an ultrasonic wave relate to the physical properties of the material the wave propagates in. Ultrasonic testing (testing using ultrsasonic waves) is highly sensitive to some changes in the material, in particular the elastic constants. The exact inspection procedure implemented depends on the material, geometry, defect size and defect geometry. There are several different ways in which a ultrasonic wave can propagate in a material, these are known as wave modes. Acoustic wave modes can be classified into two main groups, that of bulk waves and guided waves.

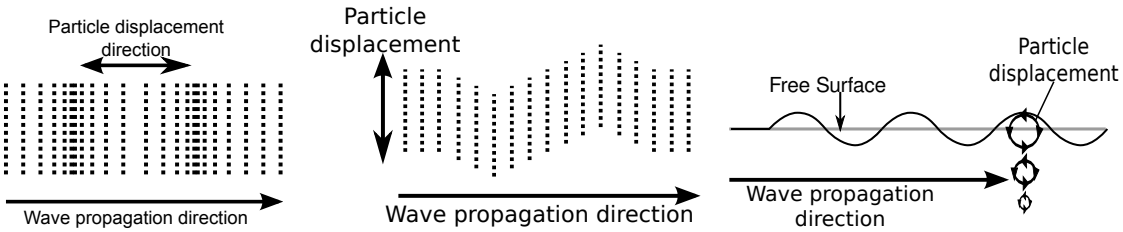

(a) Longitudinal wave (b) Shear wave (c) Rayleigh wave

Figure 2.2: Diagram representing the particle displacement with relation to the direction of propagation of a longitudinal wave (a), a shear wave (b) and a Rayleigh wave (c)

2.3.1 Bulk waves

Bulk waves propagate internally through a medium, though can be found at the interface of materials (such as surface skimming longitudinal waves). Bulk waves are used to assess defects in the bulk of a material such as discontinuities like cracks and disbonds, along with material properties such as elastic modulus.

Longitudinal (compression) bulk wave

A longitudinal bulk wave is an acoustic wave where the movement of the medium is in the same direction or opposite to the direction of propagation of the wave (see figure 2.2a). The medium is compressed and rarefied in the same direction as the wave is propagating in.

Shear (transverse) bulk wave

A shear wave is an acoustic wave where the movement of the medium is normal (perpendicular, see figure 2.2b) to the direction of propagation.

2.3.2 Guided waves

Guided waves relate to waves which propagate solely at the interface between two materials or at a free surface. The different types of acoustic guided waves include Rayleigh and Lamb waves.

Rayleigh waves

Rayleigh waves, also known as surface acoustic waves (SAWs), have both longitudinal and shear components, the particle displacement is elliptical in nature (see figure 2.2c). They propagate on the surface of materials that are much thicker than a wavelength of the probing acoustic wave. The energy of the wave is mostly confined in the region between the surface and a depth of one wavelength, decaying exponentially as it goes into the bulk of the material. Particle displacement is minimal below a depth of two wavelengths, so Rayleigh waves are insensitive to changes in a material at depths greater than two wavelengths from the surface. This selectivity allows Rayleigh waves to be used to probe effects that occur on the surface of a material such as the formation of micro-defects.

Rayleigh waves have been used to study a variety of features such as surface breaking cracks [40, 41], measuring stress [42–45], assessing surface roughness [46, 47] and imaging the surface structure [48–51]. These waves are non-dispersive so will propagate with the same velocity independent of frequency. Rayleigh waves are used in this work because of their ability to probe the surface, where some authors [6,29,30] report that micro-defects initiate, and their non-dispersive nature, allowing precise control over the interaction between the waves.

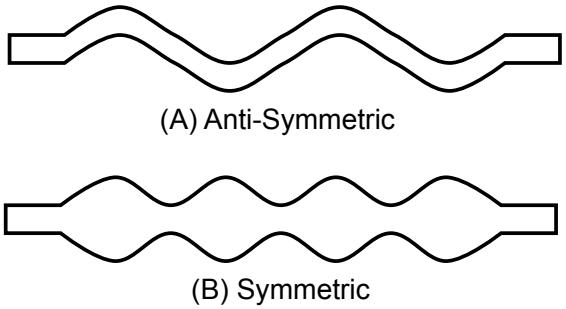

Figure 2.3: Diagram respresenting the surface displacement for anti-symmetric (A) and symmetric (B) lamb waves

Lamb wave

Lamb waves are the principal wave mode in the instance where the thickness of the material is of the order of 2 wavelengths or less. The energy of the wave penetrates the entire thickness of the sample causing displacements on both top and bottom surfaces. Again these waves have both shear and longitudinal components. Lamb waves are dispersive. There are two main types of mode group for lamb waves, antisymmetric (figure 2.3 A) and symmetric (figure 2.3 B). Lamb waves can propagate large distances and so can be used to inspect large structures [52]. Lamb waves have been used to inspect a range of defects such as delaminations [53, 54] and cracks [55,56]. The technique developed in this work avoids using Lamb waves due to their dispersive nature, which would complicate the interaction between the two waves used as part of the technique.

2.3.3 Linear ultrasonic techniques

Linear ultrasonic techniques assume that the elastic moduli only include those up to the second order (C_2). This assumption is fair as the third and higher order elastic constants (C_3 + ...) are much smaller than the second order (C_2) elastic constants. The comparative sensitivity of linear and nonlinear ultrasonic

techniques to the fatigue process is initially discussed to explain the rationale behind the investigation of the sensitivity of the technique developed and described in this thesis. This section discusses the equations that describe how a linear ultrasonic wave propagates through a material, so as to highlight the difference between the linear techniques and the nonlinear techniques discussed later. The section then goes on to discuss two linear techniques that are of interest due to their sensitivity to fatigue.

Comparative sensitivity of linear and nonlinear ultrasonic techniques

Various authors [1–3] have highlighted that nonlinear ultrasonic techniques are more sensitive to the formation of micro-defects caused by fatigue than linear ultrasonics. In order to detect any change in the linear ultrasonic response due to the small defects caused by fatigue, the number of defects must be high. By the time a component reaches this point it is beyond its safe usage life. Interest has grown in nonlinear techniques that are potentially more sensitive to the early onset of fatigue.

However Botvina et al. [38] have found that linear techniques, such as the measurement of attenuation, are sensitive to the formation of fatigue. Repeatable measurements using attenuation techniques can be difficult to acquire. Other linear techniques such as velocity measurements are far more repeatable. The conflict in opinions over the comparative sensitivity of linear and nonlinear techniques requires further investigation. In determining which technique is preferential the repeatability and accuracy of each measurement are important features. In section 5.7.3 linear velocity measurements are compared to the nonlinear acoustoelastic measurements made to investigate a change in fatigue.

Linear wave equation

The origin for the equation of motion for linear waves is well defined in many texts [57,58]. Starting from Newton's second law, the equation for the propagation of a linear acoustic wave in a three dimensional body can be found and is given as:

$$\rho \frac{\partial^2 u}{\partial t^2} = \nabla \cdot \sigma \tag{2.3}$$

$$\sigma = \frac{\partial E}{\partial x_i} \tag{2.4}$$

where u is the deformation with a given displacement x_i away from the initial position X, where $u = x_i - X$. In the linear case the elastic strain energy is given by:

$$E = gC_{ij}\epsilon_{ij} + \frac{1}{2}C_{ijkl}\epsilon_{ij}\epsilon_{kl} \tag{2.5}$$

where g is a constant. If the static strain (ϵ_{ij}) is set to zero, the linear wave equation includes contributions from the second order elastic constants and the density (ρ). In this case the wave velocity is proportional to the density and the fourth-rank stiffness tensor c_{ijkl}, where $\sigma_{ij} = c_{ijkl}\epsilon_{kl}$. The solution takes a number of different forms depending on the wave mode propagating.

An important feature in the linear case is that it satisfies the principle of superposition. This means that at any location and time the solution of the wave equation can be described as the sum of the component waves. In a linear model, if the elastic constants have an imaginary component, the solution gains an extra parameter (α) which describes the loss effect of the material on the propagating wave. The overall solution for a longitudinal one dimensional wave takes the form:

$$U_x = A_1 e^{-\alpha x} \sin(kx - \omega t) \tag{2.6}$$

where U_x is the instantaneous displacement of the wave in the x direction, A_1 is the amplitude of the wave, k is the wave number and ω is the angular frequency.

The next section introduces two main linear ultrasonic techniques. Both of these methods are discussed due to their proposed sensitivity to defects that are smaller than the wavelength of the investigating ultrasound.

Linear velocity measurements

The linear velocity of a propagating wave is defined by the second order elastic constants and the material density. The presence of micro-defects produced in the fatiguing process will affect the porosity of the material and so the localised elastic constants and density. This can affect the linear velocity of an ultrasonic wave. By measuring the change in velocity a potential increase in micro-defects can be detected.

Linear velocity measurements are used in this work as part of the registration protocol. The elastic constants of an anisotropic material are directionally dependent. This results in the velocity of a propagating wave in an anisotropic material being directionally dependent. Polycrystalline materials consist of multiple crystals in random orientations. By measuring the velocity across the surface of a polycrystalline material an image of the microstructure can be produced. This will be used later to perform precise re-registration of measurements on the sample.

A range of techniques to monitor the linear velocity of an ultrasonic wave have been developed in the literature [59]. Discussed in section 4.4 is a linear technique known as spatially resolved acoustic spectroscopy (SRAS) which is used in this work to re-register samples. Other techniques not discussed here include pulse-echo time of flight measurements, pulse interference and resonance techniques.

Attenuation

As an acoustic wave propagates in a material it will reduce in amplitude, this is known as attenuation. The cause of attenuation can be divided into two sources. The first, called scattering, is due to changes in the direction of the acoustic wave due to small localised changes in the material. This change in direction means that some of the energy is not returned to the detection system resulting in a reduction in detected energy, it is an entirely linear process as no energy conversion takes place. The other source of attenuation is called absorption. This process involves the conversion of some of the propagating acoustic wave energy into another form such as heat.

In an initially homogeneous material the attenuation will be low. Oparina and Botvina [60] have shown that as a homogeneous material goes through the fatigue process micro-defects form. These defects act as both scatters and absorption particles causing attenuation of a propagating wave [38]. By measuring the attenuation of a propagating wave a measure of the non-terminal damage can be made.

Attenuation measurements are difficult to make due to a range of practical issues. The coupling efficiency must be high and kept constant to ensure that any reduction in the acoustic wave is due to the material and not the coupling of the system. The sample geometry must also be considered, where unaccounted for geometries (wedge effects and non-parallelism) could mean that the acoustic wave travels in a direction not expected resulting in an attenuation of the detected signal.

2.4 Nonlinear ultrasonic techniques

Nonlinear ultrasonic methods describe the group of techniques where the stress-strain relationship in a propagating wave is assumed to be nonlinear. This relationship is the result of the effects of the third-order and higher elastic constants. Various methods have been developed to measure the effects of these constants. Nonlinear ultrasonic techniques are less developed than linear ultrasonic techniques. However nonlinear ultrasonic techniques show promise by being potentially more sensitive than linear ultrasonics techniques to material property changes, such as fatigue [1–3].

Listed here are brief description of each of the general nonlinear techniques discussed further in the next section. The most prolific nonlinear technique is that of harmonic generation where the effect of the higher order elastic constants is measured by the production of harmonics of an initial wave introduced into the sample. Other techniques rely on measuring the production of sum and difference terms by the interaction between two waves as they co-propagate. The acoustoelastic technique monitors a change in the velocity of a wave with the appliciation of stress, due to the third-order elastic constants. A non-co-propagating nonlinear technique monitors the effects of the third-order elastic constants by measuring the production of a third acoustic wave when two acoustic waves interact in a volume under certain circumstances. The final group of nonlinear techniques rely on measuring a non-classical nonlinear parameter which causes a hysteresis effect. This can be measured from the shift in resonance peak frequency with amplitude (NRUS) or through the mixing of two co-propagating ultrasonic waves (NEWS).

2.4.1 Nonlinear wave equation

The nonlinear wave equation is similar to the linear wave equation, the only difference is it includes third-order and higher order elastic constant terms. A full description of the nonlinear wave equation has been presented by other authors [7–9, 61, 62]. The one dimensional nonlinear wave equation takes the form:

$$\frac{\partial^2 u}{\partial t^2} = \frac{C_2}{\rho}\frac{\partial^2 u}{\partial x^2}(1 + \beta\frac{\partial u}{\partial x_i} + ...) \tag{2.7}$$

where β is the contribution from the third-order elastic constants in the direction denoted by x_i. The third-order elastic constants are orientation specific, just as the second order elastic constants are. The number of unique third-order elastic constants can be reduced by symmetry, in isotropic materials the number of unique third-order elastic constants can be reduced to 3 (l,m,n in Murnaghan notation [63] and A,B,C in Landau and Lifshitz notation [64]), despite starting off as a sixth order tensor D_{ijklmn}. Due to the symmetry in the tensors they can be be simplified to the following form, $c_{ijkl} = c_{IJ}$ and $D_{ijklmn} = D_{IJK}$ where I is the matrix notation for the tensor notation of ij and the others follow suit (see table 2.1).

The important feature of the nonlinear wave equation is that the higher order elastic constant terms are multiplied by a strain factor ($\frac{\partial u}{\partial x}$) which is then multiplied by the second derivative of the strain factor. This results in nonlinear interaction (multiplication) in the solutions for the deformation term (u). This term allows the transfer of energy between waves and so the generation of new waves. The amount of energy transferred between waves is proportional to the nonlinear parameter β. By measuring the energy transfer between waves, nonlinear ultrasonic techniques can measure β and so the effects of the third-order elastic constants. Whilst each

Matrix notation	Tensor notation
1	11
2	22
3	33
4	23
	32
5	13
	31
6	12
	21

Table 2.1: Table describing the relationship between matrix notation and tensor notation

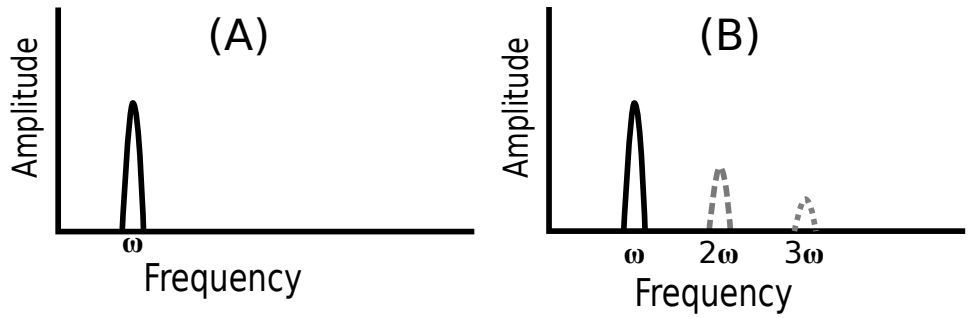

Figure 2.4: Illustration of harmonics of fundamental being generated by the fundamental as it propagates in a nonlinear material

technique is applied in a different way the underlying principle of the measurement is essentially the same.

2.4.2 Harmonic generation

If only one wave is propagating in a nonlinear medium it will interact with itself. The result of this interaction is the generation of waves with frequencies that are harmonics of the initial wave (see figure 2.4). Harmonic generation techniques measure the relationship between the amplitude of the harmonics and the amplitude of the initial wave, this is related to the nonlinear response of the material. This can be demonstrated mathematically by finding the first order perturbation solution of

the nonlinear wave equation. The first order perturbation solution takes the form:

$$u = u_0 + u', u_0 >> u'$$

By inserting the trial solution into the nonlinear wave equation for the longitudinal (for simplicity), one dimensional wave and removing the negligible terms, the wave equation takes the form:

$$\frac{\partial^2 u'}{\partial t^2} - c_l^2 \frac{\partial^2 u'}{\partial x^2} = \beta c_l^2 [\frac{\partial u_0}{\partial x} \frac{\partial^2 u_0}{\partial x^2}] \tag{2.8}$$

where c_l is the longitudinal velocity. For the case of a single longitudinal wave propagating in a material the initial solution takes the form:

$$u_0 = A \sin(kx - \omega t)$$

Differentiating this solution and entering it into the reduced wave equation results in:

$$\frac{\partial^2 u'}{\partial t^2} - c_l^2 \frac{\partial^2 u'}{\partial x^2} = \frac{-A^2 k^2 \beta c_l^2}{2} \sin 2(kx - \omega t) \tag{2.9}$$

The presence of the $\sin 2(\omega t - kx)$ term denotes a second harmonic is generated. This results in the first order perturbation solution taking the form:

$$u' = Bx \sin 2(\omega t - kx) + Cx \cos 2(\omega t - kx) \tag{2.10}$$

After differentiating (2.10), placing it into the wave equation (2.9) and collecting like terms it is found that:

$$B = 0, C = \frac{A^2 k^2 \beta}{8}$$

The total first order perturbation solution takes the form:

$$u = A\sin(kx - \omega t) + \frac{A^2k^2x\beta}{8}\cos 2(kx - \omega t) \tag{2.11}$$

The solution in (2.11) gives a method for measuring the nonlinear elastic response (β) of the material. This is apparent when the amplitude of the second harmonic is rearranged to give β:

$$B = \frac{A^2k^2x\beta}{8} \tag{2.12}$$

$$\beta = \frac{8}{k^2x}\frac{B}{A} \tag{2.13}$$

From equation (2.13) by measuring the amplitude of the first and second harmonics, knowing the wave number and distance the wave has propagated a measure of the nonlinear response β can be made. This technique can be applied to all wave mode types, determining the β value simply becomes more involved. The harmonic generation technique has been performed using Rayleigh waves [14, 65]. The nonlinearity parameter can be found using a Rayleigh wave by using the following expression [65]:

$$\beta = \frac{8u_z(2\omega)}{k_l^2xu_z^2(\omega)}\left(\frac{k_s^2\sqrt{k_R^2 - k_l^2}}{2(2k_R^2 - k_s^2)k_R}\right)$$

Where $u_z(\omega)$ and $u_z(2\omega)$ are the out of plane displacements of the Rayleigh wave for the first and second harmonic respectively. Also k_l, k_s and k_R are the longitudinal, shear and Rayleigh wave numbers respectively.

Due to the relatively small effect of the higher order elastic constants, extremely sensitive measurements are required of large amplitude waves. The larger the amplitude of the propagating wave, the larger the generated second harmonic and so the easier it is to detect.

The harmonic generation technique is extremely popular in the reviewed literature [3, 6, 10–17, 28, 66–68]. Early nonlinear acoustic experiments to monitor fatigue damage were conducted by Buck [6, 28] using this method. A range of different systems have been developed to implement the harmonic generation technique, including the use of capacitive transducers [11, 12], EMATS [66], piezoelectric transducers [3, 15–17, 68] and interferometers [13, 14]. Both bulk and SAW waves are used. Using this method many workers have reported a large change in the measured nonlinear response of various materials with an increase in fatigue [3, 6, 10–17] . The reported increases in the nonlinear parameter varies but some workers report an increase of the order of several hundred percent [10,13,15]. Other workers have reported a more complicated relationship between fatigue and the measured nonlinear response [66, 67].

Effects of nonlinearity on the propagation of a single wave

The change seen in the wave due to the additional harmonics caused by the nonlinearity of the material is that the peaks and troughs of the wave start to accelerate/ decelerate. The wave can be considered to be 'self-stressing', i.e. the velocity of the wave is dependent on the stress imposed on the sample. The additional harmonics produce a sawtooth wave front.

Measurement of other harmonics

Monitoring the nonlinear response of a material by measuring the second harmonic amplitude in proportion to the first harmonic amplitude has been outlined. Higher harmonics are also generated due to the nonlinear processes in the material. The third harmonic and higher can be related to the nonlinearity of a material. These harmonics are relatively small and have been used to investigate materials with

high levels of nonlinearity [69, 70]. The nonlinear wave equation also allows for the generation of sub-harmonics ($\frac{1}{2}$, $\frac{1}{4}$) of the initial wave. The generation of sub-harmonics is attributed to an adhesion force between any microdamage features [71].

Weakness of harmonic techniques

The primary difficulty in implementing the harmonic generation technique is in removing the harmonics generated by the instrumentation. Both the coupling medium and amplifiers used can produce harmonics. Special care needs to be taken in designing any instrumentation to monitor harmonic generation. Some workers have gone to great lengths to remove the effects of systematic nonlinearity in their instrumentation [66]. Care also needs to be taken when measuring the relative amplitudes of the harmonics due to attenuation and systematic issues such as coupling efficiency. These features make implementing the harmonic generation, practically, very difficult.

2.4.3 Co-propagating wave interaction

In this section techniques to measure material elastic nonlinearity using two co-propagating waves in a medium are discussed. As two waves co-propagate in a nonlinear material they will interact, this interaction can be monitored in several ways, which are discussed in the following section. To illustrate the effect of two waves on the nonlinear wave equation (2.8), the first order perturbation solution must be found. The initial solution for two longitudinal waves takes the form:

$$u_0 = A_1 \cos(k_1 x - \omega_1 t) + A_2 \cos(k_2 x - \omega_2 t)$$

where the subscript 1 relates to the first wave terms and the subscript 2 relates to the second wave terms. Differentiating and entering this into the nonlinear wave equation (2.8), the result is:

$$\frac{\partial^2 u'}{\partial t^2} - c_l^2 \frac{\partial^2 u'}{\partial x^2} = A_1^2 k_1^3 \beta c_l^2 \sin 2(k_1 x - \omega_1 t) + A_2^2 k_2^3 \beta c_l^2 \sin 2(k_2 x - \omega_2 t) + A_1 A_2 k_1 k_2 (k_1 + k_2) \beta c_l^2 \sin\left((k_1 + k_2)x - (\omega_1 + \omega_2)t\right)$$

The first order perturbation solution takes the form:

$$u' = D_1 \cos 2(k_1 x - \omega_1 t) + D_2 \cos 2(k_2 x - \omega_2 t) + D^+ \cos\left(k_1 + k_2)x - (\omega_1 + \omega_2)t + D^- \cos\left((k_1 - k_2)x - (\omega_1 - \omega_2)t\right)$$

The overall solution takes the form [72]:

$$u = u_0 + u' = A_1 \cos k_1 x - \omega_1 t + A_2 \cos k_2 x - \omega_2 t + D_1 \cos 2(k_1 x - \omega_1 t) + D_2 \cos 2(k_2 x - \omega_2 t) + D^+ \cos\left((k_1 + k_2)x - (\omega_1 + \omega_2)t\right) + D^- \cos\left((k_1 - k_2)x - (\omega_1 - \omega_2)t\right)$$

where: $D_1 = \frac{\beta k_1^2 A_1^2 x}{8}$, $D_2 = \frac{\beta k_2^2 A_2^2 x}{8}$ and $D^+ = D^- = \frac{\beta k_1 k_2 A_1 A_2 x}{4}$

In this solution second harmonics are generated from the initial two waves. Waves with the sum and difference frequency content (ω_1+ω_2 and ω_1-ω_2) of the two initial waves are also generated (see figure 2.5). The amplitude of the sum and difference frequencies is proportional to the nonlinear parameter. Two distinct groups of techniques have been developed to monitor the generation of the sum and difference frequency waves, and from this the nonlinear parameter. One group measures a change in the frequency modulation due to interaction between the

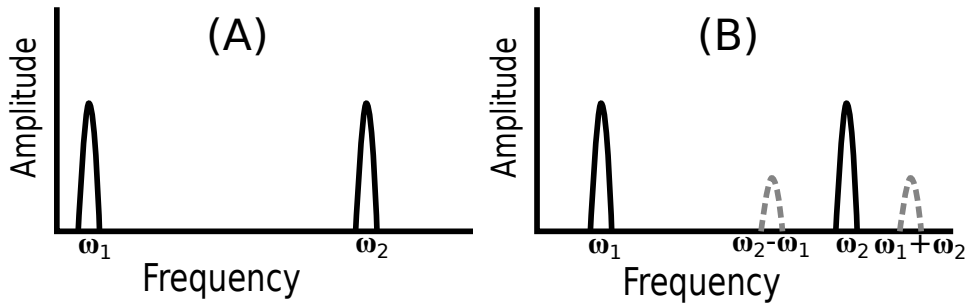

Figure 2.5: Illustration of the generation of sum and difference terms of two waves in a nonlinear material. (A) shows the frequency content of the initial waves. (B) shows the final frequency content of the waves having co-propagated in a nonlinear material.

two waves. The other group measures a phase modulation in one wave due to the interaction with the other.

Frequency domain analysis

Different methods have been developed to monitor the frequency domain changes related to the wave interaction caused by the nonlinear elastic response of the material. The most common monitors the amplitude of the sum and difference frequency components relative to the amplitude of the initial waves [20, 22, 72–74]. By carefully selecting the frequencies of both waves the sum and difference terms can be kept away from harmonic frequencies, removing the impact of instrumentally generated harmonics. Another method monitors the bandwidth of the signal around the initial frequency, any additional sum and difference terms extend this bandwidth [21].

The lower frequency wave (pump) can be generated using several techniques including piezoelectric transducers [72], hammers (producing resonance harmonics) [20], shakers [73,74] and actuators [21,22]. Thermal methods have also been used to produce an equivalent pump wave by causing the surface to thermally contract and expand [75, 76]. Both bulk waves and SAWs have been used as the high frequency

wave (probe).

Phase modulation

When the two wave frequencies are sufficiently separated (approximately $\omega_{HF} > 10\omega_{LF}$ [77]) the separation between the sum and difference frequency becomes very small. This means that when the high frequency wave is acquired only a small part of the difference wave is recovered. This is observed as a change in the phase of the high frequency wave. In the longitudinal case the wave solution can be expressed as:

$$u(z,t) = A_{HF}\cos\left(k_{HF}z - \omega_{HF}t - \Phi_p\right)$$

where

$$\Phi_p(z,t) = \frac{k_{LF}z}{2V_l}\beta\omega_{LF}A_{LF}\sin\left(K_{LF}z - \omega_{LF}t\right)$$

By measuring the phase modulation of the probe wave and the particle velocity of the low frequency wave the nonlinear parameter (β) can be found. This technique has been used to measure the nonlinear response of materials such as fused silica, polystyrene, aluminium and titanium [78–80] and fluids such as water and ethanol [77]. These workers all used bulk waves and measure the nonlinear parameter (β), the length of the probe wave is sufficient to interact with the whole of the pump wave. Staszewski et al. [55] used a shaker to observe a phase modulation in a ultrasonic wave around fatigue crack.

Initial work conducted at the University of Nottingham [81–83] used SAWs to measure the acoustoelastic nonlinear response of aluminium and fused silica. In this case the probe wave is not sufficiently long to interact with the whole of the pump wave, so the probe wave is only subjected to the stress generated by a small region of the pump wave. These stresses can be thought of as static, so

the measurement takes the form of measuring the acoustoelastic coefficient (A). The acoustoelastic coefficient is unique to the wave mode of probing wave [84], in this case Rayleigh waves are used (hence A_R). By altering the interaction point between the waves a range of stress states can be probed.

The co-propagating phase modulation technique is used to measure the nonlinear response in the form of the acoustoelastic coefficient of the material in this work. It was chosen due to its insensitivity to variations in amplitude and systematic nonlinearity. Temperature variations can affect the velocity of a propagating wave and must be minimised.

Acoustoelastic effect

The acoustoelastic effect is the change in the velocity of an acoustic wave with applied stress. The theory describing this effect is well developed and discussed at length by many authors [85–89]. The acoustoelastic effect is directly related to the third-order elastic moduli [86] and has been used to measure them by various authors [84, 87].

By monitoring the velocity of an ultrasonic wave as a sample is stressed the effects of the third-order elastic constants can be found. The stress used can take any form including a propagating wave, hence the inclusion of this technique in the discussion of co-propagating wave techniques. More commonly the stress applied to the sample is induced statically using mechanical uniaxial loading [19, 45, 87, 89, 90] or by bending [42, 88]. A high frequency wave is introduced and the velocity is measured at zero and several other stress states. This technique requires highly sensitive equipment to measure the velocity changes [42]. The fractional velocity change due to stress is small (of the order 10^{-6} MPa^{-1}), so either large stresses (of the order of 100 MPa) must be applied or very sensitive velocity change

measurements must be made (of the order of mms^{-1}, relative to an initial velocity of $\approx 3000\ ms^{-1}$). The latter applies for the technique developed in this thesis.

The acoustoelastic coefficient (the measurement of the level of acoustoelasticity a material exhibits) varies with the direction of propagation [90] of the wave relative to the crystallographic orientation of the material, the wave mode of the probing wave and the applied direction of stress [84]. The acoustoelastic coefficient for longitudinal waves and the nonlinearity parameter (β) have been reported, by Li et al [72], to be linearly related in isotropic materials . Techniques based on the acoustoelastic effect have been used to measure changes in materials due to fatigue by some authors [19,45]. This technique has also been used to measure the internal residual stress in a sample [44]. The velocity of the wave is highly temperature dependent. This is normally mitigated by using large stresses so as to reduce the effect of the temperature variation.

2.4.4 Non-co-propagating wave interaction -Three phonon mixing

Under certain circumstances the energy transfer between waves due to material nonlinearity takes the form of a mode conversion. If two waves, for instance two shear waves (see figure 2.6), intersect at a specific angle a third wave is generated, in this case a longitudinal wave. The interaction occurs at a single location, the two waves do not co-propagate but pass through a point. Full theoretical descriptions of the process have been developed in the literature [91, 92]

The frequency of the generated wave and its wave number are equal to either the sum or the difference of the frequency of the two initial waves and their wave numbers. The optimum angle between the two initial waves to generate a third wave is proportional to the velocity and frequency of the waves involved [91]. This

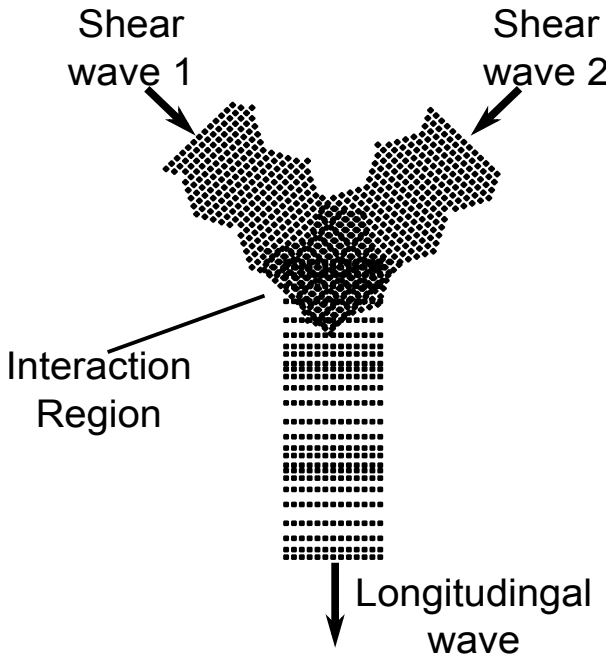

Figure 2.6: Diagram of the nonlinear three phonon interaction process, in this case the interaction takes place between two shear waves to produce a third wave (in this case longitudinal)

has been demonstrated experimentally [93].

During the interaction the wave mode is converted. Many potential different wave mode conversions (e.g. shear and longitudinal waves combining to form a shear wave) exist but most are difficult to implement practically. This process is only related to two of the three isotropic third-order elastic constants (l and m of the Murnaghan). By measuring the amplitude of the generated wave a measure of the nonlinearity of the material can be made. By controlling the beam paths of each initial wave the entirety of the sample's bulk can be investigated. Surface investigations using Lamb waves have been completed by Furgason and Newhouse [94, 95].

This technique is spatially selective (the generated and detected waves end up at different points) and the frequencies of the initial waves can be selected so that the technique is less sensitive to systematic nonlinearity. Monitoring the

amplitude of the generated wave is complicated by variations in coupling efficiency and attenuation. Croxford et al [18] have implemented a system using two shear wave sources to probe both plastic strain and the fatigue process.

2.4.5 Nonlinear elastic wave spectrosopy (NEWS)

This group of techniques arises from the concept that classical atomic nonlinearity (see figure 2.7 B) is not sufficient to describe the changes observed in samples that have undergone fatigue [2]. The techniques are developed from the observation of hysteresis and discrete memory in the stress strain relationship (see figure 2.7 C) in samples that have been fatigued. The mechanism for this effect has not been fully explained, though this is not required for utilisation of NEWS techniques. The additional feature is accounted for in the literature by the addition of an extra term to the stress-strain relationship where:

$$\sigma = \int K(\epsilon\dot{\epsilon})d\epsilon \tag{2.14}$$

$$K(\epsilon\dot{\epsilon}) = K_0(1 - \beta\epsilon - \delta\epsilon^2 - \alpha[\Delta\epsilon + \epsilon(t)sign(\dot{\epsilon})]) \tag{2.15}$$

where $\Delta\epsilon = \frac{(\epsilon_{max} - \epsilon_{min})}{2}$, $\dot{\epsilon} = \frac{d\epsilon}{dt}$ and $sign(\dot{\epsilon}) = 1$ if $\dot{\epsilon} > 0$ else = -1.

β is the contribution from the third-order elastic constants and δ is the contribution from the higher order elastic constants that form the classical nonlinear coefficients. α is the measure of the material hysteresis. Not all materials exhibit this hysteresis, but it is of interest in materials such as rocks and composites. There are two distinct methods of implementing NEWS described in the literature [2, 23, 96] and are discussed below.

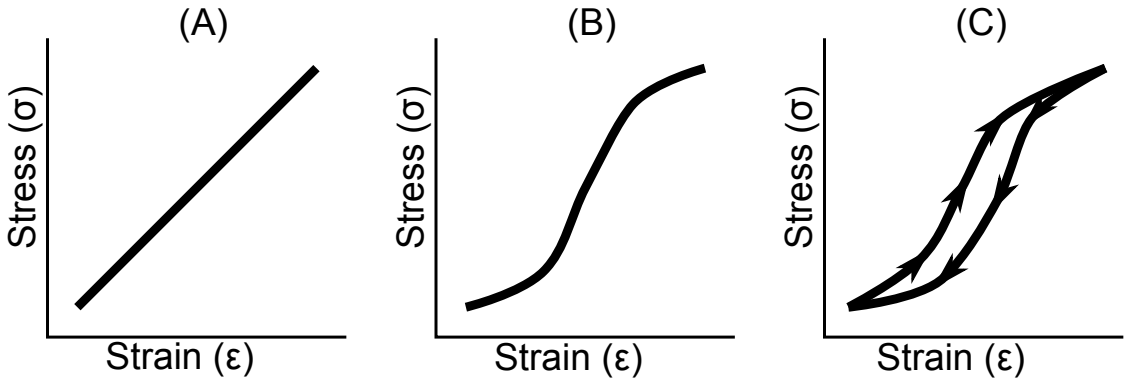

Figure 2.7: Representation of the stress strain relationship for linear (A), classical nonlinear (B) and the hysteresis case (C)

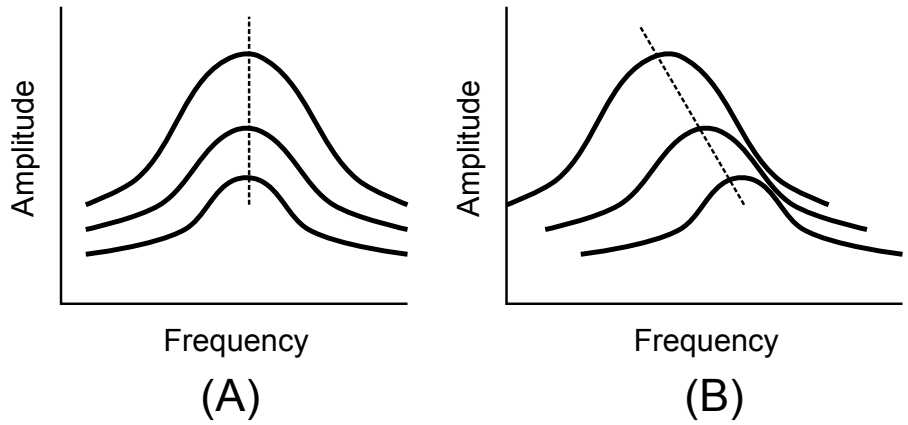

Figure 2.8: Diagram illustrating the change in resonant peak for the linear case (A) and the nonlinear case (B)

Nonlinear resonant ultrasound spectroscopy (NRUS)

Nonlinear resonant ultrasound spectroscopy (NRUS), also known as SIMONRUS [97] where a single mode is used, is similar to the classical harmonic generation technique in that a single wave is propagated into the material. The driving frequency of the ultrasonic source is scanned through to find the resonant peak of the sample. This is repeated at different driving amplitudes. In a linear material the resonant peak will stay at a fixed frequency (see figure 2.8 (A)). In a damaged sample displaying hysteresis, as the amplitude is increased the frequency of the resonant peak changes (see figure 2.8 (B)).

The hysteresis term is given by:

$$\alpha\Delta\epsilon = \frac{f_0 - f_i}{f_0}$$

where $\Delta\epsilon$ is the average strain amplitude, f_0 is the initial natural frequency of the material when undamaged or the lowest resonance mode measured and f_i is the natural mode for the subsequent driving amplitudes. This technique can also be used to investigate the harmonic content of the generated wave [2].

Nonlinear wave modulation spectroscopy (NWMS)

This technique is similar to the frequency modulation co-propagation technique developed for classical nonlinearity. The hysteresis term (α) will cause mixing between two co-propagating waves producing side bands with frequencies of $\omega_1 \pm 2\omega_2$ and an amplitude of $\alpha A_1 A_2$. These side bands are unique from those created by the classical nonlinear effect, by careful analysis of the spectrum the dominant nonlinear effect can be revealed. Van-den-Abeele et al. [98] have shown that under certain circumstances the increase in the $\omega_1 \pm 2\omega_2$ peaks is much more than the increase in the $\omega_1 \pm \omega_2$ peaks with the development of fatigue cracks in a sample. The limitation of the NEWS techniques comes from the difficulty in repeatedly measuring amplitudes of ultrasonic signals and that the hysteresis appears only in certain materials.

2.5 Generation and detection of ultrasound

Previous sections outlined the principles of the use of ultrasonic signals to detect changes in materials. This section describes the methods that have been developed to produce and detect ultrasonic signals in materials. The methods discussed here

include piezoelectric transducers, electro-magnetic transducers (EMATS) and laser generation and detection techniques.

2.5.1 Piezoelectric Transducers

A piezoelectric transducer consists of an active element which is made out of a piezoelectric material. When a mechanical force is applied to a piezoelectric material it generates a voltage. Equally when a voltage is applied to piezoelectric material its dimensions change. Piezoelectric materials exhibit this effect due to their molecular structure, usually a perovskite structure [99]. Below the Curie temperature this comes in the crystallographic form of a tetragonal structure. In this form each unit cell has a dipole, which means each molecular structure has a slight charge differential between each end. When an electric field is applied to these materials the polarized molecules align themselves to the field creating a mechanical force. Using piezoelectric materials acoustically coupled to a material, ultrasonic waves can be generated and detected. One of the main advantages of these transducers is the ability to produce large amplitude waves. The limitation of piezoelectric transducers is that they do not work at high temperatures and require a coupling medium.

2.5.2 Electro-magnetic acoustic transducer (EMATS)

Electro-magnetic acoustic transducers (EMATs) rely on the process of electromagnetic induction to create and detect acoustic waves. In this process a rapidly changing electrical current in a coil induces a magnetic field. This magnetic field will induce an opposite electric current in any nearby conductors, known as eddy currents. If a static magnetic field is also present then, from Lorentz law, a force is created [100, 101] of the form:

$$F = J \times B$$

where J is the induced current, B is the static magnetic field and F is the force per unit. As the induced current in the conductor (sample) rapidly varies with the current in the coil, this creates a rapidly varying force and so an ultrasonic wave. The EMAT does not require physical contact with the sample, so is a non-contact technique. EMATs can function at higher temperatures than piezoelectric transducers.

2.5.3 Laser ultrasound techniques

A wide range of techniques have been developed using optical methods to both generate and detect ultrasound in a material, a good review of the literature can be found in Steve Sharples' PhD thesis [102]. For detection techniques a highly temporally and spatially coherent light source is required and for generation techniques a highly spatially coherent source is required, hence lasers are used. The reasons for the interest in laser ultrasound techniques include:

- Laser ultrasonic techniques are non-contact which gives several benefits. Being a non-contact technique allows laser ultrasonic techniques to probe regions that are not easily accessible, only line of sight is required. Laser ultrasonic techniques also do not load the sample surface. This is beneficial as loading the sample surface can affect the propagation of an ultrasonic wave.

- Laser ultrasonic techniques do not require a coupling medium, which has several benefits. Coupling mediums can cause variability in the measurement, reduce scanning speed (though this can be mitigated by using immersion inspection) and the working temperature of couplants is limited. Couplants

can also be a source of systematic nonlinearity. Removing the need for a coupling medium removes these issues.

- The physical size of transducers used in other techniques limits the spatial resolution, laser ultrasonic techniques are not limited by these factors as the light beams can be made extremely small.

- Laser ultrasonic detection methods can also have a high degree of absolute displacement accuracy in theory, as the measurements can be calibrated against the wavelength of light.

The drawbacks of laser ultrasound techniques include:

- Laser ultrasound techniques offer poor sensitivity when compared to contact methods such as piezoelectric transducers [103].

- Large amplitude waves are difficult to generate without damaging the sample surface. This can be tolerated in some instances, although it is not technically a non-destructive technique.

- Detection sensitivity of laser ultrasonic techniques is low and is affected by the amount of light reflected by the sample surface. Some laser ultrasound detection techniques require a optically smooth surface finish. Interest has grown in developing laser ultrasound detection techniques that can monitor ultrasonic signals on rough surfaces [104, 105]. At present laser ultrasonic systems capable of rough surface measurements are costly (in the region of tens of thousands of pounds).

- Laser ultrasound systems add complexity to the measurement of ultrasound which brings additional cost compared to other ultrasonic techniques such as

piezoelectric transducers and EMATs. Laser ultrasound systems tend to be more complicated to operate and align than other ultrasonic techniques.

Unlike piezoelectric transducers and EMATs, laser ultrasound systems normally require two separate components for detecting and generating the ultrasound. The components can be utilised with other sources/detection system of ultrasound [75].

Optical detection of ultrasound

A range of laser ultrasound techniques have been developed for the detection of ultrasound. Good reviews by Dewhurst [104] and by Royer and Dieulesaint [106] are available. To aid in their description these techniques are divided into two groups. The first group operates by detecting the deflection of a incident light wave by the presence of the wave on the surface of a sample. The second group relies on interferometric (the interference of light waves) process to detect displacements or velocities of the sample surface due to ultrasonic waves.

Deflection technique

Figure 2.9 demonstrates the operating principle of a deflection technique. This technique is also known as the modified knife-edge technique for historical reasons. A beam of light is directed at a sample. As an acoustic wave propagates under the location where the light beam meets the sample it alters the surface gradient, changing the angle of reflection of the light. This alters the intensity of light falling on each of the two photo-diodes. A signal proportional to the gradient of the sample can be produced by taking the difference between the photo-currents induced in each of the photo-diodes. The displacement of the sample surface can be derived from the gradient. This technique is not suitable for rough surfaces, which cause the light beam to be reflected in a speckled pattern. The speckle

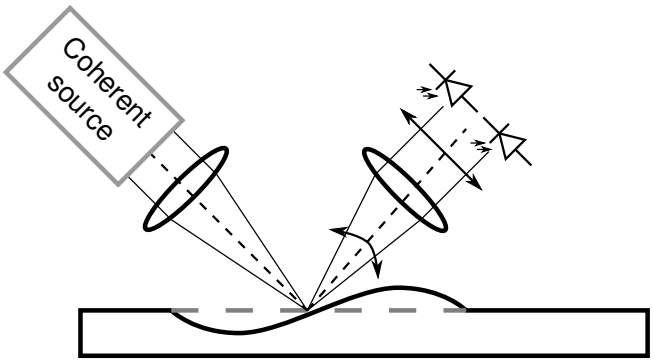

Figure 2.9: Illustration of how a 'knife-edge' detector functions to detect changes in the gradient of the surface

pattern affects the variation in the amplitude of the light at the photo-diode due to the change in gradient of the sample.

Interferometry

Optical interferometry uses the principle of superposition [107]. In this technique the interaction between light waves allows phase changes in a light wave to be converted into amplitude variations. For interferometry to be a practical technique it requires a highly monochromatic and coherent source (a laser is normally used). There are two groups of interferometer. One type measures absolute displacement whilst the other measures the velocity of the displacement of the surface. The two types are discussed below.

Displacement interferometry Displacement interferometers work by interfering a wave reflected by a material surface with a reference wave. Several different types of displacement interferometer exist including the Michelson, Mach-Zehnder and Sagnac interferometers. To illustrate the principles of a displacement interferometer a Michelson type is discussed. A Michelson interferometer takes the form seen in figure 2.10. When the sample surface is displaced this changes the path

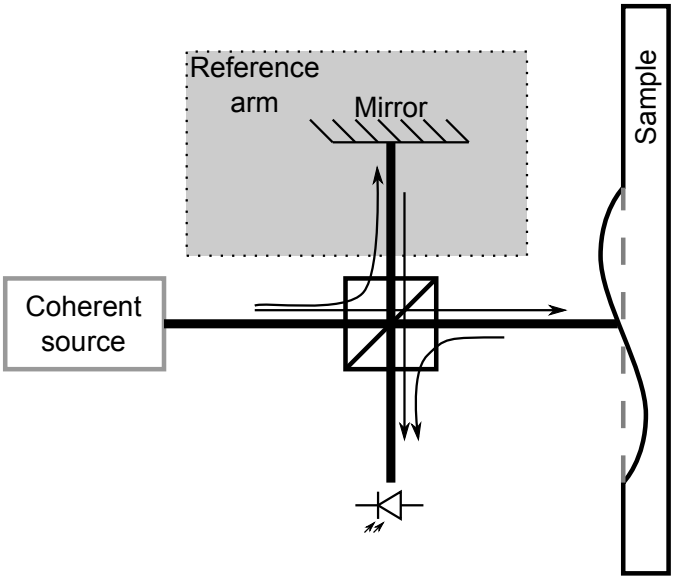

Figure 2.10: Schematic of a Michelson interferometer

length of one arm of the interferometer. The change in path length causes a change in relative phase between the two arms, affecting how the beams interfere when they are recombined and so the intensity of the recombined light. The amplitude of the signal from the photo-diode is proportional to the displacement of the surface.

Displacement interferometers are negatively affected by the speckle pattern created by a rough surfaces. This is because the speckle pattern can be considered to consist of a large number of sources that have a random phase relation, so only a small fraction of the reflected light (approximately one speckle) can be used due to coherence considerations.

Velocity interferometry Velocity interferometry detects the small shift in the frequency and so wavelength of reflected light from a moving sample surface due to the Doppler effect [107]. This is done by mixing the reflected light wave from the sample with a slightly time delayed wave from the same location. When these beams are mixed the resultant intensity of the light is proportional to the velocity of the surface of the sample. One method used to produce a time delay is to

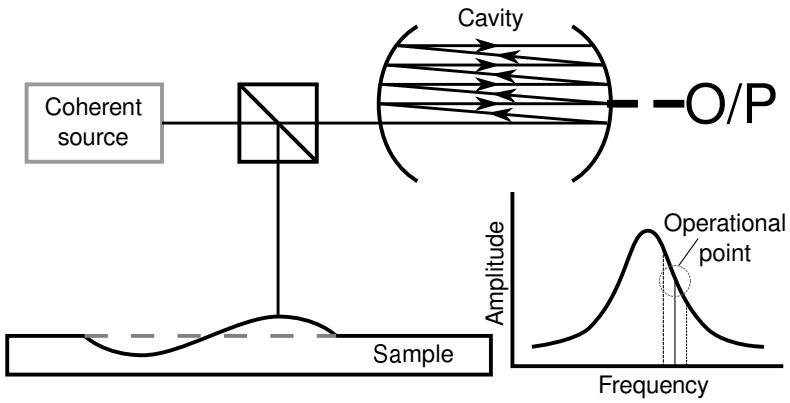

Figure 2.11: Schematic of a Fabry-Pérot interferometer. Note the cavity is shown where the light reflects and interacts with one another. A diagram of the transmission amplitude against frequency with the operating point shown in the bottom right.

reflect the beam many times across the volume where the beams interfere. This is how a Fabry-Pérot interferometer (also known as an étalon) functions. The waves returning from the surface are reflected multiple times and interfere with each other in a resonance cavity composed of partially reflecting mirrors (see figure 2.11). A change in wavelength alters the interference pattern between the waves, changing the reflectance or transmittance of light from the cavity.

The benefits of using a velocity interferometer come when working on a rough surface that produces a scattered light pattern. This is because the velocity interferometer 'self-references' so the speckle effect caused by the scattered light is combined with itself in the interferometer rather than with a Gaussian reference.

Laser Generation

The generation of laser ultrasound occurs through two main groups of physical processes or regimes. Both regimes involve the introduction of light from a spatially coherent source to the sample surface. The light is both reflected and absorbed by the sample. The absorption of the light produces heat.

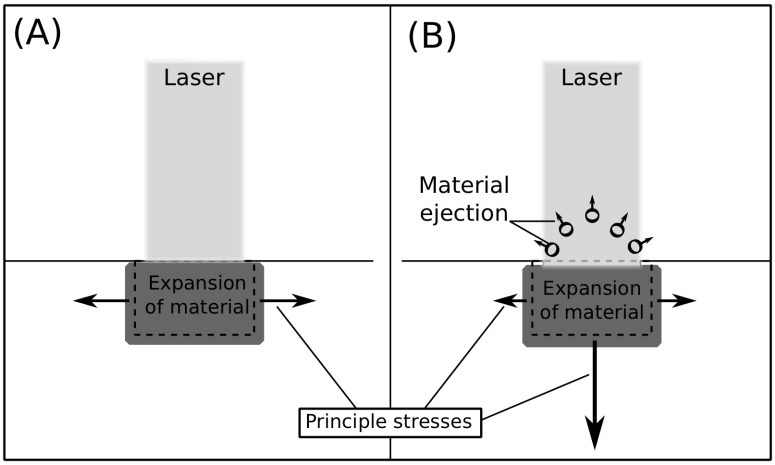

Figure 2.12: Diagram depicting the different generation regimes for laser ultrasound. (A) represents the thermoelastic regime. (B) represents the ablative regime. Arrows indicate principal stresses generated

In the thermoelastic regime the power density is not sufficient to cause vaporisation of the sample. In this regime the localised heating causes the local volume to expand, generating stress that propagates away from the illuminated material, generating both bulk and surface waves (see figure 2.12 (A)). This regime is non-destructive and so is used in this work to generate the probe waves.

In the ablative regime significantly higher power densities are used, generating higher temperatures. In this regime the thermal energy produced raises the temperature of the sample, exceeding the latent heat of vaporisation for the material surface, so ablating it. As the sample ablates, plasma is ejected from the surface (see figure 2.12 (B)). From Newtons second law of motion a resultant force is introduced into the sample. Both bulk and surface waves are produced in this process. Waves perpendicular to the surface are far more effectively produced in the ablative regime than in the thermoelastic regime.

Generation configurations A range of generation configuration have been developed throughout the literature. The different types of configurations control the type, amplitude and adaptability of waves produced. The complexity of each configuration varies.

The simplest laser generation configuration consists of a point source produced by focusing a laser into a spot on the sample [108]. This technique produces both bulk waves and surface waves, which expand radially from the location of the spot. Using a point source it is difficult to generate large amplitude waves without ablating the surface and impossible to specifically select the wave mode generated.

Imaging the light through a cylindrical lens produces a single line of illumination on the sample [109]. This both serves to spread the energy over the sample surfaces and control the direction of propagation of the SAWs that are generated. This technique can also easily cause ablation.

By spreading the incident laser energy over the sample surface a larger total energy can be applied without ablation. Selecting the distribution pattern of the laser energy gives control over the principal wave mode generated (other modes may still be generated but not as efficiently) and the direction of propagation of the wave. For instance by imaging lines onto a sample surface a SAW can be generated. The separation between lines can be used to control the wavelength of generated ultrasound.

By generating multiple lines across the sample even higher energy levels can be used. Several different techniques exist to produce multiple line illumination for the production of SAWs. Some of these techniques include the use of amplitude gratings or masks, multiple fibre-optic fibres [110], interferometry using two interfering light beams, diffraction gratings [111], computer generated holograms [112, 113] and spatial light modulators [114].

Each of the techniques discussed above have relative advantages and disadvantages. The aim of this work is to develop a robust, effective and low cost system, to this end the high frequency probe wave is generated using an amplitude grating to spatially modulate the light. This gives the advantage of being a relatively low cost non-contact system with high spatial resolution.

2.6 Summary

In this chapter the fatigue process in materials has been outlined, the importance of the ability to monitor it is also discussed. Material microstructure and elastic constants were described as they have an important effect in the formation and detection of fatigue. A range of non-destructive testing techniques are outlined with detail given on those techniques capable of detecting the fatigue process.

Ultrasonic techniques are of particular interest due to their potential for the detection of fatigue. Linear ultrasonics techniques are initially discussed including attenuation and velocity measurements. Linear ultrasonics are relatively insensitive to the fatigue process. Nonlinear techniques are sensitive to the third and higher order elastic constants. The fatigue process affects the third and higher order elastic constants. A variety of nonlinear techniques are discussed including self referencing harmonic generation, co-propagating, non-copropagating and hysteric techniques. Finally a range of ultrasonic generation and detection techniques is discussed.

A technique using two waves co-propagating is developed in this work. The effect of the material nonlinearity causes the phase of one of the waves to be modulated by the other wave. The interaction allows the measurement of the acoustoelastic coefficient for Rayleigh waves (A_R) of a material. The A_R of a

material is proportional to some of the third-order elastic constants. The aim of the work in this thesis is to investigate the effect that the fatigue process has on the acoustoelastic measurement.

Chapter 3

Instrumentation

3.1 Introduction

In this chapter the design of the instrumentation in terms of optical and electronic configuration is discussed. The generation and detection systems are outlined along with the high speed control electronics. The physical equipment configuration was developed synchronously with the experimental method discussed in chapter 4.

3.2 Experiment overview

The collinear technique used to investigate the acoustoelastic coefficient of a material outlined previously (see chapter 2) requires the co-propagation of two acoustic waves. The measurement takes the form of monitoring the change in velocity of a probe wave due to the localised stress field of a pump wave, the level of interaction between the two waves gives a measurement that is related to the higher order elastic constants [78]. The system overview can be seen in figure 3.1.

The pump wave that stresses the material is generated using a contact transducer (see section 3.3.1). The probe wave that investigates the stress state is

generated using a laser ultrasonic technique (see section 3.3.2). The two waves co-propagate on the sample. They are then detected by two separate detectors, due to bandwidth limitations (see section 3.4). The temporal point at which the two waves interact is controlled by precisely timing when the two waves are generated relative to one another, the point at which the two waves are generated is controlled by a Field Programmable Gate Array (see section 3.8). Changing the point of interaction between the two waves allows a range of stress states to be probed. Measuring the variation in the velocity of the probe wave with the change in induced stress, due to the pump wave, produces a measurement of the acoustoelastic coefficient.

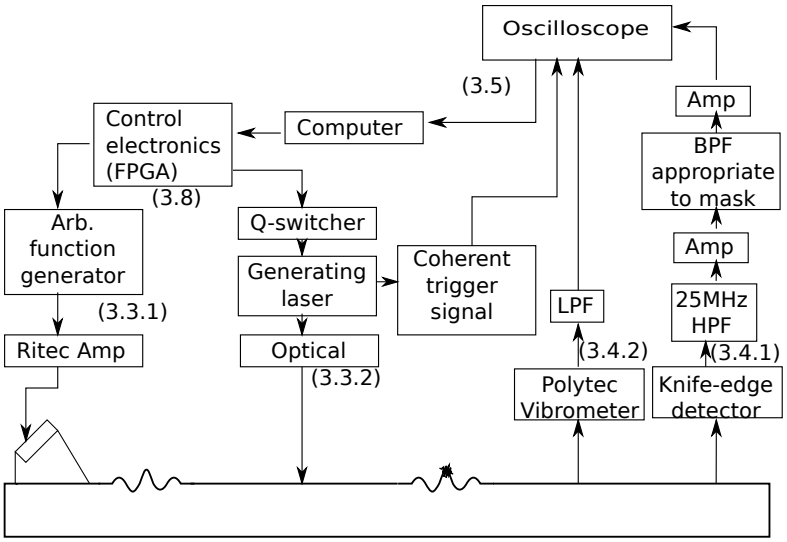

Figure 3.1: System diagram including (3.3.1) Pump wave generation, (3.3.2) probe wave generation, (3.8) control electronics and (3.4) detection systems. Numbers correspond to the sections detailing each component.

3.3 Generation

Using the collinear technique two waves are required to co-propagate. These two waves are generated using different techniques which are discussed here.

3.3.1 Pump wave generation

The low frequency high amplitude pump wave that stresses the material as it propagates is generated using a contact piezoelectric transducer (a range of transducers were used for different frequencies including the Olympus- Panametrics A414S-SB for 0.5MHz waves, A402S-SB for 1MHz waves and the A404S-SB for 2.25MHz waves). The transducer is coupled to the sample via a Perspex wedge at an angle above the second critical shear angle, so a Rayleigh wave is generated. The centre frequency of these transducers for these experiments is 0.5, 1 and 2.25MHz. These frequencies are chosen for various reasons including the availability of affordable transducers and amplifiers that could produce a large stress field. Another reason these frequencies were chosen was to allow a large frequency gap between the pump and probe wave, whilst not overly reducing the resolution of the instrument. The large frequency gap between the waves is advantageous because separating the two waves via filtering is simpler and it allows the modulation of the probe wave to be seen as a phase shift [77].

A contact transducer was chosen as the method to stress the sample over other techniques, such as ablative laser generation, so the generation of the pump wave would not permanently damage the sample and affect any future measurements. Producing the pump wave with a piezoelectric transducer also allows a stress wave to be produced of sufficient amplitude so as to induce a large velocity change that can be measured.

Bonding

The transducer is bonded to the wedge and the wedge is bonded to the sample by Phenyl salicylate, which removes the requirement to use a liquid couplant (see figure 3.2 A). This is advantageous as liquid couplants are a known source of nonlin-

earity [65]. Other methods of coupling the low frequency waves into samples were also investigated. Edge coupling [65] by using a standard longitudinal transducer to couple Rayleigh waves into a sample was explored. The transducer is coupled to the sample by means of clamping it to the edge of a sample at a set angle which is above the second critical shear angle (see figure 3.2 B). This method was investigated with and without a coupling medium. The resultant wave forms were recorded using a Polytec interferometer as described in the pump wave detection section (see section 3.4.2).

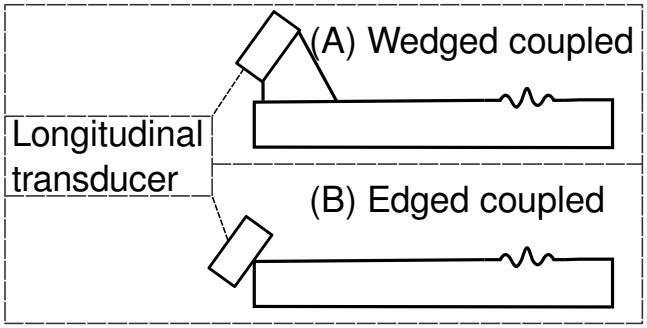

Figure 3.2: Diagram representing two methods of coupling the pump wave transducer to the sample. Using either a fixed angle wedge (A) or by side coupling the transducer (B)

The displacement of the waves can be seen in the figure 3.3, the generation source is the same for both waves so each waveform can be seen to represent the efficiency of the coupling. It is found that the benefits of edge coupling were negligible compared to the use of bonded transducers, especially when the difficulty of positioning and maintaining the angle to couple the waves into the sample was taken into account.

Electronic generation

The initial pump wave signal is generated by an Agilent 33250A signal generator that is triggered by the timing electronics. The pump wave signal consists of a

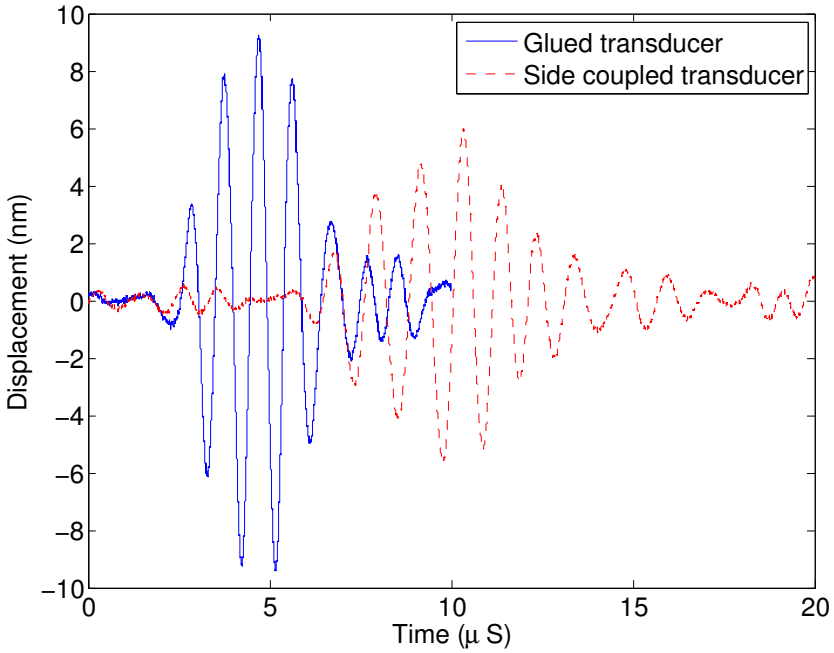

Figure 3.3: Comparison of displacements generated using glued wedge (solid blue line-) and side coupled transducers(dashed red line –)

three cycle packet with a peak voltage of 550 mV. This was then amplified by a Ritec RPR-4000 gated amplifier and the output sent to the transducer, the linear bandwidth of the amplifier is 50kHz to 2MHz. With this configuration a gain of 67dB is achieved at 1MHz.

3.3.2 Probe wave generation

The high frequency probe wave is generated using a laser ultrasonic technique. This gives several advantages including high spatial resolution and allowing the technique to be partially non-contact. This allows the sample surface to be easily scanned in a high level of detail. The laser ultrasound generation system is outlined in diagram 3.4.

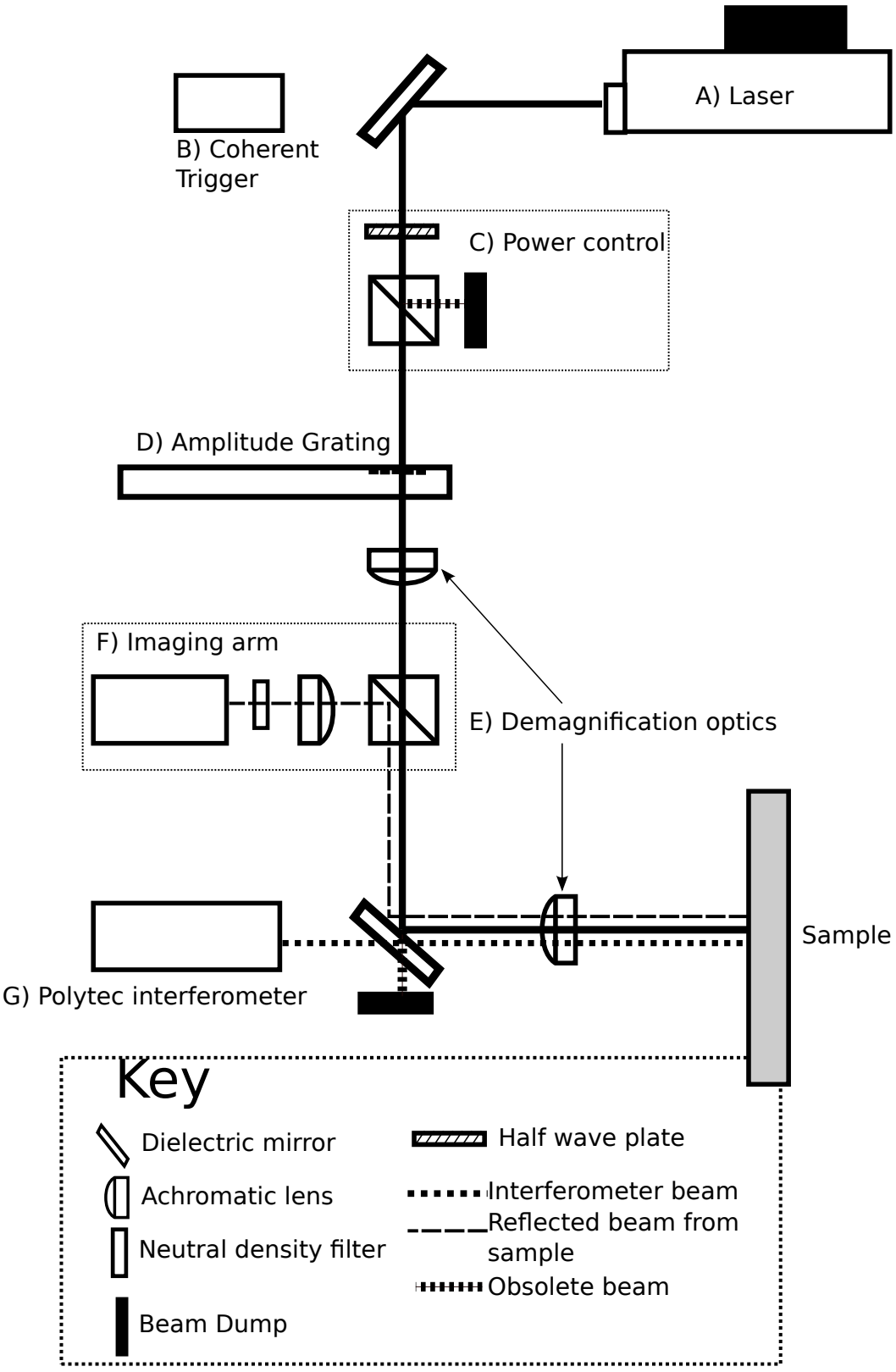

Figure 3.4: Generation optics schematic

Generation source (A)

A Q-switched laser with a wavelength of 1064nm is used to produce a pulse of 10ns duration (giving a bandwidth of 100MHz). The Q-switcher is controlled externally by the high speed control electronics which allows precise control over the point of emission for the laser relative to the generation of the pump wave. The laser used is an Elforlight FQ1000.

Coherent trigger detector (B)

Timing is very important in this experiment as highly accurate fractional velocity measurements must be made which require highly accurate timing measurements. The initial triggering point from which all timing measurements are made in this experiment is the optical pulse from the Q-switched laser which is used to generate the high frequency wave. This event is recorded by the coherent trigger. The coherent trigger is positioned behind a dielectric mirror which sits in front of the Q-switched laser angled at 45°. The dielectric mirror is 99.5% efficient at the 1064nm wavelength of the laser. This means that the majority of the power from the laser is reflected to the rest of the experiment, but a tiny proportion is transmitted through the mirror to the the coherent detector. This detector consists of a single photo-diode.

The signal it produces consists of a single peak with a duration and amplitude that is related to the intensity of the pulse produced by the laser. The oscilloscope used in the experiment to record the acoustic signals is triggered from this single peak.

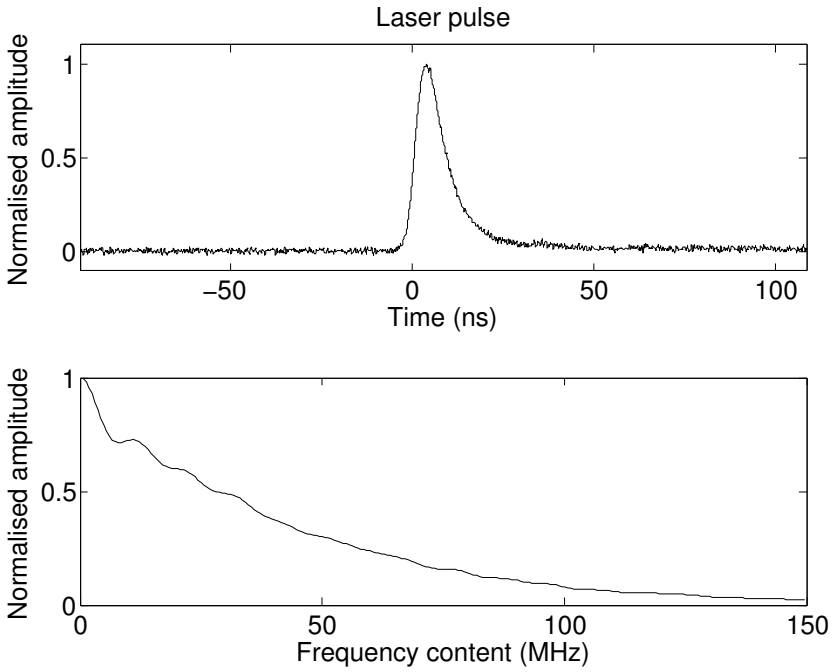

Figure 3.5: Laser pulse, time and frequency domain content

Power control (C)

The 99.5% of the power produced by the Q-switch laser that is reflected from the mirror to the rest of the experiment travels into the power control optics. This allows the level of power involved in the experiment to be controlled so ensuring that the process is entirely non-destructive and the rest of the probe wave generation arm is easier to align. The power control optics consist of a half wave plate placed before a Glan-Taylor prism. The Glan-Taylor prism will either reflect or transmit any light entering it dependent upon its polarization. The polarization is separated into its ordinary (o-ray) and extraordinary (e-ray) ray polarizations respectively [115]. In the case of the Glan-Taylor prism the e-ray polarization is transmitted and o-ray polarization is reflected. As such in this configuration light from the laser (initially vertically polarized) will pass through the half wave plate and will be polarized according to the the rotation of the plate, this will then be

passed into the Glan-Taylor prism and the e-ray components are transmitted and the o-ray components are reflected (see figure 3.6). This allows the amount of power transmitted to the rest of the experiment to be controlled by rotating the half wave plate. A Glan-Taylor is necessary, as opposed to using a polarised beam splitter, because of its ability to deal with high power densities without ablating.

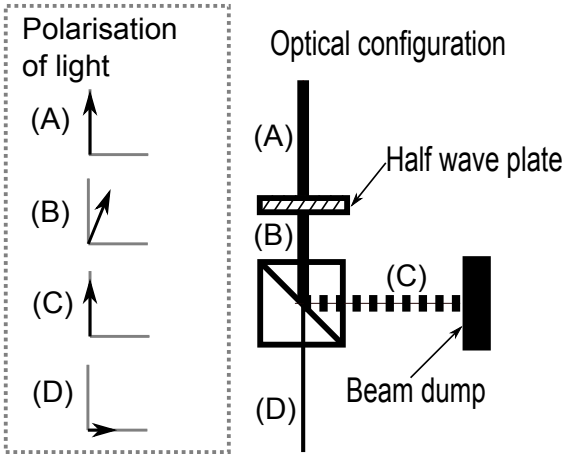

Figure 3.6: Optical configuration of power control optics including a polarization description

Amplitude grating (D)

The pulse is subsequently directed through an adjustable iris and then through an amplitude grating with a specific line spacing. The amplitude grating consists of a piece of quartz with a coating of chrome. Using a standard lithography technique available from JD Photo-Tools a pattern is formed in the chrome layer by removing areas of the chrome. This is a highly precise technique with an accuracy of 8μm.

The chrome top layer will reflect any incident light whilst anywhere the chrome is not present will transmit the light through the quartz. This produces a spatially modulated pulse. Several of these gratings are included on a single piece of quartz (known as a mask) in a circle so that different acoustic wavelengths can be generated by rotating the mask so that the correct grating is in the path of the beam.

Both arcs and straight line patterns of different wavelengths are included so as to allow the choice between focused and plane wave sources. Each grating pattern is 8mm by 10mm. The initial beam from the Q-switched laser is 2mm in diameter. The laser beam divergence is quoted as a 1mRad, it was found that by the time the beam reached the mask it is of sufficient diameter to illuminate a significant section of the 10mm diameter grating. The set line spacing when imaged onto the sample creates localised heating and expansion that generates an acoustic wave. The grating will generate ultrasonic signals most efficiently at the wavelength that matches the line spacing of the mask. However due to the limited number of lines on the grating other frequencies are also generated giving the generated ultrasound a finite bandwidth. See figure 3.7.

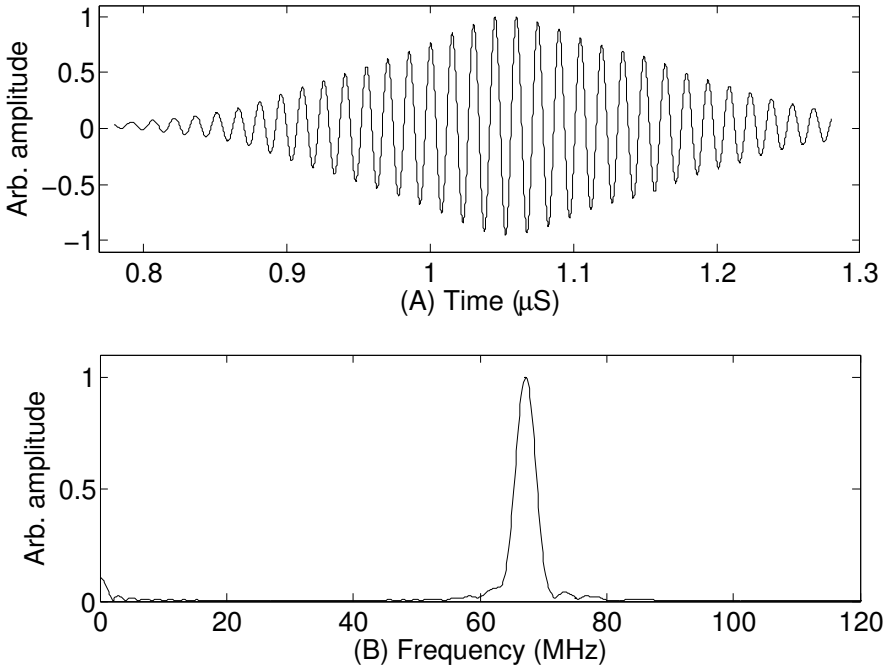

Figure 3.7: Example of generated ultrasonic wave packet (A), example of frequency content of generated ultrasound (B)

The laser produces a TEM_{00} beam which is effectively a 2D Gaussian envelope, this results in an increased power at the centre of the mask. The result of this is

that the ultrasound produced has a Gaussian packet (see diagram 3.8).

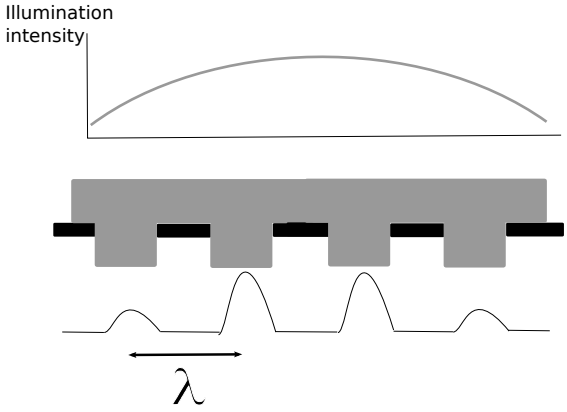

Figure 3.8: Localised heating due to modulated light from amplitude grating causes localized expansion and so generates an acoustic wave. Due to TEM_{00} nature of the beam, ultrasound produced has a Gaussian envelope.

Demagnification optics (E)

The resultant pattern is imaged onto the sample by demagnification optics. The demagnification optics consist of a pair of achromatic lenses with a focal length of 200mm and 75mm. With a collimated input into the pair, thin lens approximation gives a magnification of -0.375. The imaged pattern on the sample is 1 mm in diameter dependent on the setting of the adjustable iris prior to the amplitude mask.

$$\frac{D_2}{D_1} = -\frac{F_2}{F_1}$$

CCD arm (F)

The CCD (Charge Coupled Device) arm allows the monitoring of the positioning and focusing of the generation arm and detection optics. The CCD arm consists of a polarizing beam splitter that is positioned in between the demagnification optics. This allows light from the amplitude mask (having already been polarized by the

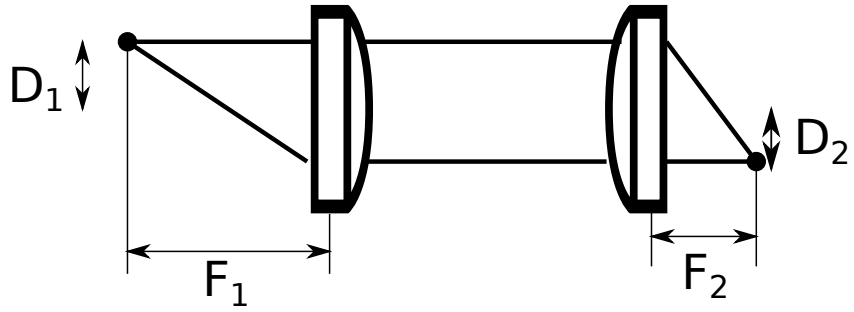

Figure 3.9: Pair of achromatic lenses separated making a magnification system. Focal lengths F_1 and F_2 determine the magnification

power control optics) directly through to the final demagnification lens and onto the sample. The reflected light from the sample is partially depolarised, so it is polarized in such a way that instead of passing through the polarizing beam splitter it is reflected at 90° to the direction that it entered. This reflected light then passes through an achromatic lens positioned at such a distance from the CCD sensor so that the effective focus for the CCD is infinity, allowing the image of the sample to be formed on the sensor. In between the CCD sensor and the achromatic lens is a neutral density filter that limits the intensity of the light falling on the CCD to protect it from damage and over saturation.

3.4 Detection systems

This experiment has two requirements with regard to detection. The first requirement is the detection of the displacement of a relatively low frequency pump SAW to discern the stress applied to the sample. The absolute displacement needs to be known, various commercial detection systems are available to this end. The second requirement is the detection of the phase of a high frequency SAW, where the absolute displacement is not required. There are few commercial systems available that meet both of these requirements. Initially an knife-edge detector produced

in-house was used to do both. Details of its calibration to measure displacements can be found in appendix A. A Polytec interferometer is also installed in the system to confirm the calibration of the knife-edge. On testing it was found that the uncertainty in the detection of the pump SAW using the knife-edge was very high compared to the Polytec interferometer (see section 3.4.2). As both could be used simultaneously for measurements the experimental procedure was modified to include this. Optical detection systems were used primarily due to the aim of developing a non/minimal-contact technique, removing the need for couplant and the need for high spatial resolution for imaging.

3.4.1 Probe wave detection

The high frequency probe SAW is detected by a non-contact knife-edge detector. This detector has a wide bandwidth (400 kHz-450 MHz). The primary role of knife-edge detector is the detection of the high frequency probe SAW. The knife-edge detector is mounted on computer controlled X-Y stages (PI M-605.2DD 50mm travel 0.1μm resolution linear encoder) to allow the sample to be scanned. The principle of operation of a knife-edge detector is discussed in section 2.5.3. Here the optical and electrical configuration are explored.

Optical configuration

A continuous wave laser source is used for the knife-edge detector, in this experiment a doubled neodymium-doped yttrium aluminum garnet (2×Nd-YAG) laser, producing a continuous waveform (CW) 532nm wavelength, is used. The maximum output power of this laser is 400mW, with the ability to control output power levels between 50 and 400mW. This was fibre coupled with an efficiency of 65% giving a maximum output of 260mW. The fibre outputs a 0.7mm width beam

which is then expanded by a set of beam expanding lenses (with the same function as the demagnification lenses in section 3.3.2) to 2.1mm. This is done to ensure the optimum focused spot size of the beam for the detection of the high frequency ultrasound (wavelength of 34μm at 86MHz on aluminum). The efficiency of the detector is related to the size of the focused spot relative to the acoustic wavelength that is being detected. The beam is then focused onto the sample by a 60mm focal length lens, resulting in a NA of 0.0175. Using the general relationship:

$$NA \simeq \frac{\lambda_0}{\pi r_0}$$

where $2 \times r_0$ is the diameter of the beam at its narrowest point and λ_0 is the wavelength of laser in a vacuum. This gives a focal spot size of 9.7μm.

The optimum detection [116] takes place at

$$\frac{r_0}{\lambda_{SAW}} = 0.279$$

Giving a minimum theoretical λ_{SAW} of 34.7μm. With a relatively low numerical aperture we gain a detector that is less sensitive to lower frequency disturbances whilst still being sensitive to the high frequencies of the propagating ultrasound. The reflected light from the sample is then collected by a second 60mm focal length lens to produce a collimated beam, this is then focused by a third lens with a focal length of 80mm.

Electronic configuration

The photo-diodes convert the light falling on them into an electrical current. The physical size of the diodes dictate how rapidly they can respond to changes and hence their bandwidth. In this system a Hamamatsu S6058 quad photodiode is

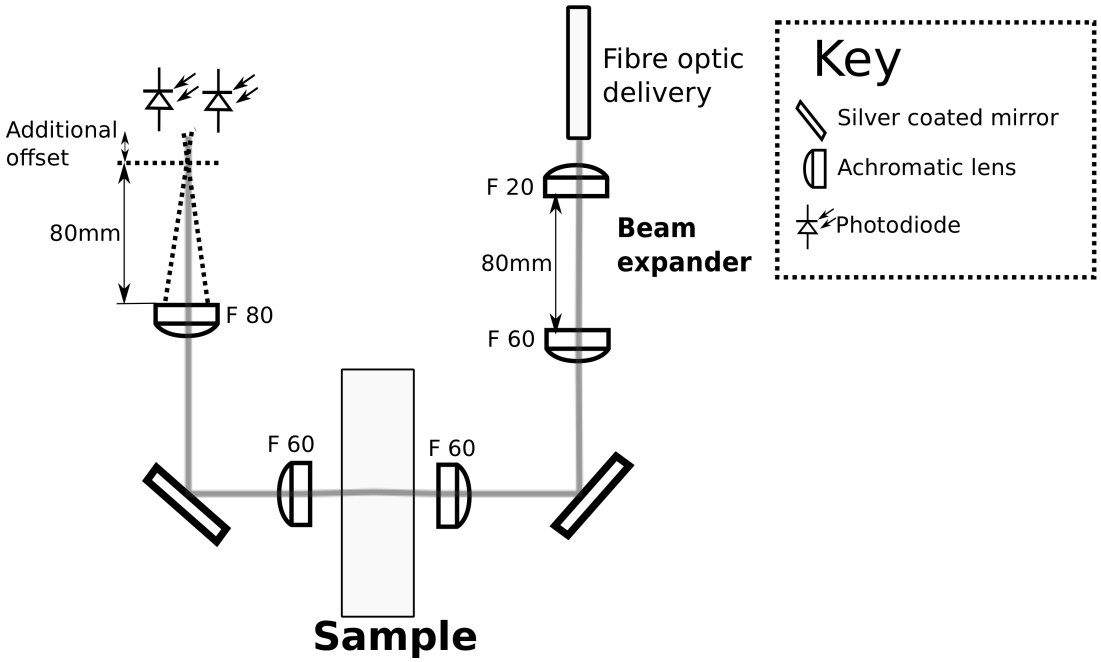

Figure 3.10: Optical configuration of knife-edge detector

used, each quadrant measuring 0.295 by 0.595mm, though only two are used.

The diodes are reverse biased via resistors so as to improve their response by reducing their capacitance. The two photo-diodes are connected to the positive rail by a 510Ω resistor so as to limit the maximum current they can draw and so protect them. The output of the diodes are connected, via a 100Ω resistor, to either side of the primary coil of a transformer. An Minicircuits ADT4-6T transformer with a bandwidth from 60kHz to 350 MHz is used. When the incident light on the photo-diodes from the sample is stationary (there is no SAW propagating under the knife-edge beam) then there is no variation in the current of the two diodes, therefore no current is induced in the secondary winding of the transformer. However when a SAW does perturb the optical beam this alters the amount of light falling on each photo-diode and so the amount of current produced by each photo-diode, creating an alternating current in the primary winding of the transformer which induces a current in the secondary winding. The secondary winding is connected

to a MAV-11 monolithic amplifier with a gain of 12.7dB. The bandwidth of the amplifier ranges from 50MHz to 1GHz, the lower cut off being controlled by the coupling capacitors used, in this case 300kHz. The knife-edge is less efficient at lower frequencies as it is sensitive to the the gradient of the slope of the sample. At lower frequencies, for a given amplitude, the gradient and so the output voltage of the knife-edge is lower.

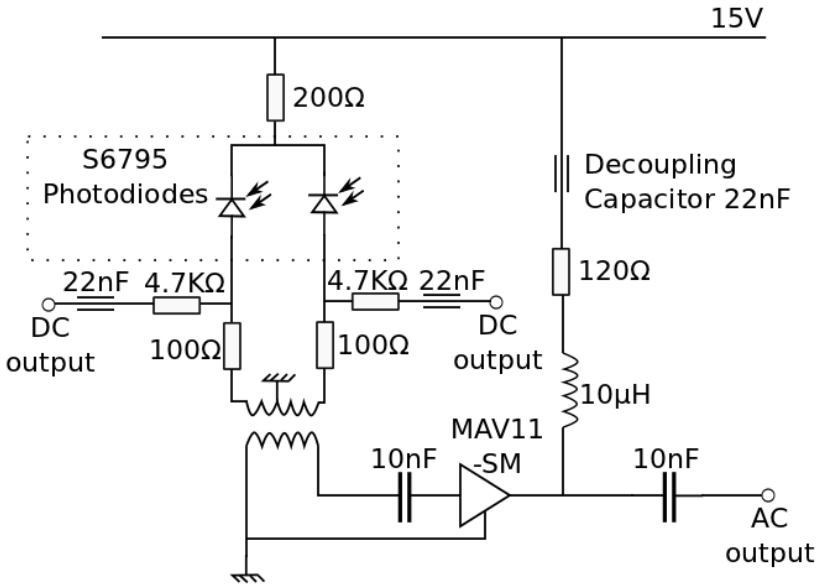

Figure 3.11: Electronic configuration of knife-edge detector

DC outputs from each photo-diode are also included through two resistors. The DC signal goes into a difference and a summing amplifier. The values of the output of the amplifiers are displayed on voltmeters. The summing amplifiers output is useful for determining the amount of light returning from the sample and is recorded by the oscilloscope for use if necessary for calculation of displacement of the waves or in explaining signal drop out. The output from the difference amplifier is useful in determining the spot location on the photo-diodes and is useful to balance the level of light on each detector and ensure its optimum operation. The output from both amplifiers is also useful in ensuring neither photo-diode is

saturated.

The AC output from the MAV-11 amplifier is coupled into a high pass filter to remove any frequency associated with the detected pump SAW and any low band noise. Removing evidence of the pump SAW is necessary before going into the rest of the amplification chain otherwise the amplifiers are over driven and no longer amplify linearly. If the knife-edge is being used to measure the displacement of the pump SAW an AC splitter is used here to separate the signal. One half is then amplified and recorded to determine the displacement, the other half goes off to be filtered. The AC output signal from the filter is then amplified by a ZFL500LN+ Minicircuits amplifier (bandwidth of 0.1-500 MHz and a gain of 28dB), the output is band-passed filtered, and further amplified by a ZFL500LNH+ amplifier (bandwidth of 10-500MHz and a gain of 20dB). Finally the signal is input into a TTL driven switch, this is controlled by the main control board for the experiment and its purpose is discussed later (see section 3.8). The overall gain for this amplifier filter chain after the output from knife-edge detector for in band signals is 39dB including the loss from the filters and the splitter.

Calibration

The measurement of the knife-edge detector is proportional to the gradient of the sample. It is theoretically possible to convert this measurement of the gradient into an absolute displacement using geometrical optics analysis. The absolute displacement can be used in calculating the stress induced by the propagating pump SAW. The calibration of the knife-edge detector is outlined in appendix A. The absolute displacement of the SAW is related to the output of the knife-edge

detector as follows:

$$A_{SAW} = \frac{\lambda_{saw}(NA)Z_{DC}}{8kG_{MAV}G_{AMP}}\frac{V_{scope}}{V_{DC}} \tag{3.1}$$

$$A_{SAW} = C_{cal}\frac{V_{scope}}{V_{DC}} \tag{3.2}$$

where C_{cal} is the calibration constant, (NA) is the numerical aperture of the knife-edge detector, k is the wave number of the acoustic wave, λ_{saw} is the wavelength of the acoustic wave, Z_{DC} is the impedance of the knife-edge detector, G_{MAV} is the gain of the MAV amplifier in the knife-edge, G_{AMP} is the gain of the amplifier chain after the knife-edge detector, V_{DC} is the summed DC voltage from both arms of the knife-edge detector and V_{scope} is the time varying signal recorded by the oscilloscope. Where $V_{scope} = V_{AC}G_{AMP}$, V_{AC} being the AC output from the knife-edge detector (see figure 3.11). This gives a relationship between the displacement of the SAW, the DC voltage and final voltage recorded scope.

3.4.2 Pump wave detection

Polytec interferometer

To confirm the calibration of the knife-edge detector, an interferometer is also included in the design of the system. An interferometer enables the measurement of the displacement caused by the pump SAW, which can be compared to the output from the knife-edge detector or used to calculate the induced stress. The interferometer used is a heterodyne interferometer produced by Polytec (OFV-5000), it uses a helium-neon laser with a central wavelength of 633nm. The interferometer gives a calibrated output in terms of displacement in nm. The decoding card used in the Polytec interferometer is the Polytec DD300 which has a maximum bandwidth of 24 MHz. This particular card is limited to an amplitude range of $\pm$75 nm

with a stated resolution of 0.2nm.

The Polytec interferometer beam is injected into the main optical generation arm of the instrument. The beam is introduced to the generation arm through the back of the final mirror which angles the generation arm down onto the sample. This is possible as the mirror is a dielectric mirror with a central wavelength of 1064nm. The infra-red generation beam is reflected whilst the beam from the interferometer passes through the mirror. Due to this configuration the positioning of the interferometers spot can only be a maximum of 2.5mm away from the center of the generation spot. As the knife-edge detector is on a separate x-y position it can be positioned much further away. This leads to difficulties in relating the displacement of the pump SAW measured to the velocity shift of the high frequency SAW. Calibrating this difference is discussed in section 4.2.5.

Confirmation of calibration of knife-edge detector

On page 66 the calibration of the knife-edge detector is introduced, the displacement of a propagating SAW is related to the measured V_{DC} and V_{SCOPE}. Here an investigation into the calibration is conducted by comparing the output of the Polytec interferometer to V_{DC} and V_{SCOPE}. The Polytec interferometer gives a displacement measurement which is independent to the amount of light returning to the detector. If the light level returning is too low then no measurement can be made.

To investigate the calibration of the knife-edge detector, measurements of a 1 MHz SAW are made at various locations on a sample with both detectors. The outputs are compared. Figure 3.12 shows the 1 MHz frequency spectrum content at different locations on the sample. Figure 3.13 compares the output of the interferometer to the knife-edge.

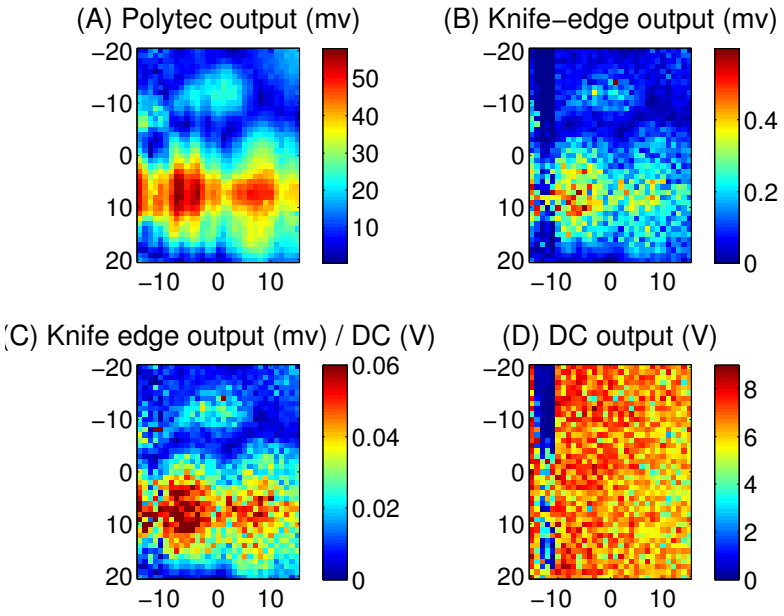

Figure 3.12: Area scans of displacements from a wedge-coupled piezoelectric contact transducer operating at 1 MHz for two detectors. (A) is the voltage of the 1 MHz frequency component from the Polytec interferometer. (B) is the voltage of the 1 MHz frequency component from the knife-edge detector. (C) is the the voltage of the 1 MHz frequency component from the knife-edge detector divided by the DC voltage. (D) is the DC from the summing amplifiers.

The correlation between the two detectors is relatively low (see figure 3.13). This is because the knife-edge detector is sensitive to the gradient of the sample. At lower frequencies this gradient is smaller, making the knife-edge detector less sensitive. This results in a high level of uncertainty when measuring the displacement of the pump SAW using the knife-edge detector. A solution is to use the interferometer to measure the displacement of the pump SAW and the knife-edge to detect the phase of the probe SAW (as the bandwidth of the interferometer is to low to detect the probe SAW). This introduces complications in relating the displacement of the pump SAW to the shift in arrival of the probe SAW (see section 4.2.5).

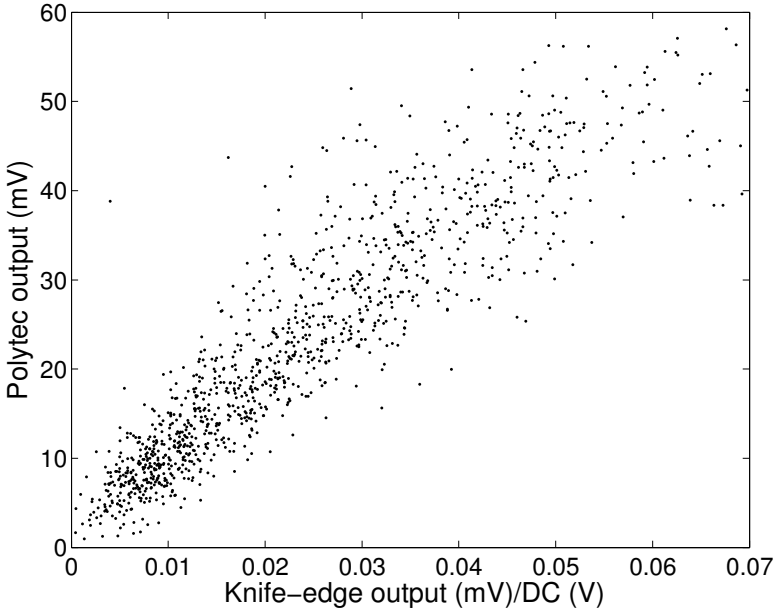

Figure 3.13: Comparison of the 1 MHz component of signal from the knife-edge detector divided by the V_{DC} and the Polytec interferometer. The correlation for the points should be high, however this is not the case as a high level of scatter is observed.

3.5 Acquisition of signals

The coherent trigger signal, the pump wave displacement signal from the Polytec interferometer and the signals from the knife-edge are acquired by an Agilent DSO80404B oscilloscope. These signals are averaged, digitised and transferred to a computer which controls the operation of the experiment. Processing is carried out on this data after each experiment.

3.6 Sample positioning

The generation and detection optics are mounted above the sample on an optical breadboard. The sample is mounted onto a sample holder board which consists of a modified optical breadboard. This breadboard is connected onto a tip-tilt stage (Thorlabs KM200B/M type) which is in turn mounted onto a z-stage. This

arrangement allows for the focusing of the optics used in generation and detection, also the sample can be levelled. This arrangement is finally mounted onto a set of long travel (300mm PI M-531.DD with 0.1 μm linear encoder) stages allowing the sample to be scanned in the x-y directions.

3.7 Environmental effects

Ultrasonic velocity is defined by the second order elastic constants of a material, these are related to many different physical factors. One of these is temperature. The relationship between the change in velocity with temperature is given by the formula:

$$\Delta v = k\Delta T$$

where k for aluminium has a quoted value of -0.752ms^{-1} °C^{-1} for shear waves, -1.089 ms^{-1} °C^{-1} for longitudinal waves [117] and has been measured experimentally using this instrument to have a value of -1ms^{-1} °C^{-1} for Rayleigh waves (see figure 3.14). Not only does the velocity of the material change with temperature but also the geometry of the optics changes. For example changing the distance between the detection and generation points would result in a phase change in the detected SAW that could be misinterpreted as a velocity change.

In order to make measurements of velocity with the best possible resolution, the temperature of the experiment needs to be carefully controlled. In the experiment several different techniques are applied in order to limit the effect of temperature variation on the measurement of the velocity of the SAWs. One of these methods is the use of a temperature control chamber inside which the experiment takes place. The temperature inside the chamber is carefully controlled. This also reduces draughts and the associated low frequency mechanical vibrations caused by them.

Another method used to reduce the impact of temperature on the measurement is the use of an interleaved differential technique implemented using the control electronics.

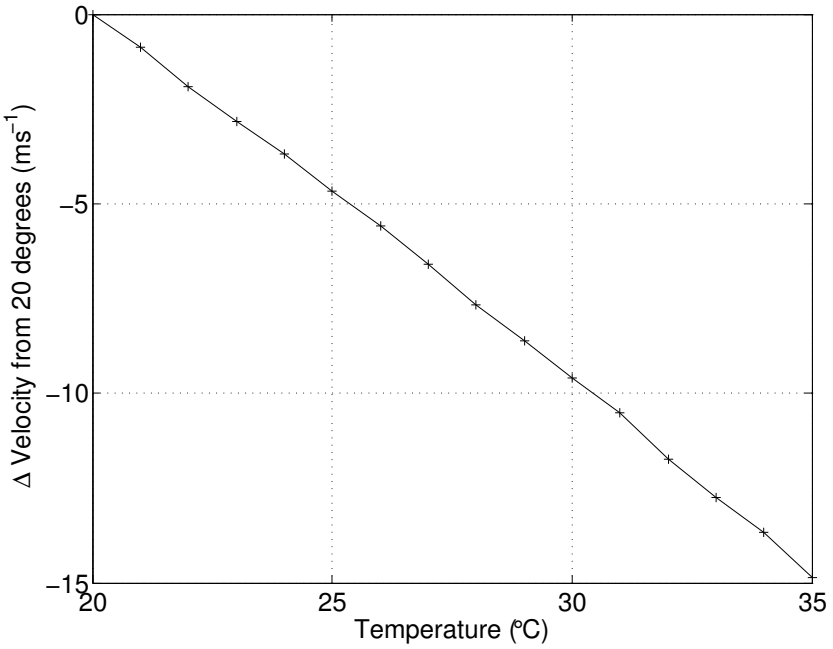

Figure 3.14: Relationship between variation in temperature and shift in velocity

3.7.1 Temperature control enclosure

The temperature control chamber used for this instrumentation consists of a box with walls and a lid made from thermally insulating Correx plastic. Insulating the enclosure reduces the effect on the internal temperature by external thermal variation. In order to minimise the fluctuation within the enclosure, efforts were made to exclude any equipment from it that would generate heat. In particular the power supplies for the stages and the generation laser head were kept external to the enclosure to help minimise the effect the heat they generate would have on the experiment. The internal temperature is further regulated by a 33.4W Peltier effect heat pump. One side of the heat pump is connected to a large aluminum

block which acts as a thermal mass. The other side of the heat pump is connected to a finned heat sink with a fan attached to it. The fan drives air from the enclosure over the fins of the heat sink which exchanges thermal energy with the load. The Peltier is controlled by a proportional integral derivative (PID) controller (Supercool: PR59), this controls the direction and magnitude of the current going to Peltier. The response of the PID controller is set by an RS232 connection from the computer. A thermocouple attached below the sample measures the temperature within the enclosure, which is sent to the PID controller. This is also sent to the computer and recorded at 5 minute intervals or once each time a measurement is made.

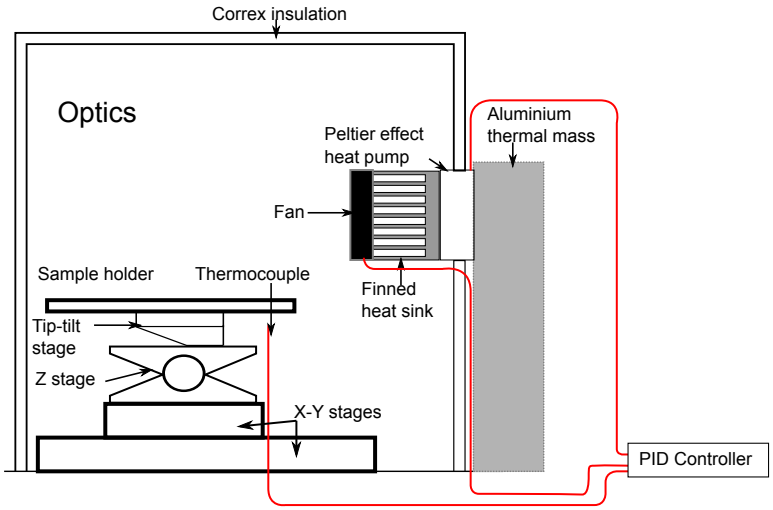

Figure 3.15: Diagram of environmental chamber including configuration of sample positioning stages

3.7.2 Effectiveness of temperature control enclosure

To assess the effectiveness of the temperature control enclosure, the temperature inside was monitored every 5 minutes over a 24 hour period with the system turned

on. It was found that during this period the maximum change in temperature was 0.2°C (see figure 3.16). This equates to a velocity shift 0.2 ms^{-1}.

The temperature stability was also monitored over a shorter period (every six seconds for one hour) with the PID set to a higher temperature (21°C), to demonstrate the capacity of the enclosure to maintain different temperatures. The monitoring of the enclosure was only started when it had reach a constant temperature having been increased. The maximum change in temperature over a hour was found to be 0.1 °C (see figure 3.17), which equates to a velocity shift of $0.1ms^{-1}$. The maximum rate of change (found between 33-35 minutes) was found to be 0.014 °C a minute, which equates to a velocity change of $0.014ms^{-1}$ a minute. The maximum rate at which the temperature can be sampled (every 6 seconds) by this system limits the rate of variation in the temperature that can be detected. It is assumed that high frequency variations in temperature are small and their effects are partially averaged out by the finite length of the time a measurement takes.

This demonstrates that the enclosure system has relatively good control over the temperature of the sample and instrumentation. However, the instrument is required to measure velocity changes of the order of mms^{-1} (see page 33). This requires a temperature stability that the enclosure alone is not capable of maintaining. So additional techniques to mitigate the effect of the temperature variation are also employed (see section 3.8).

3.8 Control electronics

In order to make highly accurate velocity measurements the instrument has to precisely control the generation of each of the SAWs used. In this system this is done by using a high speed field programmable gate array (FPGA) operating at

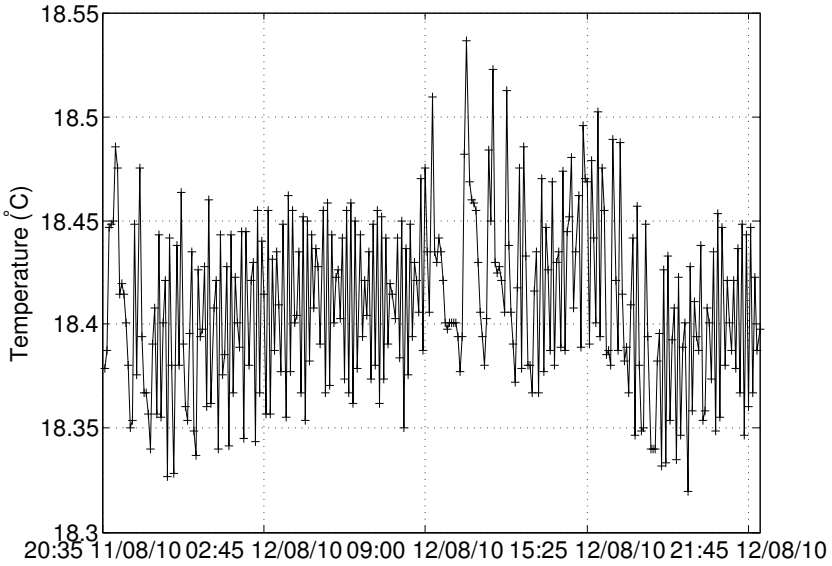

Figure 3.16: Temperature variation of experiment over 24 hour period

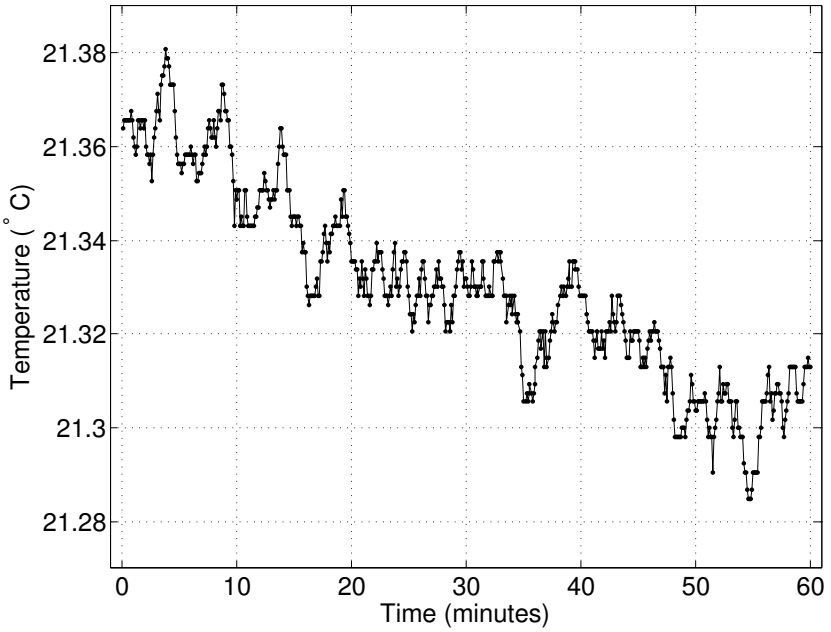

Figure 3.17: Temperature variation of experiment over 1 hour period

a clock frequency of 100MHz (giving a timing resolution of 10ns). This control board acts as the primary clock for the experiment with all triggers being derived from it. The repetition for each cycle of triggers is set on the board by the state of two switches. These switches encode the repetition rate, both switches down being 500Hz, switch 0 up being 1kHz, switch 1 up being 2kHz and both up being 3kHz. The FPGA delay values are set by computer via a USB connection.

The computer sends the FPGA two numerical values. These are the delays in nanoseconds between the trigger signal for the generation of the pump SAW and the trigger for the probe SAW. The FPGA triggers for a set number of counts for one delay before switching to the second of the two delays. The number of times each delay is repeated is set by another group of switches on the FPGA, up to a maximum of 63 times. This means the switching rate between the two delays can be controlled from 500 to 16 Hz, (see figure 3.18). Using this system the interaction between the two SAWs can be precisely controlled.

A differential technique can be implemented using this system to reduce the impact of temperature variation on the measurement of the change in velocity of the probe wave due to the stress induced by the pump wave. At one delay the probe SAW doesn't interact with a region of stress due to the pump SAW, any velocity shifts are due to environmental effects such as temperature variations. At the other delay the probe SAW interacts with a point on the pump SAW. The two different SAWs are separated out using a radio frequency (RF) transistor transistor logic (TTL) controlled switch (minicircuits ZSWA-4-30DR) that is controlled by the FPGA. In this way the probe SAW experiencing the stress state appears at one port of the switch while the probe SAW which has not experienced a stress appears at the other port. By switching the interaction point rapidly between the two delays it allows a differential technique to be implemented which is independent

of external environmental effects. The temperature variation between the different interaction is minimal (of the order of 10^{-4} °C see figure 4.2). This results in the system being able to measure very small velocity changes due to stress.

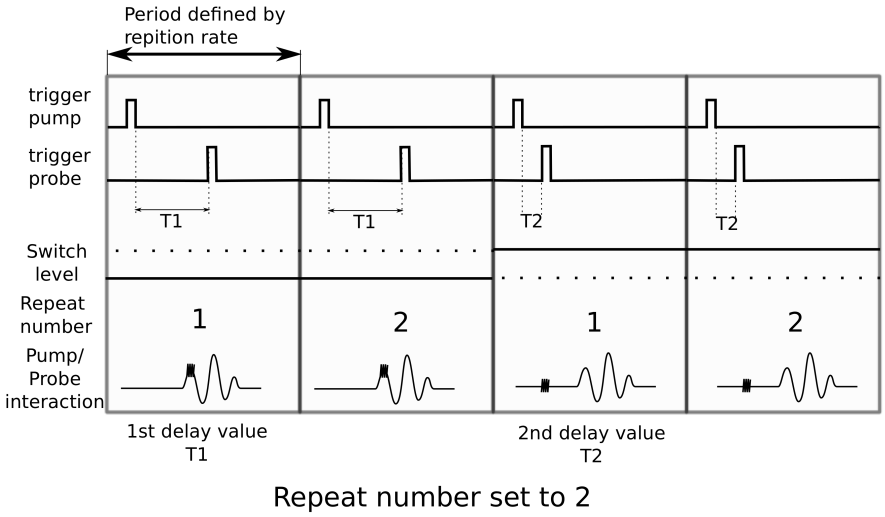

Figure 3.18: Diagram of the timing configuration of the FPGA. Spikes in each of the trigger channels represent a triggering event. Pump/probe interaction diagrams show the interaction between the pump and probe waves for these delay settings.

3.9 Summary

In this section the design of a laser ultrasound system capable of making highly sensitive acoustoelastic measurements is described. Some of the difficulties in achieving this have been explored. The configuration developed represents a flexible system for measurements.

Chapter 4

Methods

4.1 Introduction

This chapter starts by discussing the measurement of the acoustoelastic coefficient for Rayleigh waves (A_R) and the procedure developed to monitor it (see section 4.2), this procedure was developed in conjunction with instrumentation discussed in chapter 3. Developments in this procedure came about due to the observed experimental results presented in chapter 5. The methods presented in this chapter have been organised in order of increasing measurement complexity. The experimental results are presented in chapter 5. Other topics covered in this chapter include:

- Section 4.3 - the noise, errors and uncertainties in the acoustoelastic measurement and the associated variables are investigated experimentally and by modelling.
- Section 4.4 - a technique to image A_R is developed to investigate spatial variation in A_R found in chapter 5 (section 5.4).

- Section 4.5 - the configuration of an experiment to investigate the impact of fatigue on the imaged A_R is outlined

4.2 The acoustoelastic coefficient for Rayleigh waves (A_R)

The acoustoelastic effect (see section 2.4.3) is used to determine the acoustoelastic coefficient (A) of a material. The acoustoelastic coefficient is dependent on the wave mode that is probing the material, in this case Rayleigh waves are used, so that the acoustoelasic coefficient for Rayleigh waves (A_R) is monitored. The direction of both the applied stress and the propagation of the probing wave, influences which acoustoelastic coefficient is measured. In this case the acoustoelastic coefficient measured is the A^1_{R1} coefficient, where the superscript (1) denotes the direction of the applied stress and the subscript (1) denotes the direction of propagation of the probe wave. In this case used here the stress is applied in the same direction as the propagation of the wave. For brevity the measured acoustoelastic coefficient is subsequently referred to as A_R.

Measuring A_R requires the measurement of the fractional velocity change of a Rayleigh wave with applied stress. The technique developed in this thesis uses a large amplitude low frequency ultrasonic pump wave (0.5–2.5MHz) to stress the material. A second wave, the high frequency ultrasonic probe wave (38–68MHz), co-propagates with the pump wave so experiencing a stress, which alters the probe wave velocity. The velocity change (caused by the stress of the pump wave) is extremely small (of the order of 10^{-6} per MPa). The stress experienced by the probe wave can be changed by altering the interaction point of the two waves or by altering the amplitude of the pump wave, for experimental reasons the former has

some advantages. The relative timing of the generation of the two waves determines the regions of the waves that interact and so the effective stress experienced by the probe wave due to the pump wave.

To make the measurement of A_R two separate variables are measured, the induced *fractional velocity change* and the *stress*. They are indirectly measured by measuring the time of arrival of the probe wave, the out of plane displacement due to the pump wave and the length of the probe wave packet discussed in sections 4.2.2, 4.2.3 and 4.2.4.

4.2.1 Fractional velocity change

The fractional velocity change ($\frac{\Delta V}{V_0}$) is the change in the velocity of a propagating wave over the unstressed wave velocity. In this case:

$$\frac{\Delta V}{V_0} = \frac{V_\sigma - V_0}{V_0} \tag{4.1}$$

where V_σ is the velocity of the wave under the influence of stress and V_0 is the unstressed wave velocity.

The measurement of the velocity change is complicated by the temperature dependence. The temperature dependence is -1 $\text{ms}^{-1}\text{C}^{-1}$ and the experiment is contained in a temperature controlled enclosure capable of controlling the temperature of the sample to 0.2° C over a 24 hour period. The maximum variation in the velocity due to temperature variations is found to be 0.014 ms^{-1} over a time scale of 60 seconds (see section 3.7.2 and figure 3.17).

The measurements of ΔV in this thesis are of the order of 0.040–0.050 ms^{-1} which means that the temperature dependence is very significant. Consequently to achieve velocity measurements that are more independent of temperature vari-

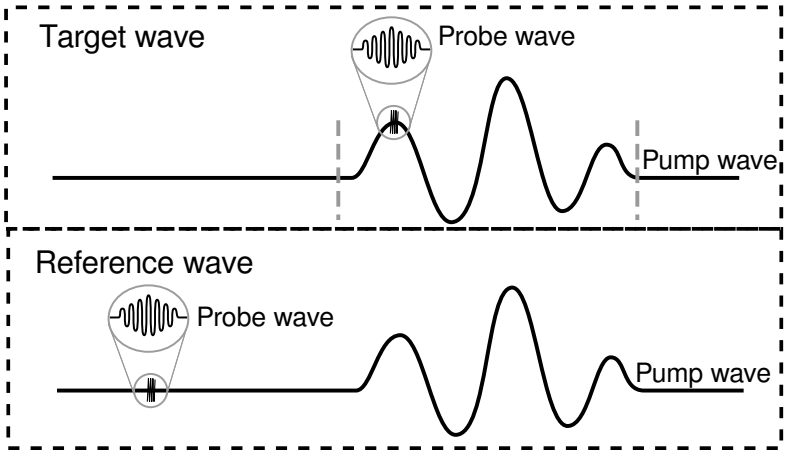

Figure 4.1: Diagram showing the different interaction locations of the target and reference probe waves with the pump wave. By placing the target wave at different locations between the grey dashed lines (- -) different levels of stress due to the pump wave can be investigated.

ation an interleaved differential technique is used to acquire the fractional velocity change.

Interleaved differential acquisition of the fractional velocity change

Using an interleaved differential technique improves the temperature independence of the measurement of the fractional velocity change. To implement this technique two probe waves are acquired. One of the probe waves, known as the target wave, interacts with the pump wave at a time where stress is present. The other probe wave, known as the reference wave, interacts with the pump wave at a time where stress is not present (see figure 4.1). Both waves experience similar changes in velocity due to temperature variations. By interleaving and rapidly switching the acquisition of the target and reference waves, the temperature difference between the two is small (see figure 4.2b).

An interleaved measurement with 16384 averages takes 40 seconds to complete which means a maximum temperature change less than 0.014 C°. Figure 4.2 shows

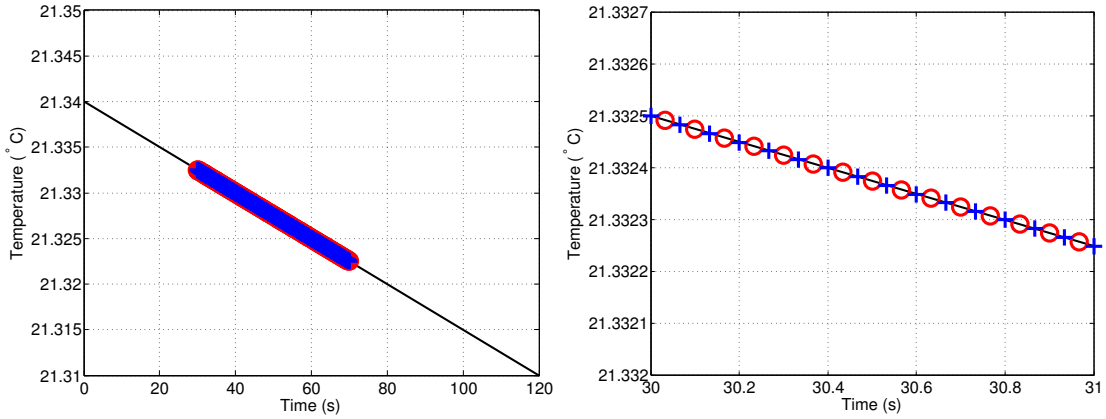

(a) Temperature variation with interleaved acquisition

(b) Temperature variation with interleaved acquisition (1 second)

Figure 4.2: Demonstration of difference in temperature between the target and reference probe waves based on maximum reported variation of 0.014° in a 60 second period from figure 3.17. A red cross (+) denotes the acquisition of a reference wave and a blue circle (○) denotes the acquisition of a target wave

the maximum reported variation in temperature along with the interleaved acquisition process. Taking this value the variation in the temperature between the acquisitions of the reference and target waves will be less than 1×10^{-4} °C, as can be seen in figure 4.2b, assuming there are no unobserved high frequency variations.

The target and reference waves are acquired on separate oscilloscope channels, selected by the RF switch controlled by the FPGA (see section 3.8). By subtracting the reference wave velocity from the target wave velocity, the majority of the velocity change due to temperature variation is eliminated. This leaves the velocity change due to stress (ΔV). The temperature difference between the target and probe waves (1×10^{-4} °C) equates to a difference in velocity of 0.0001ms^{-1}. This velocity shift represents an uncertainty in the A_R of 0.03×10^{-6} MPa^{-1}. In section 4.3.1 the error in A_R is found to be 0.5×10^{-6} MPa^{-1}. The contribution to the error in A_R due to fluctuation in temperature is therefore small.

4.2.2 Measuring the time of arrival of the probe wave

The interaction distance (D) between the waves is kept constant, using the following equalities:

$$V_0 = \frac{D}{t_0}, \qquad V_\sigma = \frac{D}{t_0 + \Delta t}$$

the fractional velocity change can be described as:

$$\frac{\Delta V}{V_0} = \frac{-\Delta t}{t_0 + \Delta t} \tag{4.2}$$

From equation (4.2) the fractional velocity change can be found by measuring Δt and t_0. Where Δt is the time difference between the arrival of the reference and the target wave. t_0 is the time taken for the wave to propagate in an unstressed condition.

Measurement of Δt

The time difference between the arrival of the reference probe wave and the target probe wave is determined by either taking the phase of the largest spectral component of the probe wave (via FFT, known as the phase method) or by using the "full spectrum method" as described in [118]. Both techniques are compared by numerical modelling in section 4.3.5 and experimentally in section 4.3.2. The latter proved to have better signal to noise characteristics and was used for most of the subsequent experiments.

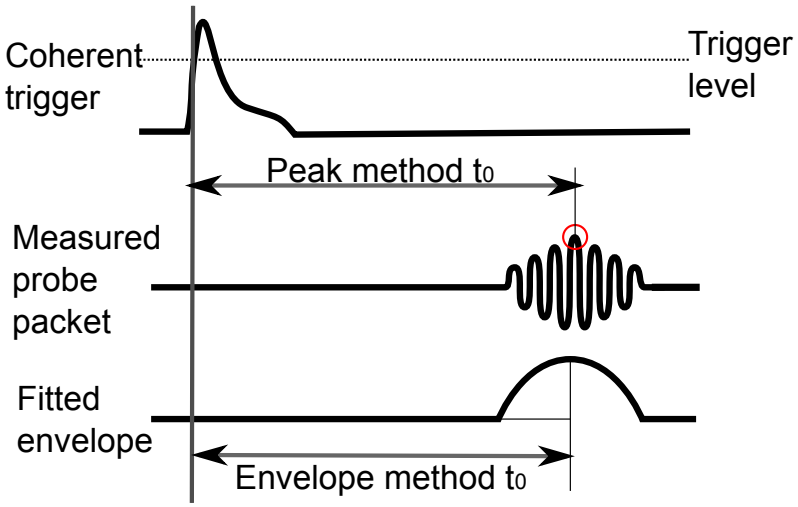

Figure 4.3: Diagrammatic representation of different techniques used to extract t_0 from reference probe wave

Measurement of t_0

The time t_0 is the interaction time between the probe and pump waves. It is the time taken for the probe wave to travel to the detector from the point where it is generated (the pump wave being generated earlier). This is measured by either finding the maximum of the envelope or by fitting a Gaussian packet to the probe wave envelope (see figure 4.3). Both methods become unstable under different conditions, well conditioned data is therefore vital for both techniques. Finding the maximum of the envelope technique is more sensitive to amplitude noise, however it is less resource intensive and so is used for most of the subsequent experiments.

4.2.3 Measurement of the material stress under the pump wave

The stress applied to the material under the probe wave is produced by co-propagating a low frequency SAW called the pump wave. The stress is measured by measuring the out of plane displacement of the SAW and then calculating the stress using Viktorov [119] thus:

$$\sigma_{xx|z=0} = U_0 \left[\frac{\lambda \left(k^2 - q^2\right) + 2\mu k^2 \left(1 - \frac{2sq}{k^2+s^2}\right)}{q \left(1 - \frac{2k}{k^2+s^2}\right)} \right] \tag{4.3}$$

Further details are given in appendix B.

Using Viktorov to plot the stress profile into the sample (see figure 4.4), it is seen that out of plane stress at the surface is zero and in plane stress at the surface is finite. The stress produced by the probe wave interacts with the top region of the sample to a depth of 0.025 of the wavelength of the pump wave (see figure 4.4b), one can confidently make the approximation that the probe wave only interacts with in plane stresses from the pump wave.

Multiple interaction points between pump and probe wave

The delay between the generation of the pump wave and the generation of the probe wave determines the interaction point between the two waves. By altering the delay for the generation of the target probe wave, a range of different displacements, and so stresses, will be experienced by the probe wave due to the pump wave (see figure 4.5). This allows a measurement of A_R to be taken.

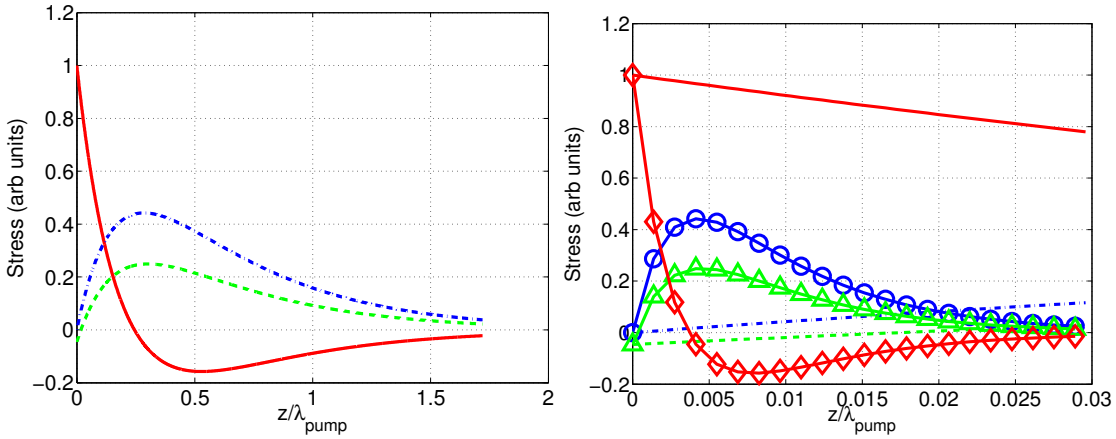

(a) Stress component contribution

(b) Cropped section showing probe wave stress components with depth

Figure 4.4: Stress components contribution with penetration depth pump wave, The solid red line (−) represents stress in the xx direction, the dashed green line (−−) represents stress in the zz direction and the dashed-dotted line (−.−) represents the xz direction. In figure 4.4b stress components of the probe wave are also plotted (red diamond ◇ σ_{xx}, the blue circle ∘ σ_{xz}, green triangle △ σ_{zz}). The probe wave stress is confined to less than $0.025\lambda_{pump}$ and the variation in the stress is less than 20%

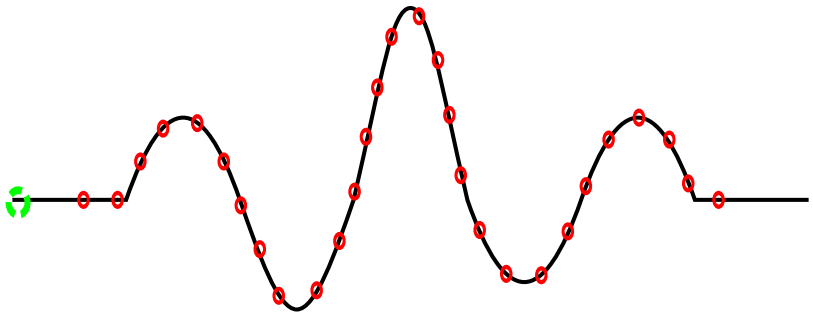

Figure 4.5: Diagram showing example of different interaction points (red circles, ∘) between the target probe wave and the pump wave, produced by varying the delay between the generation of the two waves. The reference point (the timing delay where no interaction between the pump and probe takes place) is also shown (broken green circle ∘).

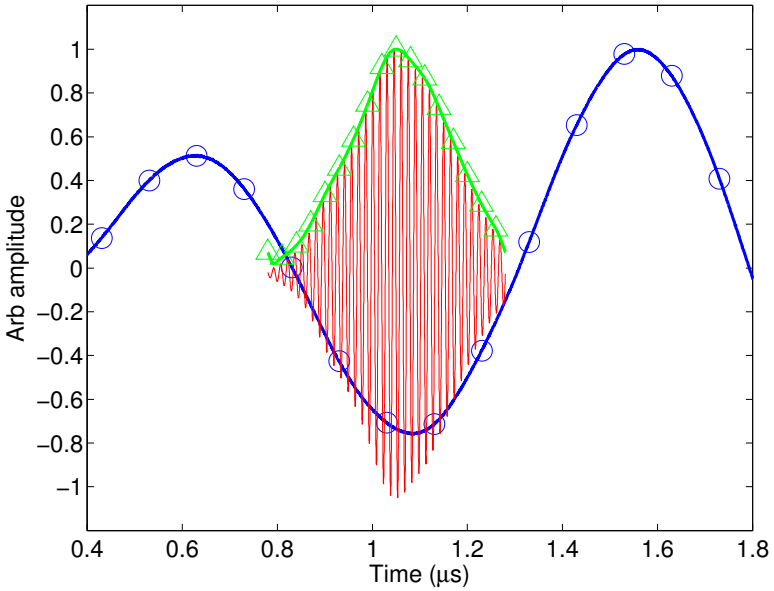

Figure 4.6: Graph showing the relative interaction period of the pump (blue circles, ○) and probe (red solid line, −) waves. The probe wave packet envelope is also shown (green triangles, △). The stress used in the measurement of A_R is the average of the stress due to the pump waveform weighted by the probe envelope.

4.2.4 Probe wave packet length and its effect on the measurement

Since the high frequency probe waveform has a relatively long packet compared with the period of the low frequency pump waveform, different parts of the probe experience different stress levels (see figure 4.6). The methods used to measure the phase or time delay of the probe wave (see section 4.2.2), measure an average phase or delay for the entire packet weighted by the amplitude (or envelope) of the probe waveform. Consequently, the stress used in the calculation of A_R is the average of the stress waveform under the pump wave, weighted by the probe envelope.

The validity of this approach can be demonstrated by considering the probe wave packet as three separate sections (see figure 4.7a). Each section interacts with a slightly different part of the pump wave and so experiences a different stress, inducing a different phase change in each section. In a phasor diagram (see

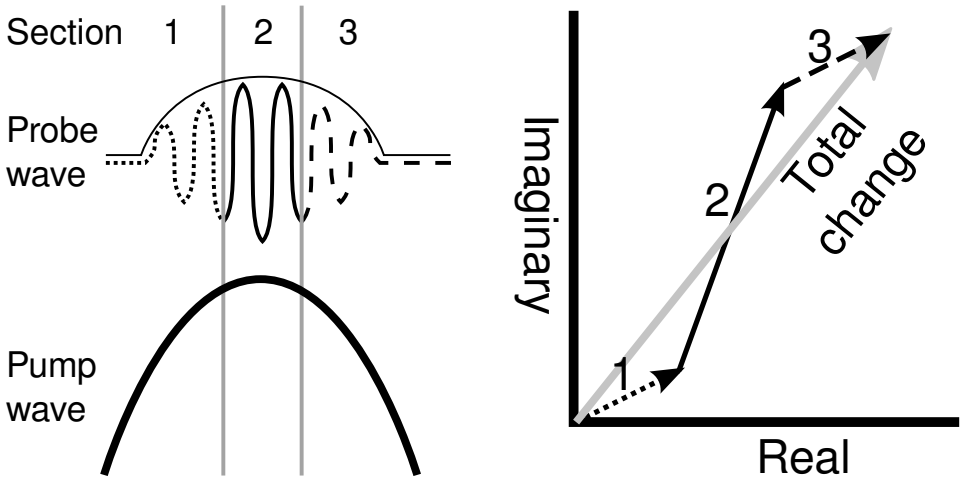

(a) Separation of probe wave packet into 3 sections

(b) Phasor diagram showing amplitude dependence of the contribution of all the components to the overall phase change

Figure 4.7: Demonstration of the validity of averaging the stress due to the pump wave, weighted by the probe envelope.

figure 4.7b) the contribution of each of these components to the total phase shift is proportional to the amplitude of each section. As each components' contribution to the phase shift is proportional to its amplitude, the stress from each section must be weighted by the same amount to give the effective stress experienced by the whole packet. This is only an illustration of the process. In reality the stress is proportional to the integral of the probe wave packet, rather than three successive sections.

The probe envelope can be measured by shifting the frequency spectrum of the probe waveform to DC and taking the inverse Fourier transform, see figure 4.8.

4.2.5 Relating observed stress to velocity change (calibration)

An interferometer (see section 3.4.2) measures the displacement of the pump wave and a knife-edge detector measures the gradient of the probe wave. The inter-

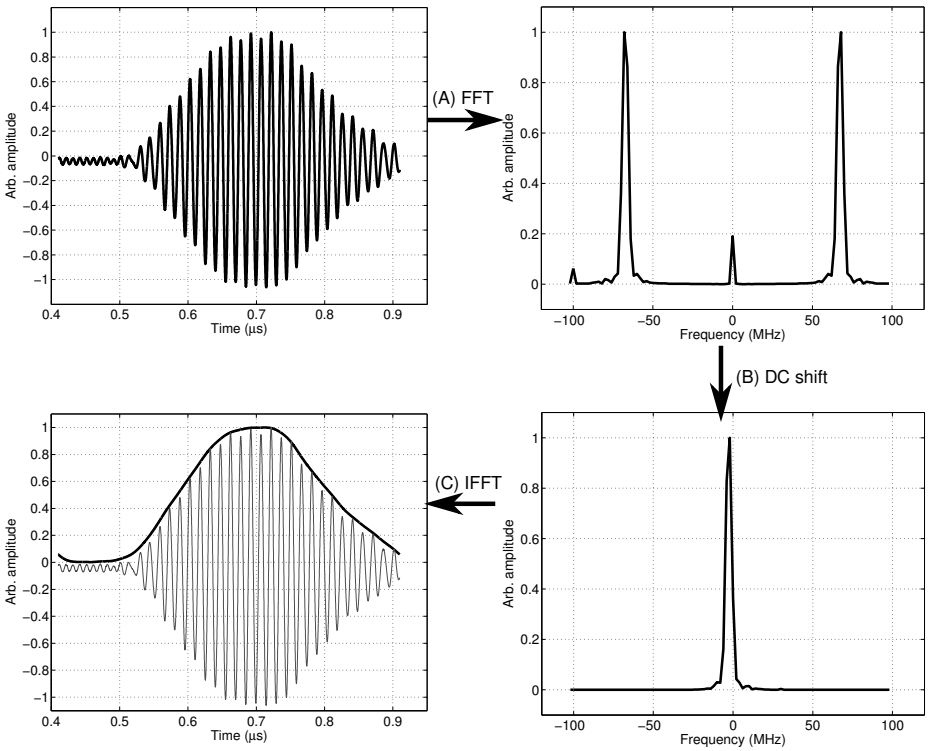

Figure 4.8: Process of obtaining the probe wave packet, a FFT is applied to the probe wave (A), the frequency spectrum is shifted to move the probe wave spike to DC position (B) and a IFFT is applied to the frequency spectrum to give the probe wave envelope (C).

ferometer measures a displacement and the knife-edge measures a gradient which means the two detectors are 90° out of phase relative to each other. The detection points of the two detectors are separated due to the physical practicalities of introducing both onto the sample. This separation of the detection points also introduces a phase shift between the acquired signals and there are some other small phase shifts due to different signal paths through the electronics.

To correct for the phase shifts between the acquired signals, the time of arrival of the pump wave is shifted during the processing of the signals in the computer. The shift in time allows the displacement, and so the stress, of the pump wave at the point it interacts with the probe wave to be determined. This shift applied to

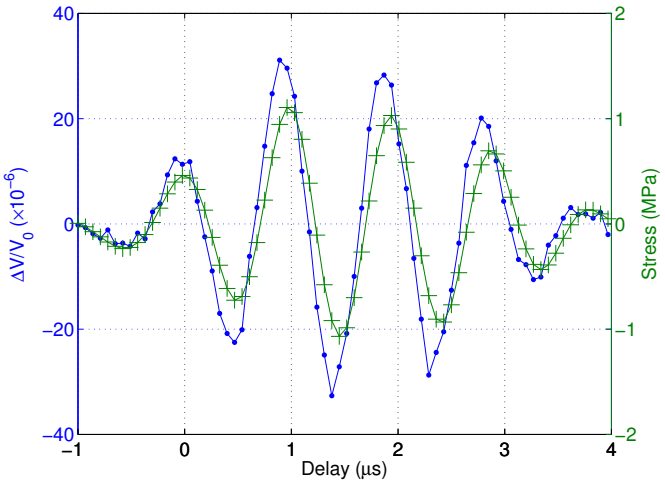

Figure 4.9: Fractional velocity change ($\frac{\Delta V}{V_0}$) against delay between the generation of pump and probe waves (blue dotted line, .-). Stress calculated from non-shifted pump wave (green cross line, +-). The difference in phase between fractional velocity change and the stress can be seen

the displacement of the pump wave is found using a fixed procedure.

The procedure probes several different stress states of the pump wave using the target probe wave (as described in section 4.2.3). The interaction of the probe wave with the pump wave is set by adjusting the delay between the generation of the pump and probe waves. A different fractional velocity change is recorded at each change in delay. The stress induced from the non-shifted pump wave is calculated for each delay. Comparing the the stress calculated from the non-shifted pump wave displacement and the fractional velocity change the phase difference between the two detectors is observed (see figure 4.9). The phase difference is found by curve fitting and the displacement due to the pump wave is shifted appropriately.

This procedure assumes that the fractional velocity change and the pump wave stress are either 0 or 180° out of phase. This is a fair assumption as the majority of the stress that interacts with the probe wave is in the in-plane or xx direction (see section 4.2.3). Therefore it is assumed the fractional velocity change is only induced by the in-plane stress.

The difference in phase between the detectors is monitored for all experiments conducted in chapter 5. The phase difference remains constant during each experiment.

4.3 Noise, errors and uncertainties

In order to make valid conclusions from the data acquired in chapter 5 and to optimise the measurements of A_R, the noise, errors and uncertainties are investigated in this section.

The error in the acousotelastic measurement where multiple interactions between the pump and probe wave occur, is found from the least mean square fit applied to the data (see section 4.3.1). The uncertainty in the acoustoelastic measurement comes from the uncertainty in each of the variables contributing to its measurements. The sources of the uncertainties in these variable are investigated to determine which is most prevalent (see section 4.3.2). These sources include instrumental and processing uncertainties. Quantifying the uncertainties in each of the measurements allows an approximation of the uncertainty in A_R to be made when the least mean squares fit cannot be used (in imaging). A demonstration of the relative contribution to the overall uncertainty, of both the stress and fractional velocity change, by the uncertainties in the associated variables is given in section 4.3.3. The effect of different configurations of the instrument including data acquisition, pump wave frequency, probe wave frequency and co-propagation distance influence the noise in the measurement and are also investigated (see section 4.3.5).

4.3.1 Error in the acoustoelastic coefficient (A_R)

A least mean squares fit is applied to data where numerous interactions (> 3) between the pump and probe waves are used to find A_R. This occurs only for single location (point) measurements. When a least squares fit is applied to a set of data, it is possible to calculate the standard error in the fit parameters, in this case the stress and fractional velocity change. To do this, the sum of the squared residuals (difference between the actual data points and the fitted value, SSE) is calculated and then divided by the degrees of freedom (df, number of samples - freedom for each parameter (2)):

$$s = \frac{SSE}{df}$$
$$SSE = \sum_{n=1}^{N} \delta_{\left(\frac{\Delta V}{V_0}\right)}$$

where $\delta_{\frac{\Delta V}{V_0}}$ is the uncertainty in the fractional velocity change $\frac{\Delta V}{V_0}$. The standard error (SE) in the fit and the standard error of the gradient (in this case $\delta_{\frac{\Delta V}{V_0}/\sigma}$) are given by:

$$SE = \sqrt{s}$$
$$\delta_{\left(\frac{\frac{\Delta V}{V_0}}{\sigma}\right)} = \frac{SE}{\sqrt{SS_\sigma}}$$

where the SS_σ is the sum of the squares of, in this case, the stress which is given by:

$$SS_\sigma = \sum_{n=1}^{N} \sigma^2 - \bar{\sigma}^2$$

Using a standard least mean squares fit is problematic when the uncertainty in the variables is not constant. In this situation the uncertainty in the data is said to

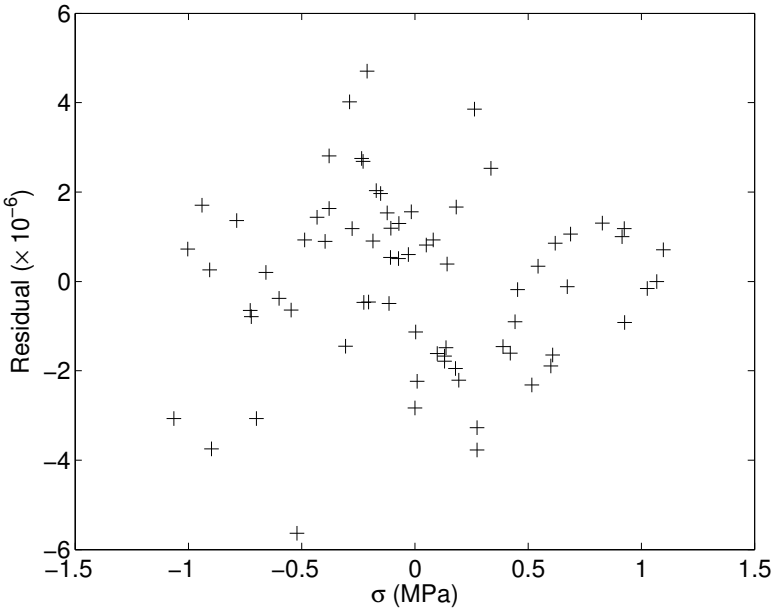

Figure 4.10: Plot of residual values from least mean squares recessional fit against the stress. No clear correlation is seen so it is assumed the variance in data is not a function of the stress.

be heteroskedastic. In this case a least mean squares regression fit will no longer give the best linear unbiased fit values. This issue is removed by implementing a weighted least mean square regression fit. A method of determining if this is necessary, is to plot the residuals against the variables. If the scatter of residual changes with the variable, the confidence in the measurement is dependent on the magnitude of the variable and so an appropriate weighting must be applied. In this case, the residuals are plotted against the stress for data acquired in section 5.2 on fused silica (see figure 4.10). No clear correlation is shown, so it can be assumed that the variance is non-heteroskedastic.

For the single point acoustoelastic measurement, the standard error of the gradient is 0.44 $\times 10^{-6}$ MPa^{-1}. The acoustoelastic measurement for fused silica is 27.5 $\pm$ 0.5 $\times 10^{-6}$ MPa^{-1}.

4.3.2 Uncertainty in acoustoelastic coefficient

Instrumentation and processing techniques both have an effect on the certainty with which the measurement can be made. The A_R is calculated from several variables. Each variable has a uncertainty which contributes to the final uncertainty in A_R. This section explores the level of precision with which the variables making up the acoustoelastic measurement can be found. Figure 4.11 shows a diagrammatic representation of the system with sources of uncertainty included.

The uncertainties encountered in this analysis can be allocated into one of two groups: random error and systematic error. Random errors are noise sources that are unpredictable in nature and affect the precision of the measurement. Systematic errors are caused by range of features including poor calibration and changes in the environment. Systematic errors introduce biases in the measurement and so affect its accuracy. The majority of experiments conducted in this thesis are comparative, monitoring a change in A_R between an initial measurement and subsequent measurements. This means the random errors are the most significant errors, as systematic errors will affect successive measurements in a similar way. In this section each of the uncertainties is classified into one of these two groups.

Uncertainty in fractional velocity change

A variety of sources of uncertainty in the measurement of the fractional velocity change exist. The single shot signal to noise ratio (SNR) of the probe wave is used as a metric to define the quality of each measurement. In this section the SNR is experimentally linked to the variation in the variables used to calculate the fractional velocity change. This is used to analyse measurements presented later in this thesis (see chapter 5). Finally, the effect of random systematic noise on the uncertainty in the fractional velocity change measurement is investigated.

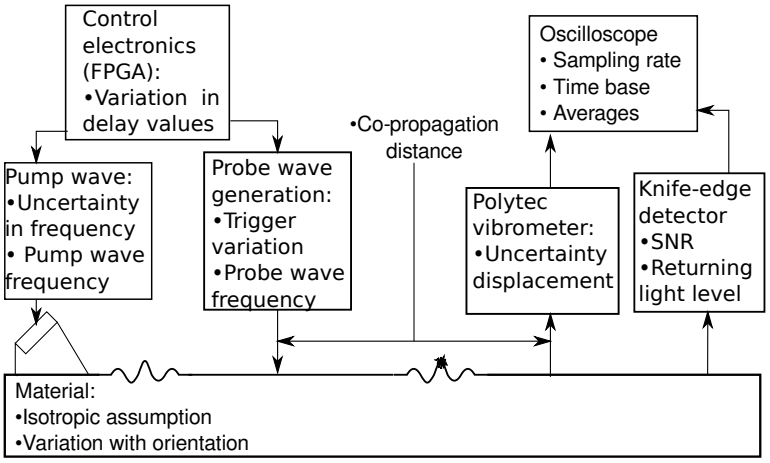

Figure 4.11: System diagram including sources of uncertainty or factors that could affect the uncertainty (labelled with a •).

Single shot signal to noise ratio

Variations in the generation, propagation and detection of the probe wave in a sample means that the amplitude of the detected probe wave signal will vary. The amplitude of the noise varies randomly. The effects of noise is dependent on its bandwidth. Noise that is outside of the bandwidth of the signal can be removed. Noise inside the bandwidth of the signal is more difficult to remove and must be accounted for. The higher the level of noise with respect to the signal, the higher the uncertainty in any measurement. To quantify the quality of the measurement, the signal to noise ratio is used.

The signal to noise ratio (SNR) is found in this system by sampling a non-averaged (single shot) probe wave. The length of the sampled data is sufficient so that both the probe wave envelope and a region away from the probe wave is recorded (see figure 4.12). The signal is defined as the section of the trace with the greatest root mean squared value over a pre-set length (defined by the packet size). The noise is defined as the standard deviation of the section away from the probe wave. The SNR is defined here as the root mean squared value of the signal over

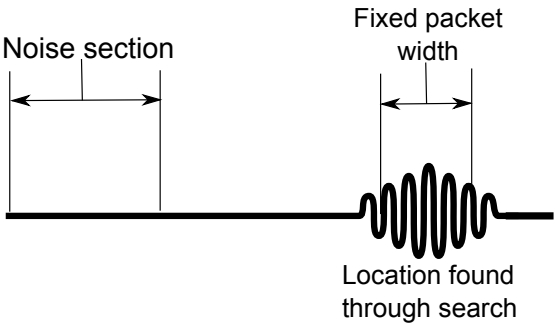

Figure 4.12: Diagram of the locations of signal and noise components used to calculate the signal to noise ratio from single shot trace

the standard deviation of the trace away from the signal. Several measurements of the SNR are taken and averaged to give a value for a location.

Measured uncertainty in variables used to calculate the fractional velocity change

The relationship between the uncertainty in the measurement of Δt, t_0 and the single shot signal to noise ratio is explored experimentally in this section. The Δt variable is investigated, t_0 being discussed after.

To measure the uncertainty in Δt, 20 measurements are taken at a location. Each measurement consists of taking an average of 16384 traces of the probe wave packet. This number of averages is selected as the optimum number of averages from modelling conducted in section 4.3.5 and it is subsequently used for all experiments in chapter 5. The reference and target probe waves are acquired using the interleaved differential technique described in section 4.2.1. The delay for triggering the probe wave generation is fixed. The probe wave is generated using a mask with a line spacing of 43.5 μm (see section 3.3.2). Both methods of finding Δt (phase and full spectrum methods) described in section 4.2.2 are used. The uncertainty in these measurements is defined as the standard deviation of their

values. This procedure is repeated at 40 randomly selected locations. For each location, the SNR is found by taking the average of multiple measurements at that location.

Two samples were used to allow a range of signal to noise values to be investigated. One of the samples is made from fused silica. Due to the high optical transmittance of fused silica the sample is coated with a layer of aluminium ∼100nm thick. Fused silica is highly isotropic meaning that wave propagation is unaffected by features such as aberration. For this reason high signal to noise ratios are achieved on the fused silica sample. This sample is known as an ideal sample. To provide lower signal to noise ratios a second sample made from aluminium is used.

Attenuating the light returning to the knife-edge detector could have also achieved a range of SNR values, though this would only probe the effect of changes in the optical response of the system.

Figure 4.13 shows the logarithm of the standard deviation (uncertainty) in Δt, with respect to the logarithm of the mean signal to noise ratio, for each of the points collected on the two samples. A linear decreasing trend is observed in the log of the standard deviation of Δt with an increase in the log of the signal to noise. The phase method of extracting Δt has a higher standard deviation for a given SNR compared to the full spectrum method, especially at lower SNR values. This is expected as the phase technique is less bandwidth efficient. The phase method is bandwidth inefficient as only part of the frequency spectrum of the probe wave is used to determine the change in phase, where as the full spectrum method uses all of the spectrum to determine the phase change. One of the locations on the ideal sample shows an uncertainty greater than the general trend. The exact reason for this is unclear, though a single measurement is responsible (repeat 9 for location 39). Both processing techniques are affected.

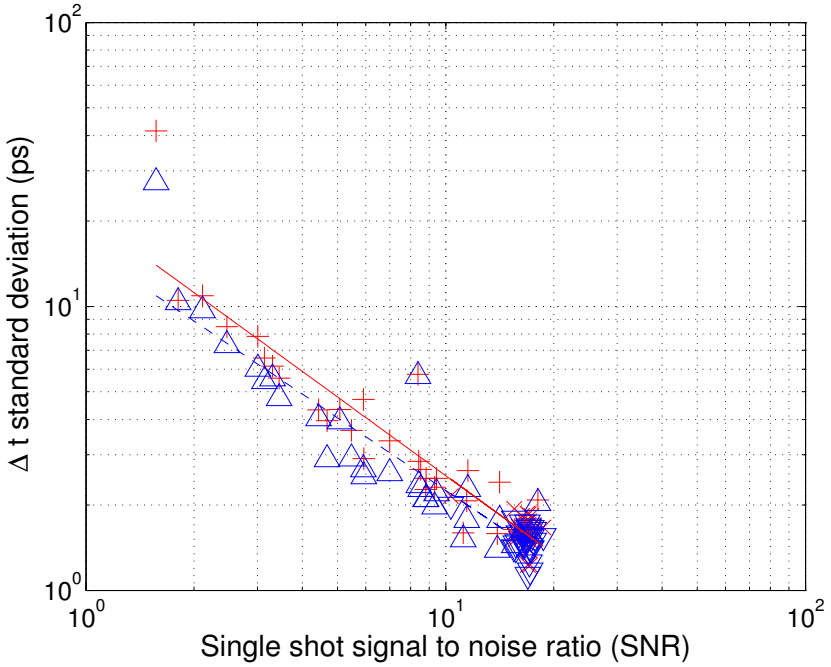

Figure 4.13: Log-log graph showing the standard deviation (uncertainty) of Δt against signal to noise ratio (SNR, based on amplitude). Includes data found using the phase technique on aluminium (red crosses, $+$) and fused silica (red x, $\times$). Data found using the full spectrum technique on aluminium (blue triangle point up, $\triangle$) and fused silica (blue triangle point down,$\triangledown$) is also included. Linear fit lines are included for the phase method (solid red line, $-$) and the full spectrum (dashed blue line, $--$).

Data collected to calculate the uncertainty in Δt can also be used to relate the uncertainty in t_0 to the SNR. A single trace of the probe wave is used. Two methods, peak and envelope fitting, described in section 4.2.1 for finding t_0, are employed to find the value for each data point. The value of the standard deviation of t_0 is found for each location. The logarithm of the standard deviation is plotted against the logarithm of the mean signal to noise value for each location (see figure 4.14). As the signal to noise ratio increases the uncertainty in t_0 decrease. For a high SNR the envelope method has a lower uncertainty than that of the peak method. For a low SNR the peak method has a lower uncertainty than that of the envelope method. Overall the peak method of determining t_0 is more stable.

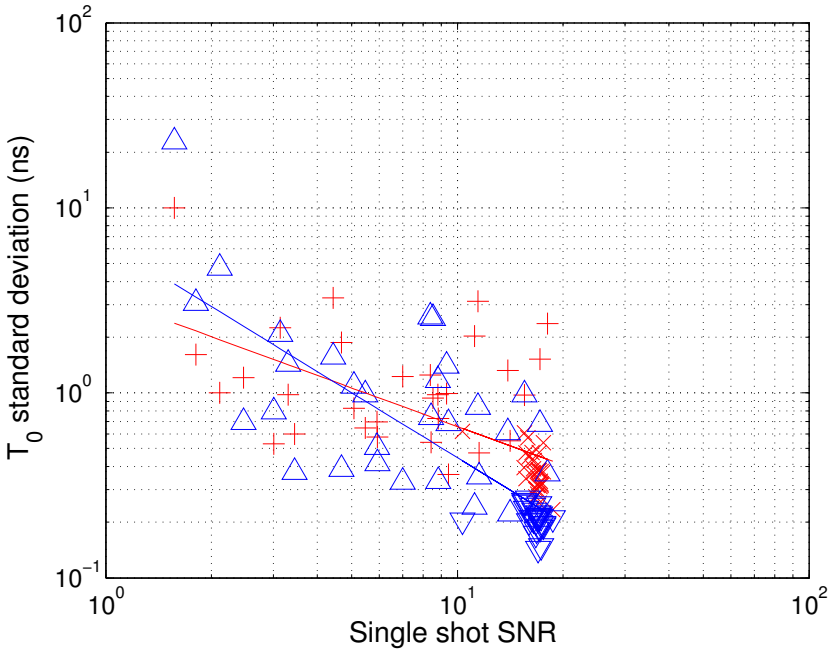

Figure 4.14: Log-log graph showing the standard deviation (uncertainty) of t_0 against signal to noise ratio (SNR). Includes data found using the peak technique on aluminium (red cross, $+$) and fused silica (red x, $\times$). Data found using the envelope technique on aluminium (blue triangle point up, $\triangle$) and fused silica (blue triangle point down, $\triangledown$) is also included. Linear fit lines are included for the peak technique (solid red line, $-$) and the envelope (dashed blue line, $--$).

Sources of uncertainty in fractional velocity measurement

In the previous section the uncertainty in the measurement of Δt and t_0 is measured experimentally. A variety of sources of noise contribute to the uncertainty in these measurements. The next section investigates, experimentally, some of these noise sources to determine their impact. These sources can be broken down into two groups, those caused by the generation of the probe wave and those caused by the detection of the probe wave.

Generation sources Uncertainty in the probe wave arrival comes from variation in the triggering of the laser to generate the probe wave. The effect of changes in the optics used to generate the probe wave is mitigated by the use of

the differential technique described in section 4.2.1. Variations in the phase and arrival timing of the probe wave are of prime interest, though amplitude variations are also measured. To ensure good SNR levels the ideal sample is used in these investigations.

Laser trigger timing variation The FPGA controls the timing of the triggering of the laser to generate the probe wave. Between the FPGA triggering the laser to fire and the laser firing there is a finite delay. The finite delay varies according to a host of variables such as the temperature of the laser cavity, power levels and other factors. This causes a random error in the measurement.

Data acquisition for the experiment is triggered by the coherent trigger, which means the variation in triggering of the laser should not affect the timing of the acquisition of the wave. However this variation will change the nature of the pulse produced and so the ultrasound wave packet generated.

To measure this variation experimentally the laser Q-switcher is set to trigger from the FPGA output. The FPGA output is also used to trigger an oscilloscope that records the resultant laser pulse from the coherent trigger. For statistical significance a total of 1000 coherent trigger waveforms were recorded (see figure 4.15 showing the first 10 triggers).

Each waveform is fitted to, so as to find the peak amplitude and time of arrival relative to the FPGA trigger signal (see figures 4.16a and 4.16b respectively). A weak correlation is observed between the size of the pulse and the delay in the arrival of the pulse (see figure 4.17). The standard deviation of the delay between the FPGA triggering and the arrival of the pulse is 41.83 ps. The effect of this variation will be reduced when the waves produced are averaged. This variation represents a fundamental limit in the precision .

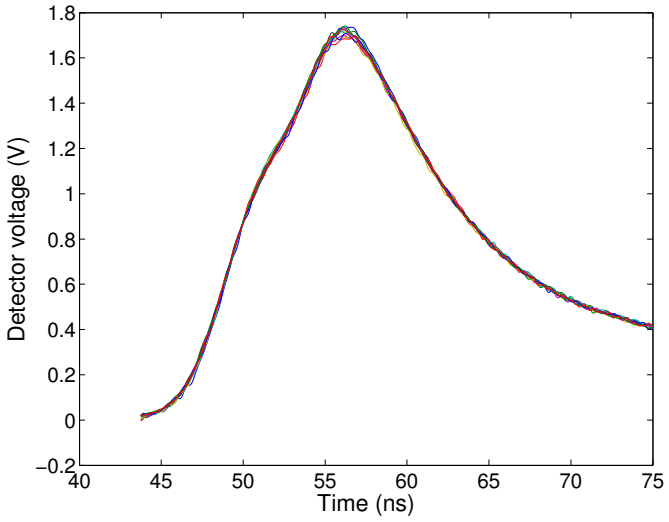

Figure 4.15: First ten pulses from Q-switched laser recorded by the coherent trigger, the x-axis shows the time since the FPGA trigger signal in nano seconds.

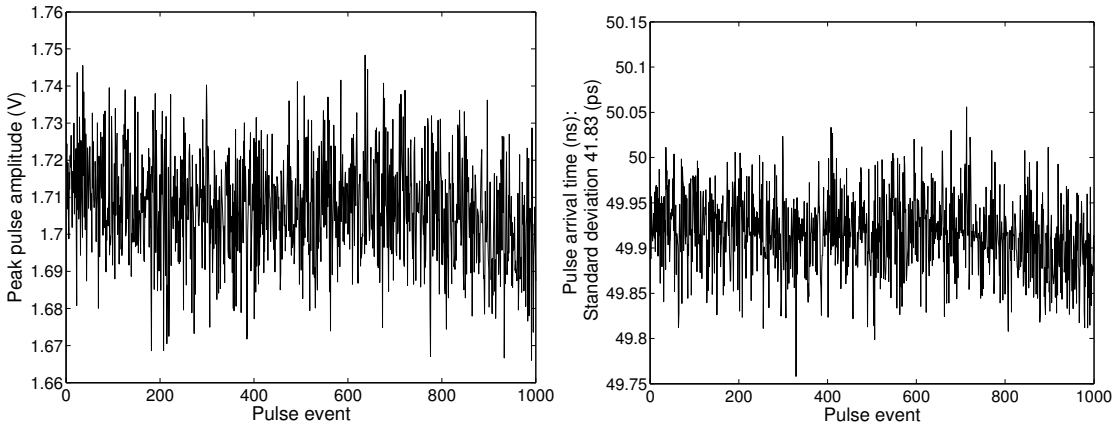

(a) Peak amplitude (b) Delay

Figure 4.16: Peak amplitude (a) and delay between FPGA triggering and arrival of pulse (b). For each of the 1000 recorded pulse from Q-switched laser recorded by the coherent trigger, values were found through fitting.

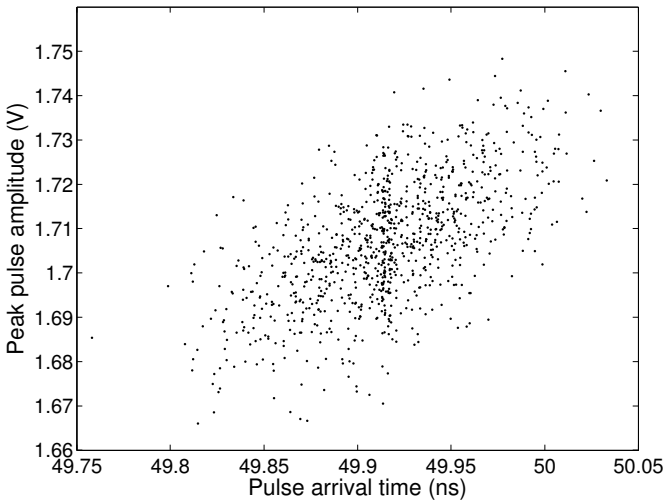

Figure 4.17: Comparison between laser pulse peak amplitude and delay between triggering signal from FPGA and detection of pulse. A weak correlation is observed.

Change in delay values for firing Q-switched laser Due to switching delays between the generation of the pump and probe waves, controlled by the FPGA, there is a finite change in the amount of time between the triggering of the laser to generate the probe wave. This is minimized by padding the delay window between switching values.

However, varying the timing of the laser triggering affects the amount of energy released from the laser cavity. This alters the rise time of the coherent trigger signal. The coherent trigger starts the acquisition of data, changing it affects the measurement of Δt. This causes a random error in the measurement.

The affect of altering the delay values is investigated experimentally by changing the delay to several different values successively. The pump wave is not generated so no stress is present. The reference and target probe waves are acquired synchronously using 16384 averages. From these Δt is found using the full spectrum method (see figure 4.18).

The standard deviation for the Δt values is 1.6 ps. This variation is the same as that found on the ideal sample when comparing the variation in Δt with the signal

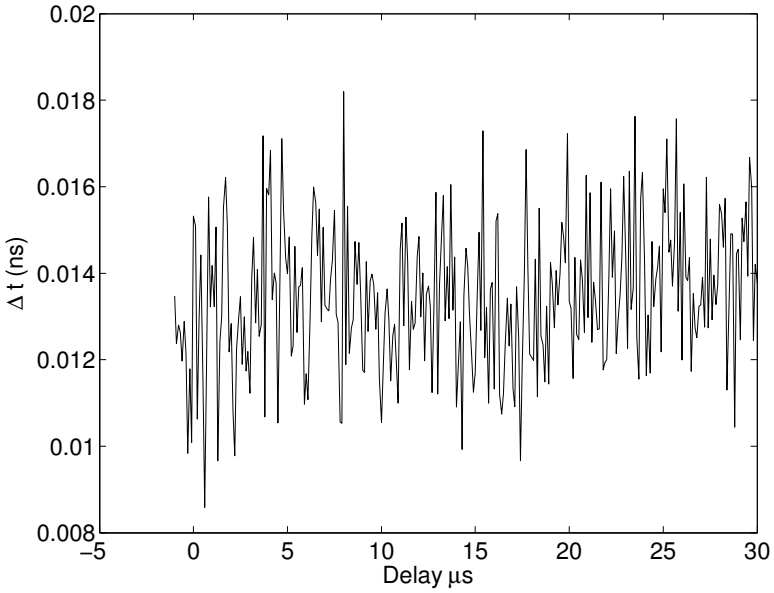

Figure 4.18: Comparison of Δt between two waves with respect to variation in delay used by the FPGA. The standard deviation of Δt is 1.66 ps

to noise ratio (see figure 4.13). From these results, varying the delay between the generation of the waves has little affect on the uncertainty in the measurement of Δt.

Detection sources The probe wave is detected by a knife-edge detection method described in section 2.5.3. Noise in the signal from the knife-edge detector can come from a wide range of sources such as flicker noise in the laser, shot noise from the laser/detection electronics and electromagnetic interference (EMI) in the detection circuit and amplifiers. Some noise sources are mitigated, at least partially, through the design of the system. The use of electromagnetic shielding to reduce the impact of EMI being an example. Noise from the knife-edge detector is a source of uncertainty in the measurement of both Δt and t_0. It is important to investigate the nature of dominant noise sources.

Variation in returning light level The intensity of light returning to the knife-edge detector will affect the amount of photo-current produced. This will affect both the amplitude of the signal and the amplitude of the noise. In a shot noise limited system the signal to noise ratio is related to the square root of the intensity of the returning light [104]. This next section investigates the relationship between the signal to noise ratio and returning light level.

The experiment to investigate the relationship between the signal to noise ratio and the intensity of the light, focuses the knife-edge detector onto an ideal sample. The amount of returning light is controlled by adjusting the output intensity of the CW laser used in the knife-edge detector. The light level falling on the detector is measured as the summed DC voltage from the detector. Several different intensities of light are achieved. A probe wave is generated. The measurement of the signal to noise ratio is conducted as described on page 95 of this chapter.

Above a threshold the signal to noise ratio is a linear function of the square root of the DC voltage from the knife-edge detector (see figure 4.19). The threshold is approximately at 1 volt. Above this threshold the knife-edge appears to be shot noise limited. Below this threshold other noise sources dominate, such as flicker noise from the laser and EMI. These features cause a random error in the measurement.

To ensure the precision of measurements any data below a set signal to noise ratio is discarded (see section 4.5.4), this corresponds to intensity of light returning to the detector above the threshold and a large uncertainty in Δt.

Calculating uncertainty in fractional velocity change

Each variable used to calculate the fractional velocity change has an associated uncertainty that has been found by experimentation. These uncertainties accu-

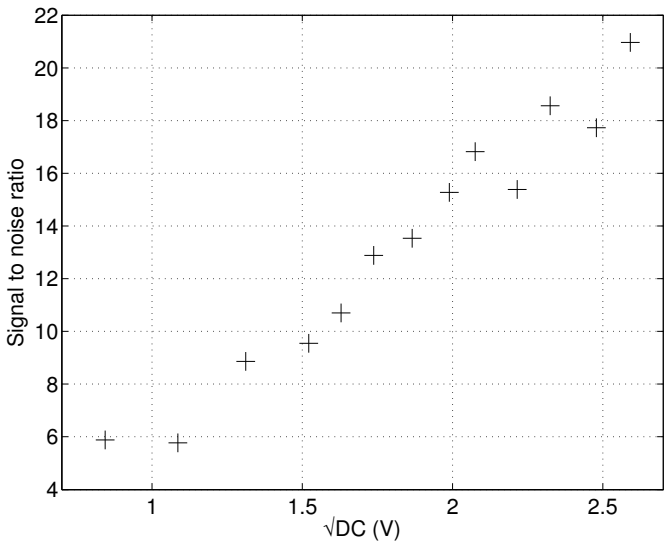

Figure 4.19: Graph comparing the $\sqrt{DC}$ voltage level to the signal to noise ratio. The summed DC voltage from the knife edge is a function of the the intensity of the illumination.

mulate when calculating the fractional velocity change. The total uncertainty in the fractional velocity change can by found using the propagation of uncertainty technique. The uncertainties in Δt and t_0 are assumed to be independent. This is fair provided there are no systematic errors present in the acquisition of the timing.

In the propagation of uncertainties technique, the localised gradient of the independent and dependent variable is multiplied by the uncertainty. Each independent variable contributes to the uncertainty in the dependent variable. The uncertainty in the dependent variable is equal to the square root of the sum of the squares of each of the product of localised gradient and uncertainty. In this case the uncertainty in the fractional velocity change ($\delta_{\left(\frac{\Delta V}{V_0}\right)}$) is:

$$\delta_{\left(\frac{\Delta V}{V_0}\right)} = \sqrt{\left(\delta_{\Delta t}\frac{\partial\frac{\Delta V}{V_0}}{\partial\Delta t}\right)^2 + \left(\delta_{t_0}\frac{\partial\frac{\Delta V}{V_0}}{\partial t_0}\right)^2}$$

where:

$$\frac{\partial \frac{\Delta V}{V_0}}{\partial \Delta t} = \frac{-t_0}{(t_0 + \Delta t)^2}$$
$$\frac{\partial \frac{\Delta V}{V_0}}{\partial t_0} = \frac{\Delta t}{(t_0 + \Delta t)^2}$$

where δ_{t_0} is the uncertainty in t_0 and $\delta_{\Delta t}$ is the uncertainty in Δt.

Uncertainty in displacement and stress

The uncertainty in the stress arises from the uncertainty in the measurement of the displacement, the uncertainty in the properties of the pump wave and the uncertainty in the material constants. These are investigated in this section so as to assess the overall uncertainty in the measurement of the stress.

Uncertainty in displacement

The minimum resolution of the calibrated output of the Polytec interferometer for a displacement is ± 0.2 nm as quoted by the manufacturers. The minimum resolution is confirmed experimentally by taking single shot displacement measurements on a static ideal sample at 30 different locations, repeated 50 times (see figure 4.20). The average standard deviation is 0.05 nm. This indicates the uncertainty in the measurement is lower than the stated resolution. However this may be affected by the amplitude of the displacement measured. The uncertainty in the displacement used in calculating the uncertainty of the stress is 0.2 nm. This causes a random error in the measurement.

A minimum displacement resolution of ± 0.2 nm equates to an uncertainty in the stress of ± 0.0225 MPa. The effects of incoherent noise sources are mitigated by coherent averaging (256 averages are used) when acquiring the pump wave.

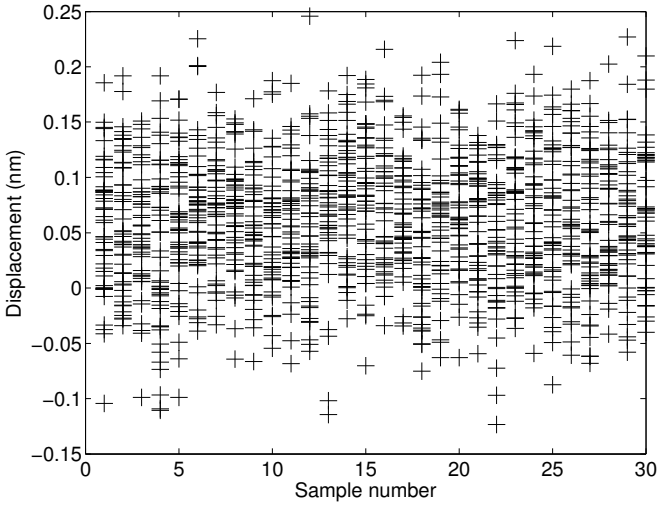

Figure 4.20: Recorded displacements for 30 different locations repeated 50 times.

Uncertainty in the pump wave frequency The frequency of the pump wave is used to determine the stress induced by it. A single value is used for the frequency of the pump wave in the calculation of the stress. The use of this single frequency introduces uncertainty in the measurement of the stress. This causes a random error in the measurement.

One reason for this is that the pump wave consists of several frequencies, as it has a finite length. This is seen when comparing the spectrum of a single pump wave on fused silica (see figure 4.21) for different pump wave frequencies. Each pump wave has a spectrum with a finite width. The central frequency of the pump wave spectrum is selected as the frequency of the pump wave. This assumption is fair as the pump wave is considerably longer than the probe wave so the probe wave experiences a stress that is effectively from an infinite, monochromatic source.

Uncertainty in the central frequency of the pump wave spectrum contributes to the uncertainty in the calculated stress. Variations away from this central frequency can be caused by a range of factors including electronic pickup, nonlinear amplification (though this would be small as the amplifier is operated in its linear

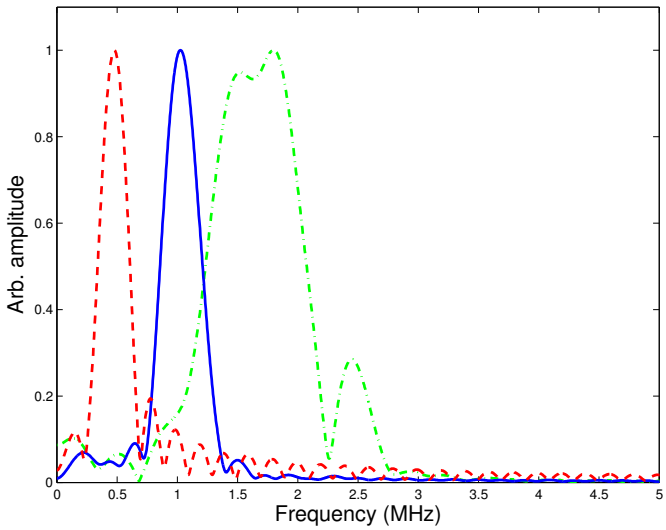

Figure 4.21: Spectrum's of 0.5 MHz (red dashed line, −−), 1.0 MHz (blue solid line, −) and 2.0 MHz (green dashed-dotted line, .−) pump waves that have propagated in fused silica. No higher order harmonics are seen, indicating a linear system.

regime) or due to the propagation of the wave in the material. To quantify the uncertainty in this frequency, 200 single shot measurements are made using a 1MHz transducer to generate the pump waves and are detected using the Polytec interferometer. The pump wave propagates in the ideal sample. Fitting a Gaussian to each pump waves frequency spectrum allows the central frequency to be found (see figure 4.22). The standard deviation of these measurements is 359 Hz. The uncertainty in the pump wave frequency is therefore 0.03%.

Uncertainty in material properties The material constants are used in the calculation of the induced stress due to the displacement caused by the pump wave. The accuracy of the material properties affects the accuracy of the stress. Two main sources of uncertainty in material properties exist. The first is due to fundamental uncertainty in referenced values. The second is the uncertainty due to the use of isotropic material properties for anisotropic materials. Both are discussed. These cause systematic errors in the measurement.

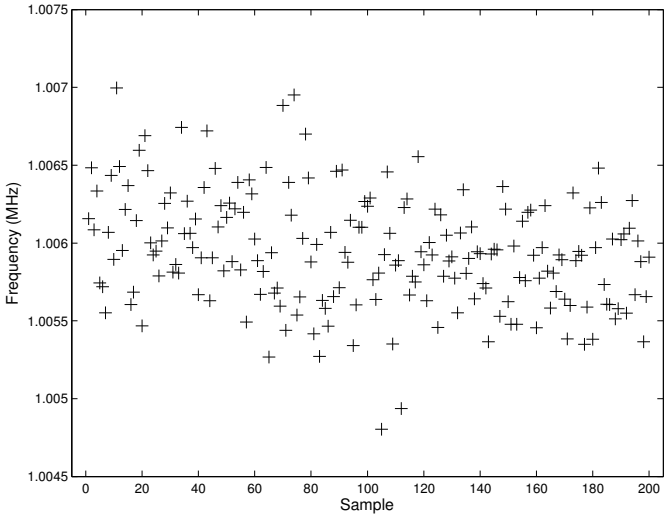

Figure 4.22: Graph of central frequency of pump wave packet recorded for 200 samples. The standard deviation of the frequency is 359Hz and the mean value is 1.006 MHz.

Material	Density (kgm^{-3})	Young's Modulus (GPa)	Shear Modulus (GPa)
Aluminium	2698	70.3	26.1
Fused Silica	2200	73.1	31.2
Titanium	4508	115.7	43.8
Assumed level of accuracy	1	0.1	0.1

Table 4.1: Table of material constants and assumed accuracy for relevant materials used in experiments in this thesis

Uncertainty in referenced isotropic material properties Material constants can be found in a variety of sources for the bulk isotropic case for various materials. The material properties used in this work are given in table 4.1. They are based on values in [120] and they haven't been cross-referenced. As no level of accuracy is established for each material property, an assumed value is used (see table 4.1).

Variation in material properties with direction The material properties in anisotropic materials are dependent on direction. In the case of anisotropic poly-

crystalline materials the anisotropy is a function of the microstructure. Where the scales of a materials microstructure is sufficiently small, it is assumed an homogonised anisotropic value for the material properties can be used, as the variation in material properties with orientation of the microstructure is averaged out. This assumption fails when the scale of the microstructure is of the same order as the interaction distance between the pump and probe wave used to measure A_R of the material. This only occurs on certain samples, which are investigated in section 5.6. In this case the directional dependence of the material properties becomes important. This section investigates the directional dependence of the material properties used in calculating the stress to qualitively demonstrate the impact of this variation.

In the anisotropic case the relationship between ϵ_{ij} and σ_{ij} is given in the linear approximation by:

$$\sigma_{ij} = \sum_{k=1}^{3}\sum_{l=1}^{3} c_{ijkl}\epsilon_{kl}$$

where c_{ijkl} is the second order elastic constants. The Young's and shear modulus are related to the second order elastic constant. The second order elastic constants vary with direction in an anisotropic material. The directional dependence of the second order elastic constants is well known [121, 122]. These published values can be used to calculate the directional dependence of the Young's and shear modulus by matrix algebra using existing code [123]. Two anisotropic materials are investigated in this work: aluminium and titanium. The variation of the material properties can be seen in figure 4.23a for aluminium and figure 4.24a for titanium. The variation in the material properties is symmetrical, it repeats every 180°.

The Young's modulus of aluminium varies from 63 to 72 GPa (13% of the mean) and the shear modulus does not vary remaining at 28.3 GPa. The Young's modulus of titanium varies from 105.9 to 149.1 GPa (35% of the mean) and the

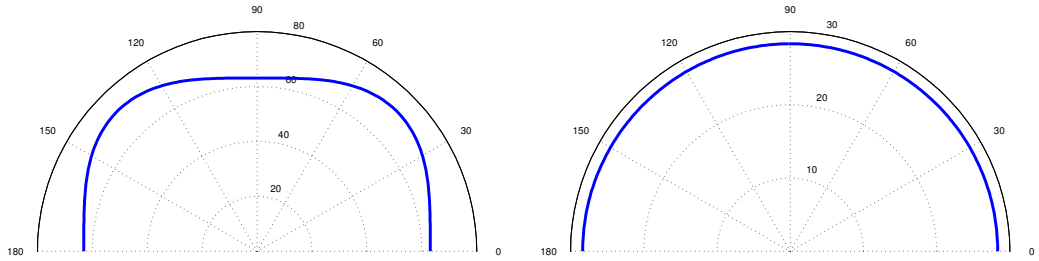

(a) Young's modulus of aluminium versus direction

(b) Shear modulus of aluminium versus direction

Figure 4.23: Two diagrams depicting the variation over 180° of the Young's (a) and shear (b) modulus for aluminium.

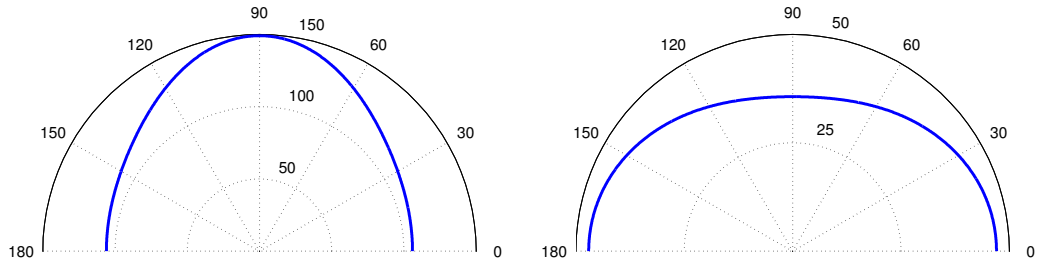

(a) Young's modulus of titanium versus direction

(b) Shear modulus of titanium versus direction

Figure 4.24: Two diagrams depicting the variation over 180° of the Young's (a) and shear (b) modulus for titanium.

shear modulus varies from 35.7 to 47.0 GPa (28% of the mean). This represents large changes in the material properties with direction which must be accounted for when investigating large grain samples. For samples with small grains, the material properties are assumed to be an homogonised anisotropic value.

Calculating uncertainty in stress

The equation relating the displacement to the stress consists of several variables. The measured or known variables (dependent variables) are the Young's modulus

(E), shear modulus (G), frequency (f), density (ρ), velocity (vel) and displacement (U_0). From these, further values are calculated including the various wave numbers (k, k_s and k_l), the difference in wave numbers (q and s) and the Lamé constants (λ and μ). Each of these variables has an uncertainty that is either assumed, found experimentally or can be calculated from the propagation of uncertainty. These uncertianties are used to calculate the overall uncertainty in the stress measurement. Only two of the variables, the Young's and shear modulus, are assumed to be dependent. The others variables are assumed to be independent.

The stress in the xx direction is described by [119]:

$$\sigma_{xx|z=0} = A\left(\lambda\left(k^2 - q^2\right) + 2\mu k^2\left(1 - \frac{2sq}{k^2+s^2}\right)\right)$$

$$A = \frac{U_0}{q\left(1 - \frac{2k^2}{k^2+s^2}\right)}$$

The uncertainty in $\sigma_{xx|z=0}$ can be described by:

$$\delta_{\sigma_{xx|z=0}} = \sqrt{\left(\delta_A\frac{\partial\sigma_{xx}}{\partial A}\right)^2 + \left(\delta_\lambda\frac{\partial\sigma_{xx}}{\partial\lambda}\right)^2 + \left(\delta_k\frac{\partial\sigma_{xx}}{\partial k}\right)^2 + \left(\delta_q\frac{\partial\sigma_{xx}}{\partial q}\right)^2 ... \\ \overline{+\left(\delta_G\frac{\partial\sigma_{xx}}{\partial G}\right)^2 + \left(\delta_s\frac{\partial\sigma_{xx}}{\partial s}\right)^2} \quad (4.4)$$

The partial differentials for equation 4.4 can be found in appendix C.

Uncertainty in combination of stress and fractional velocity change measurement

To determine the accuracy of the shifting arrangement, discussed in section 4.2.5, data from the single point acoustoelastic measurement carried out in section 5.2 is investigated. This uncertainty is a form of systematic error. This is done by applying a least mean squares linear fits to the data as it is shifted through a range

of delays. The average size of the residuals (the difference between the fit values and actual values) is used to estimate the accuracy of the fit. The result is seen in figure 4.25.

A minimum average residual is reached close to that of the shift found analytically (denoted by the ∘) value. The analytically found location of the peak does not reduce the residuals to a minimum. Indicating that in this case calculating the location of the first peaks failed to find the optimum shift value. In order to ensure that the minimum error due to shifting is achieved, the residual checking procedure outlined above is carried out on all data collected.

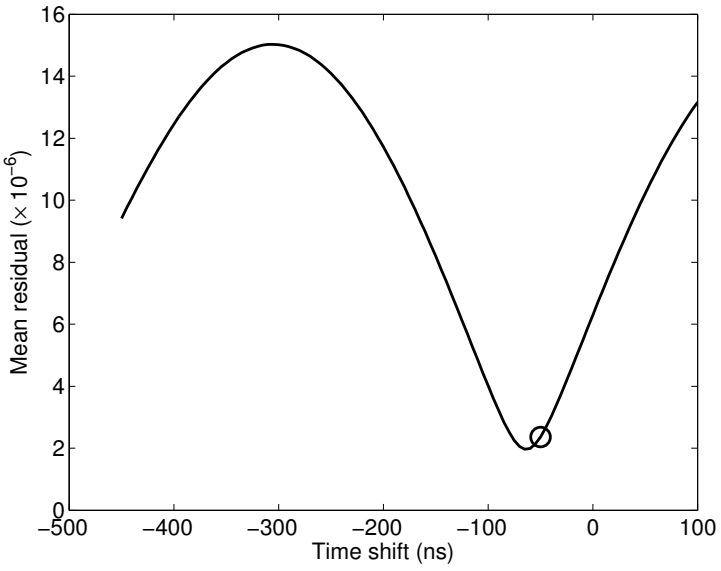

Figure 4.25: Graph of the shift applied to the pump wave displacement versus the mean residual value from least means squares fit. The circle (∘) represents the shift found analytically.

4.3.3 Demonstration of relative magnitudes of uncertainties

To give an insight into the relative magnitudes of the uncertainties in the acoustoelastic measurement, the value of the variables and the calculated uncertainties

Variable	Value (Val)	Calculated uncertainty (δ)	$\frac{Val}{\delta} \times 100$ (%)	% contribution to $\delta_{\left(\frac{\Delta V}{V_0}\right)}$
$\frac{\Delta V}{V_0}$	31.1×10^{-6}	1.35×10^{-6}	4.3	-
Δt (ps)	28.6	1.24	4.3	99.9975
T_0 (ns)	917	0.19	0.02	0.0024

Table 4.2: Calculated uncertainty in fractional velocity change and associated variables for an arbitrary interaction between pump and probe wave on fused silica.

Variable	Value (Val)	Uncertainty (δ)	$\frac{Val}{\delta} \times 100$ (%)	% contribution to δ_σ
Stress (σ, MPa)	1.104	0.0235	2.1	-
Displacement (nm)	-11	0.2	1.8	70.9
Angular frequency (ω, Hz)	6.28×10^6	2255.7	0.03	2.55
Youngs mod (E, GPa)	73	0.1	0.1	1.5
Shear mod (G, GPa)	31	0.1	0.3	23.4
Density(ρ, kgm^{-3})	2200	1	0.045	0.29

Table 4.3: Calculated uncertainty in stress and associated variables for arbitrary interaction between pump and probe wave on fused silica. The angular frequency refers to the angular frequency of the pump wave. Systematic uncertainties are presented in the last three rows

are presented. Table 4.2 presents the calculated uncertainty in fractional velocity change and associated variables. Table 4.3 presents the calculated uncertainty in stress and associated variables for arbitrary interaction. The error in the pump wave frequency could be found directly by acquiring the whole of the pump wave. As the uncertainty in the pump wave frequency is small (0.03%, see section 4.3) the error is not found as part of the procedure to acquire the acoustoelastic measurement, this is to reduce the number of data points acquired. The effect of the anisotropy is assumed to be small as the pump and probe waves co-propagates through many grains. The data is from a single pump- probe wave interaction. The interaction took place on fused silica.

From the results presented in table 4.2 the largest contribution to the uncertainty in the fractional velocity change comes from the uncertainty in the measurement of Δt. The results in table 4.3 show that the largest contribution to the uncertainty in the stress induced by the pump wave is from the uncertainty in the measurement of the displacement. The uncertainty in the shear modulus is the next largest contributor to the uncertainty in the stress.

4.3.4 Comparison of calculated uncertainties to least mean squares fit

To assess the calculated uncertainty in the stress and fractional velocity change a single point acoustoelastic measurement is plotted with error bars in figure 4.26. The error bars are based on the uncertainty calculated for the stress and fractional velocity change. The data used is taken from the single point acoustoelastic experiment carried out in section 5.2. These uncertainties come from the standard deviation of observed values for set conditions (SNR). The error bars represent a level of confidence, in this case that there is a 68% probability that the value of the variable will fall within this region. The confidence regions of most of the points, meet the fit line, indicating the calculated errors are reasonably representative.

4.3.5 Instrument configurations impact on noise

This section discusses the configuration of the instrument to optimise the precision of the measurement of A_R. These parameters include the acquisition of data, the frequencies and the length of interaction of the waves. The optimum configuration is found through a combination of modelling and experimental work. Experiments to determine the impact of changing these instrumental features, probe the A_R

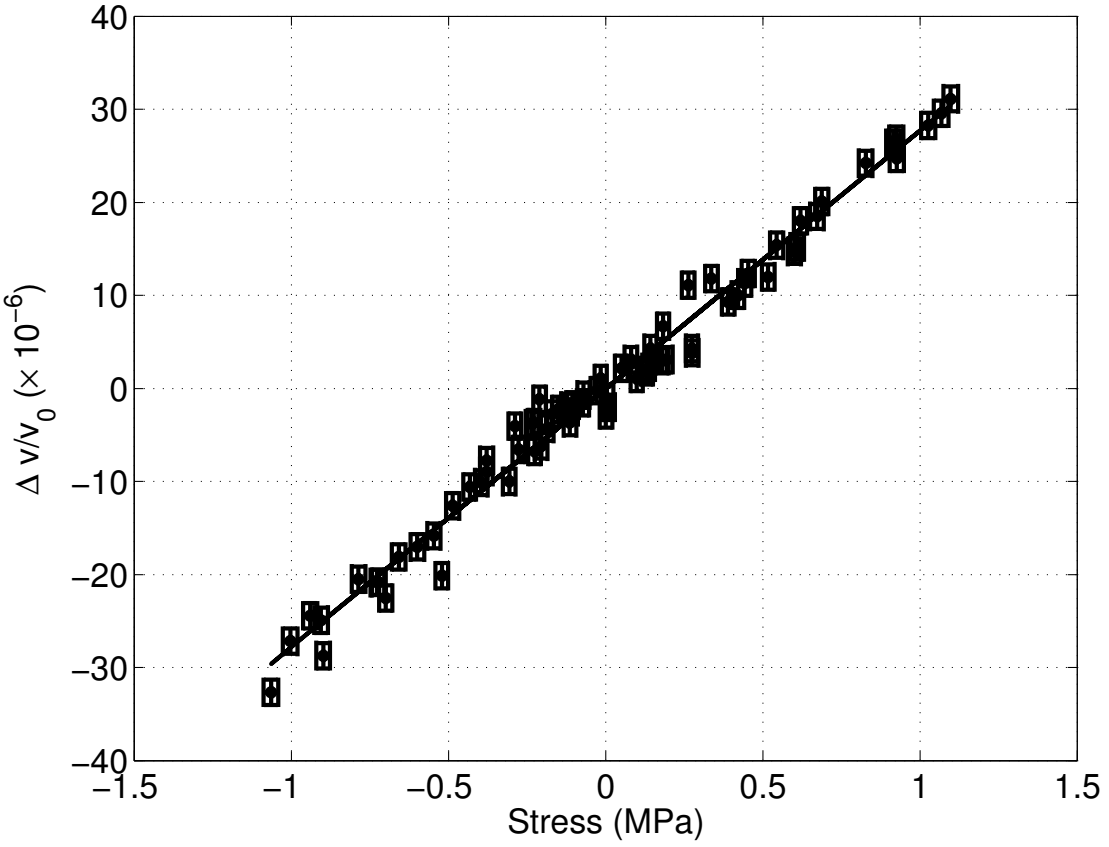

Figure 4.26: Graph of applied stress against fractional velocity measurement. The error bars describe the calculated uncertainty in the applied stress and fractional velocity change, defined as one standard deviation or 68% level confidence. The least mean squares regression fit can be seen as the solid line (-).

of fused silica. These acoustoelastic measurements are carried out as discussed in section 4.2 and 5.2. Unless stated otherwise the configuration of the equipment for all the experimental work is as follows. The probe wave is generated using a 55 μm grating, giving a frequency of 63 MHz on fused silica. The pump wave was produced using a 1 MHz transducer being in the centre of the amplifier's linear regime. The probe wave is generated and subsequently detected at a distance 3 mm away from the centre of the imaged generation spot.

Modelled acquisition of probe wave

The way the probe waves are acquired and processed can impact the level of uncertainty in the measurement of Δt and t_0. In order to best configure the acquisition and processing of these signals, modelling of the acquisition and processing was carried out. The acquisition features that were explored relate to the configuration of the oscilloscope recording the waves. These features include coherent averaging, time-base and sampling rate. Both amplitude and phase based noise were investigated by adding randomly generated fluctuations to the signal. The modelling process involves creating a set of waveforms of different signal to noise ratios and then sampling them with different acquisition settings and processing techniques. The waveforms are created using the following formula:

$$y = A_n + [A\cos(2\pi t + \phi_n)\, G] \tag{4.5}$$

where A is the amplitude of the wave, t is the time, G is a Gaussian packet expression with a centre at the centre of the timing window and a width of half the window, ϕ_n is the phase noise and A_n is the amplitude noise. The level of noise is then calculated as the standard deviation in the output of each processing

method (either Δt or t_0). A thousand waveforms of each signal to noise ratio were simulated to make the modelling statistically relevant.

When comparing processing techniques to find Δt and t_0, it was found that the full spectrum method and the envelope method resulted in lower noise levels. The full spectrum technique will be used for calculating Δt. The peak method of finding t_0 will be used. This is because the improvement in noise resilience of the envelope method does not justify the additional time taken to process. Also the peak method is more stable at lower SNR values.

Modelling for coherent averaging of the signals showed improvement in resilience to both amplitude and phase noise. The more averages taken, the lower the impact of the noise on the signals. Coherent averaging takes time, over which factors can change. For this technique to be practical, the amount of time to take a measurement needs to be limited. The best compromise between improvement in resilience to noise and time taken to acquire the signal was found to be 16384 averages from the modelling conducted. The number of averages is selected as a base 2 number to simplify quantifying the improvement in signal to noise.

The time base defines the length of time over which the sample is acquired. When combined with the sampling rate this gives the number of points in a trace. The time base controls the length of signal that is acquired. Three time bases are modelled (20, 50 and 100ns per division). From the model, the optimum setting was found to be 50ns. When using the 50ns time base the full extent of the probe wave envelope is captured without removing parts of it (20ns time base does remove parts) or including regions where no signal is present (100ns).

The sample rate relates to the number of points per second that are captured in a trace. The sampling rate defines the number of points acquired for each trace. The more points acquired, the longer the time it takes for processing and transfer.

An optimum number of points records the wave form accurately, whilst taking the minimum of resources. Three sampling rates are modelled (1, 10 and 20 GSa s^{-1}). An improvement in the resilience to amplitude noise is seen with an increase in sampling rate. However the improvement in noise resilience between the 10 and 20 GSa s^{-1} is not commensurate to the increase in use of resource. As such the optimum sampling rate is found to be 10 GSa s^{-1}.

Combined effect of amplitude and phase noise To investigate the effect of the combination of amplitude and phase noise several models were created. The phase noise for each model was kept constant, with the value being varied from model to model. The amplitude noise was varied to produce a range of amplitude SNR values. For each SNR value 1000 waveforms are created. The standard deviation of the Δt is used as a metric to determine the uncertainty in Δt. In figure 4.27 it can be seen that the size of the phase noise dictates the fundamental lowest uncertainty in the Δt measurement. Above this fundamental phase noise limit the SNR value determines the uncertainty in the Δt measurement as would be expected.

Different probe wave frequency

When calculating the stress induced by the pump wave it is assumed that the majority of the stress experienced by the probe wave is due to stress in the xx direction (as $\lambda_{probe} << \lambda_{pump}$). As the probe wave frequency is increased (reducing λ_{probe}) this assumption becomes more valid, reducing the uncertainty in the measurement of the stress.

To investigate the effect of the probe wave frequency on the measurement of A_R a series of measurements are taken on fused silica with different probe wave

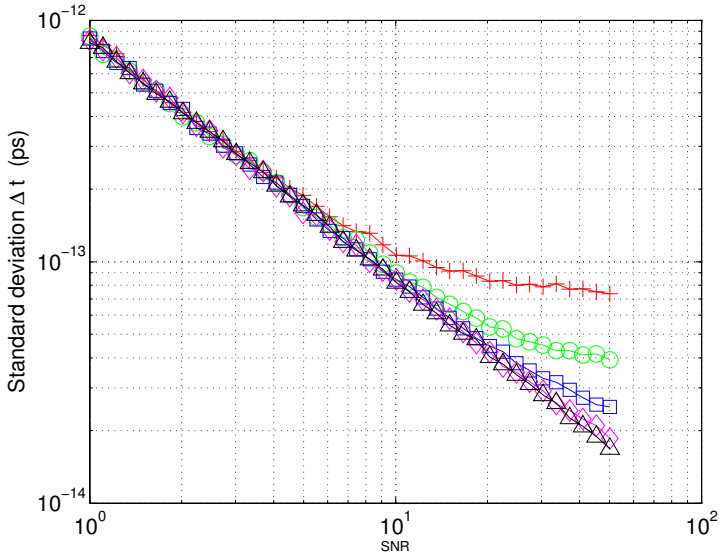

Figure 4.27: Graph showing the effect on the modelled data for Δt noise against signal to noise ratio. Where red crosses (+) represents data acquired with a fixed phase noise of 16 milliRadians (mRad), green circles (○) have a fixed phase noise of 8 mRad, blue squares (□) have a fixed phase noise of 4 mRad, purple diamonds (◇) have a fixed phase noise of 2 mRad and black triangles (△) have a fixed phase noise of 1 mRad.

frequencies. To alter the probe wave frequency, the mask used to generate the probe wave is changed. For each frequency the optimum band pass filter is used in the electronics chain after the knife-edge detector. Three different probe wave frequencies are investigated, 30, 44 and 63 MHz. The resultant stress against fractional velocity change data can be seen in figure 4.28.

The acoustoelastic measurement for the 30MHz probe wave is 33.6 $\pm$ 1.0 $\times 10^{-6}$ MPa^{-1}, for the 44MHz pump wave it is 34.0 $\pm$ 0.9 $\times 10^{-6}$ MPa^{-1} and for the 63MHz probe wave it is 34.0 $\pm$ 1.0 $\times 10^{-6}$ MPa^{-1}. The difference between the acoustoelastic measurements is below the certainty in each measurement. No trend between the probe wave frequency and the acoustoelastic measurement can be discerned. Whilst increasing the probe wave frequency theoretically improves the certainty in the stress (as discussed above), this is not observed practically at these

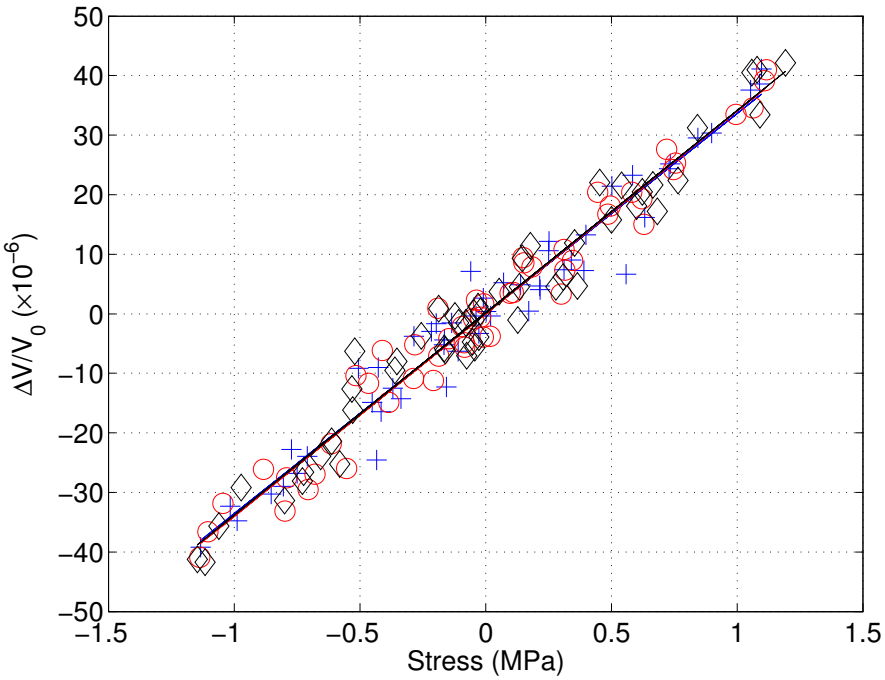

Figure 4.28: Stress plotted against fractional velocity change the gradient of which is A_R. Blue crosses (+) are data points for 30 MHz waves , the gradient is 33.6± 1.0×10^{-6} MPa^{-1}. Red circles (◯) are data points for 44 MHz waves, the gradient is 34.0± 0.9 ×10^{-6} MPa^{-1}. Black diamonds (◇) are data points for 63 MHz waves, the gradient is 34.0± 1.0 ×10^{-6} MPa^{-1}. Linear least mean square fits are applied to data points and are shown as lines of appropriate colour.

frequencies.

The attenuation and scattering of a propagating wave is proportional to its frequency [124], the higher the frequency the greater the attenuation of the wave as it propagates and so the lower the signal to noise ratio of the detected wave. The spectral content of the Q-switched laser at higher frequencies is also much reduced, lowering the amplitude of any wave produced in this region. A compromise is reached between the need to use a high frequency probe wave to reduce the uncertainty in the stress and the need for a good signal to noise ratio. In practice it is found that the optimum configuration generates probe waves in 60-70 MHz bandwidth.

Different pump wave frequencies

For a given displacement, the induced stress at the surface is proportional to the frequency of the pump SAW. The calculation of the stress from the displacement has a frequency term. The higher the frequency the larger the induced stress for a given displacement at the surface in the xx direction.

To investigate this effect several different pump SAW frequencies are used to conduct acoustoelastic measurements on fused silica. The range of frequencies used is limited by the Ritec amplifier (RPR-4000), which has a maximum power range confined to the bandwidth between 0.5 and 2 MHz. Three frequencies are selected due to the availability of transducers with operating frequencies within the peak power bandwidth of the amplifier. These frequencies are 0.5 MHz, 1.0 MHZ and 2 MHz. The resultant stress velocity plots can be seen in figure 4.29.

The A_R for the 0.5MHz pump SAW is 28.9 $\pm$ 0.7 $\times 10^{-6}$ MPa^{-1}, for the 1MHz pump SAW it is 27.7 $\pm$ 0.4 $\times 10^{-6}$ MPa^{-1} and for the 2MHz it is 27.2 $\pm$ 1.6 $\times 10^{-6}$ MPa^{-1}. The stated accuracy comes from the standard error in the least

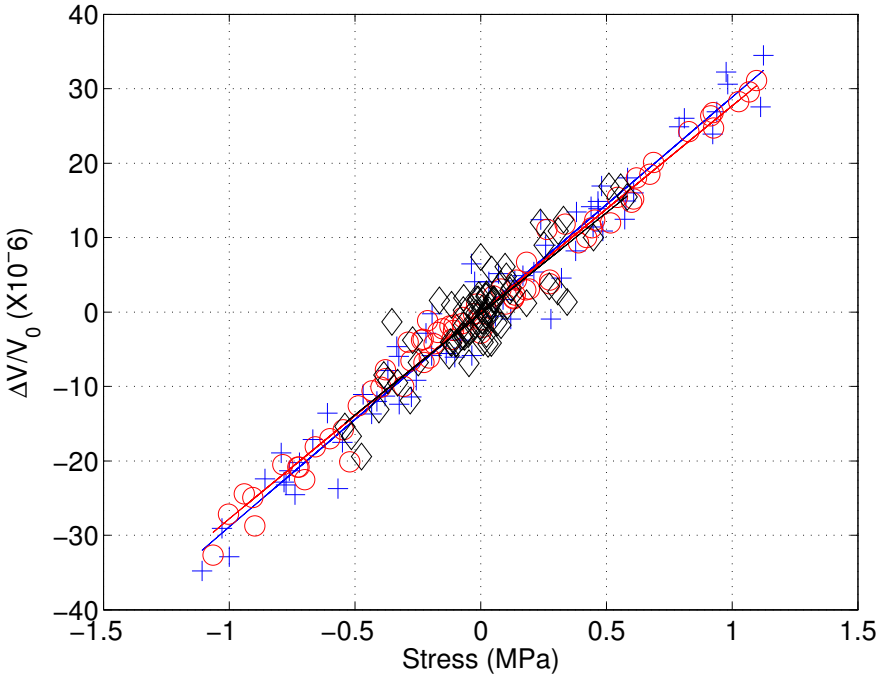

Figure 4.29: Stress plotted against fractional velocity change denoting the change in measured acoustoelastic coefficient due to change in pump SAW frequency. Blue crosses (+) represent data points where the pump frequency was 0.5 MHz, the gradient of these points is 28.9 ± 0.7 $\times 10^{-6}$ MPa^{-1}. Red circles (◯) represents data points where the pump frequency was 1 MHz, the gradient of these points is 27.7 ± 0.4 $\times 10^{-6}$ MPa^{-1}. Black diamonds (◇) represents data points where the pump SAW frequency was 2 MHz, the gradient of these points is 27.2 ± 1.6 $\times 10^{-6}$ MPa^{-1}. Linear least mean square fits are applied to data points and are shown as lines of appropriate colour.

mean squares fit as derived in section 4.3.1. The 2MHz pump SAW data has a higher standard error than the other data sets as the 2MHz transducer generates a smaller displacement and so a lower stress field, which results in a lower fractional velocity change. This reduces the size difference between the fractional velocity change and the noise in the measurement, increasing the impact of the noise. The difference between A_R for each pump SAW frequency is below the uncertainty in the measurements. The A_R produced using different pump SAW frequencies is uniform as would be expected.

The 1MHz transducer is selected for use in further experiments as it has a smaller physical size than the 0.5 MHz transducer allowing it to be attached to a range of samples. The 1MHz transducer can also produce larger stress values than the 2MHz transducer and is in the center of the maximum power range of the Ritec amplifier.

Impact of varying the co-propagation distance

As the pump and probe SAWs co-propagate, they interact. This results in a fractional velocity change in the probe SAW. The fractional velocity change is measured in part by the difference in the time of arrival of the reference and target SAWs (Δt). The fractional velocity change is independent of the distance the probe and pump SAWs co-propagate. However the change in Δt is related to the co-propagation distance. The uncertainty in Δt is dependent upon the signal to noise ratio of the probe SAW (see section 4.3.2). When the co-propagation distance is too small, the change in Δt due to the stress will become proportional to the uncertainty in Δt.

To assess the impact of the co-propagation distance on the measurement of Δt, an experiment is conducted to measure A_R of fused silica for different co-

propagation lengths. The co-propagation length is changed from 0.5 mm to 4.5 mm in 0.5mm steps. The distances are measured from the center of the generation pattern to the point of detection. The resultant modulation of Δt can be seen in figure 4.30 and the associated fractional velocity measurement can be seen in figure 4.31.

As expected Δt changes with propagation distance while the fractional velocity change does not. As the co-propagation distance drops below 1.5 mm the modulation of the fractional velocity change starts to differ from the modulations seen for longer co-propagation distances. At this point the size of the modulation of Δt due to the stress becomes similar to the size of the noise in Δt. For this reason all further experiments are conducted with co-propagation length longer than 1.5mm.

To reduce the impact of the noise in Δt the maximum co-propagation distance should be used. Practically this is complicated by the attenuation of a propagating SAW. The optimum co-propagation distance is 3mm.

4.3.6 Verification of acoustoelastic measurement experimentally

The purpose of this section is to experimentally assess the accuracy of the acoustoelastic measurement. A weakness of some nonlinear techniques (see section 2.4.2) is the difficulty in separating nonlinear effects caused by the instrumentation from the genuine nonlinear effects caused by the sample. The effect of the nonlinearity of the instrument on the measurement is investigated by a null test which involves detecting both pump and probe SAWs that have propagated in such a way that causes minimal modulation of the probe SAW.

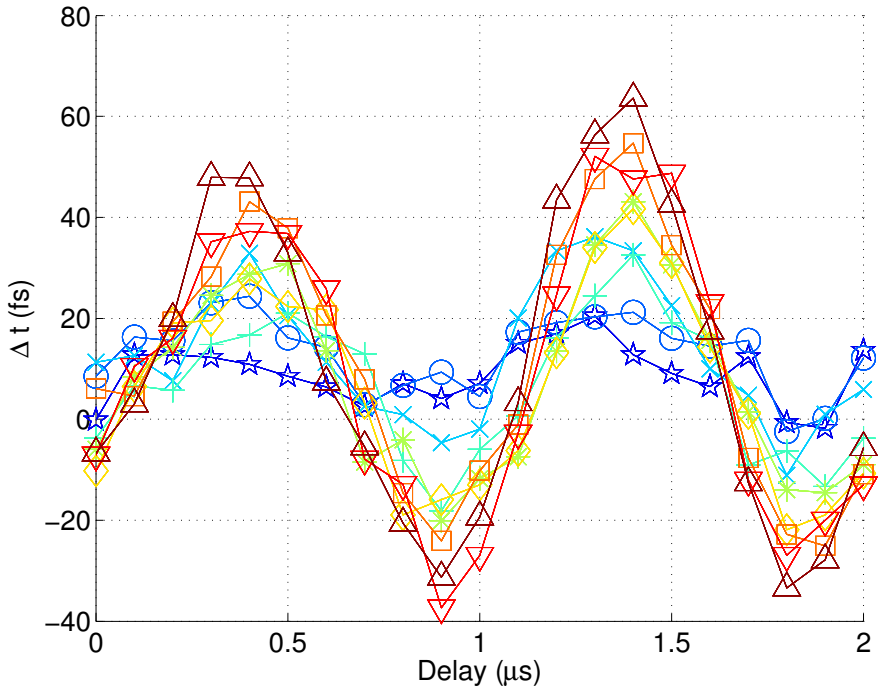

Figure 4.30: Plots of Δt against pump-probe trigger delay for various propagation distances ($\star$ = 0.5 mm, $\bigcirc$= 1.0 mm, $\times$= 1.5 mm, $+$= 2.0 mm,$*$= 2.5 mm, $\diamond$= 3.0 mm,$\square$ = 3.5 mm,$\triangledown$= 4.0 mm and $\triangle$= 4.5 mm).

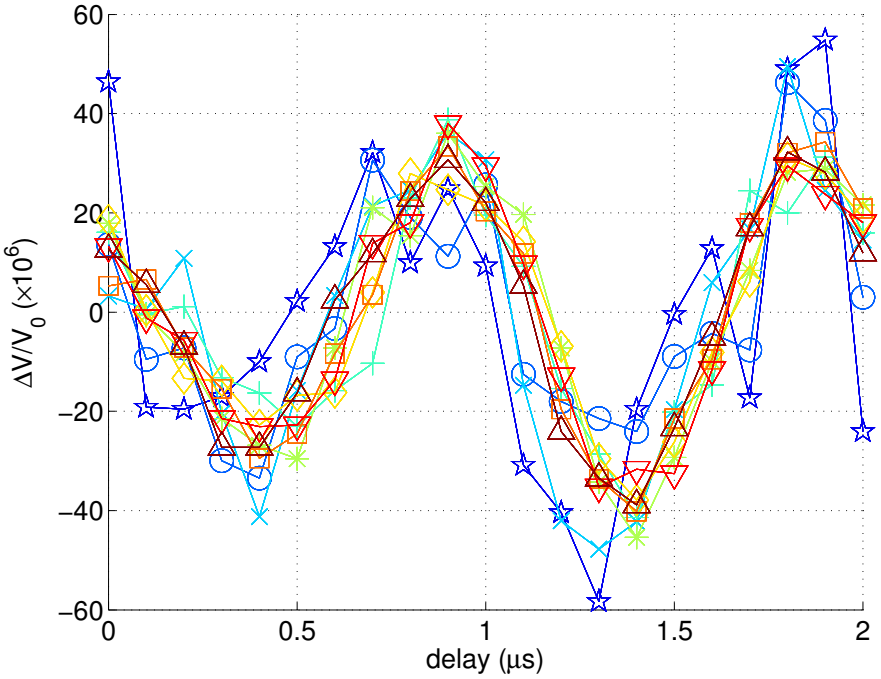

Figure 4.31: Plots of $\frac{\Delta V}{V_0}$ against pump-probe trigger delay for various propagation distances($\star$ = 0.5 mm, $\bigcirc$= 1.0 mm, $\times$= 1.5 mm, $+$= 2.0 mm,$*$= 2.5 mm, $\diamond$= 3.0 mm,$\square$ = 3.5 mm,$\triangledown$= 4.0 mm and $\triangle$= 4.5 mm).

Anti-propagation test

Instrumental effects, such as nonlinear behaviour in the detection electronics, can contribute to the acoustoeleastic measurement. To asses the impact of the instrumental effects on the acoustoelastic measurement and to verify that the measured nonlinear response is due to the material, an experimental investigation is conducted. The experiment alters the direction in which the pump and probe SAWs propagate on the sample. Both SAWs are detected by the detection electronics but interact in a way that does not produce a defined modulation on the sample.

In the first part of the experiment the pump and probe SAW are configured to co-propagate. The probe SAW interacts with a single point on the pump SAW. The delay between the generation of pump SAW and the probe SAW is varied. The probe SAW experiences a range of stresses due to the pump. The fractional

velocity change is modulated in accordance to the level of stress experienced.

In the second configuration (see figure 4.32) the probe and pump SAWs propagate in opposite directions (anti-propagation). In this configuration the probe SAW interacts with a finite section of the pump SAW as it propagates. As such the probe SAW experiences both positive and negative stresses. The average stress experienced by the probe SAW is low in this configuration. Dependent on the length of interaction and the starting location, the probe SAW will experience a small overall stress at some delay points. Provided the instrumental contributions to the measurement of A_R are low then the fractional velocity change in this instance will also be low.

In figure 4.33 the fractional velocity change for the co-propagation and anti-propagation case is shown. A reduction in the modulation in the fractional velocity change is seen for the anti-propagation configuration. The majority of the modulation in the fractional velocity change is due to acoustic SAW interaction on the surface of the sample rather than instrumental effects. This investigation does not completely rule out instrumental effects causing part of the modulation seen in the acoustoelastic measurement but it shows that any instrumental affects are comparatively small.

4.4 Imaging and texture

In section 5.5 a technique is developed to image the spatially correlated variation in the acoustoelastic measurement. The instrumentation developed in this work is in a unique position to do this due to its relatively high spatial resolution compared to other techniques. This allows imaging of the A_R of a material that can be related to the microstructure of the material. Acoustoelastic images produced using this

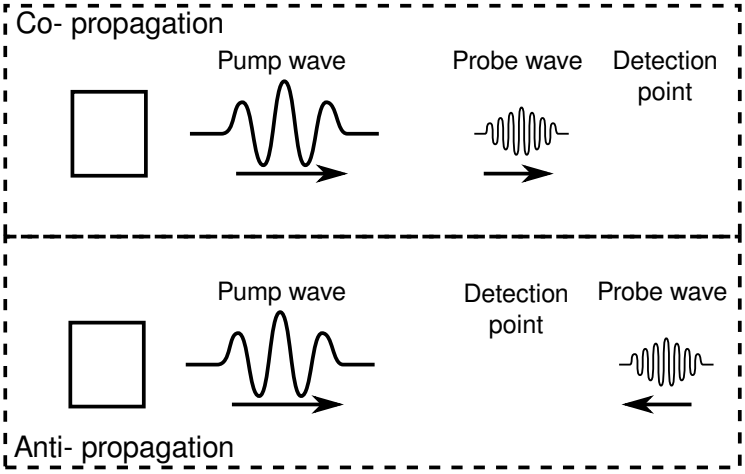

Figure 4.32: Diagram of interaction between probe and pump SAW for co-propagation and anti-propagation experiments.

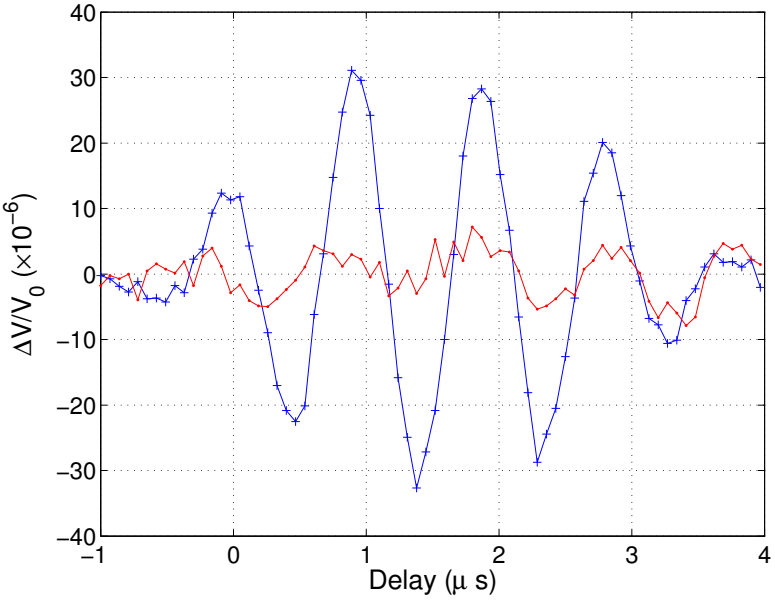

Figure 4.33: Fractional velocity change for the case of the anti-propagation (red dotted line, .−) and the co-propagation (blue crossed line, +−) of the pump and probe SAWs with delay values

technique can be seen from section 5.5.1 onwards.

A linear velocity measurement technique called Spatially Resolved Acoustic spectroscopy (SRAS) is used to map the microstructure prior to and during the acquisition of the acoustoelastic image. This technique allows the re-location of a scan area and comparison between A_R and microstructure. It is described briefly below.

4.4.1 Acoustoelastic imaging technique

The imaging technique developed uses a raster scanning approach. To reduce the effect of incoherent noise a large number of coherent averages are required for acquisition of the probe SAW. For each single interaction between the pump and probe SAWs, 16384 averages are taken. Acquiring this number of averages can take in excess of 20 seconds. The technique developed by Ian Collison [4] used between 5 and 72 interaction points for a measurement on a single location. Similar measurements are taken for the single point measurements at the beginning of chapter 5. The total time taken to make a single point acoustoelastic measurement could be up to 40 minutes. This would make the raster scanning of the acoustoelastic coefficient for several locations tedious and impractical.

To make raster scanning possible, the number of interactions between the pump and probe SAW is reduced to two. Using only two interactions reduces the amount of time taken to acquire a single point measurement to 40 seconds, making the acquisition speed sixty times faster. The uncertainty in fractional velocity change and stress remains constant for all pump and probe SAW interaction as it is non-heteroskedatic. The optimum interaction points of the probe and pump SAWs are those where the stresses are furthest separated from each other. This is because the measurement of the gradient is equal to the change in the values of the stress

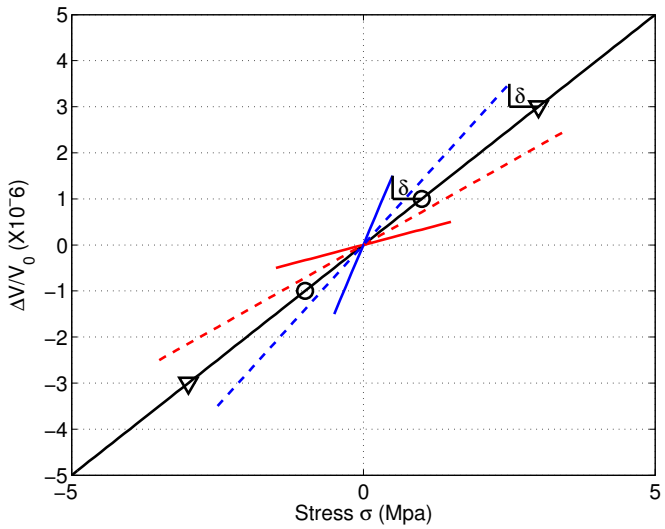

Figure 4.34: Graph demonstrating the improvement in certainty of the gradient by separating the measurements, if the uncertainty in the variables is non-heteroskedatic. The gradient of the solid black line is sought. The uncertainty (δ) in measurements is 0.5. The blue lines represent the maximum gradient due to uncertainty in measurement of the points. The red lines represent the minimum gradient. The difference between the maximum and minimum gradients is lower measuring at the $\bigtriangledown$ points than at the $\bigcirc$.

and the fractional velocity change. The larger the change in the stress and the fractional velocity change, the smaller the contribution of the uncertainty in each of these measurements to the overall uncertainty in the gradient (see figure 4.34). The optimum interaction locations are those where the probe SAW interacts with the maximum peak and trough of the pump SAW.

Locating the peak and trough points on the pump SAW is complicated by the use of two separate detectors for the detection of the pump and probe SAWs. Section 4.2.5 outlines a procedure to find the delay in detection between the two detectors using multiple interactions between the pump and probe SAW. The locations where the probe SAW interacts with the peak and trough of the stress SAW can be found analytically from this delay with reference to the arbitrary reference delay defined in section 4.2.5.

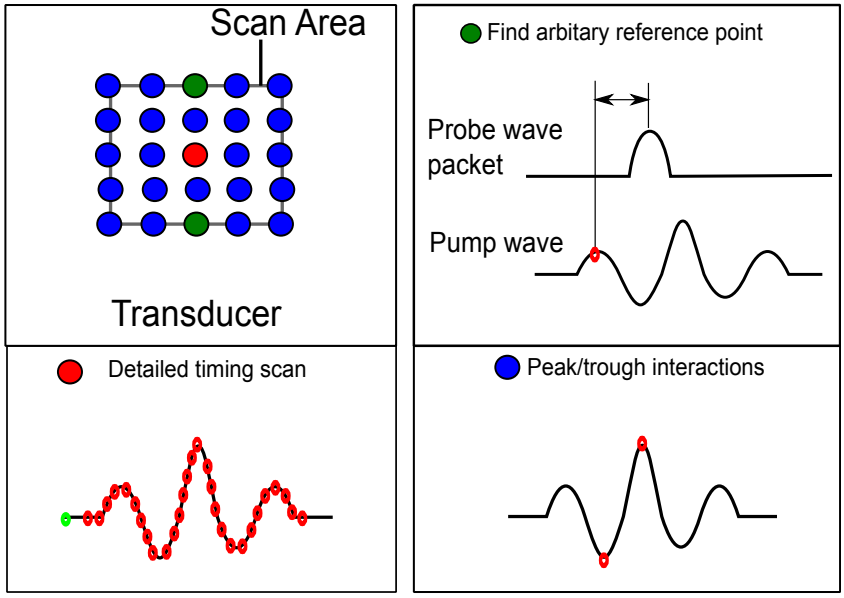

Figure 4.35: Diagram demonstrating the different procedures used in calculating the delay required for the probe SAW to interact with the peak and trough of the pump SAW.

The arbitrary reference delay changes with the distance between the transducer and detection location. Finding the reference delay for the points closest to and furthest from the transducer (see figure 4.35) allows the range of the arbitrary delays to be determined. The arbitrary reference delays for points in between can be determined from these values through linear extrapolation.

Calculating the acoustoelastic coefficient (A_R)

As only two interaction points are used, a least squares fit is not appropriate to calculate the gradient of the data points. Instead the gradient (A_R) is calculated from the difference between the values, given as:

$$A_R = \frac{\frac{\Delta V}{V_0}_2 - \frac{\Delta V}{V_0}_1}{\sigma_2 - \sigma_1}$$

The uncertainty in this measurement is calculated by assuming each measure-

ment has a unique independent uncertainty associated with it. The error in the gradient is calculated as the sum of the squares of the uncertainty in the fractional velocity change and the stress for both points. The uncertainty in the gradient can be defined as:

$$\delta_{A_R} = \sqrt{\left(\delta_{\left(\frac{\Delta V}{V_0}_2\right)} \times \frac{\partial A_R}{\partial \frac{\Delta V}{V_0}_2}\right)^2 + \left(\delta_{\left(\frac{\Delta V}{V_0}_1\right)} \times \frac{\partial A_R}{\partial \frac{\Delta V}{V_0}_1}\right)^2 + \left(\delta_{\sigma_2} \times \frac{\partial A_R}{\partial \sigma_2}\right)^2 + \left(\delta_{\sigma_1} \times \frac{\partial A_R}{\partial \sigma_1}\right)^2}$$

where

$$\frac{\partial A_R}{\partial \frac{\Delta V}{V_0}_2} = \frac{1}{\sigma_2 - \sigma_1}, \qquad \frac{\partial A_R}{\partial \frac{\Delta V}{V_0}_1} = \frac{-1}{\sigma_2 - \sigma_1}$$

$$\frac{\partial A_R}{\partial \sigma_2} = \frac{-\left(\frac{\Delta V}{V_0}_2 - \frac{\Delta V}{V_0}_1\right)}{\left(\sigma_2 - \sigma_1\right)^2}, \qquad \frac{\partial A_R}{\partial \sigma_1} = \frac{\left(\frac{\Delta V}{V_0}_2 - \frac{\Delta V}{V_0}_1\right)}{\left(\sigma_2 - \sigma_1\right)^2}$$

The uncertainty in the acoustoelastic effect is calculated from the uncertainty in the fractional velocity change and stress, calculated earlier. The larger the separation between σ_2 and σ_1, the lower the uncertainty in the gradient.

4.4.2 Spatially Resolved Acoustic spectroscopy (SRAS)

The velocity of the wave is equal to the product of the frequency and the wavelength:

$$v = f\lambda$$

By generating a wave with a fixed value for one of the terms (either the frequency or wavelength), scanning through the other and determining the efficiency of generation for each value, the velocity of the material can be found. This is a form of spectroscopy. SRAS was developed at the University of Nottingham [48]. It normally utilises laser ultrasonic techniques, though it can be used with other gen-

eration and detection systems. There are two distinct types of SRAS which relate to the parameter that is held constant. In k-SRAS (k for wave number) the wavelength of the generated ultrasound is varied whilst the generation frequency is held constant. As the wavelength is changed, the generation efficiency changes. By determining the optimum wavelength for generation and knowing the frequency, the velocity can be found. The alternate type is F-SRAS, where by a relatively broadband signal is induced into a sample with a fixed wavelength. The most efficiently generated frequency is found and the velocity is found from this.

In a polycrystalline material the velocity of the generated wave is related to the orientation of the grain that the wave is being generated on. By taking several measurements of the velocity over an area, an image of the microstructure is produced.

The SRAS technique allows the exact microstructure on the sample to be relocated. This is used in chapter 5 to re-register samples in-between experiments. The linear ultrasonic velocity data produced by the SRAS technique can also be used in conjunction with results from the acoustoelastic techniques to allow a direct comparison between a linear and nonlinear techniques.

4.5 Fatigue experiment design

The following sections describe the design and development of an experiment to investigate the relationship between fatigue and A_R. The experimental results are presented in chapter 5. The type and number of samples are discussed, along with the fatiguing procedure and data conditioning.

4.5.1 Samples

This section describes the size and composition of the samples used in the investigation of the effect of fatigue on A_R. The aim of this work is to develop a technique that is industrially relevant and many of the design choices reflect this.

Material Two materials are used to investigate the fatigue process effect on the acoustoelastic measurement. These are aluminium 2024-T351 and titanium Ti-64Al-4V. Both are used widely in the aerospace industry due to their light weight and high strength performance. Both aluminium and titanium have different types of phases (cubic and a combination of cubic and hexagonal respectively). The titanium samples have a sizeable microstructure, whilst the aluminium samples have a smaller microstructure. Both materials have a different acoustoelastic coefficient. Using two different materials allows the investigation of fatigues effect on different acoustoelastic coefficients.

Dimension The sample shape and dimensions are selected to optimise the generation of fatigue in specific regions in a reliable way. A "dogbone" shaped sample is selected (see figure 4.36). The ends of the samples are secured by the 4-point bending jig used to fatigue the sample. The width of the central section narrows which increases the localised strain in the middle of the sample when it is deformed. The increase in localised strain increases the stress at the central location and so the level of fatigue.

The thickness of the samples is set to give the different materials samples similar fatigue properties. Aluminium samples are 14mm and titanium samples are 7mm in depth. This is sufficiently thick to ensure that SAWs generated with a 1MHz transducer are not dispersive.

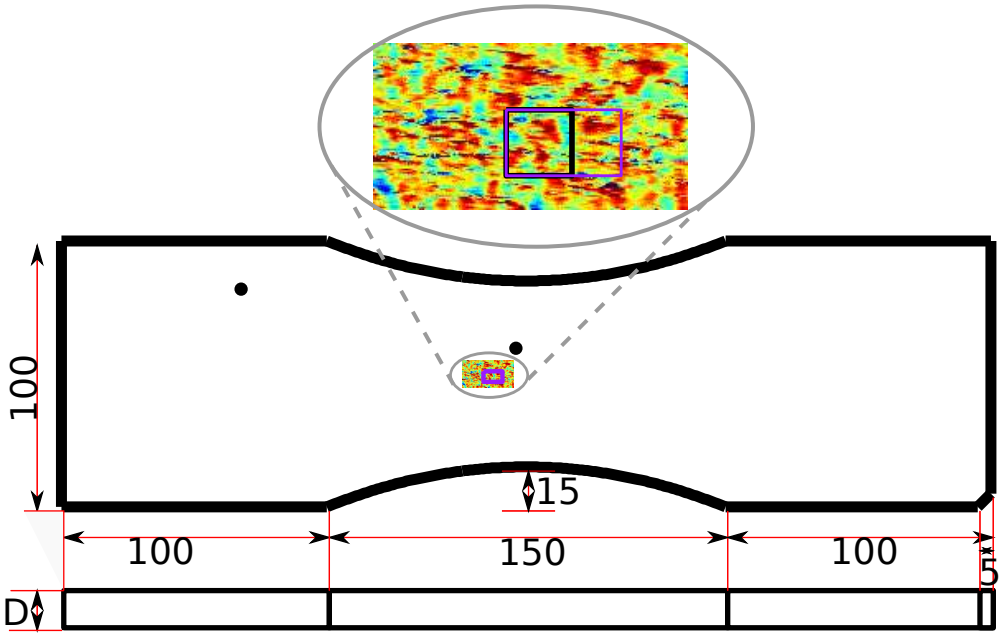

Figure 4.36: Dimensions of the samples used for the fatigue experiments. Measurements are in millimetres. Depth (D) is dependent on the material the sample is made of; aluminium D = 14mm and titanium D = 7mm. Black circles are registration marks. Also shown are the relative sizes of the scanned areas. The multi-coloured rectangle is the SRAS scan (see 4.4.2). The violet square is the region the pump and probe waves interact in. The black square is the scan coordinates for the acoustoelastic image.

Two reference points are placed on each sample for registration (see figure 4.36). Both serve as optical marks. One mark, made using a punch, is placed in a corner. The other mark is placed 10 mm to one side of the centre of the sample. The central mark is made using permanent pen so as not to create a fatigue nucleation spot. Sacrificial samples used in range testing tended to form large cracks at the centre of the sample. To avoid terminal cracks forming by the central mark, the latter is offset.

The sample is registered using these marks. To do this the knife-edge detector is first centred with respect to the generation arm. This is done by positioning the detection spot at the centre of a circular generation mask. The sample is then moved so the knife-edge detector spot scans over the registration marks. The DC light level from the knife-edge is recorded and a centroid function is applied to the data to determine the center of the marks.

4.5.2 Number of each sample

To enable future complementary testing such as X-ray diffraction and positron annihilation spectroscopy (for further examples see section 2.2), a range of aluminium samples are produced. Samples with a variety of intermediary and final fatigue lives are investigated. By producing aluminium samples with a range of final fatigue lives it will allow future comparison between the acoustoelastic measurement and complementary testing. A total of 12 aluminium samples are investigated. The table 4.4 outlines the final fatigue level for each sample and the intermediary fatigue increments that each sample is scanned at, using the acoustoelastic technique. The fatigue level is expressed as a percentage of the fatigue life. The full fatigue life is defined as the average number of cycles till failure of ranging samples. This is used as a qualitative measurement of a samples progression to failure.

Sample name	Fatigue life scanned levels (%)	Final fatigue level (%)
Aluminium 01	80	80
Aluminium 02	0, 20, 40, 60, 80	80
Aluminium 03	0, 20	20
Aluminium 04	0, 20, 40	40
Aluminium 05	0, 20, 40, 60	60
Aluminium 06	0	0
Aluminium 07	20	20
Aluminium 08	0,20,50	50
Aluminium 09	0, 20 ,30 ,60, 80	80
Aluminium 10	0, 20, 60	100
Aluminium 11	0, 20, 60,70	100
Aluminium 12	0, 50, 90	100

Table 4.4: Table of aluminium samples intermediary and final fatigue lives

Complementary testing was due to be completed using X-ray diffraction technique. The size of the microstructure was found to hinder this measurement making it impractical. The use of other complementary techniques is discussed in the further work chapter 6.

Two titanium samples are investigated. Both are fatigued to a final fatigue life of 80%. Intermediary acoustoelastic scans are performed every 20% increment of the fatigue life of the titanium samples.

4.5.3 Fatiguing of samples

The samples are fatigued under contract by Serco. A custom 4 point bending jig capable of delivering 40 kilo-newtons force is used. The system is displacement controlled. For different materials different strains are applied. For aluminium -0.3% to +0.5% strain is applied. For titanium -0.4% to +0.6% strain is applied. Loading is cycled at 0.2 Hz. Cycling the strain in the sample creates fatigue. In this case low cycle fatigue is produced. The fatigue schedule was developed with consultation from industrial partners. The strain levels were selected to be

Material	Range test 1	Range test 2	Range Test 3
Aluminium	15162	17103	19280
Titanium	16656	17991	21000

Table 4.5: Table of range testing results (number of fatigue cycles until failure)

representative of strains experienced by components used in real world applications, whilst ensuring the time taken to fully fatigue the samples is sufficiently short so as to be practical. Asymmetrical strain is applied to focus the formation of fatigue on one side of the sample.

Ranging tests are conducted on sacrificial specimens. The average number of cycles until failure for aluminium is 17200 cycles and for titanium it is 18550. The average number of cycles until failure are used to estimate the fatigue life experienced by each sample at intermediary fatigue stages. The fatigue life is assumed to be a linear function of the number of cycles.

Samples are inspected using the acoustoelastic technique before being sent to be fatigued. At intermediate fatigue lives the samples are returned, inspected and sent back to be fatigued further. The delay between scanning and fatiguing of the samples limits the practical number of samples that can be investigated.

Uncertainty in fatigue life

The range in the number of cycles until failure for the sacrificial samples is relatively small for each material. Variation in the number of cycles until failure does result in some uncertainty in the percentage fatigue life estimations. Table 4.5 gives the number of cycles each sacrificial sample went through until they failed.

The average number of cycles to reach failure point for aluminium is 17181 and for titanium it is 18549. A 20% increase in fatigue life is equal to 3440 cycles for aluminium and 3710 cycles for titanium. The uncertainty in the fatigue life is

defined as the maximum difference between ranging tests and the average failure point. The uncertainty in the measurement of the fatigue life is 12% for aluminium and 13% for titanium over the entire course of the fatigue life of the samples.

The uncertainty in the fatigue life of each sample is small before they are fatigued as the samples are all produced and handled in a similar way. At 0% fatigue life, the uncertainty in the fatigue life is effectively zero. The uncertainty in the fatigue life increases with fatigue level. A fair assumption is that the uncertainty in the fatigue life increases linearly with fatigue life. So the uncertainty in the fatigue life increases by 2.4% for aluminium and 2.6% for titanium every 20% increment in fatigue life.

The uncertainty in the fatigue life could be removed by terminally fatiguing the sample. This was not done so that some of the samples could be used in the future for comparison with complementary techniques.

Scan area

The general scan area for each sample is selected as the centre of the sample. The center of each sample is where the highest strain and so stress is produced during fatiguing. In section 5.7.1 an acoustoelastic scan along half the length of a fatigued sample shows the largest acoustoelastic coefficient is at the centre of the sample.

During range testing, terminal fatigue cracks formed around the exact centre of each sample. To avoid the scan area being in a location directly affected by a fatigue crack, each scan area is off set from the direct center of the sample. Fatigue cracks can still form in this region, though are less likely to do so.

The size of the scan area is limited by the acquisition time for each point. Each single point measurement takes 40 seconds. A 41×41 point square takes 18 hours to acquire. A step size between points of 100μm is selected. This resolution allows

comparison between the microstructure of the material (of the order of 20-30 μm in aluminium) and changes in the acoustoelastic measurement. A scan area of 16mm^2 is achieved using this configuration. The region the pump and probe waves interact in is larger than this (28mm^2, see figure 4.36).

SRAS scans are used to select the specific scan area. Defined microstructure, such as grain interfaces, is selected to help with re-registration. To begin with, areas are relocated in between fatiguing cycles manually. Image correlation software confirmed the error in re-registration to be less than a pixel (100μm).

4.5.4 Data conditioning and validity

From experimental work conducted in section 4.3.2, a relationship between the uncertainty in fractional velocity and the signal to noise ratio (SNR) of the probe SAW is found. A probe SAW with a SNR below 3 would have an uncertainty in Δt of 6.27ps or more. This equates to an uncertainty in the fractional velocity change of 5.98×10^{-6}. If an aluminium sample is inspected with a pump SAW producing 1MPa stress, the acoustoelastic effect produces a fractional velocity change of 17 $\times10^{-6}$. With a SNR of 3 or below the fractional uncertainty in the measurement will be 35%. Points with a low SNR can be justifiably removed without biasing the expectation value. This will improve the variance of the measurements. A SNR of 3 is the arbitrary level at which data points are removed.

The Polytec intereferometer gives a calibrated displacement, provided a sufficient intensity of light returns from the sample. If there are localised defects in the sample finish, the amount of light reflected from the sample surface is reduced. When the returning light level is reduced too much, the displacement from the interferometer is no longer valid. Over small areas,the variation in the stress produced by the pump SAW is minimal. Random significant changes in the stress can

be attributed to reflection variations of the interferometer beam. Averaging the stress over the scan area removes these effects. Averaging is appropriate providing the area scanned is relatively small.

4.6 Summary

In this chapter a procedure is developed to measure the acoustoelastic coefficient (A_R) of a material to be used in conjunction with the instrumentation developed in section 3. The errors, noise and uncertainty in the acoustoelastic measurement are explored. From a least mean squares regression fit, the uncertainty in A_R is found to be 0.44×10^{-6} MPa^{-1} for the single point acoustoelastic measurement made on fused silica in chapter 5 (see section section 5.2). The uncertainty in the variables used to calculate A_R are found experimentally and by modelling. A relationship between the uncertainty in the variables used to find the fractional velocity change and the single shot signal to noise ratio of the probe SAW is demonstrated. The optimum instrument configuration for the acoustoelastic measurement is found to be a co-propagation distance of 3 mm between the pump and probe SAWs, a pump SAW frequency of 1 MHz and a probe SAW frequency in the region of 60- 70 MHz dependent on the attenuation of the material.

In section 5.4 A_R is found to vary by more than the uncertainty in the measurement on polycrystalline materials. A procedure is developed to allow the imaging of A_R over the surface of the sample. Relating the measurement of the pump SAW to the arrival of the probe SAW complicates this procedure.

Finally, the configuration of a series of experiments to investigate the impact of fatigue on the acoustoelastic measurement over an area is outlined. The samples, fatigue, scan area and the data treatment are discussed. Twelve aluminium and

two titanium samples are used. A strain controlled four-point bending jig is used to induce low cycle fatigue in the samples. The central region of each sample is where the highest strain is found during fatiguing. A 16mm^2 square area located at the centre of each sample is scanned at different levels of fatigue. Data points with an arbitrary SNR lower than 3 are excluded due to the high level of uncertainty in the fractional velocity change. The stress over the area is averaged.

Chapter 5

Experimental Results

5.1 Introduction

Chapter 5 presents experimental results obtained using the instrument developed in chapter 3 and the procedure outlined in chapter 4. The results in this chapter are organised according to the complexity of the measurement used to acquire them. This order is used to simplify the description of the results.

A single point measurements of A_R (the acoustoelastic coefficient) on fused silica is presented first (see section 5.2). A single point measurement using the technique developed in this work is then compared with a technique which uses a static strain to find the acoustoelastic coefficient (A_R, see section 5.3). In section 5.4 the single point measurement of A_R on fused silica is compared to the coefficients for aluminium and titanium. All three materials have been reported to have different acoustoelastic coefficients [68, 78, 125]. The investigations using the single point measurement of A_R seek to demonstrate the accuracy and sensitivity of the system developed.

The spatial variation of A_R is imaged in section 5.5 using the technique devel-

oped in section 4.4. The repeatability of the imaging technique is demonstrated in section 5.5.2. In section 5.6 the imaged A_R is compared to the microstructure present under the measurement. Finally the impact of fatigue on the imaged A_R is investigated (section 5.7).

5.2 Single point measurements of the acoustoelastic coefficient (A_R)

This section demonstrates the acquisition of the acoutoselastic coefficient (A_R) of a material. The experimental set-up for this particular measurement is discussed.

Material used The single point measurements of A_R is made on fused silica. Fused silica is used as it is isotropic. Also fused silica has been reported to be highly nonlinear [68, 78, 125], resulting in a larger change in the velocity of the probe SAW for a given stress than on another material. Also the sign of the nonlinear response of fused silica is opposite to the sign of other materials such as aluminium and titanium.

Experimental set-up To make the single point measurement of A_R on fused silica, the experiment is configured as follows. The pump SAW is produced using a transducer with a central frequency of 1MHz. A 3 cycle 1MHz wave is used to excite the pump wave transducer to produce a SAW. The pump SAW is detected using the Polytec interferometer, the wave is sampled at a rate of 1GSa s^{-1} and coherently averaged 256 times. The probe SAW is generated using a grating that when imaged onto the sample produces lines with a period of 55μm. Producing a SAW with a centre frequency of 63MHz. This SAW is acquired using the knife-edge

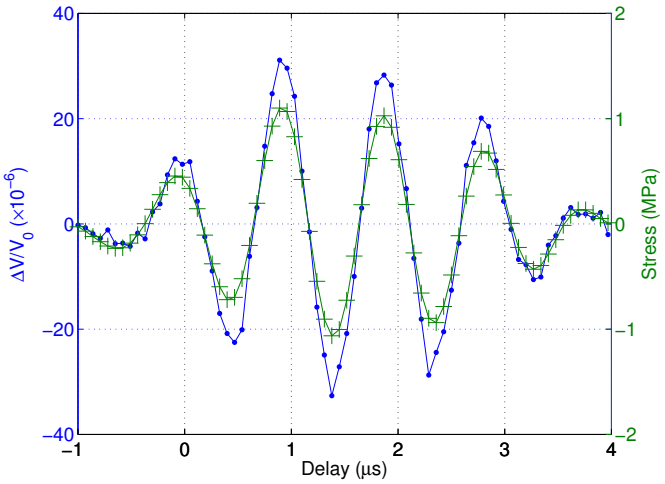

Figure 5.1: Graph of fractional velocity change ($\times 10^{-6}$, blue dotted line .–) against the delay value between the generation of the pump SAW and the probe SAW. Note that the first peak corresponds to zero, the arbitrary reference. The stress (MPa) calculated from the displacement experienced by the envelope of the probe SAW, with appropriate time shift applied, can also be seen (green crossed line, −+).

detector. This is sampled at a rate of 10GSa s^{-1} and coherently averaged 16384 times.

The stress and the fractional velocity measurements are extracted from the acquired SAWs as described in section 4.2. The acquired pump SAW displacement trace is shifted by -110 ns to account for the separation and phase difference between the two detectors. The resultant plots for the stress and fractional velocity can be seen in figure 5.1.

A good correlation between the stress and fractional velocity can be seen. When the fractional velocity change is plotted directly against the stress, a clear linear relationship can be seen (see figure 5.2). A least mean squares fit to this has a gradient of 27.5 $\times 10^{-6}$ MPa^{-1} . This gradient is the A_R for fused silica.

The error in the linear least squares fit is 0.44 $\times 10^{-6}$ MPa^{-1}, as found in section 4.3.1. The measurement of A_R on fused silica from this experiment is found to be 27.5 $\pm$ 0.5 $\times 10^{-6}$ MPa^{-1}.

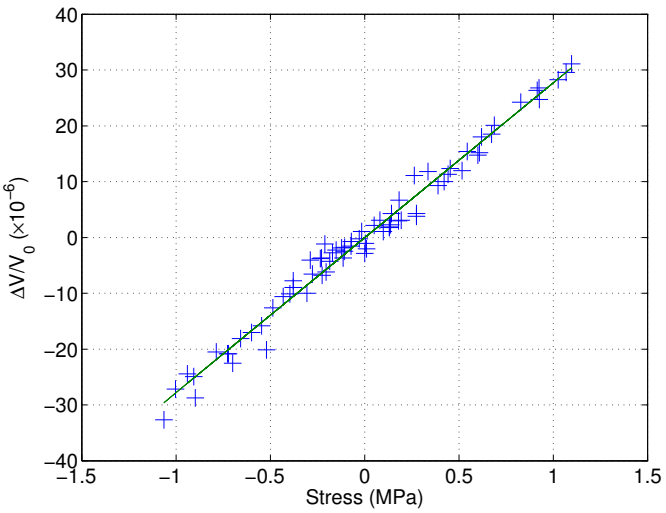

Figure 5.2: Graph of fractional velocity change against the stress (blue crosses, +), a least mean square linear fit (green line, −) can also be seen

5.3 Comparison of acoustoelastic coefficient (A_R) between measurement techniques

The technique described in chapter 4 is compared to an different technique for the measurement of A_R. Instead of using a SAW to induce stress in a sample, the alternate technique generates a stress by applying a static strain. In this case a custom 4-point bending jig is used to strain the sample. The use of a bending jig allows much larger stresses to be generated than using an acoustic wave, so larger fractional velocity changes are measured. Implementing differential acquisition using this static straining technique is not possible, as such temperature fluctuations have a large effect on the results.

An aluminium (2024) sample is used as opposed to a fused silica sample, this is because that large strains can be applied without damaging the sample. The microstructure of the aluminium is sufficiently small that the sample can be considered isotropic. The sample is fitted with a strain gauge (RS -632-146, measurable strain range 3-4% max) and placed in the bending jig.

An initial velocity measurement under a no strain condition is taken using the probe wave generation and detection system. The strain applied to the sample is increased slowly. Measurements of velocity and strain were made at regular intervals. To monitor for hysteresis measurements are also made as the strain is also decreased.

The full spectrum method is used to extract the time difference between the waves propagating in an unstressed state and in a stressed state. The time difference is converted to velocity using the known propagation distance. The stress is calculated from the strain. Figure 5.3a shows the velocity change with applied stress for the static strain acoustoelastic technique. A linear least mean squares fit produces a line with a gradient of -17.6 $\pm$ 1.7 $\times 10^{-6}$ MPa^{-1}.

On a different sample of aluminium (due to the small size of the sample used in the static strain experiment), the two wave mixing technique developed in this work is used to take a measurement of A_R. The technique is applied in the same way as to the fused silica sample. The result can be seen in figure 5.3b. A linear least mean square fit produces a gradient of -16.7 $\pm$ 0.5 $\times 10^{-6}$ MPa^{-1}. This shows that the sign of the measurement of A_R for aluminium is opposite from that of the fused silica and that the A_R is lower than that found for the fused silica. This agrees with results reported by other workers [68, 78, 125].

Comparison between results from the static strain and the co-propagating SAW interaction techniques show that both techniques produce similar measurements of A_R (see 5.3c). The small discrepancy between the two could be due to uncertainty in the measured stress for the static strain process or the influence of temperature. This validates the precision of the technique developed in this work, which can produce similar results to the static strain technique whilst applying a small fraction of the stress.

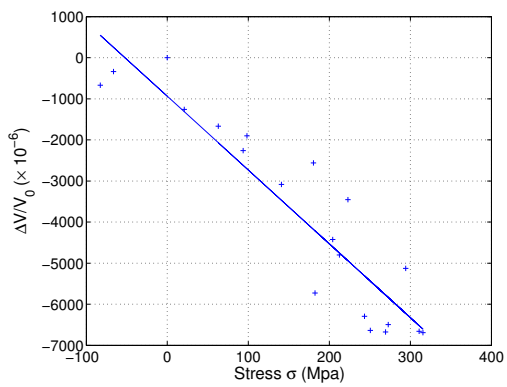

(a) Static stressing on aluminium

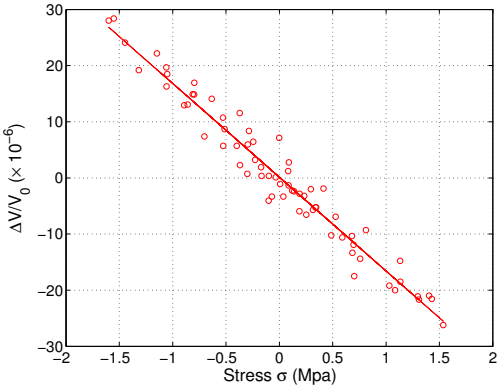

(b) Two wave mixing technique on aluminium

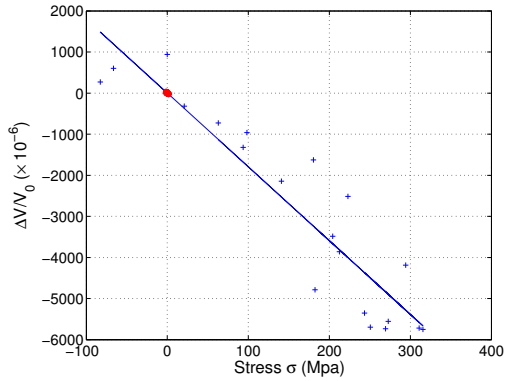

(c) Two wave mixing technique result transposed on to static technique result

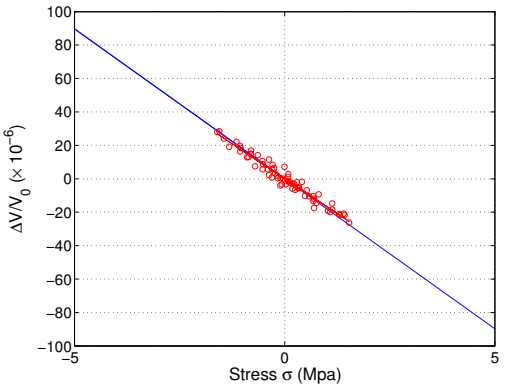

(d) Zoomed in plot of two wave mixing technique result transposed on to static technique result

Figure 5.3: Comparison between acoustoelastic coefficient measurements using two different techniques. (a) measurement of acoustoelastic coefficient by straining sample in a bending jig, (b) Using a variable stress field from a transducer, (c) overlay results from both techniques. (d) is a scaled version of (c).

5.4 Variation of measurement of the acoustoelastic coefficient (A_R) between materials

Several authors [68,78,125] have established that different materials have different nonlinear responses. To calibrate and confirm the instrument is working correctly a series of investigations are made into the A_R of three materials. Single point measurements of the value of A_R of each of the three materials are made. Two of the materials investigated are used widely in the aerospace industry, aluminium and titanium. Fused silica is also included for the reasons given in section 5.2. The resultant stress-fractional velocity change plots can be seen in figure 5.4. For aluminium and titanium the measurements are made in arbitrary directions through random microstructure. This gives an average A_R for each of these materials.

The A_R is measured as the gradient of a least mean squared fit line, fitted to the stress-fractional velocity change data. For fused silica, the gradient of the line is 27.7±0.5 $\times 10^{-6}$ MPa^{-1}, for aluminium it is -16.7±0.4 $\times 10^{-6}$ MPa^{-1} and for titanium it is -3.8±0.2$\times 10^{-6}$ MPa^{-1}. A defined difference between the measured A_R of each material is observed, the difference is much larger than the uncertainty in each measurement. Duqennoy et al. [44] have reported an acoustoelastic coefficient of between -15.3$\times 10^{-6}$ MPa^{-1} and -15.9$\times 10^{-6}$ MPa^{-1} for aluminium depending on the orientation of the sample and the SAW propagation direction.

5.5 Spatial variation of the measurement of the acoustoelastic coefficient (A_R)

Whilst performing the measurement of A_R on aluminium and titanium, it is noted that A_R varies from location to location. Initial investigations of this effect took

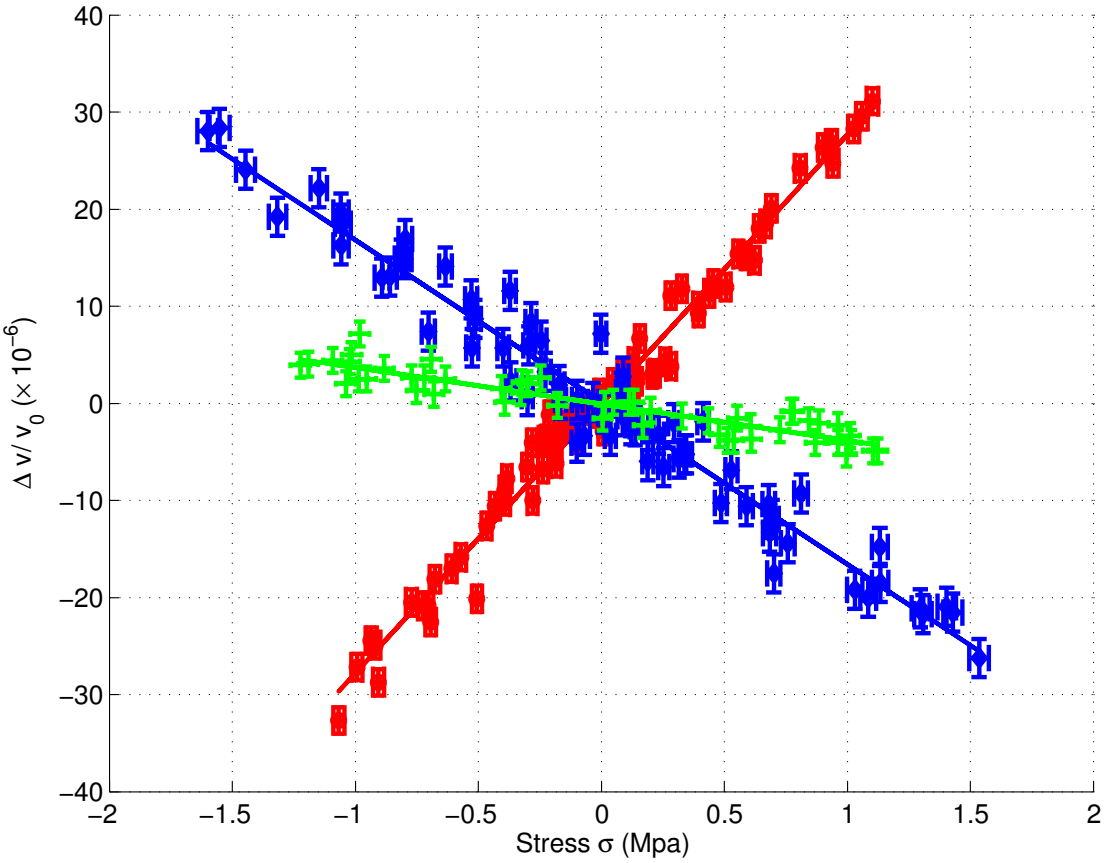

Figure 5.4: Results from measurement of A_R on three different materials. The gradient of the lines corresponds to the A_R. Blue diamonds ($\diamond$) represent aluminium data and the gradient is -16.7± 0.4 $\times 10^6$ MPa^{-1}. Green crosses ($+$) represent titanium data and the gradient is -3.8± 0.2 $\times 10^6$ MPa^{-1}. Red circles ($\circ$) represent fused silica data and the gradient is 27.7±0.5 $\times 10^6$. MPa^{-1}

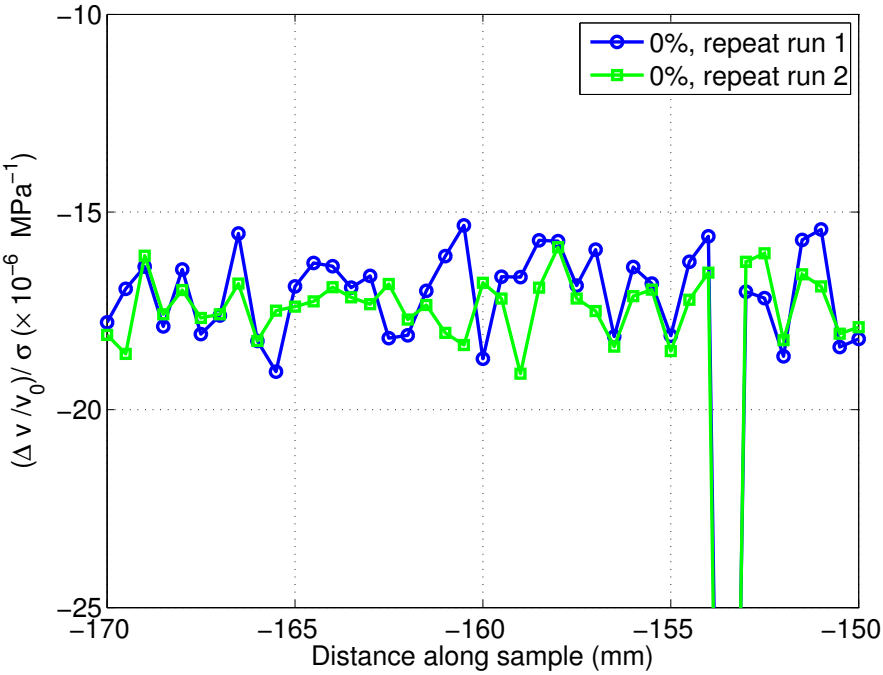

Figure 5.5: Plot of the variation of of the acoustoelastric coefficient over a line. The experiment was repeated. The first experiment points being represented by blue circles (○). The repeat experiments data point are represented by green boxes (□). The large decrease in A_R in between the -155 and 150 mm distance along the sample is attributable to the measurement of the low frequency SAW being abnormally low.

the form of measuring the acoustoelastic coefficient of an aluminium sample along a single line, away from the pump wave transducer, these measurements are repeated. A_R for both series of measurements can be seen in figure 5.5. For both repeat scans a similar variation in A_R is seen from location to location. The variations over the sample surface are attributed to variation in A_R due to microstructural anharmonicity. The large decrease in A_R between the -155 and 150 mm distance along the sample is due to the low frequency SAW amplitude being small.

5.5.1 Imaging of the acoustoelastic coefficient (A_R)

The acoustoelastic imaging technique developed in section 4 allows the monitoring of A_R over an area. In this section the initial images of the acoustoelastic variation in aluminium 2024 are presented. The typical aluminium grain size is in the region of 20-40 μm. The aluminium sample has not been fatigued. The sample is scanned over an area of 16mm^2. The measurement of the stress is not averaged. The area chosen to be acoustoelastically imaged is selected from a larger initial SRAS scan. This area is chosen for its easily identifiable microstructural features. The scan took approximately 18 hours. The resultant images can be seen in figure 5.6.

The pump SAW propagates from left to right. The scan area is acquired in the order left to right, top to bottom. The A_R shows spatially organised regions of similar intensities. The organised regions of similar intensities in A_R are independent of variation in the signal to noise ratio (E). The relationship between A_R (A) and the SRAS velocity (B) is complicated, this is discussed further (see section 5.6). The imaged stress (D) is the stress from the first interaction point subtracted from the second interaction point and probe SAW. The imaged fractional velocity change (C) is the difference in fractional velocity change between the two interactions.

5.5.2 Repeatability of acoustoelastic imaging technique

To investigate the repeatability of the acoustoelastic imaging technique a series of experiments are conducted. A second aluminium 2024-T351 sample was used to demonstrate the variation in the acoustoelastic image between samples.

The first experiment acquires an image of A_R over a 16mm^2 area. The bonding of the low frequency transducer used to produce the pump SAW is poor, so a low stress difference is achieved. The sample is then removed from the instrument. The

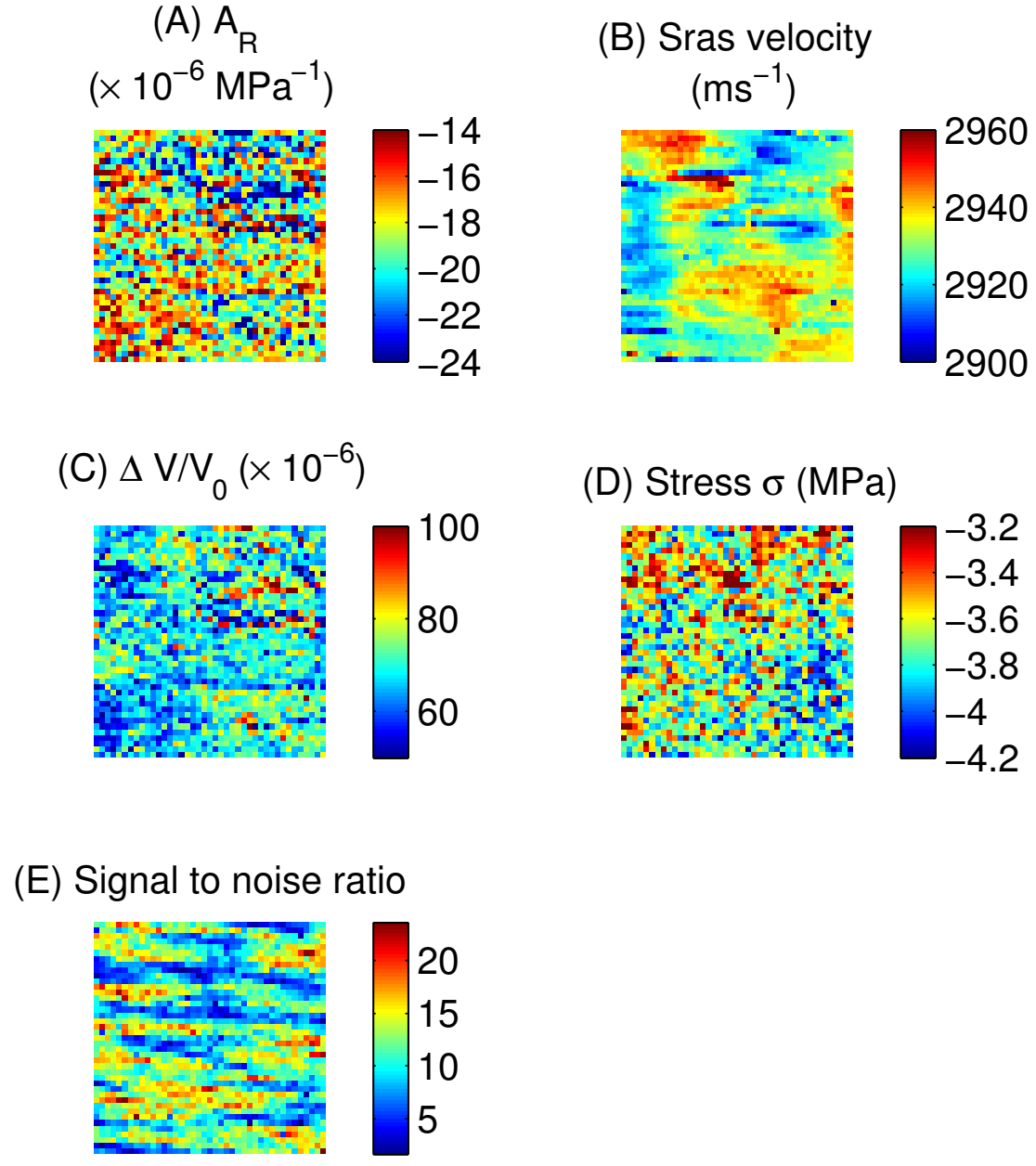

Figure 5.6: Initial area scan of A_R ($\times 10^{-6}$ MPa^{-1}) on an aluminium sample (A). SRAS velocity (ms^{-1}) scan taken using the same data acquired for the measurement of A_R, this gives information about the microstructure of the area being scanned (B). Measured difference in fractional velocity change ($\times 10^{-6}$, C) and related Stress difference (MPa, D). The signal to noise ratio (SNR) of the probe SAW indicating the certainty in the measurement of the fractional velocity change (E).

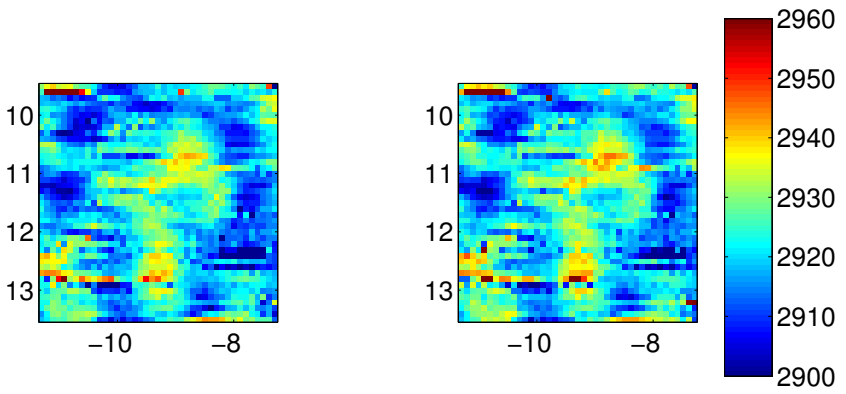

Figure 5.7: SRAS velocity data (ms^{-1}) for each area imaged for the two experiments. The left square relates to the first scan and the right relates to the second. There is a good correlation between the two demonstrating the area being re-imaged is the same as the original. X and Y axis values correspond to the distance in mm from the central reference point

pump wave transducer is then removed and re-bonded. The sample is relocated in the instrument using the techniques described in section 4.5.

Another acoustoelastic image is taken of the same area. In figure 5.7 the SRAS velocity data for each area is compared. A good correlation is seen in the velocity data which relates to the microstructure. This indicates the second area imaged is in the same region as the first area imaged. The acoustoelastic images can be seen in figure 5.9. The measured stress difference over each area can be seen in figure 5.8.

A large increase in stress difference is seen in the second imaged area. This is because of the improvement in bonding of the pump wave transducer. In comparison, the acoustoelastic data changes little (figure 5.9). A similar pattern for both acoustoelastic images is observed.

The A_R of each of the imaged areas is compared in figure 5.10. A correlation is seen. The Pearson's correlation coefficient (see section 5.6.1) for the imaged A_R for both squares is 0.5497. This is relatively weak. The weakness in correlation is due to the small stress difference in the first scanned area. A low stress difference

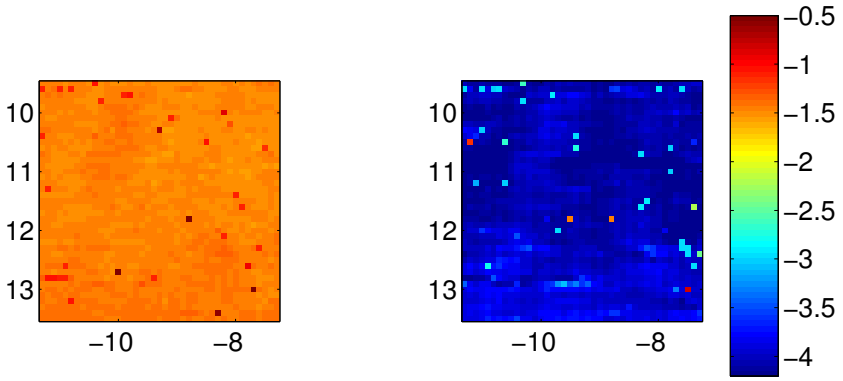

Figure 5.8: Comparison of the stress difference on each area scan. Left square is the first measured square. The right square is the second repeated square. X and Y axis values correspond to the distance in mm from the central reference point

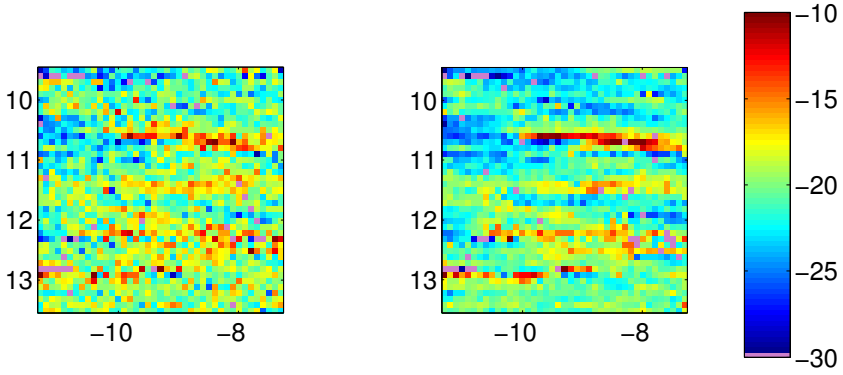

Figure 5.9: A_R for area scanned for two squares. Left square being the first square and the right square being the second.

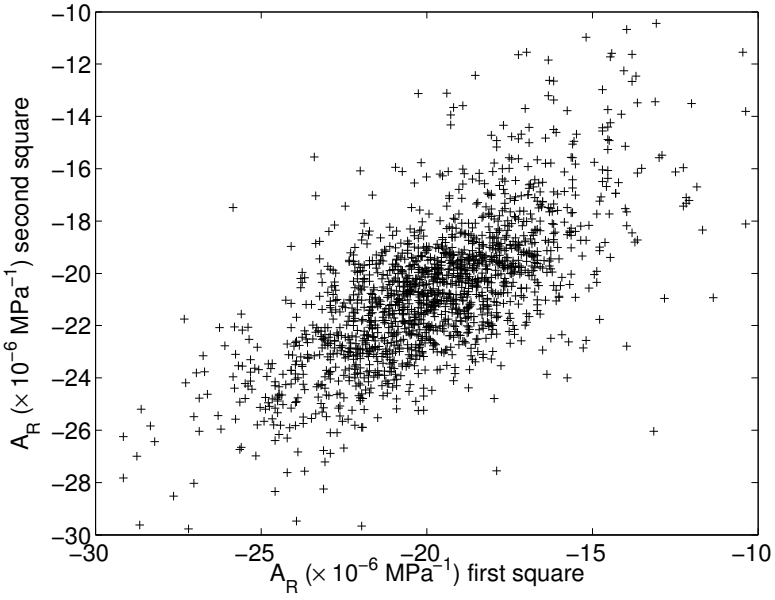

Figure 5.10: Comparison of between A_R from both squares.

introduces a high level of uncertainty in the measurement of A_R (see section 4.4). The weakness in correlation between the two experiments is a result of noise, primarily found in the first experiment.

Repeating the experiment a third time with the well bonded transducer demonstrates the repeatability of the imaging technique under good conditions. The stress (see figure 5.11) and the A_R (see figure 5.12) of each of the imaged areas where the bonding is good can be seen to be highly repeatable. The Pearson's correlation coefficient for the imaged A_R for both squares rises to 0.8764 (see figure 5.13).

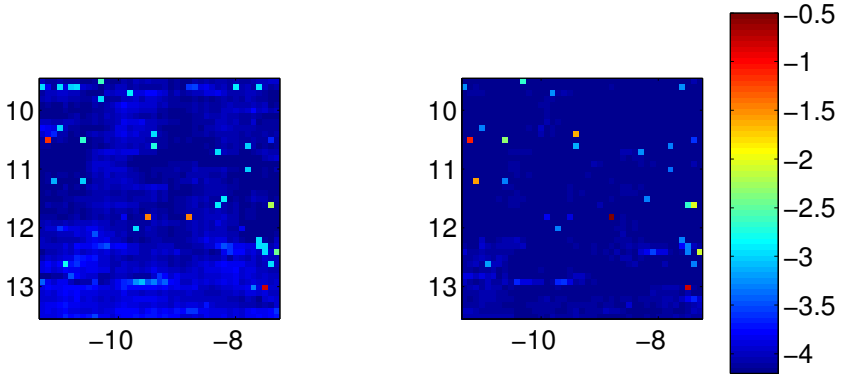

Figure 5.11: Comparison of the stress difference on each area scan under good conditions. Left square is the second measured square. The right square is the third repeated square. X and Y axis values correspond to the distance in mm from the central reference point

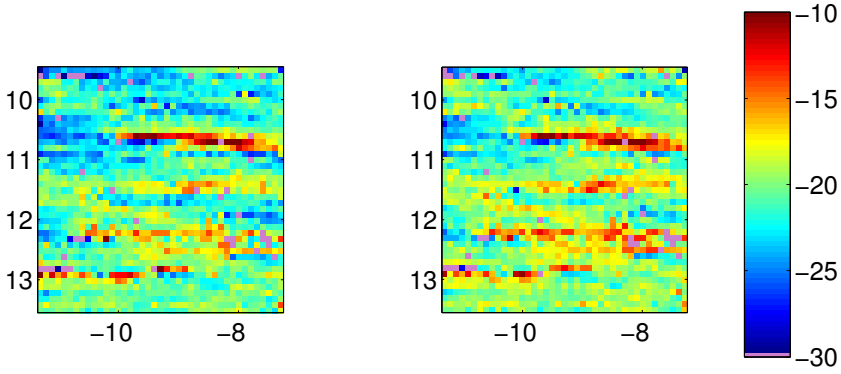

Figure 5.12: A_R for area scanned for two squares under good conditions. Left square being the second square and the right square being the third.

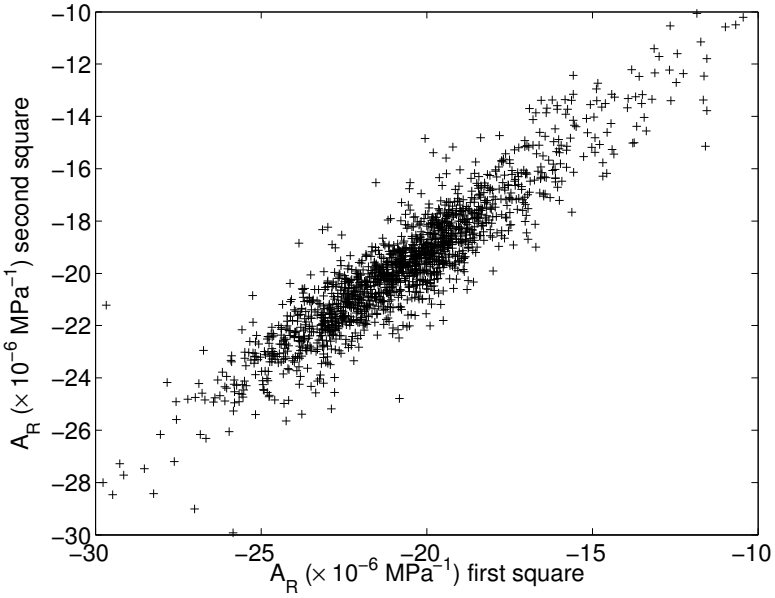

Figure 5.13: Comparison of between A_R from both squares under good conditions.

5.6 Relating microstructure to the acoustoelastic coefficient

In this section, the potential link between the spatial variation of the A_R and the microstructure is investigated. To investigate this relationship a sample with a microstructure of a similar order to the resolution, of the measurement of A_R (3mm) is used. A polycrystalline sample with a large A_R is selected to allow accurate measurement of the spatial variation of A_R. A sample of aluminium (2024) with a microstructure of the order of millimetres is used to fulfil these requirements. The SRAS technique is used to image the samples microstructure (see figure 5.14).

An acoustoelastic image is collected from a section of the sample. The area imaged is selected so that the two SAWs used in the measurement of A_R would co-propagate solely on one grain in one region, on another grain in a second region and a combination of the two in a third region. Figure 5.15 (A) shows the SRAS

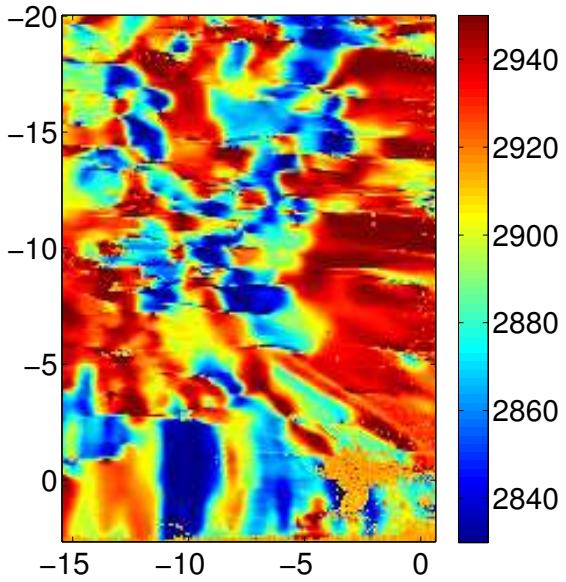

Figure 5.14: SRAS image of the microstructure of a large grained sample of Al2024. The colours indicate different velocities with a scale in ms^{-1}. The horizontal and vertical scales are positioned on the sample in millimetres away from a registration point seen as the orange cluster at the bottom right of the picture.

image of an area of the polycrystalline aluminium sample. The area included within the black dashed line is the area that is scanned with the acoustoelastic imaging technique. Figure 5.15 (B) shows the acoustoelastic image of this region.

5.6.1 Relating the area of interaction to material microstructure

Plotting A_R directly against the linear velocity calculated from the SRAS technique (which is related to the microstructure) produces a graph showing a weak correlation (see figure 5.16). The correlation between two variables can be quantified by the Pearsons product moment correlation. Defined as:

$$R = \frac{\sum_{i=1}^{n} \left(X_i - \bar{X}\right)\left(Y_i - \bar{Y}\right)}{\sqrt{\sum_{i=1}^{n} \left(X_i - \bar{X}\right)^2}\sqrt{\sum_{i=1}^{n} \left(Y_i - \bar{Y}\right)^2}}$$

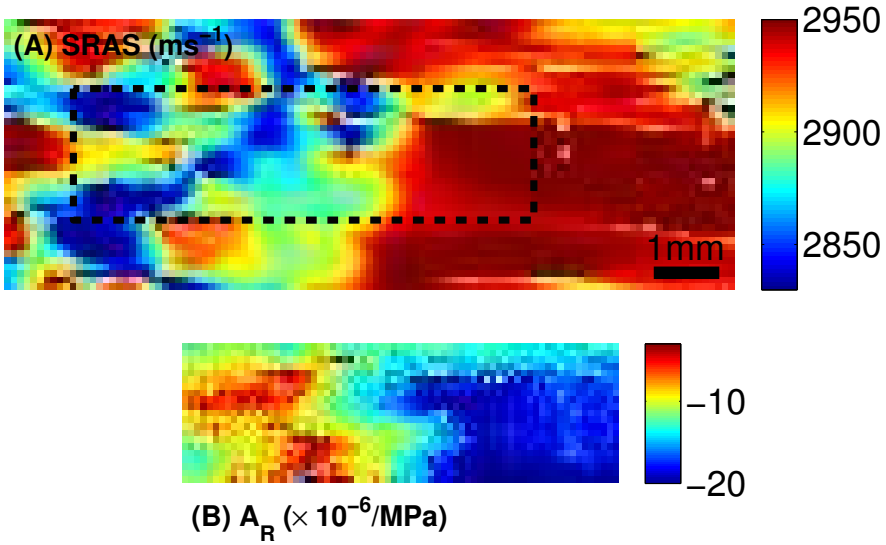

Figure 5.15: Comparison of the linear SRAS (ms^{-1}) data (A) with the imaged A_R (B) taken in the area denoted by the (–) black dashed square area

where n is the number of the two variables X and Y in the data set. R is a dimensionless value ranging between -1 and +1. The closer the coefficient is to 1 or -1 the better the correlation between the two variables. The correlation between A_R and the linear velocity is -0.41 assuming a linear relationship.

In the measurement of A_R the pump and probe SAW interact over a finite length of 3 mm. The measurement of A_R takes place in a range of microstructure along this interaction region. To correctly relate the imaged A_R to the linear velocity, and so to the microstructure of the material, the linear velocity must be averaged along the interaction region.

The probe SAW is generated using a series of arcs to produce a focused wave. The interaction region between the probe and pump SAWs takes the form of a triangle. Averaging the linear velocity over a series of triangular regions produces the velocity image seen in figure 5.17a. Plotting the triangularly averaged velocity against A_R (see figure 5.18) produces a good correlation. The correlation coefficient rises to -0.70 assuming a linear relationship. A relationship between A_R and the

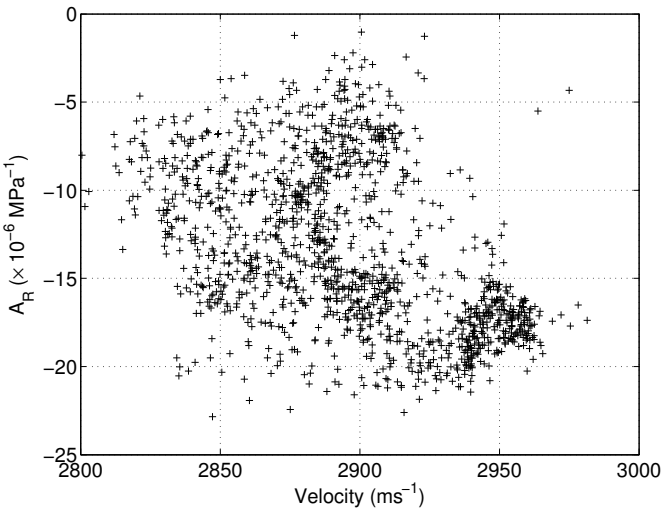

Figure 5.16: Graph of the measurement of A_R ($\times 10^{-6}$ MPa^{-1}) against the measured SRAS (ms^{-1}) velocity for that point. Correlation is weak with a coefficient of -0.41 assuming a linear relationship.

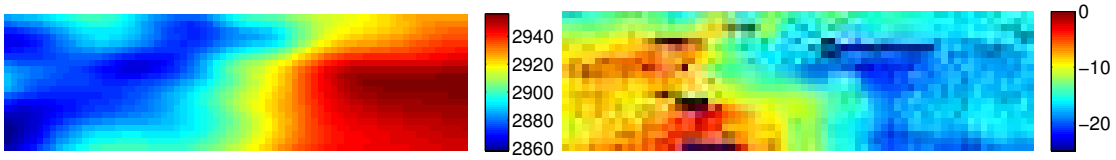

(a) Average velocity over triangle (ms^{-1}) (b) A_R ($\times 10^{-6}$ MPa^{-1})

Figure 5.17: Image of the average linear velocity over a triangular area from the center of the grating position to the detector position (a); with an image of the corresponding acoustoelastic reponse for this region (b).

microstructure is clear.

Variation of elastic constants

In section 4.3.2 it is discussed that different microstructural orientation have different elastic constants. The elastic constants are used with other constants and variables to calculate the stress field generated by the pump SAW. On samples where the microstructure is smaller than the co-propagation distance, it is assumed that the effect of the variation in the elastic constants with direction is small and so isotropic values of the elastic constants can be used. In the case of

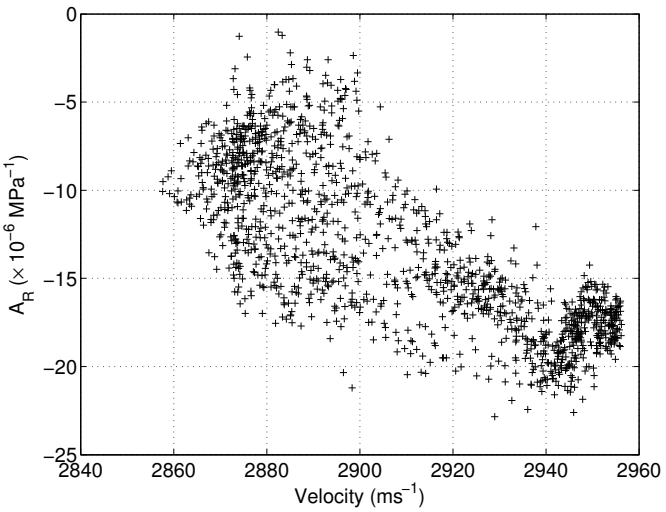

Figure 5.18: Graph of the measurement of A_R ($\times 10^{-6}$ MPa^{-1}) against the measured averaged SRAS velocity (ms^{-1}) over the triangular area from the generation point to the detection point 3 mm away. Correlation coefficient is -0.70 assuming a linear relationship

the large microstructured aluminium (2024) this assumption is no longer valid and could explain the variation seen in the measurement of A_R.

Two separate grains are imaged in the large microstructured aluminium. The variation in A_R between these regions could potentially be caused by a difference in the induced stress created by the variation in the elastic constants between the grains. The orientation of the two grains being investigated is not known. Further complementary testing to find the grain orientation is not required to qualitatively assess the impact of the variation in the elastic constants with direction.

Assuming the case where the two grains are arranged such that the elastic constants are at the maximum difference, allows the effects of the elastic moduli on A_R to be tested. Regions where the interaction takes place on both grains are assumed to have elastic constants that are averaged between the grains. The elastic constants become a function of the triangularly averaged linear velocity, representing the microstructure that the measurement of A_R interacts with. The

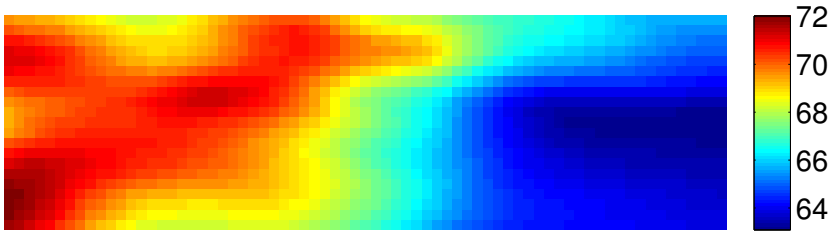

Figure 5.19: Image of maximum variation in Young's modulus (GPa^{-1}) due to difference in orientation of grains in the microstructure.

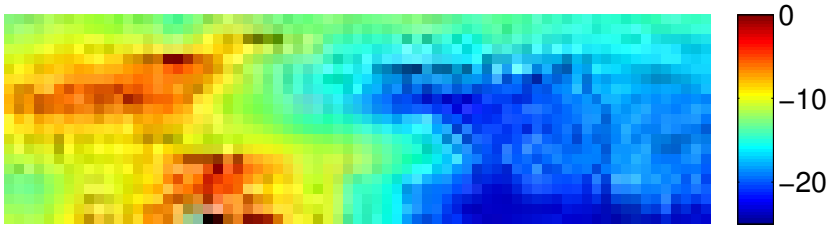

Figure 5.20: Image of A_R ($\times 10^{-6}$ MPa^{-1}) over the area with the variation of the stress field due to variation in moduli with a change in orientation of grain microstructure also taken into account.

resultant Young's modulus image can be seen in figure 5.19. The shear modulus is not shown as it remains constant (see page 110).

The maximum difference between the stress fields produced using the varying moduli values and the isotropic values is 0.15 MPa. The stress values are of the order of -3.3MPa. The fractional variation in the stress due to the change in the elastic constants is 5%. A_R varies from -5 to -20 $\times 10^{-6}$ MPa^{-1}, a difference of 400%. The calculated change in the stress field due to variation in the elastic moduli is not sufficient to produce the observed change in A_R.

Figure 5.20 shows A_R calculated from the modified stress field due to variation in the elastic constants. This figure demonstrates the minimal affect on the variation in A_R due to the variation of the elastic moduli.

The change in the elastic constants between the two grains can be further investigated by imaging the out-of-plane displacement across the sample (see figure

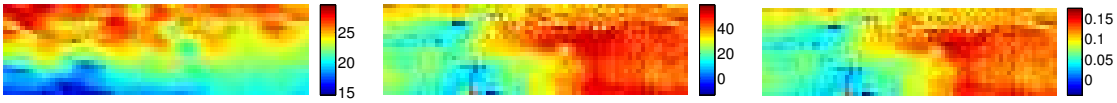

(a) Difference in out-of-plane displacement (nm)

(b) $\frac{\Delta V}{V_0}$ ($\times 10^{-6}$)

(c) ΔV (ms^{-1})

Figure 5.21: Images showing variation in variables used to measure A_R over large grain aluminium sample.

5.21a). If the elastic constants are very different a change in the amplitude of the out-of-plane displacement would be expected; however, a change with no relation to the microstructure is observed. A change is observed in the fractional velocity change ($\frac{\Delta V}{V_0}$, see figure 5.21b) that is very similar to the trend in A_R. The image of ΔV demonstrates that the change in the image of $\frac{\Delta V}{V_0}$ is not due to V_0, which varies with the orientation of the microstructure (see figure 5.21c).

5.6.2 Variation of the acoustoelastic coefficient(A_R) with microstructure orientation

A correlation between the microstructure that the measurement of A_R interrogates and A_R is found in section 5.6.1. Other workers [8,17,84,90] have also reported a relationship between the nonlinear response of a material and the crystal orientation of the grains that make up the microstructure.

To investigate the relationship between the crystal orientation of the grains that make up the microstructure and A_R a further experiment is conducted. In this experiment, A_R of a single grain is monitored as the grain is rotated. The large microstructured aluminium sample used in section 5.6.1 is used again.

Modifications to the instrumentation and experimental method are required to conduct this experiment. A physically smaller transducer is required so as to allow it to be positioned at different locations around the single grain on the aluminium

sample. The co-propagation distance of the pump and probe SAWs is reduced to 2.0mm so that the interaction occurs only on the single grain. A manual rotation and x-y stage is included as part of the sample positioning equipment to allow easy positioning and rotating of the sample around the grain. The pump SAW transducer is oil coupled and attached to an arm so that, as the sample rotates, the transducer moves over the sample surface and propagates SAWs aligned with the probe SAW.

The grain investigated is selected and positioned using SRAS velocity images (see figure 5.22). The interaction region between the pump and probe SAWs is marked onto the SRAS image. The orientation of the grain changes and so the velocity changes as the sample is rotated. The interaction region remains mainly within the single grain selected.

Images of A_R are taken at 30 degree intervals. The acoustoelastic coefficient is plotted against rotation in figure 5.23. The 120 degree orientation image has a much lower average signal to noise ratio (SNR) compared to the other orientations (8.65 as opposed to the next lowest 14). This may explain some of the divergence in values seen at the 120 degree orientation. Averaging A_R over the image for each orientation produces a trend (see figure 5.24).

The mean A_R varies sinusoidally with orientation. A change of 40% is seen in the mean acousoelastic coefficient with a change in orientation of 180 degrees. Kim et al. [17] have theoretically calculated a similar magnitude variation in the response of the nonlinear parameter with a change in orientation. The change in linear velocity with orientation is 60° in advance of the change in A_R. Duquennoy et al. [84] have noted that A_R changes sign with a change in orientation. Thorough analysis on configuration scans showed no change in sign of A_R.

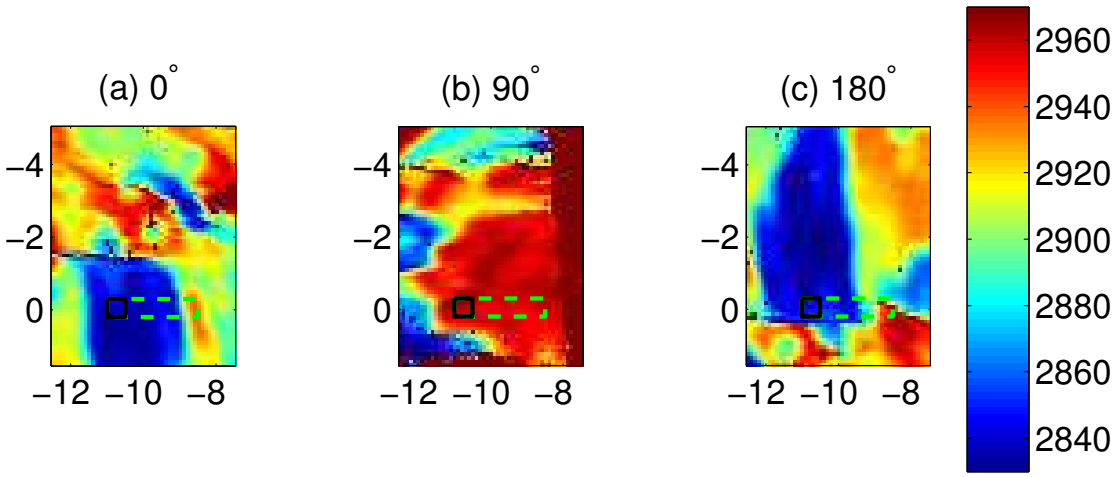

Figure 5.22: SRAS velocity (ms^{-1}) images of the microstructure of the area around the single grain selected for the acoustoelastic experiment. All distances are from a arbitrary index point. (a) represents the microstructure in the 0° orientation. (b) represents the microstructure in the 90° orientation. (c) represents the microstructure in the 180° orientation. The solid black area represents the co-ordinates of the measurement of A_R. The green dashed line (−−) represents the area of interaction between the pump and probe SAW for the measurement of A_R.

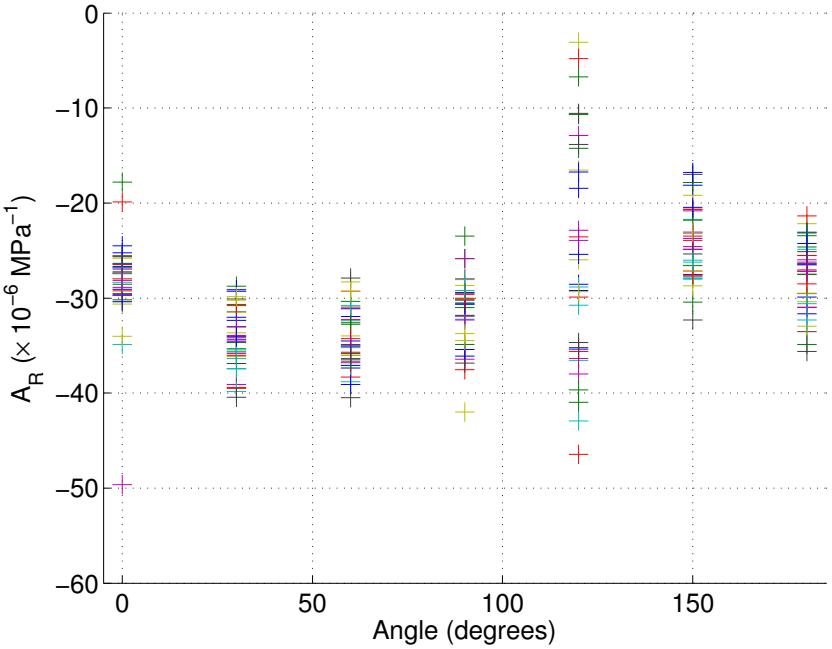

Figure 5.23: Plot of the acoustoelatic ($\times 10^{-6}$ MPa^{-1}) coefficient of area against angle of orientation from an arbitrary direction. Note angle 120° represents a direction where the signal to noise of the probe SAW was very low.

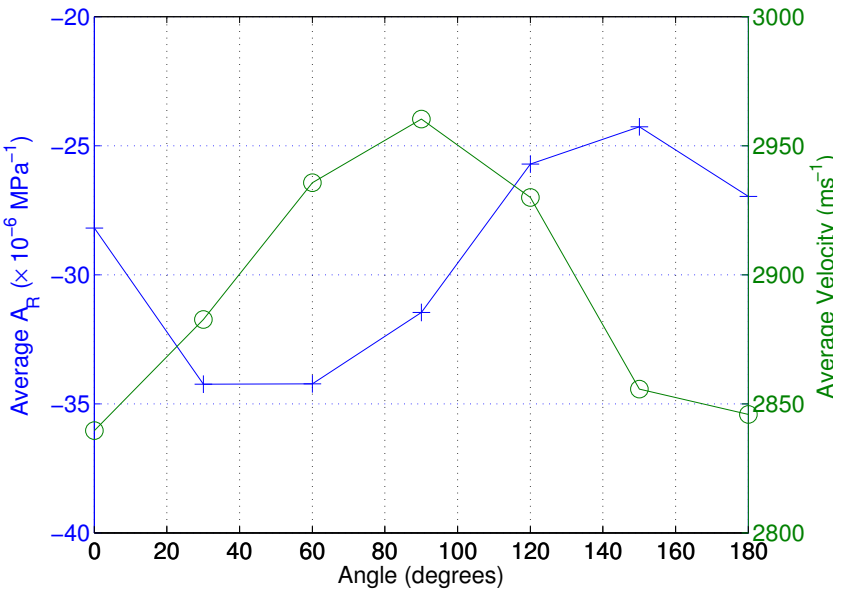

Figure 5.24: Plot of the average acoustoelatic ($\times 10^{-6}$ MPa^{-1}) coefficient of an area. against angle of orientation from an arbitrary direction. The blue crossed line ($-+$) represents the mean A_R value and the green circled line ($-\circ$) represents the mean linear velocity.

5.6.3 Discussion about relationship between microstructure and the acoustoelastic coefficient (A_R)

A_R is seen to vary by 400% across different microstructure. As the orientation of a particular single grain is rotated, a change in A_R of 40% is observed (see section 5.6.2). The dependence of A_R on microstructure has implications on the use of A_R to monitor other material features. The main implication is that the accuracy in the re-registration of the area investigated must be of the same order as the size of the microstructure. Otherwise the variation caused by the microstructure could overwhelm the variation in A_R caused by the feature being investigated.

5.7 Fatigue variation and the measurement of the acoustoelastic coefficient (A_R)

In the literature a link between the nonlinear elastic response of a material and the level of fatigue it has experienced has been reported [2,3,5,6,10–23]. Other authors have also noted a relationship between a material's elastic nonlinear response and a materials microstructure [8, 17, 83, 90], which varies spatially.

The instrument developed in this work can image the nonlinear acoustoelastic coefficient (A_R) over an area of material. Work presented in the next section investigates how the relationship between A_R over an area varies with fatigue. Variation in fatigue along a sample and the number of fatigue cycles experienced by a sample are used to investigate the effect of fatigue on the measurement of A_R.

5.7.1 Variation in the acoustoelastic coefficient (A_R) over the length of a fatigued sample

The shape of the dogbone sample is such that the greatest strain and consequently the greatest stress levels occur at the centre of the sample during the fatiguing process. The highest level of fatigue will occur where the highest level of stress occurs. Areas at the ends of the sample will be fatigued less. An experiment is conducted to investigate if the change in fatigue over the sample affects the measurement of A_R.

The experiment investigates a sample that has been heavily fatigued ($> 80\%$ fatigue life, see section 4.5.2). The sample is made from aluminium 2024-T351. The sample is designated Al02 and has intermediary fatigue life scans conducted on it (see 5.7.2). A large area is imaged across the sample length using the acoustoelastic imaging technique. The scan area measures from the centre of the sample to a point

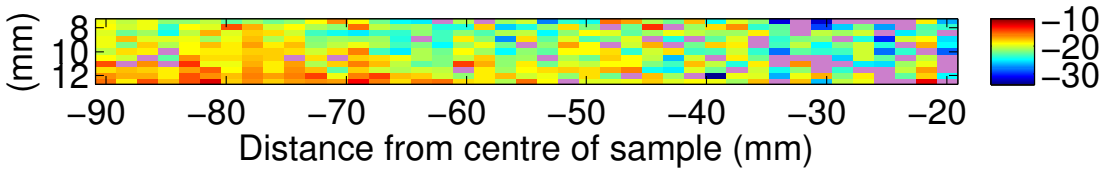

Figure 5.25: Image of A_R ($\times 10^{-6}$ MPa^{-1}) over a large section of the sample. All measurements are in mm away from the centre of the sample. The right hand side of the image being closest to the centre of the sample. Pink locations are points where the measured signal to noise ratio of the probe SAW is below 3.

90 mm away. This covers half of the curved central section of the sample. The step size along the sample is 1.75 mm. The lateral resolution is 0.5 mm. The results of the scan can be seen in figure 5.25. Figure 5.26 illustrates the size of the scan relative to the dimensions of the sample. At this resolution, discerning the precise microstructure that the measurement of A_R interacts with is difficult.

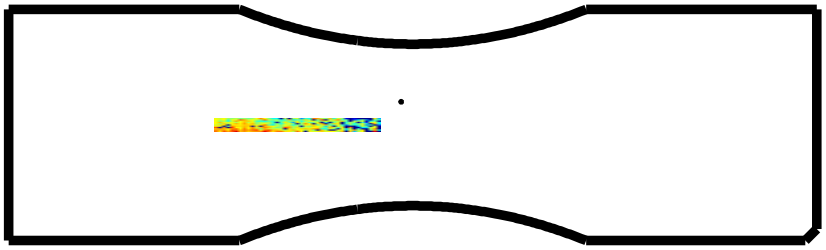

Figure 5.26: Diagram depicting scale of scan area (coloured region) relative to the dimensions of the sample.

In figure 5.25 some of the points towards the centre of the sample are coloured pink. These are locations where the probe SAW signal to noise ratio falls below 3, and are treated as null points. These points correspond to areas where surface damage is present on the sample due to the fatiguing process. The surface damage reduces the signal of the probe SAW as it attenuates the propagating SAW and reduces the amount of light returning to the knife-edge detector. The pump SAW stress reduces away from the transducer, so the stress is not averaged over the entire area. Instead, the stress is averaged across each scan line perpendicular to

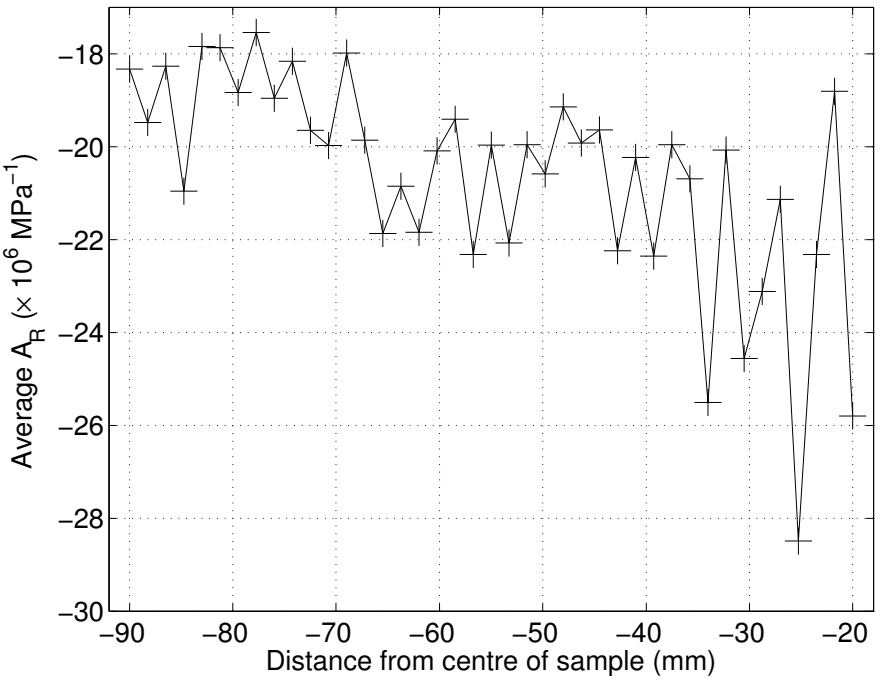

Figure 5.27: Average A_R of each column shown in figure 5.25 with respect to distance from centre of sample.

the direction of propagation of the pump SAW (each column of the image).

Figure 5.25 shows a general trend that areas closer to the registration mark (right hand side) have a lower A_R than those further away. A_R of aluminium is negative. A decrease in the value of A_R on aluminium produces an increase in the nonlinearity of the material. The nonlinearity of a material is the amount the material deviates from the linear response.

The graph in figure 5.27 shows the averaged A_R across each column of the image. The average value of A_R for each column tends to decrease closer to the center of the sample. The average A_R also tends to vary more from column to column closer to the center of the sample. The reason for this is not clear but may have to do with either a reduction in certainty in measurements due to a decline in SNR or microstructural variation at these locations. The uncertainty calculated in each point is 2×10^{-6} MPa^{-1} or less.

5.7.2 Imaging of the acoustoelastic coefficient (A_R) with fatigue life increment

In this section, the imaged A_R of a sample area is monitored with respect to an increase in fatigue life. The purpose of this is to investigate changes in A_R with fatigue. Both aluminium and titanium samples are scanned. The experimental configuration is outlined in section 4.5. Data presented includes the imaged A_R over a fixed area of the sample. The linear velocity data from the SRAS technique are also included, which are related to the microstructure of the material. Analysis of A_R data includes monitoring the mean and standard deviation for each fatigue level. Each imaged area is acquired twice to ensure repeatability. In this section, only one of the two A_R images is displayed with the SRAS velocity image for reasons brevity. The analysis includes data from the initial and repeat images of A_R.

Aluminium

A large number of aluminium samples are investigated in the course of this experiment. It is impractical and serves little purpose to show the imaged results for all the samples. In this section only samples fatigued to a high level (80% life or above) are presented. Aluminium 05 is also included due to an irregular response. For completeness, all other sample results can be found in appendix D.

Aluminium 02 Aluminium 02 is fatigued at 20% increments and scanned after each increment. The final fatigue level that Aluminium 02 reaches is an estimated 80% of its life. The imaged A_R and SRAS velocity data can be seen in figure 5.29. At higher fatigue levels the quality of the surface finish of the sample deteriorates. The deterioration is attributed to a combination of scratches on the surface due

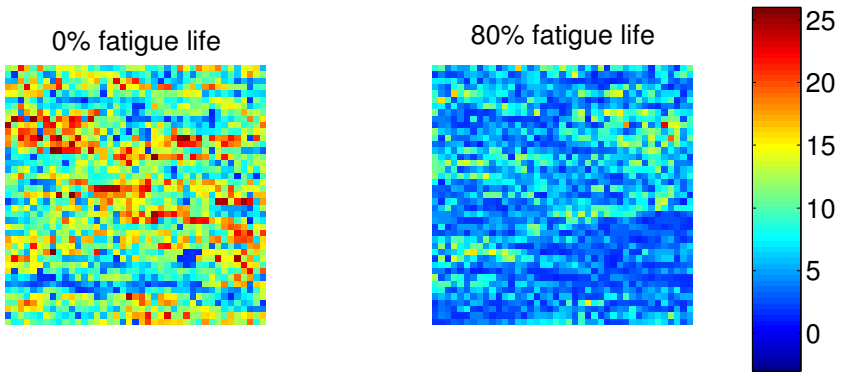

Figure 5.28: A marked degradation in the signal to ratio (SNR) of the probe SAW packet can be seen as the fatigue level of the samples increases. This is attributed to surface defects accumulated over the course of the fatiguing process. This is not a procedural effect as low life samples scanned after the high life sample do not demonstrate similar degradation in SNR

to handling, tarnishing due to heat generated in the fatiguing process and small sub-surface cracks. The reduction in the quality of the surface finish reduces the signal to noise ratio (SNR) of the propagating probe SAW (see figure 5.28). An decrease in the SNR increases the uncertainty in the measurement of A_R.

As Aluminium 02 moves through its fatigue life, the majority of the imaged values of A_R decrease (turn blue, see figure 5.29(A)). At higher fatigue levels the linear velocity image produced using the SRAS technique shows a decrease in the velocity (see figure 5.29(B)). The mean value of A_R for the imaged area decreases with an increase in fatigue life (see figure 5.30). A change of 30% (-17 to -22 $\times 10^{-6}$ MPa^{-1}) is recorded in the mean value of A_R as Aluminium 02 moves from 0% to 80% fatigue life.

The standard deviation of the imaged values of the A_R increase with fatigue life on sample Aluminium 02 (see figure 5.31). A reduction in SNR causes a reduction in certainty in the measurement of A_R. The increase in uncertainty contributes to the increase in standard deviation of A_R.

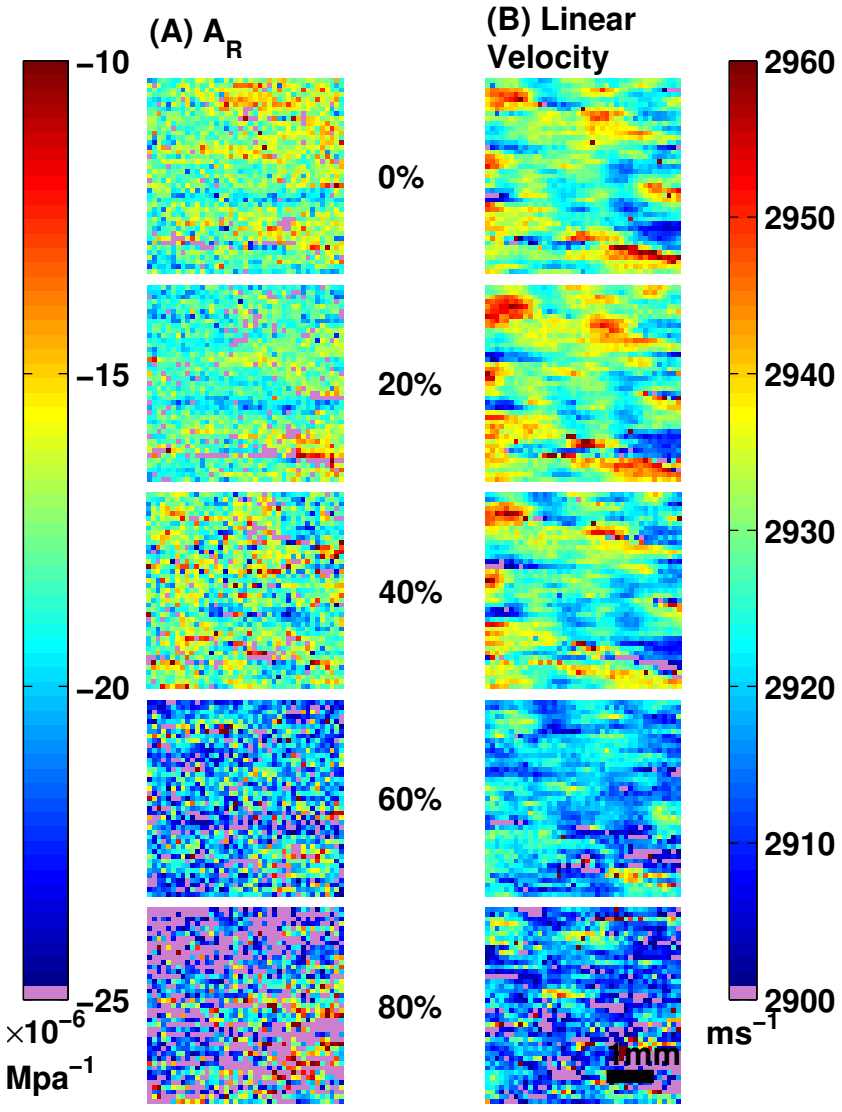

Figure 5.29: Graphs (A) imaged A_R against fatigue and (B) imaged velocity (SRAS) indicating the microstructure involved in the square for sample Aluminium 02.

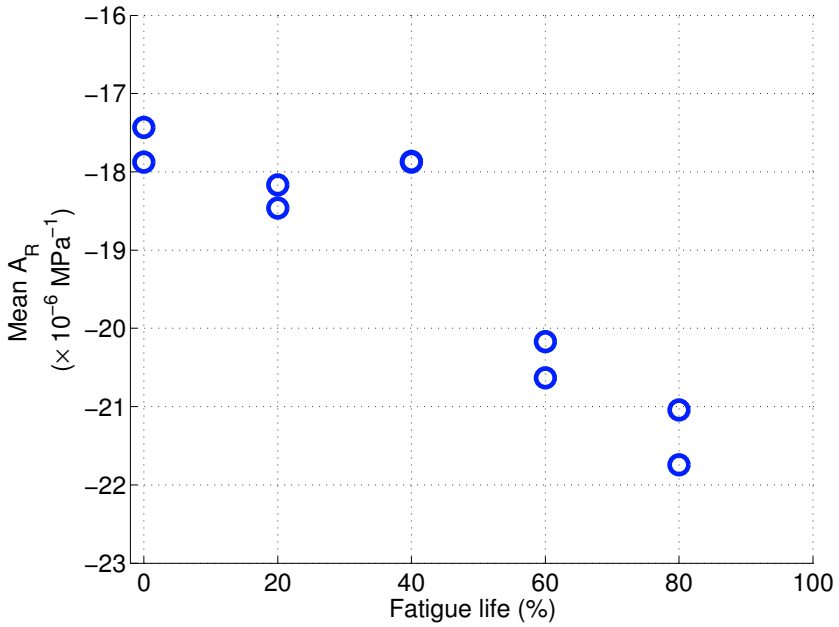

Figure 5.30: Graph of mean A_R against fatigue life for sample Aluminium 02.

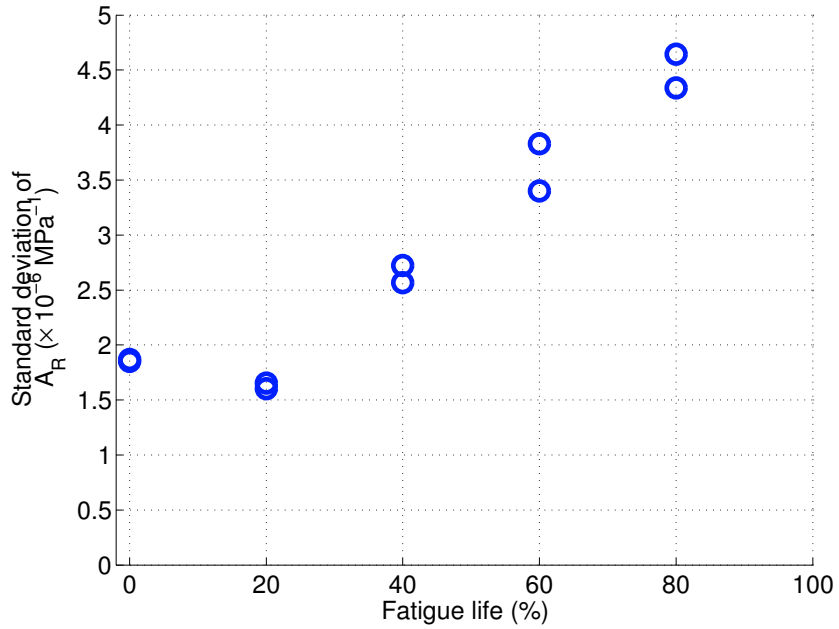

Figure 5.31: Graph of standard deviation of A_R against fatigue life for sample Aluminium 02 .

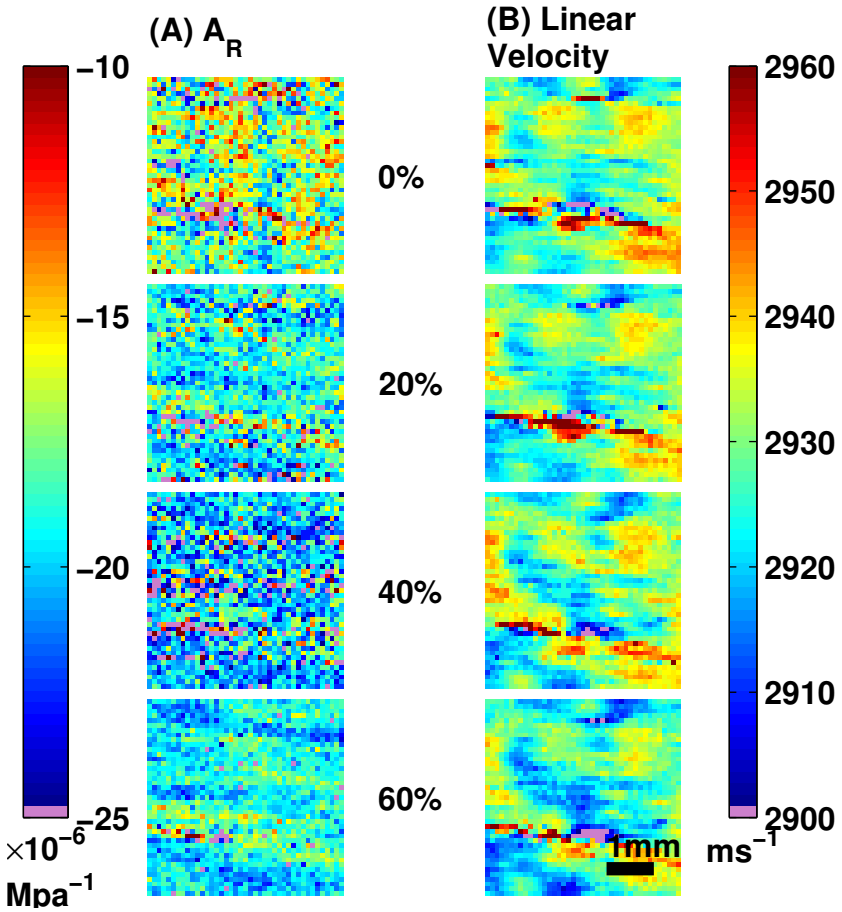

Figure 5.32: Graphs (A) imaged A_R against fatigue and (B) imaged velocity (SRAS) indicating the microstructure involved in the square for sample Aluminium 05.

Aluminium 05 Sample Aluminium 05 is fatigued to approximately 60% of its fatigue life. There is no noticeable degradation in surface finish and so the signal to noise ratio is consistently good. Good re-registration is achieved in between fatiguing of the sample.

The relationship between A_R and the fatigue level is more complicated for sample Aluminium 05 than that found for Aluminium 02 (see figure 5.32). The mean value of the imaged A_R decreases with fatigue up to 40% fatigue life (see figure 5.33). The mean value of the imaged A_R increases at a fatigue life level of 60% from the value at 40% life. A nonlinear relationship between A_R and the

fatigue life is observed on sample Aluminium 05.

The calculated uncertainty in the mean value of A_R at the 40% fatigue life (0.06×10^{-6} MPa^{-1}, see figure 5.49) is the highest measured on all of the aluminium samples. The high level of uncertainty in the mean A_R could contribute to the mean value of the 40% life measurements being reduced. The calculated uncertainty is not sufficient in size to be the sole cause of any reduction in the measured response. Another factor must also contribute to the nonlinear relationship between the fatigue life and A_R observed on sample Aluminium 05. Other authors [66,67] have also observed a nonlinear relationship between A_R and the fatigue life of a sample. This is discussed further in section 6.

Overall, a change of 10% (-17.4 to -19.2 $\times10^{-6}$ MPa^{-1}) is recorded in the mean value of A_R as Aluminium 05 moves from 0% to 60% fatigue life. The standard deviation of the imaged values of A_R remains relatively constant between 0 and 40% fatigue life. At 60% fatigue life, the standard deviation of the imaged A_R decreases from the value between 0 and 40% fatigue life (see figure 5.34).

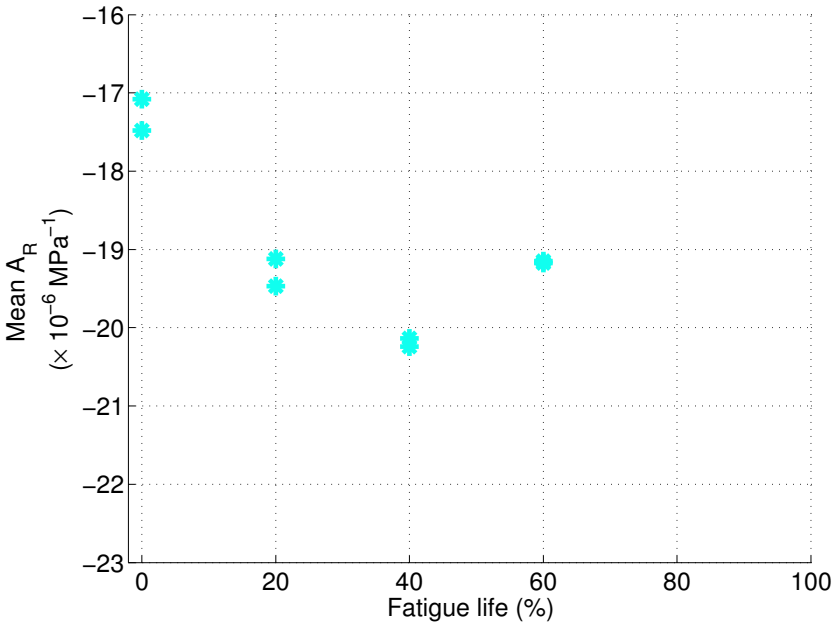

Figure 5.33: Graph of mean value of A_R against fatigue life for sample Aluminium 05.

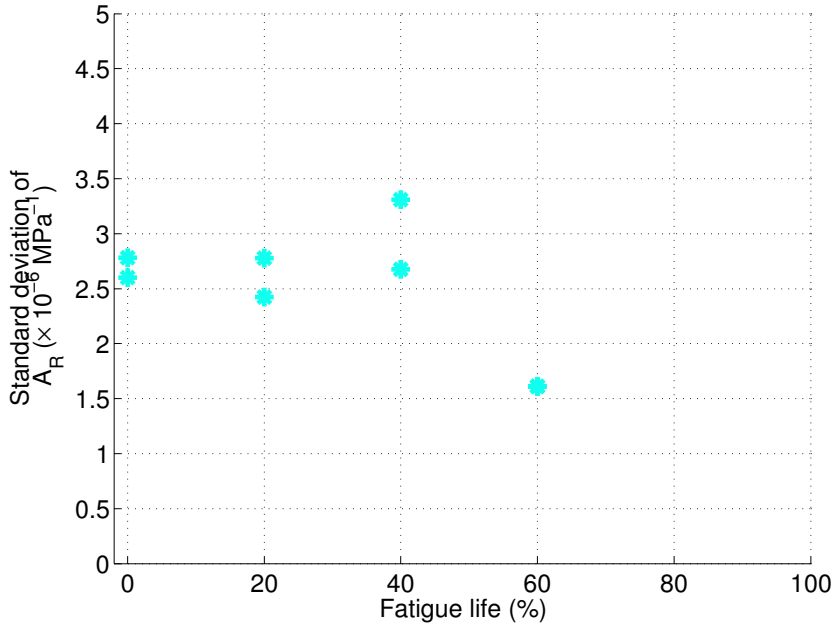

Figure 5.34: Graph of standard deviation of A_R against fatigue life for sample Aluminium 05.

Aluminium 09 Sample Aluminium 09 is fatigued in similar increments as Aluminium 02. A fatigue life of 30% fatigue life increment is investigated to allow comparison with other samples at a similar level of fatigue.

As Aluminium 09 moves through its fatigue life, A_R decreases in most regions (see figure 5.35 (A)). At higher fatigue levels the linear velocity image produced using the SRAS technique shows a decrease in the velocity (see figure 5.35 (B)). A change of 9% (-18.6 to -20.2 $\times 10^{-6}$ MPa^{-1}) is observed in the mean value of A_R as Aluminium 09 moves from 0% to 80% fatigue life. This is a smaller decrease than that observed on sample Aluminium 02. It is possible to fit a linear trend between fatigue life and in the value of A_R.

The initial 0% fatigue life mean A_R for Aluminium 09 is lower than the value for Aluminium 02. This is because Aluminium 09 has regions of low A_R (have a relatively large $|A_R|$) at the 0% fatigue life level (see figure 5.35 (A), 0%, top of image). These regions could indicate some pre-existing localised defect or strain in the sample.

At a fatigue life of 80%, an interesting feature forms in the image of A_R of the sample. A region one third of the way down the image is seen to be relatively linear (have a relatively small $|A_R|$). This region appears in both repeat images. The cause is unclear though possible reasons are discussed in section 6.

The standard deviation of the imaged values of A_R remains relatively constant between 0 and 60% fatigue life. At 80% fatigue life, the standard deviation of the imaged values of A_R increases by 0.4×10^{-6} MPa^{-1}.

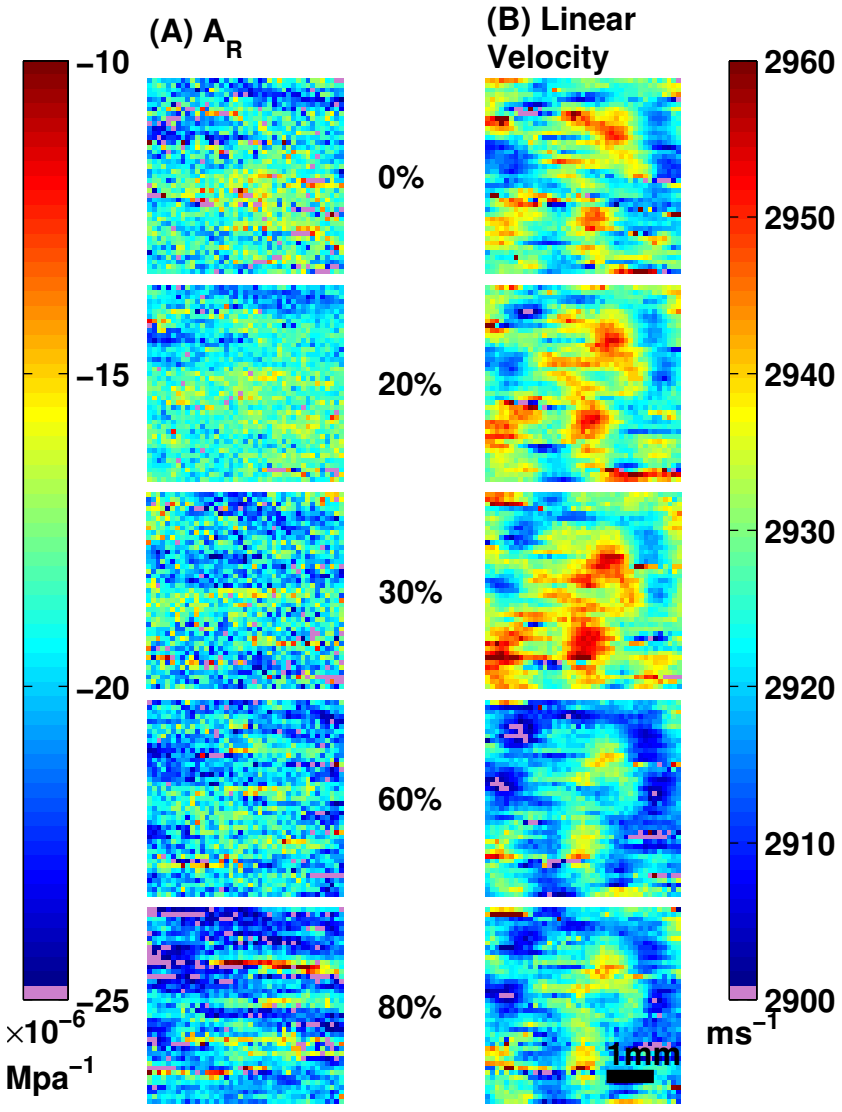

Figure 5.35: Graphs (A) imaged A_R against fatigue and (B) imaged velocity (SRAS) indicating the microstructure involved in the square for sample Aluminium 09.

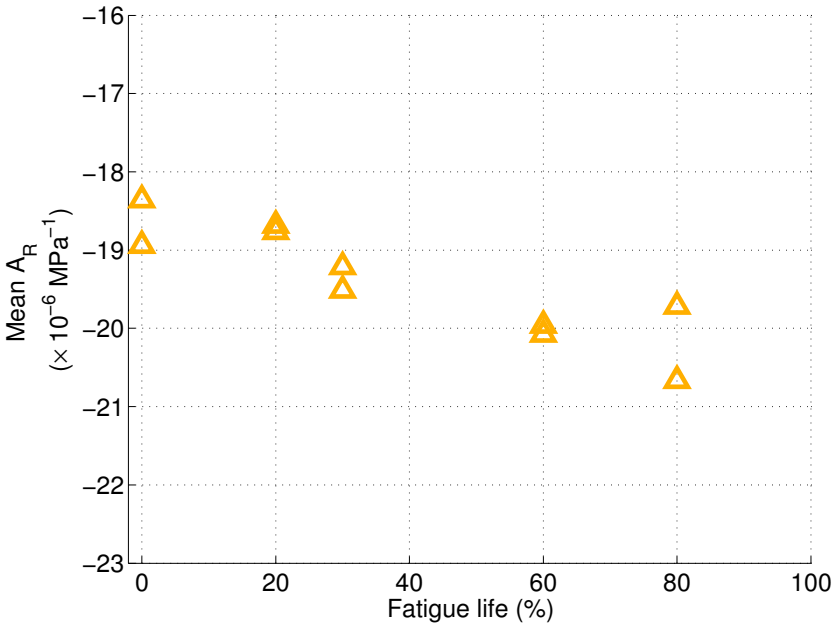

Figure 5.36: Graph of the mean A_R against fatigue life for sample Aluminium 09.

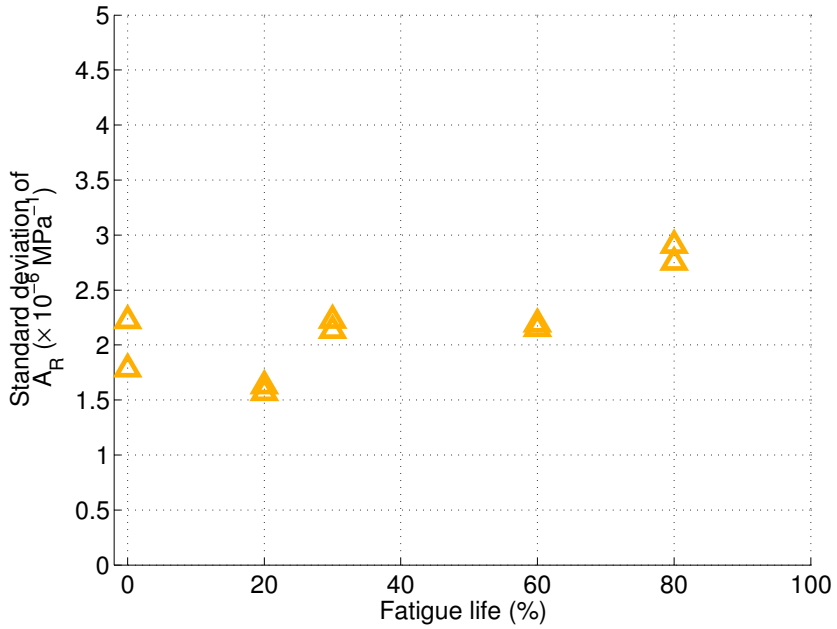

Figure 5.37: Graph of the standard deviation of A_R against fatigue life for sample Aluminium 09.

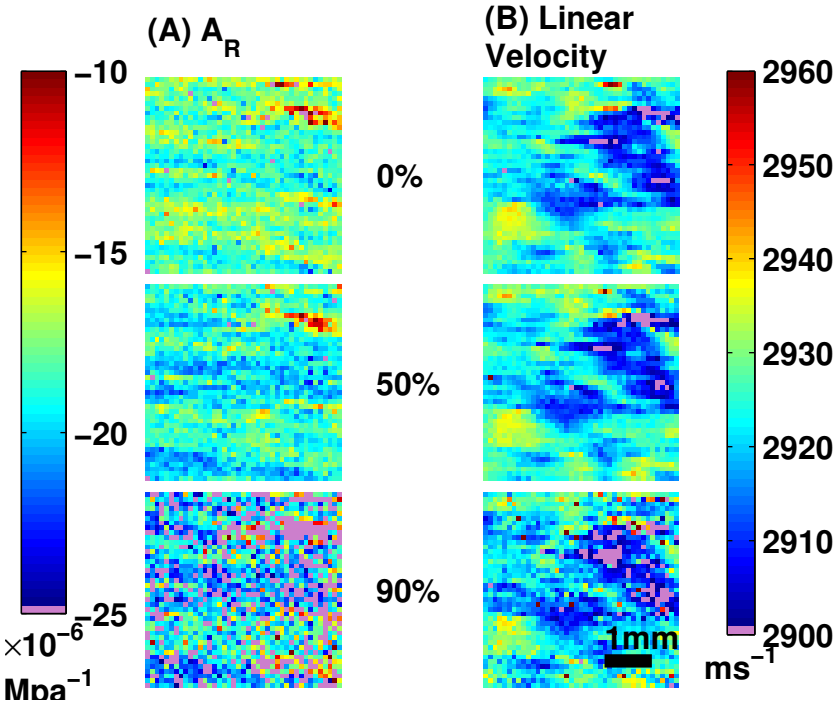

Figure 5.38: Graphs (A) imaged A_R against fatigue and (B) imaged velocity (SRAS) indicating the microstructure involved in the square for sample Aluminium 12.

Aluminium 12 Sample Aluminium 12 is the most fatigued sample still left intact. Images of A_R are taken at 0%, 50% and 90% estimated fatigue life. The resultant SRAS linear velocity scans and imaged A_R can be seen in figure 5.38.

A decrease in the SNR at the 90% fatigue life level results in some points being removed from the image of A_R. A general decrease in the mean value of A_R is observed with an increase in fatigue (see figure 5.39). A maximum change of 10% (-17.8 to -19.5 $\times 10^{-6}$ MPa^{-1}) is observed in the mean value of A_R as Aluminium 12 moves from 0% to 90% fatigue life.

The standard deviation of the imaged values of A_R remains relatively constant between 0 and 50% fatigue life. At 90% fatigue life the standard deviation of the imaged values of A_R increases by 1.2×10^{-6} MPa^{-1}.

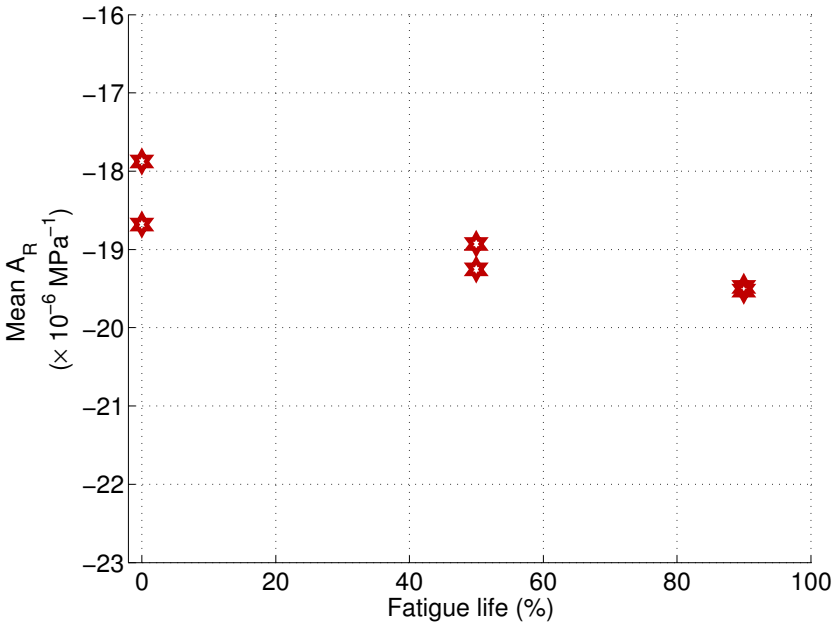

Figure 5.39: Graph of the mean of A_R against fatigue life for sample Aluminium 12.

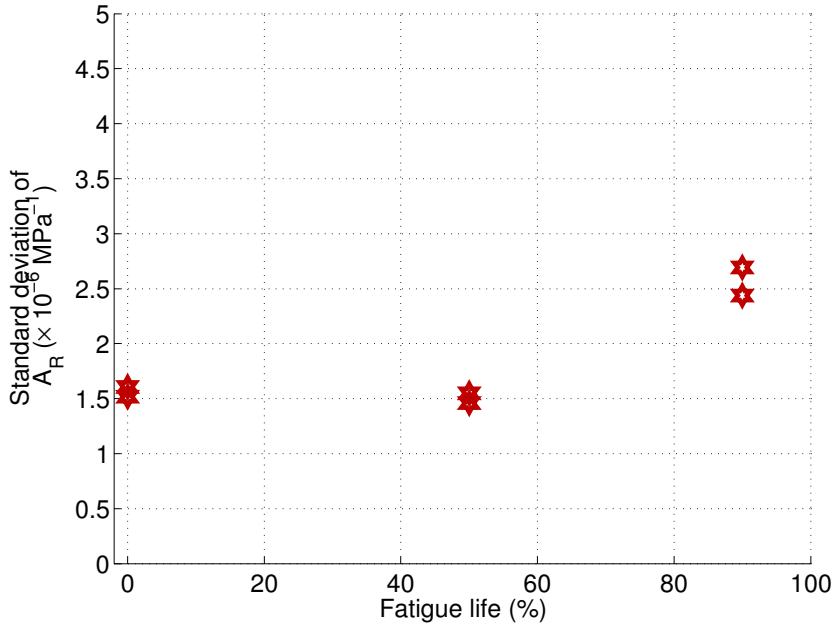

Figure 5.40: Graph of the standard deviation of A_R against fatigue life for sample Aluminium 12.

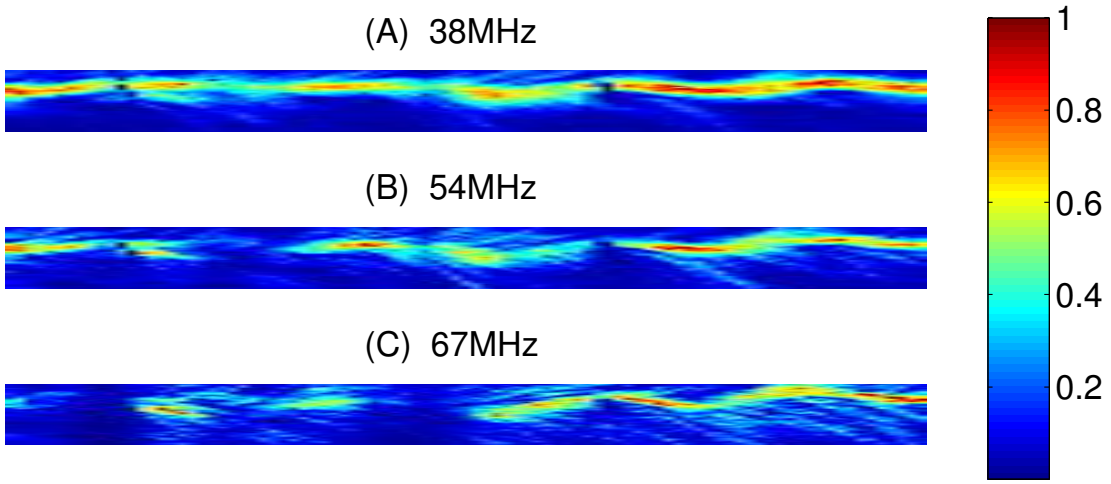

Figure 5.41: Image of the point spread function of acoustic energy 3 mm (at the focus) away from the generation area for focused waves along the surface of a titanium sample for (A) 38 MHz, (B) 54 MHz and (C) 67 MHz SAWs. This figure shows how much the position of the focus of the acoustic waves varies along the sample.

Titanium

Measuring the A_R of titanium is more difficult than measuring the A_R of aluminium. The A_R of titanium is difficult to measure as it has a comparatively low value, of the order of -4 $\times 10^{-6}$ MPa^{-1}. This means that noise has a comparatively large impact on the measurement. Measurements of A_R on titanium are also complicated by titanium aberrating the probe SAW at the frequencies used in aluminium (see figure 5.41). A lower probe SAW frequency (38 MHz) is used to measure A_R of titanium.

Two titanium samples are investigated. Both titanium samples are fatigued to approximately 80% fatigue life in 20% increments. A_R of each sample is imaged after each fatigue level increment. The same procedures developed for monitoring the areas on the aluminium samples are used for titanium. Re-registration is simplified by titanium having a large microstructure.

Titanium 02 The area selected to be imaged on Titanium 02 is chosen for its distinctive microstructure. The pump and probe SAWs co-propagate in two distinct regions of microstructure (both blue and red regions in the SRAS image see 5.42(B)).

The imaged A_R of Titanium 02 can be seen in figure 5.42(A). A variation in A_R is observed on the imaged area. The left hand side of the image produces a higher value of A_R compared to the right. These areas correspond to the different microstructure that the pump and probe SAWs co-propagate through. This effect was further investigated in section 5.6.

Titanium is harder than aluminium (331 opposed to 135 on the Brinell scale [126]). As such, titanium maintains its surface finish and so relatively high SNR throughout its fatigue life.

A general decrease in the mean value of A_R is observed with an increase in fatigue (see figure 5.43). The observed change in the mean value of the imaged A_R for sample Titanium 02 (0.9 $\times 10^{-6}$ MPa^{-1}, -3.3 to -4.2 $\times 10^{-6}$ MPa^{-1}) is smaller than the smallest change seen on aluminium samples (1.6 $\times 10^{-6}$ MPa^{-1} Aluminium 09). Expressing the change in the value of the mean A_R as a percentage of the initial mean value for Titanium 02 results in a change of 27%, which is of the same order as the highest change observed in aluminium.

The standard deviation of the value of the imaged A_R varies by 0.8×10^{-6} MPa^{-1} throughout the course of the fatigue life of titanium 02. No relationship between the variation in the standard deviation of the imaged A_R and the fatigue level is observed.

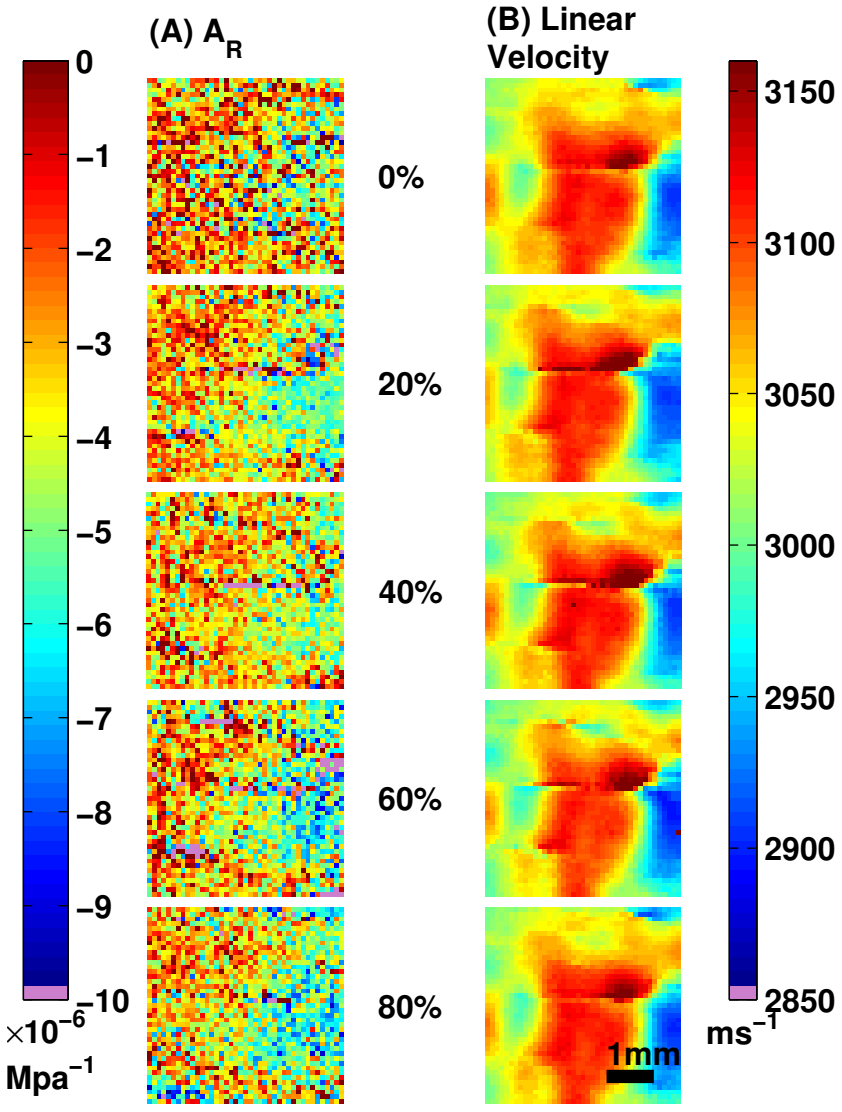

Figure 5.42: Graphs (A) imaged A_R against fatigue and (B) imaged velocity (SRAS) indicating the microstructure involved in the square for sample Titanium 02.

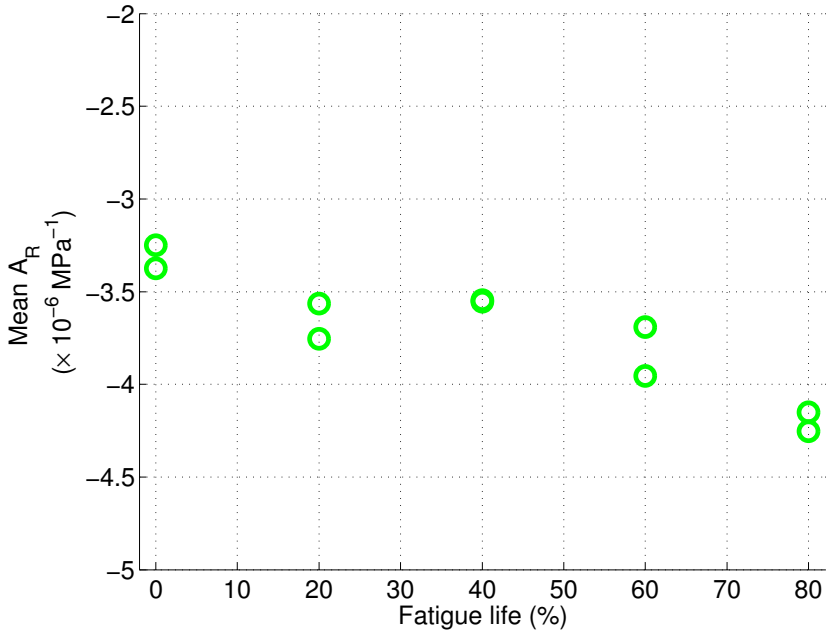

Figure 5.43: Graph of the mean of A_R against fatigue life for sample Titanium 02.

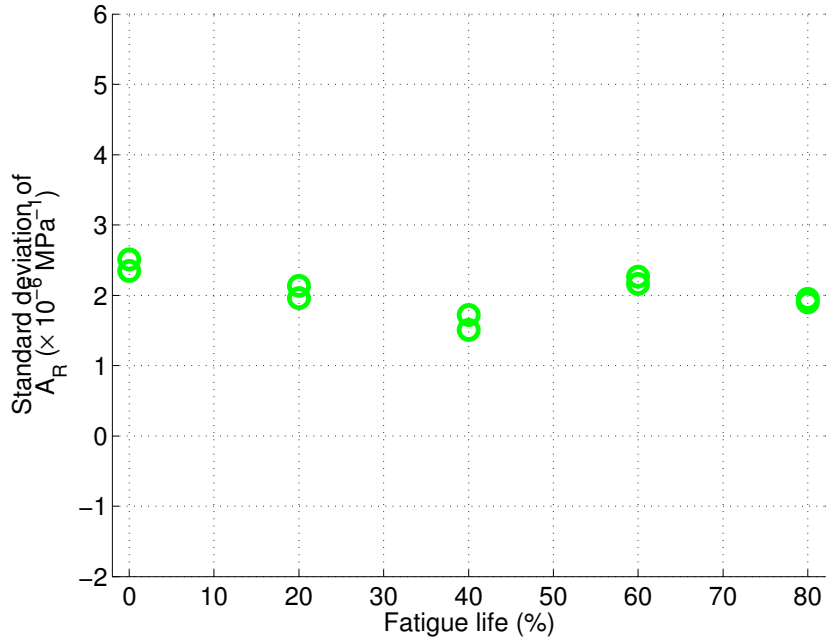

Figure 5.44: Graph of the standard deviation of A_R against fatigue life for sample Titanium 02.

Titanium 03 Titanium 03 sample demonstrates the difficulty in acquiring repeatable measurements of A_R on titanium. This sample provides a complicated result and is included due to its inconsistency with others.

The acoustoelastic data acquired for the 0% fatigue level has sufficiently good SNR to be trusted. However the imaged A_R at 0% is completely different from the coefficients imaged at higher fatigue levels (see figure 5.45). It is assumed that part of the procedure failed during the acquisition of the 0% life scan. Most likely the location of the peak and trough stresses were found incorrectly. This highlights a weakness in the technique.

The imaged A_R for the repeated 80% life scan is less reliable because a low stress field (0.75MPa) was induced on the sample due to the failure of the pump wave transducer. The mean value of A_R for this scan is presented as the faded red cross (see figure 5.46). A maximum change of 17% (-3.5 to -4.1 $\times 10^{-6}$ MPa^{-1}) is observed in the mean value of A_R as Titanium 03 moves from 20% to 80% fatigue life (see figure 5.46).

The standard deviation of the imaged values of A_R increase with fatigue life beyond 20% (see figure 5.47).

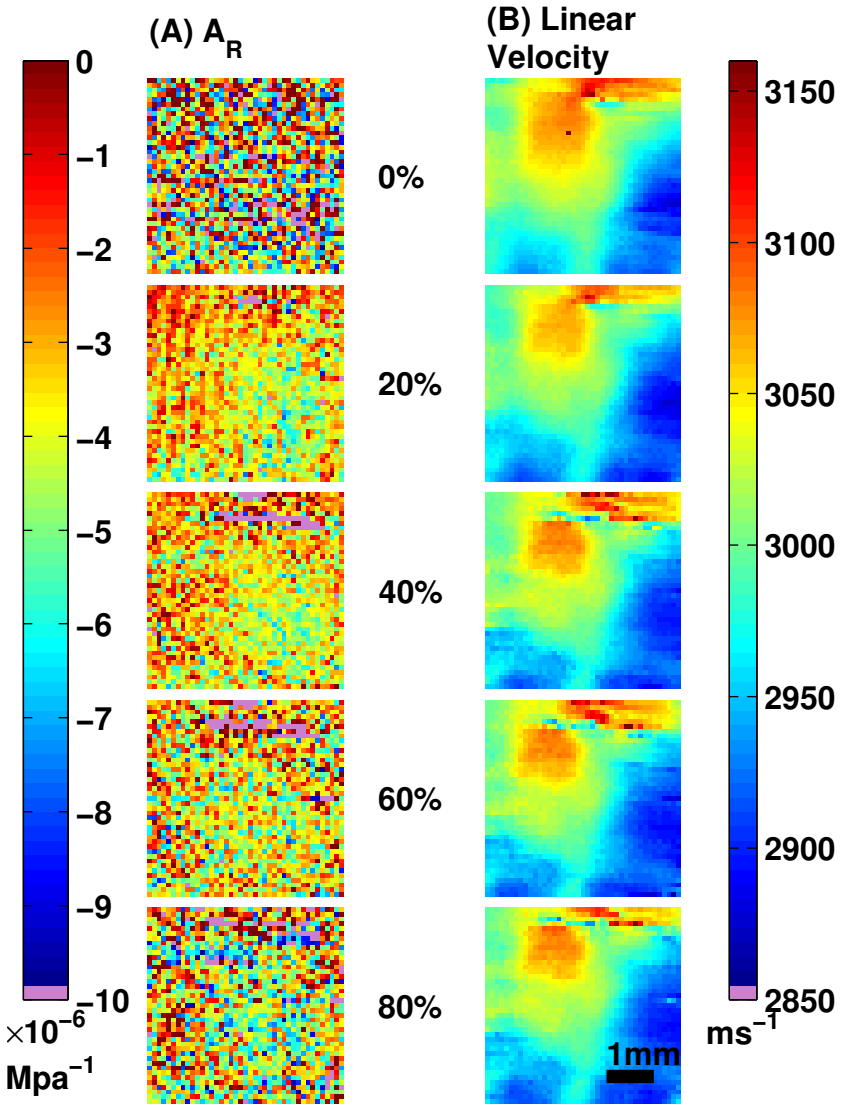

Figure 5.45: Graphs (A) imaged A_R against fatigue and (B) imaged velocity (SRAS) indicating the microstructure involved in the square for sample Titanium 03.

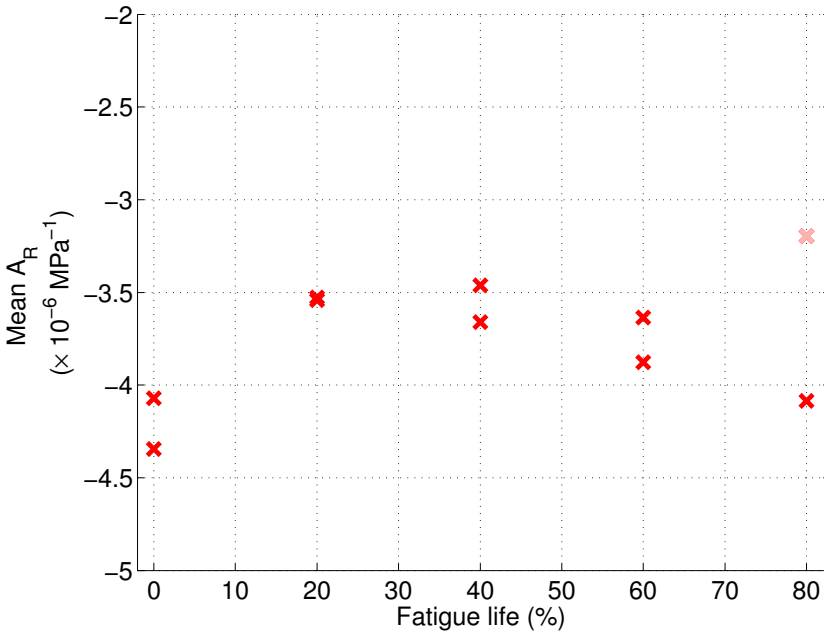

Figure 5.46: Graph of the mean of A_R against fatigue life for sample Titanium 03. Note that the data point where the average stress is less than 1 MPa is faded, to highlight the low confidence in it.

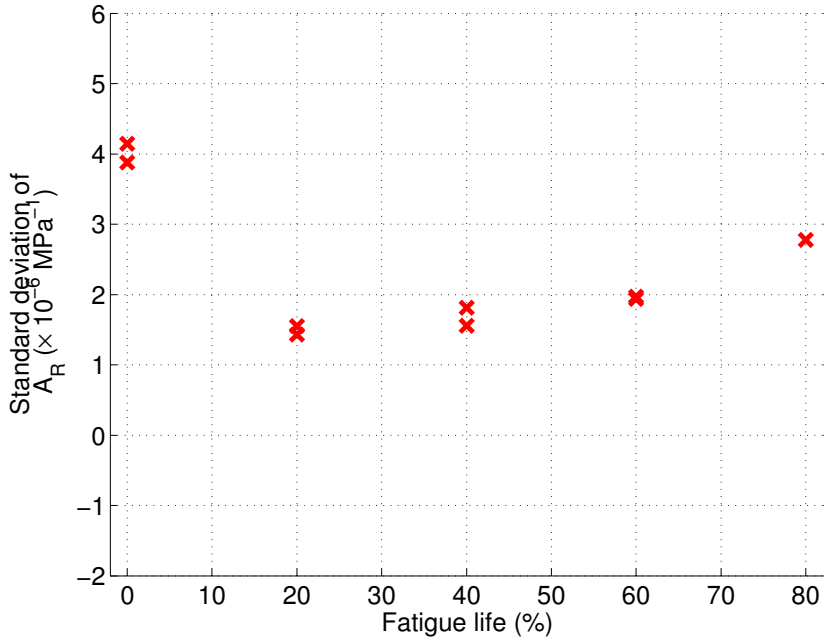

Figure 5.47: Graph of the standard deviation of A_R against fatigue life for sample Titanium 03.

5.7.3 Analysis of fatigue results

In this section a range of techniques are used to investigated trends in the imaged A_R data generated in the course of the fatigue experiments. The mean and standard deviation of the values of the imaged A_R have already been used to quantify the trends of some samples. In this section these analysis techniques are applied to data from all of the samples. Comparisons between A_R and linear velocity measurements are made. Analysis of the variation in the localised features of A_R with an increase in fatigue is conducted. The results are discussed and compared with other authors.

Change in the mean acoustoelastic coefficient (A_R) with fatigue

In order to obtain a result with comparable resolution to other techniques, the average of A_R is taken over an appropriate area of the sample, this averages out the localised variation in A_R. The samples are grouped by material, all samples tested are included.

Aluminium The mean A_R for all 12 aluminium samples are shown in figure 5.48 plotted against fatigue life. A large difference in the mean values of the imaged A_R is observed at 0% fatigue life. As all of the samples are produced and handled under similar conditions, this variation must be due to a feature that is independent of fatigue. The variation in A_R of a material is further investigated in section 5.7.4. These factors mean that any techniques developed to monitor fatigue using A_R requires prior knowledge of the 0% fatigue life.

Samples Aluminium 10 and Aluminium 11 display an abnormal trend: Both initially show a decrease in the value of the mean A_R. At later fatigue life stages (60 and 70 %) the mean value of A_R for both samples increases towards the 0%

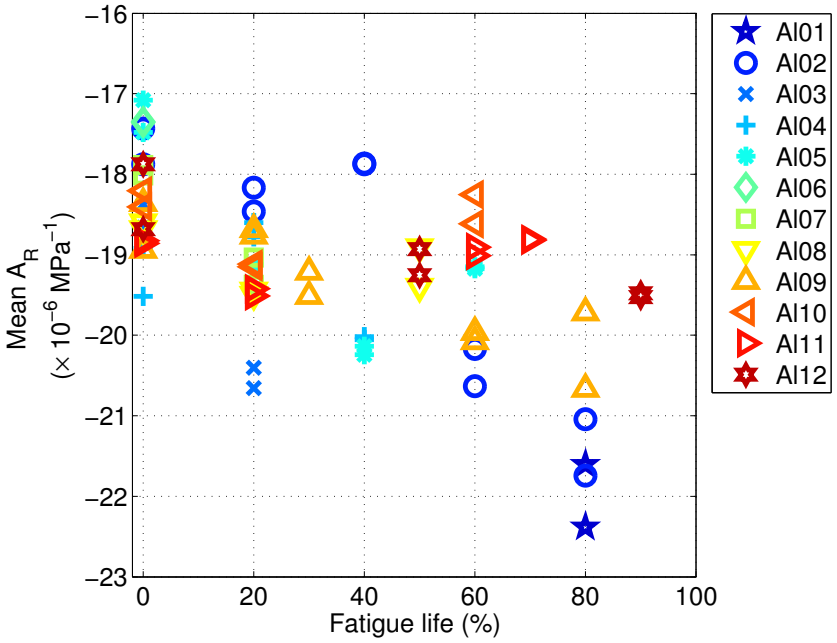

Figure 5.48: Graph of all the mean A_R against fatigue life for all aluminium samples. A wide variation in A_R can be seen for any given fatigue life. The mean value of A_R decreases as a general trend with fatigue life.

fatigue life level. A similar increase is observed in Aluminium 05. This indicates a complicated relationship between fatigue and A_R. Other authors have found similar trends between fatigue and nonlinear measurements [66, 67].

The mean value of A_R for all the samples decreases at some point during the fatigue life. The change observed in the mean A_R varies between samples from 9% to 30% with fatigue life. Other workers [2, 3, 5, 6, 10–23] have reported larger changes in nonlinear parameters with fatigue.

The calculated uncertainty in the mean A_R varies with sample and fatigue level. The variation in the calculated uncertainty of A_R ranges between 0.0179 and 0.0645 $\times 10^{-6}$ MPa^{-1} (see figure 5.49). The variation in the mean value of A_R with fatigue life is larger than the calculated uncertainties. This indicates the variation seen in the mean A_R is due to a change in fatigue rather than in the uncertainty of the measurement.

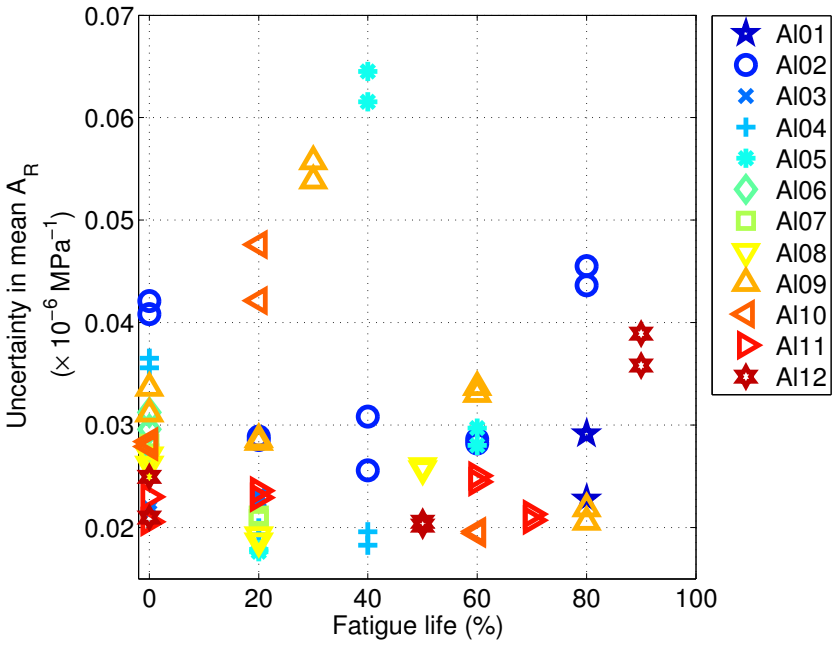

Figure 5.49: Uncertainty in mean value of the acoustoelastic coefficient for each imaged area for each sample.

Titanium The confidence in the value of the mean A_R is low for some of the areas scanned on the titanium samples. These areas include those scanned for both 0% fatigue life and the second scan area at 80% fatigue life on titanium 03. The mean value of A_R decreases for all the titanium samples provided the values of areas with low confidence are excluded. The fractional decrease in the mean value of A_R of titanium is of the same order as that observed for aluminium at 27%.

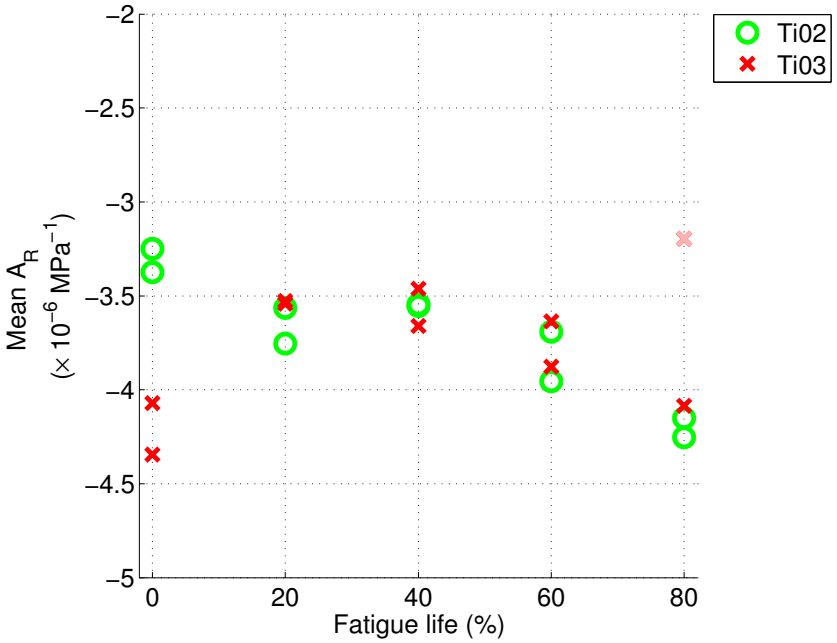

Figure 5.50: Graph of the mean acoustoelastic coefficient against fatigue life for all the titanium samples. Note that the data points where the average stress is less than 1 MPa are faded to show low confidence in them.

Change in the standard deviation of the acoustoelastic coefficient (A_R) with fatigue

In this section the relationship between the standard deviation of the imaged A_R and the fatigue life is investigated. The standard deviation of the imaged A_R is used as a metric to quantify the variation in these values. The variation in the standard deviation could be caused by an increase in measurement noise and also by the A_R of different locations changing by different amounts or directions with fatigue.

Aluminium Aluminium samples exhibit a range of values for the standard deviation in the imaged A_R at the 0% fatigue life (see figure 5.51). This range would indicate an initial variation in A_R across the imaged area that is independent of fatigue level and is specific to each sample.

As fatigue level of each of the samples increases, the standard deviation of the imaged A_R remains relatively constant. Above a fatigue life of 60% the standard deviation for all samples increases. A potential source for the increase in the standard deviation is an increase in the uncertainty in the measurement of A_R. Plotting the standard deviation of the imaged A_R against the calculated mean uncertainty in the imaged A_R shows the relationship between the two (see figure 5.52). The minimum value of the standard deviation in the measurement of A_R is always more than the calculated uncertainty. No other correlation is present. This indicates the variation in A_R is related to both the calculated uncertainty and other features independent of the uncertainty in the measurement.

Titanium The standard deviation of the imaged A_R varies throughout the fatigue lives of each of the titanium samples (see figure 5.53). The variation in the

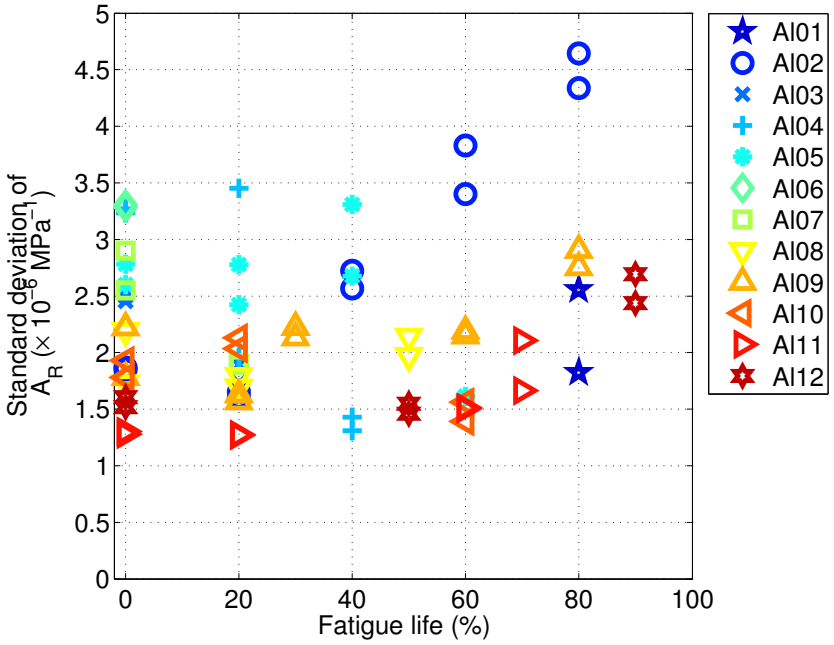

Figure 5.51: Graph of the standard deviation of the imaged A_R for all the aluminium samples.

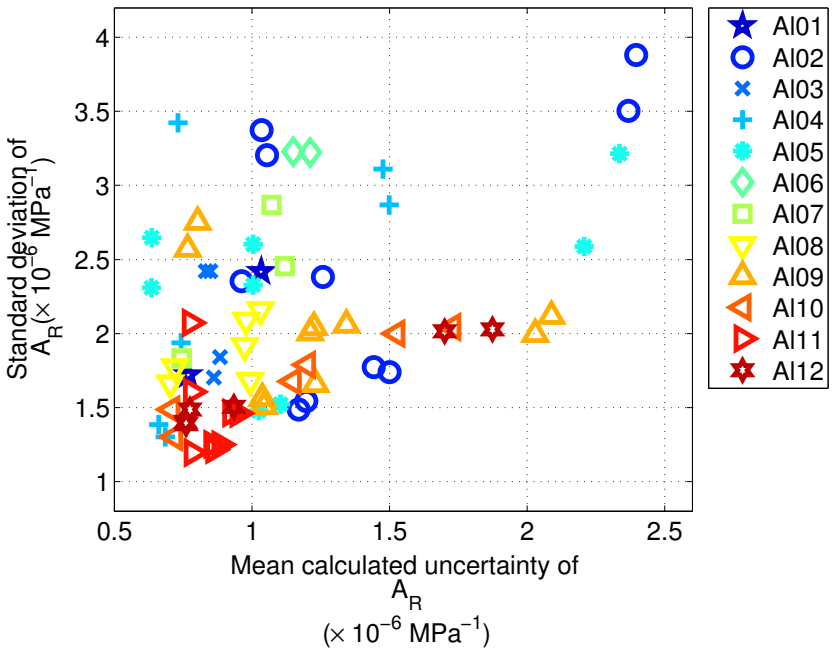

Figure 5.52: Graph of the mean calculated uncertainty in A_R against the standard deviation of A_R for all the aluminium samples. The mean calculated uncertainty is different from the uncertainty in the mean A_R.

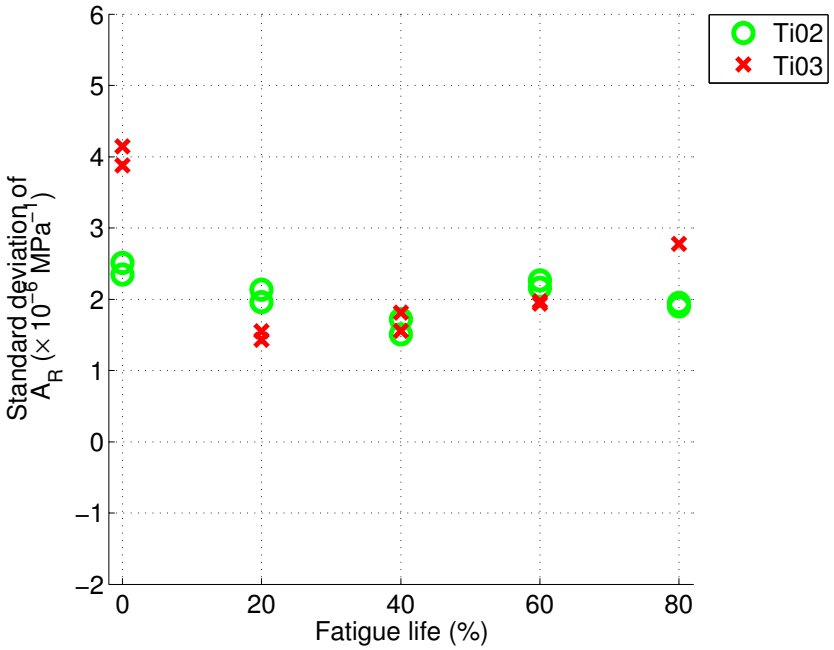

Figure 5.53: Graph of the standard deviation of the imaged A_R for all the titanium samples.

standard deviation is not dependent on the fatigue level.

Change in linear velocity measurements with fatigue

In this section, changes in linear velocity measurements with fatigue are investigated. A comparison between a linear technique and the nonlinear technique developed in this thesis is of interest, having observed a relatively small change in the nonlinear measurement with fatigue. Other workers [1–3] have demonstrated the relative insensitivity of linear ultrasonic techniques to an increase in fatigue. In this case the comparative sensitivity may be different. As a correlation between the linear velocity and A_R has been observed (see section 5.6.1) the linear velocity measurement could potentially also be sensitive to an increase in fatigue. Data collected in the process of acquiring the measurements of A_R is used to make linear measurements. The SRAS technique is applied to the reference probe SAW to produce a linear velocity measurement. The mean velocity for each imaged area is calculated.

Aluminium No repeatable trend is found between the mean linear velocity and the increase in fatigue for the aluminium samples (see figure 5.54). Some samples show an increase in mean velocity with fatigue (Aluminium 12). Other samples show a decrease in mean velocity with fatigue (Aluminium 05, Aluminium 02). Therefore monitoring the development of fatigue using this technique would be complicated, if not practically impossible.

The largest change in mean velocity is 15ms^{-1} over the fatigue life of the sample (Aluminium 02). The mean velocity of this sample at 0% fatigue life is 2920ms^{-1}. The fractional change in the mean velocity with an increase in fatigue is 0.5% for this sample. The smallest fractional change in the mean A_R with fatigue is 9%. Further comparisons between the linear velocity measurement and the measurement of A_R are discussed in section 5.7.4.

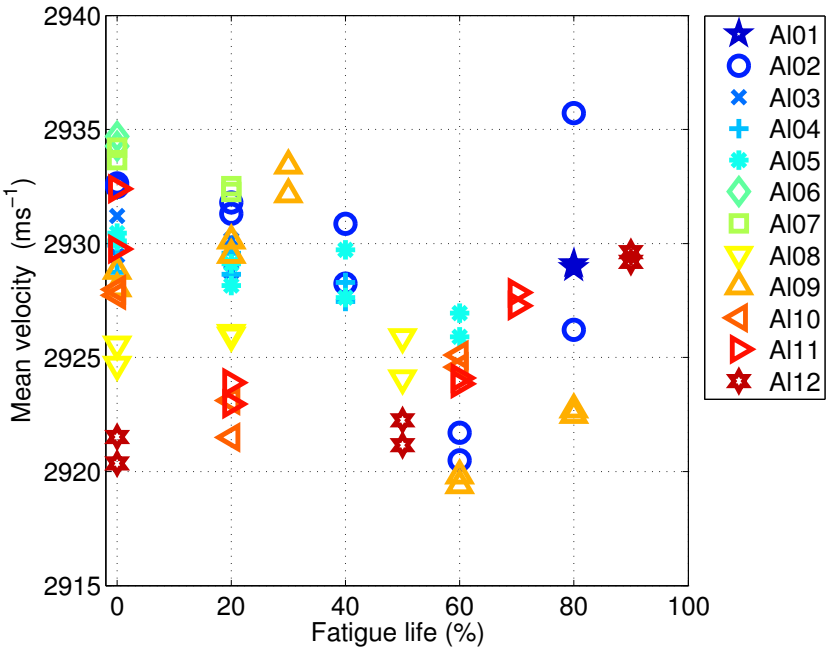

Figure 5.54: Graph of the mean linear velocity of each imaged area for all the aluminium samples against fatigue life.

Titanium Each of the titanium samples has a distinct mean linear velocity (see figure 5.55). An overall decrease in the mean velocity is observed for both samples with an increase in fatigue level. The largest change observed in the mean velocity is 18ms^{-1} over the fatigue life of the sample (Titanium 03). The mean velocity of this sample at 0% fatigue life is 3000ms^{-1}. The fractional change in the mean velocity with an increase in fatigue is 0.6%.

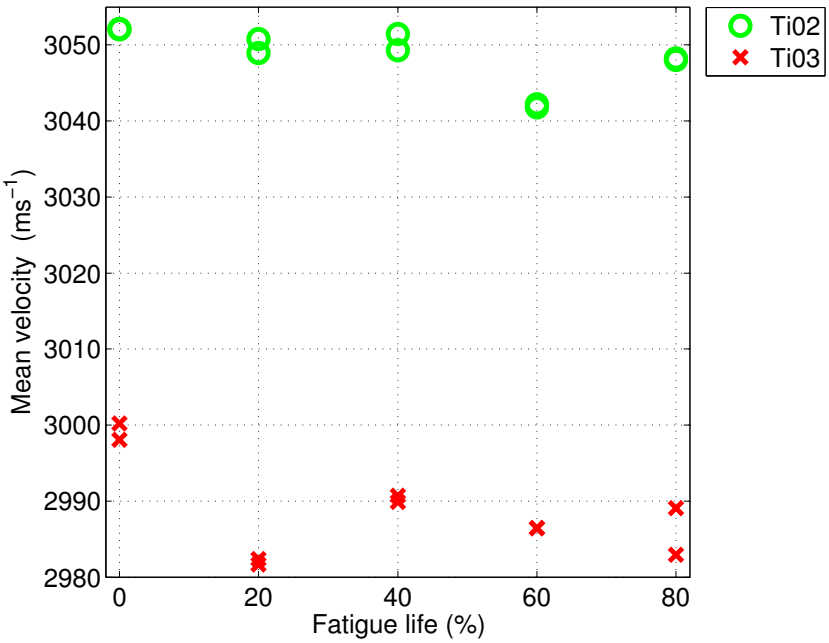

Figure 5.55: Graph of the mean linear velocity of each imaged area against fatigue life for all the titanium samples.

Localised changes in the acoustoelastic coefficient (A_R) with fatigue

In section 5.7.2 it is found that different regions in the imaged A_R of the aluminium samples change in different ways with an increase in fatigue life (on Aluminium 09 the A_R in a region is found to increase). The titanium samples did not show this variation and so are not investigated.

In this section, the variation in the imaged A_R of different regions with an increase in fatigue is investigated. The imaged A_R at 0% fatigue life for each aluminium sample is spatially low passed filtered to remove the effects of noise. This filtered image is divided into three sub-regions defined by the value of A_R in each region, for every sample. The lower bound region is defined as having an A_R less than one standard deviation below the mean value of A_R. The upper bound region is defined as having an A_R greater than one standard deviation above the mean value of A_R. The middle bound region includes those points with an A_R in between the other two regions. An example for sample Aluminium 09 is shown in figure 5.56.

These regions are fixed and the mean value of A_R of each is found at the various fatigue increments that the sample experiences. The mean value of A_R in each region is plotted against the fatigue life (see figure 5.57). A first order polynomial is fitted to the mean data for each region. The gradient of the fit relates to the rate of change in A_R of the region, with an increase in fatigue.

Figure 5.58 shows the gradients of the mean A_R against fatigue life for the upper and lower bound regions of each sample. The upper bound regions have a larger gradient than the lower bound regions. This shows that regions which start off with a smaller A_R increase more rapidly with fatigue than those areas that start with a larger A_R. For some of the samples (Aluminium 07, 10 and 11) the upper bound regions have a positive gradient indicating that A_R for these areas is

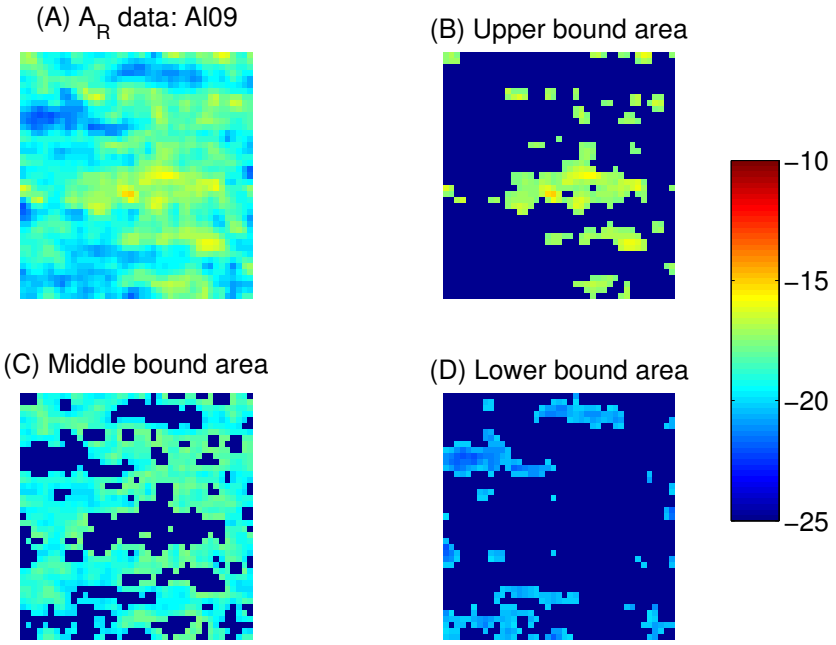

Figure 5.56: Images demonstrating how each of the A_R ($\times 10^{-6}$ MPa^{-1}) scan areas is divided into regions of similar A_R which are tracked throughout the fatigue life of the sample.

reducing.

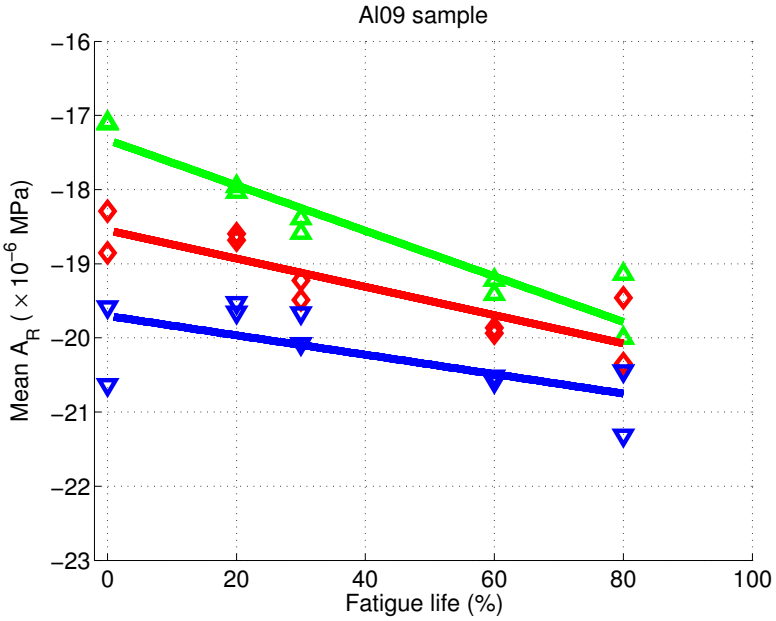

Figure 5.57: Plots of mean value of A_R ($\times 10^{-6}$ MPa^{-1}) for each region tracked through the fatigue life of the sample. The lower bound region values are represented by blue triangle with point down (▽), the mid region values are represented by red diamonds (◇) and the upper bound regions are represented by green triangles with point up (△).

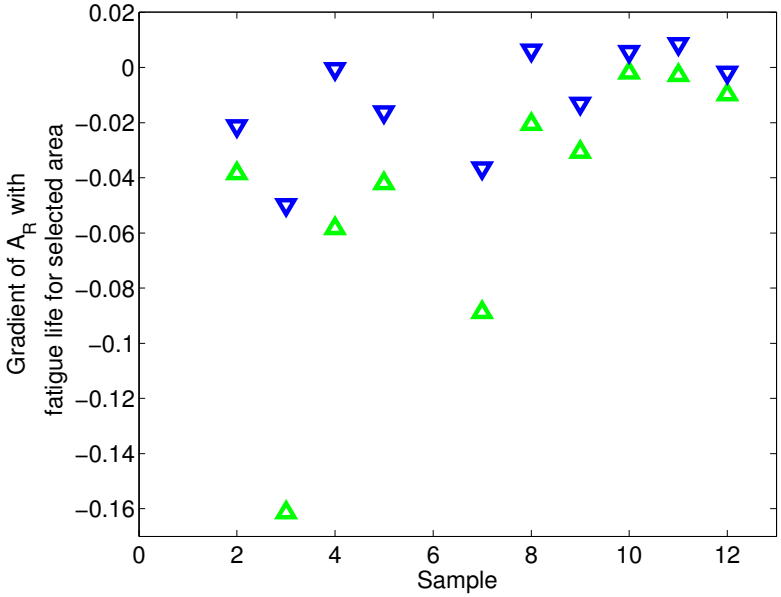

Figure 5.58: Graph of the value of the gradient of the lower (blue triangle point down, ▽) and upper bound (green triangle point up, △) regions mean A_R against fatigue life, for each sample. Note that the gradient of the lower bound is always smaller than that of the upper bound regions.

5.7.4 Discussion of observed changes in the acoustoelastic coefficient with fatigue

This section discusses the implications of the observed change in A_R with material structure and fatigue.

Variation in the mean acoustoelastic coefficient (A_R) at 0% fatigue life

Samples made from the same material show a variation in the mean value of A_R at 0% fatigue life. The mean A_R of samples at 0% fatigue life varies by 2.4×10^{-6} MPa^{-1} for aluminium and 1×10^{-6} MPa^{-1} for titanium.

As the samples are produced and handled in a similar way, the variation in A_R between them is unlikely to be caused by residual stress or fatigue. The microstructure is shown to have a large affect on A_R (see section 5.6). The variation in the mean value of A_R between samples at the 0% fatigue life can be attributed to the variation in microstructure between imaged areas.

In aluminium the observed change in A_R with an increase in fatigue is between 9-30% of the 0% fatigue life coefficients. The mean value of A_R for aluminium samples at 0% fatigue life varies by 14%. So the variation caused by the microstructure is of the same order as the variation due to fatigue. The implication of this is that in order to differentiate between the variation in A_R due to microsturcture and the variation caused by fatigue, A_R of the imaged area must be known prior to fatiguing.

Relatively small change in acoustoelastic coefficient (A_R) with fatigue

A change of between 9-30% is observed in the mean value of A_R with an increase in fatigue on the aluminium samples. A similar change of 27% is observed on the titanium samples. Other workers [2,3,5,6,10–23] have reported changes of 100% or

more in the nonlinear ultrasonic response of a sample over the course of its fatigue life. Below a few potential reasons for this difference are discussed.

The imaged A_R is found to vary by different amounts at different locations with an increase in fatigue. In some regions the value of A_R is found to increase. The mean value of A_R decrease with fatigue, an area with an increasing value of A_R goes against this trend and so reduces the decrease observed in the mean. Other measurement techniques collect data over larger regions and so may not be affected as much by these regions.

In this work, samples are not fatigued to the end of their fatigue life. So there is some uncertainty in the level of fatigue they have experienced. This uncertainty is 13% for titanium and 12% for aluminium over the fatigue life (see section 4.5.3). It is possible that the samples are scanned at fatigue levels below those assumed, resulting in a smaller change than expected in A_R. However, some samples did reach sufficient fatigue levels, even with the uncertainty, to ensure that changes in A_R should be larger than those observed.

Microstructure has been found to alter the A_R of a material by up to 400% (see section 5.6.1). The large changes in the nonlinear ultrasonic response observed by other authors could be, in part, due to errors in the re-registration, as opposed to an increase in fatigue. The scale and impact of the re-registration errors is dependent on the size of the microstructure and the variation of the nonlinear response with changes in the microstructure.

Monotonic fatigue relationship

For some samples (Aluminium 05, 10, 11) the relationship between an increase in the fatigue and the change in A_R is not monotonic. In these cases the mean value of A_R is seen to decrease initially with fatigue before increasing. It is assumed that

on these samples the mean value of A_R would continue to decrease with further fatigue. This complex relationship would make the prediction of the fatigue life using A_R difficult. Similar trends on different materials have been observed by other workers [66, 67]. It has been suggested by other workers [10, 66, 67] that the cause of this complex relationship is the formation of dislocation networks causing localised variation in the nonlinear response of the material. This would also explain regions where there is an increase in the value of A_R, such as the one observed on Aluminium 09.

Sensitivity of linear compared to nonlinear techniques

Other workers [1–3] have shown that nonlinear ultrasonic techniques are more sensitive to changes due to fatigue than linear techniques. As the change in A_R with fatigue is smaller than that reported by other workers it is important to discuss if the nonlinear technique developed in this work is more sensitive than a comparative linear technique.

A change of between 9-30% is observed in the mean value of A_R with an increase in fatigue on the aluminium samples. The linear mean velocity measurement varies by a maximum of 0.5% with an increase in fatigue. The change in A_R is on average 16 times greater than the largest change in the mean linear velocity. However the uncertainty in the linear velocity data is significantly lower than the uncertainty in A_R. Taken in isolation this suggests taking linear velocity measurements maybe preferential. The uncertainty in the linear velocity measurements is 0.017% (0.5ms^{-1}). The uncertainty in A_R is 0.3%. To select the optimum technique a figure of merit (Ω) is defined as:

$$\Omega = \frac{\Delta_{fatigue}}{\delta_{meas}}$$

where $\Delta_{fatigue}$ is the change in the measurement due to fatigue and δ_{meas} is the uncertainty in the measurement. The figure of merit for A_R is on average 53. The figure of merit for the largest change in the linear velocity is 29. In this case the acousotelastic technique is therefore more sensitive to changes, due to fatigue, than the linear velocity measurement, even with the associated increase in uncertainty. The change in A_R is also more predictable than the change in the mean velocity. The mean value of A_R generally decreases ($|A_R|$ shows a increase) with an increase in fatigue, whilst the mean velocity is seen to increase and decrease with an increase in fatigue.

5.8 Summary

In this chapter the results from a variety of measurements of A_R, investigating different features were reported. These results were presented in order of complexity to aid the narrative. The first results presented was a single point measurement of A_R on fused silica, a coefficient of 27.7±0.5 $\times 10^{-6}$ MPa^{-1} was found. Subsequently A_R from the two wave co-propagation technique developed in this work was compared to A_R from a static strain configuration on aluminium (see section 5.3). Using the static strain method an measurement of A_R of -17.6 ± 1.7 $\times 10^{-6}$ MPa^{-1} was observed. Using the two wave co-propagation technique an measurement of A_R of -16.70 ± 0.5 $\times 10^{-6}$ MPa^{-1} was observed. The similarity between the two techniques demonstrates a good level of confidence in the co-propagation technique (see section 5.4). The measurement of A_R of several different materials including fused silica, aluminium and titanium was made. Fused silica was found to have a coefficient of 27.7 ± 0.5 $\times 10^{-6}$ MPa^{-1}, aluminium has a coefficient of -16.7 ± 0.4 $\times 10^{-6}$ MPa^{-1} and titanium has a coefficient of -3.8 ± 0.2$\times 10^{-6}$ MPa^{-1}.

Experiments conducted on polycrystalline materials found variation in A_R of samples beyond that expected due to uncertainty in the measurement. This variation was found to be spatially repeatable. This led to the development of an area scanning technique that allows the measurement of the variation in A_R over the surface of a sample. The technique was described in section 4.4. Images of A_R were reported for the first time in the literature (see section 5.5). Variation in A_R was found to be independent of the variation in signal to noise ratio of the probe SAW and the induced stress field. Good repeatability was shown between imaged areas (see section 5.5.2) on the same location of a sample. A correlation coefficient between repeat images of 0.55 was found even when low stress levels are recorded, despite high levels of noise on one image. With high levels of stress a correlation coefficient of 0.87 was found.

The variation in the acoustoelastic parameter over the microstructure was investigated (see section 5.6). By using an aluminium sample with a microstructure of comparable size to the resolution of the measurement of A_R it was shown that there is a correlation between the underlying microstructure and A_R. If the triangular interaction region of the probe and pump SAWs is taken into account the correlation coefficient reaches -0.70. The relationship between A_R and the crystal orientation of the grains that make up the microstructure of a material was investigated. A change was observed in A_R from -24$\times10^{-6}$ MPa^{-1} to -34$\times10^{-6}$ MPa^{-1} over the area of a single grain with a change in propagation direction.

The imaging technique was used to monitor the variation in A_R of samples as they are fatigued (see section 5.7). Two types of materials were investigated, titanium Ti-6Al-4V and aluminium 2024-T351. Twelve aluminium and two titanium samples were investigated. Several aluminium samples were left at intermediate fatigue levels (20-80%) in order to be tested in future by complementary testing

techniques. Several analysis techniques were employed to the data generated so as to determine possible trends. The aluminium samples showed a general decrease in the value of the mean A_R with an increase in fatigue, in other words, an increase in the modulus of A_R with an increase in fatigue, because the A_R is negative for aluminium. This decrease is in the range of 9 to 30% at higher fatigue levels. The observed decrease is small compared to changes reported by other workers [2, 3, 5, 6, 10–23]. Some samples (aluminium 05, 10 and 11) developed a trend of initially decreasing the mean value of A_R with fatigue and then marginally increasing at the mid-life point. The standard deviation of A_R was found to increase with fatigue above a level of 60%. By monitoring specific regions based on the value of the 0% fatigue life A_R, it was found that regions starting with a smaller A_R increase more rapidly with fatigue than areas that start with a larger A_R. Comparative linear velocity measurements see a maximum fractional change of 0.5% with no set trend.

Titanium is a difficult material on which to take measurements of A_R. For one of the samples, the 0% fatigue life results are questionable. The general trend for both titanium samples indicates that the value of the mean A_R decreases with an increase in fatigue, in other words, an increase in the modulus of A_R with an increase in fatigue, because the A_R is negative for titanium. The fractional decrease in A_R over a 80% fatigue life is found to be 27%. The standard deviation of A_R for both titanium samples varies by little throughout the fatigue lives of the samples.

The confidence in the measured errors for the variables used in calculating A_R is high. The change observed in A_R with an increase in fatigue is larger than the derived error in A_R. This implies that the observed change in A_R due to fatigue is genuine. However this change is small compared to results presented by other workers [2, 3, 5, 6, 10–23] and so easily obscured.

Chapter 6

Further work

6.1 Introduction

In this work a technique for imaging the acoustoelastic coefficient (A_R) across a sample surface has been developed. This technique has been used to investigate material microstructure and the fatigue process. As part of this work a relationship between the acoustoelastic coefficient of a material and the underlying microstructure is observed. A change in the acoustoelastic coefficient of aluminium and titanium samples with fatigue is also observed. This chapter discusses areas where it would be interesting to carry out further work around these observed features and the potential developments for the technique.

6.2 Variation of acoustoelastic coefficient (A_R) with microstructure

A correlation between the variation in A_R of a material and the underlying microstructure has been observed. The relationship between A_R and crystal orienta-

tion needs to be quantified. There are several ways in which this can be achieved, for instance:

The plane of the grain that the acoustoelastic coefficient is found to vary with propagation direction on (see section 5.6.2) could be found. If the plane is known the acoustoelastic coefficient can be related to the orientation of the crystal. The plane of the grain can be found by fitting the variation in the linear velocity of a ultrasonic wave with propagation direction to modelled data [127]. This work is ongoing.

Alternatively the A_R of a known orientation single crystal sample could be measured. This work has been started and has generated anomalous results. To perform the acoustoelastic measurement using this instrument requires a sample with a minimum diameter of 25 mm. To ensure the propagation of Rayleigh waves at the pump wave frequency a minimum sample thickness is required. An aluminium single crystal sample with sufficient dimensions has been acquired (at great expense). Acoustoelastic measurements on this sample have produced results that are different from measurements on samples investigated in chapter 5 (see figure 6.1).

In figure 6.1 the modulation in the fractional velocity change is observed on a piece of aluminium of the same dimensions as the single crystal (red circle, ○). The fractional velocity change for the single crystal can also be seen (blue cross, +). The modulation of the fractional velocity change for the single crystal sample follows the packet of the pump wave rather than the pump wave displacement. The response remains constant with variation in orientation of the single crystal. The cause of this modulation is not know and deserves further investigation beyond the scope of this work. The confidence in the sample being a solid single crystal is low.

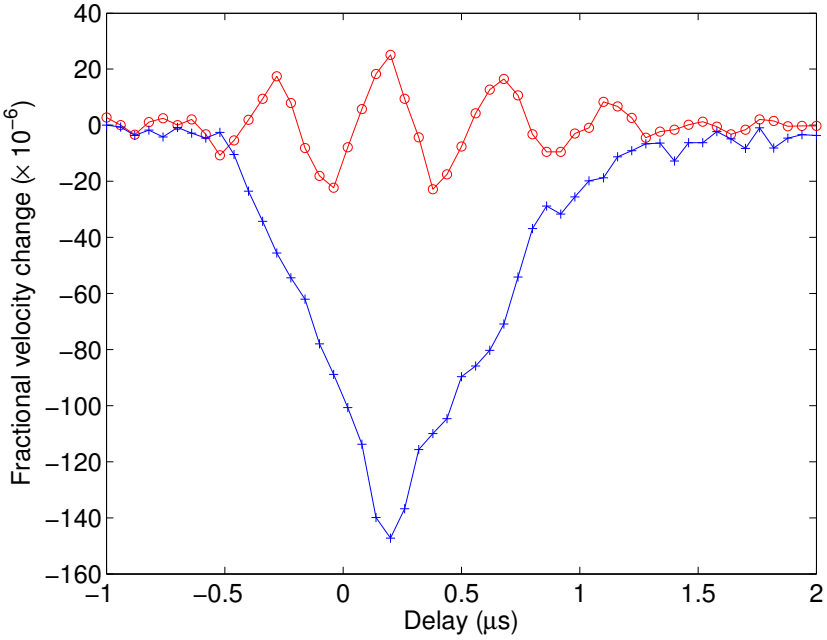

Figure 6.1: Plot of the fractional velocity shift modulation for the single crystal aluminium sample (blue crossed line, −+) and the standard heterogeneous aluminium sample (red circled line, −○)

6.3 Non-monotonic variation in acoustoelastic coefficient (A_R) with fatigue

In the majority of the literature [2, 3, 5, 6, 10–23, 128] a monotonic relationship between the nonlinear ultrasonic response and the level of fatigue a sample has experienced is reported. A more complicated non-monotonic relationship between the nonlinear ultrasonic response and increase in fatigue of the sample has been reported in other parts of the literature [66, 67].

The results from this work show both monotonic and non-monotonic changes in A_R with an increase in fatigue. The confidence in the measured changes in A_R with fatigue is high (see section 5.7.3). The microstructure on each sample investigated is different. It has been shown that the A_R of a material is correlated to the underlying microstructure. It is also found that the A_R of different locations

change by different amounts with fatigue. This affects the change in the mean value of A_R with fatigue.

An explanation for the variability in the change of A_R with fatigue is the variation of the fatiguing process within the material at the microstructural level. Localised effects of the microstructure on the fatigue process deserves further study, for instance: localised changes in in A_R with fatigue could be investigated using transmission electron microscopy (TEM). Using TEM, an image of the local dislocations can be produced, and these dislocations can then be related to the change in A_R observed. This process would require the destruction of the samples.

6.4 Redesign of fatigue samples to optimise complementary testing

X-ray diffraction was planned to be used as a complementary technique to monitor the residual stress associated with fatigue on samples scanned using the A_R method developed in this work. The microstructure of the aluminium samples was of sufficiently small scale to randomly affect the diffraction pattern of the X-rays and so the measurement of the residual stress caused by the fatigue process could not be determined. Further investigations could include a new series of samples that have been fatigued and have a microstructure which is large. The larger microstructure would allow the X-ray diffraction technique to monitor the residual stress in the sample. This could be compared with A_R.

6.5 Development of new techniques to monitor the acoustoelastic coefficient

The uncertainty in the acoustoelastic coefficient measured using the technique developed in this thesis is small (see section 4.3.3). Improving the certainty and so the quality of the measurement would be costly and difficult. A better approach may be to develop different techniques to monitor changes in the higher-order elastic constants.

For instance using larger stress fields would produce greater velocity changes, which could be detected using other processing technique such as SRAS. Using larger stresses would also reduce the effect of the variation in temperature of the velocity.

The third-order elastic constants are temperature dependent [129]. By inducing a temperature change and monitoring a propagating ultrasonic wave, further insight in to the third-order elastic constants maybe gained. This may give more information about the process effecting the higher order elastic constants.

The linear ultrasonic techniques used in this work are proportionally less sensitive to changes in fatigue than the nonlinear technique developed. However linear measurements can be obtained with a higher level of accuracy than nonlinear measurements. Further study could investigate if linear techniques can be improved in terms of accuracy, to reliably monitor the comparatively small change in linear properties due to fatigue.

6.6 Application of developed technique to alternate problems

In this work it has been observed that A_R is sensitive to the effects of fatigue damage. Other mechanisms have been explored using similar nonlinear techniques. A relationship between creep damage and the nonlinear ultrasonic response has been found [130–132]. Residual stresses have also been monitored using nonlinear ultrasonic techniques by other workers [133]. The investigation of other mechanical processes such as residual stress and creep, using the technique developed in this work, could potentially provide a wider application for this technique.

Chapter 7

Conclusion

The aims of the work described in this thesis were:

- Develop an instrument and procedure for the monitoring of the nonlinear ultrasonic response of a material.
- Develop a technique to image the nonlinear ultrasonic response over the surface of a material.
- Investigate the effects of microstructure and fatigue on the nonlinear ultrasonic response of aerospace materials.

In chapter 2 the importance of being able to monitor the fatigue process in materials is described. Other material features, such as microstructure, affect the formation of fatigue and so are also discussed. Nonlinear ultrasonic techniques have been found by other workers to be sensitive to the formation of fatigue. This thesis has presented the development of instrumentation and a procedure capable of making highly accurate nonlinear acoustoelastic measurements. This technique has been used to acquire images of the acoustoelastic coefficient for Rayleigh waves (A_R) across a sample surface. These are the first images of the acoustoelastic

coefficient (A_R) ever taken using this technique. This imaging technique was used to investigate the effects of microstructure and fatigue on A_R. The next sections summarises the content and discusses the impact of the work carried out in the chapters that outline the instrument, procedure and experimental results produced for the measurement of A_R.

7.1 Instrumentation

In chapter 3 the instrumentation that makes up the system was described in detail. The system used laser ultrasound techniques to generate the probe SAW (see section 3.3.2) and to detect both the pump and probe SAWs (see section 3.4). The pump SAW was generated using a piezoelectric transducer. A combination of a temperature control chamber and a differential acquisition technique improved the measurement of a change in ultrasonic velocity (see section 3.7). This system allows highly accurate and high resolution acoustoelastic measurements to be made.

7.2 Methods

In chapter 4 the measurement method and uncertainty in the measurements are discussed. The procedure to measure A_R is discussed in section 4.2. A relationship between the uncertainty in the variables used to find the fractional velocity change and the single shot signal to noise ratio of the probe SAW is demonstrated (see section 4.3.2). The uncertainty in each of the variables that contribute to the measurement of A_R is assessed (see section 4.3.3), the major sources of uncertainty come from the measurement of the displacement (70.9% of the uncertainty in the stress) and Δt (99.9% of the uncertainty in the fractional velocity change). Work

conducted in section 4.3.2 allows a high level of confidence in the uncertainty in the measurement of A_R, this is vital for assessing changes observed in A_R in chapter 5.

A procedure was developed to allow the imaging of A_R over the sample surface (see section 4.4). This was achieved by speeding up the procedure to measure A_R. The design of an experiment to investigate the effect of fatigue on the imaged A_R was presented in section 4.5. A strain controlled four-point bending jig was used to induce low cycle fatigue in the samples. A 4×4mm^2 area located at the centre of each sample was scanned at different levels of fatigue. Two types of materials were investigated, titanium Ti-6Al-4V and aluminium 2024-T351. Twelve aluminium and two titanium samples were investigated.

7.3 Experimental results

In chapter 5 experimental results were presented in the order of complexity of each measurement. The first result presented (see section 5.2) was a single point acoustoelastic measurement on fused silica giving a response of 27.5 ± 0.5×10^{-6} MPa^{-1}. The A_R from the two wave co-propagation technique was compared to A_R from a static strain technique on aluminium (see section 5.3). Using the static strain method an acoustoelastic measaurement of -17.6 ± 1.7 ×10^{-6} MPa^{-1} was observed. Using the two wave co-propagation technique on a different aluminium sample (due to size constraints) an acoustoelastic measurement of -16.7 ± 0.5 ×10^{-6} MPa^{-1} was observed. The similarity between the two techniques demonstrates a good level of accuracy of the two wave co-propagation acoustoelastic technique. The A_R of several different materials including fused silica, aluminium and titanium were measured (see section 5.4). Fused silica was found to have

a response of 27.7±0.5 $\times 10^6$ MPa^{-1}, aluminium was found to have a response of -16.7± 0.4 $\times 10^6$ MPa^{-1} and titanium was found to have a response of -3.8± 0.2$\times 10^{-6}$ MPa^{-1}. This demonstrates the A_R of different materials is different and that the procedure and instrument developed in this work is sensitive to this.

In chapter 5 the imaging technique was used to investigate the spatial variation of the acoustoleastic response. The images of A_R were found to be highly repeatable (see figure 5.7). Using an aluminium sample with a microstructure of comparable size to the resolution of the acoustoelastic measurement it was shown that there is a correlation between the underlying microstructure and the imaged A_R. If the triangular interaction region of the pump and probe SAW was taken into account the Pearsons product-moment correlation coefficient reaches -0.70 (1 or -1 being a perfect correlation, see figure 5.18). The relationship between A_R and the crystal orientation of the grains that make up the microstructure of a material was also investigated. A change was observed in A_R from -24$\times 10^{-6}$ MPa^{-1} to -34$\times 10^{-6}$ MPa^{-1} over the area of a single grain, due purely to a change in propagation direction (see figure 5.22). The relationship between microstructure and A_R appears genuine. Further work is required to quantify this relationship.

The results from the fatigue experiments were presented at the end of chapter 5 (see section 5.7). The aluminium samples showed a general decrease in the mean value of A_R with an increase in fatigue, in other words, an increase in the modulus of A_R with an increase in fatigue, because the A_R is negative for aluminium. Uncertainty in A_R was found to be in the region of 0.2-2.5$\times 10^{-6}$ MPa^{-1} dependent on the signal to noise ratio of the probe SAW and the stress induced by the pump SAW. At higher fatigue levels the decrease in the mean value of A_R was in the range of 9 - 30% (see figure 5.48). The observed decrease was small compared to changes reported in the literature [2, 3, 5, 6, 10–23]. The standard deviation of A_R

was found to increase with fatigue life above a level of 60% (see figure 5.51). By monitoring specific regions based on the value of A_R at 0% fatigue life it was found that regions starting with a smaller A_R increase more rapidly with fatigue than areas that start with a larger A_R. Comparative linear velocity measurements saw a maximum change of 0.5% with no set trend (see figure 5.54).

The general trend for both of the titanium samples indicates that the mean value of A_R decreases with an increase in fatigue, in other words, an increase in the modulus of A_R with an increase in fatigue, because the A_R is negative for titanium. The fractional decrease in A_R over an 80% fatigue life was found to be 27% (see figure 5.50). The standard deviation of A_R for both titanium samples varies little throughout the fatigue life of the samples (see figure 5.53). Comparative linear velocity measurements on titanium saw a maximum change of 0.6% with no set trend (see figure 5.55).

In chapter 5 (see section 5.7.4) the implications of the results found in this work with respect to fatigue were discussed. The implication of the correlation between A_R and the microstructure is that all repeat measurements of A_R must be re-registered to a level of accuracy of the same order as the size of microstructure, which was accomplished here by using the SRAS technique. The variation in the acoustelastic response at 0% fatigue life means that when investigating the fatigue process using A_R, A_R must be known prior to fatiguing. Different regions in the imaged A_R were found to change by different amounts with an increase in fatigue. The variation between these regions was attributed to microstructural differences. This variation contributes to a non-monotonic relationship between fatigue and A_R. Further work needs to be completed to investigate the complex relationship between fatigue and A_R, before this technique can be used to monitor the fatigue process.

A summary of the achievements of this work includes:

- Development of a new system capable of making highly accurate acoustoelastic measurements (chapter 3).
- Rigorous analysis of the uncertainties and errors in the measurement of the acoustoelastic coefficient (section 4.3).
- Good comparison between the two wave co-propagation and the static strain acoustoelastic measurement (figure 5.3).
- Measurement of the acoustoelastic coefficient of three different materials (figure 5.4).
- The development of the procedure to increase the measurement speed by a factor of 60 to allow imaging of the acoustoelastic coefficient (section 4.4).
- Production of a repeatable acoustoelastic image with a spatial resolution of 1 by 3 mm (figure 5.9).
- Demonstration of the correlation between the acousotelastic response of a material and the microstructure (figure 5.18).
- Investigation of the relationship between the acoustoelastic coefficient of two aerospace materials (aluminium and titanium) and the fatigue process (section 5.7).

The work conducted in this thesis has led to the development of an instrument and procedure that is capable of imaging the acoustoelastic coefficient across a sample surface. This imaging technique has been used to investigate the effect of microstructure and fatigue on the acoustoelastic coefficient.

Appendix A

Calibration of knife-edge detector

The initial SAW wave can be described by the following equation moving in the x-direction (into the depth of the material in the z-direction)

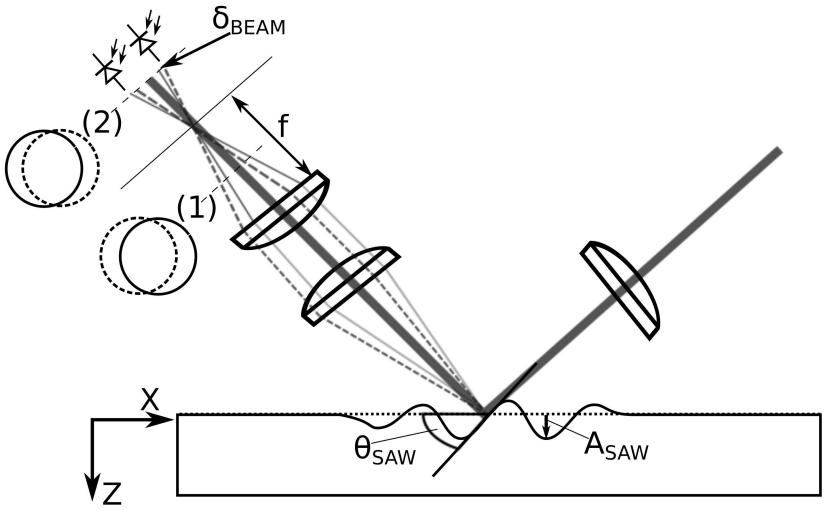

Figure A.1: Diagram demonstrating the knife-edge detection scheme. As a SAW propagates under the imaged spot of the detector it causes a displacement (δ_{BEAM}) in the lateral position of the spot. Photo-diodes can be placed at either position (1) or (2), though there is 180° phase change.

$$z = A_{SAW} \sin kx - \omega t$$

The gradient of the propagating saw wave gives us

$$\frac{dz}{dx} = kA_{SAW}\cos kx - \omega t$$

The angle of the slope of the surface can be written as

$$\theta_{SAW} = \tan^{-1}\left(kA_{SAW}\cos kx - \omega t\right)$$

From geometric optics the relationship between the surface angle and the change in the reflected angle of the beam is

$$\theta_{BEAM} = 2\theta_{SAW} = 2\tan^{-1}\left(kA_{SAW}\cos kx - \omega t\right)$$

The angular deviation corresponds to a lateral displacement δ_{BEAM} after the collection lens that is related to the focal length F by the relationship

$$\delta_{BEAM} = F\tan\theta_{BEAM} = F\tan\left(2\tan^{-1}\left(kA_{SAW}\cos kx - \omega t\right)\right)$$

As θ_{SAW} is small the small angle approximation can be used, so

$$\delta_{BEAM} = 2F\left(kA_{SAW}\cos kx - \omega t\right)$$

The largest displacement of this beam then is

$$\delta_{BEAM} = 2FkA_{SAW}$$

The change in current from a photo diode is related to the quantum efficiency

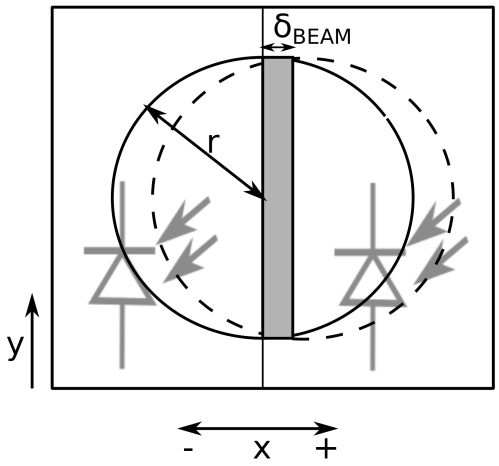

Figure A.2: Diagram of shift in reflected light falling on photo-diodes, the shaded area represents the change in area illuminated on photo-diode.

Q_ϵ by the equation

$$\delta_i = Q_\epsilon \int \int_{-r}^{r} E_{(x,y)} dy dx$$

where $E_{(x,y)}$ is the illumination of the photo-diode. This equation can be simplified as δx is relatively small compared to δy and so the change in area can be though of as a rectangle with size δx by δy. Where $\delta x = \delta_{BEAM}$.

$$\delta_i = Q_\epsilon E_{line} 2k A_{SAW} F$$
$$E_{line} = \int_{-r}^{r} E_y dy$$
$$E_y = \frac{P}{\pi r^2}$$
$$\delta_i = \frac{4 Q_\epsilon P k A_{SAW} F}{\pi r}$$

where $NA = r/F$ and $k = \frac{2\pi}{\lambda_{SAW}}$

$$\delta_i = \frac{8 P Q_\epsilon A_{SAW}}{\lambda_{SAW} NA}$$

The ac output from the knife-edge electronics is proportional to the induced current calculated above. As this current propagates through the electronics of the knife-edge a potential difference V_{ac} occurs that is proportional to the impedance of the circuit which is related to the impedance of the primary coil Z_P. In the primary winding the change in current is double (due to the two arms), hence the V_P is twice V_{ac}. The induced voltage in the secondary winding is half that of that in the primary due to the difference in number of windings.

$$V_S = \delta_i Z_P$$

The optical power falling on the photo-diodes (P) is related to the V_{DC} output from the knife edge. Where:

$$V_{DC} = G_{+amp}(I_{DC} Z_{DC}) = G_{+amp}(Q_\epsilon Z_{DC} P)$$

in this case G_{+amp} is the gain of the summing amplifier and Z_{DC} is the impedance of the knife-edge detector. The final output of the knife-edge and the amplification chain after to the scope is:

$$V_{scope} = V_S G_{MAV} G_{AMP} = \delta_i Z_P G_{MAV} G_{AMP}$$

Where G_{MAV} is the gain of the monolithic MAV-11 amplifier and G_{AMP} is the gain of the amplifier chain and filters. The output of the voltage to the scope is related to the amplitude of the saw by:

$$V_{scope} = \frac{G_{MAV} G_{AMP} 8 A_{SAW} V_{DC} Z_P}{\lambda_{SAW} N A Z_{DC} G_{+amp}}$$

Rearranging this gives:

$$A_{SAW} = \frac{\lambda_{SAW} N A Z_{DC} G_{+amp}}{8 G_{MAV} G_{AMP} Z_P} \frac{V_{scope}}{V_{DC}}$$

$$A_{SAW} = C_{cal} \frac{V_{scope}}{V_{DC}}$$

Appendix B

Stress calculation from displacement due to SAW

The stress can be calculated from the out of plane displacement following the description in Viktorov's book *Rayleigh and Lamb Waves* [119]. The particle displacement in the z-direction (out of plane, see figure B.1) is described by:

$$U_z = \frac{\partial \varphi}{\partial z} + \frac{\partial \psi}{\partial x}$$

where φ is the scalar potential of displacements and ψ is the vector potential of displacement. Suggested solutions are:

$$\varphi = -A \exp^{i(kx-\omega t)-qz} \tag{B.1a}$$

$$\psi = iA\frac{2kq}{k^2+s^2} \exp^{i(kx-\omega t)-sz} \tag{B.1b}$$

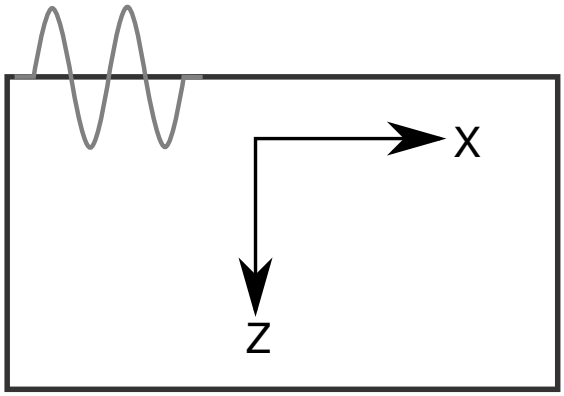

Figure B.1: Diagram of conventions of labelling for sample with a surface wave propagating through it where the half space of the medium is effectively infinite in thickness

where

$$q^2 = k^2 + k_l^2, \qquad s^2 = k^2 + k_s^2$$
$$k_l = \omega\sqrt{\frac{\rho}{\lambda + 2\mu}}, \qquad k_s = \omega\sqrt{\frac{\rho}{\mu}}$$
$$\lambda = \frac{G(E - 2G)}{(3G - E)}$$

and k is the wave number, k_l is the longitudinal wave number, k_s is the shear wave number, μ & λ are the làme constants, ρ is the density, G (μ) is the shear modulus and E is the Young's modulus. From these solutions

$$\frac{\partial\varphi}{\partial z} = Aq\exp^{i(kx-\omega t)-qz}$$
$$\frac{\partial\psi}{\partial x} = -kA\frac{2kq}{k^2+s^2}\exp^{i(kx-\omega t)-sz}$$
$$U_z = Aq\left(\exp^{-qz} - \frac{2k^2}{k^2+s^2}\exp^{-sz}\right)\cos kx - \omega t$$

For the measured displacement (z=0)

$$U_0 = Aq\left(1 - \frac{2k^2}{k^2+s^2}\right) \tag{B.2}$$

$$A = \frac{U_0}{q\left(1 - \frac{2k^2}{k^2+s^2}\right)} \tag{B.3}$$

The stress in a propagating Rayleigh wave can be described by three principal components:

$$\sigma_{xx} = \lambda\left(\frac{\partial^2\varphi}{\partial x^2} + \frac{\partial^2\varphi}{\partial z^2}\right) + 2\mu\left(\frac{\partial^2\varphi}{\partial x^2} - \frac{\partial^2\psi}{\partial x\partial z}\right) \tag{B.4a}$$

$$\sigma_{zz} = \lambda\left(\frac{\partial^2\varphi}{\partial x^2} + \frac{\partial^2\varphi}{\partial z^2}\right) + 2\mu\left(\frac{\partial^2\varphi}{\partial z^2} + \frac{\partial^2\psi}{\partial x\partial z}\right) \tag{B.4b}$$

$$\sigma_{xz} = \mu\left(2\frac{\partial^2\varphi}{\partial x\partial z} + \frac{\partial^2\psi}{\partial x^2} - \frac{\partial^2\psi}{\partial z^2}\right) \tag{B.4c}$$

The solution for σ_{xx} takes the form:

$$\sigma_{xx} = A\lambda\left(k^2 - q^2\right)\exp^{-qz} + 2\mu Ak^2\left(\exp^{-qz} - \left(\frac{2sq}{k^2+s^2}\right)exp^{-sz}\right)\cos kx - \omega t$$

Using the assumption z=0 (at the surface) and taking the instantaneous displacement, the solution takes the form

$$\sigma_{xx|z=0} = A\left(\lambda\left(k^2 - q^2\right) + 2\mu k^2\left(1 - \frac{2sq}{k^2+s^2}\right)\right)$$

Re-describing A in terms of displacement from equation B.3:

$$\sigma_{xx|z=0} = U_0\left[\frac{\lambda\left(k^2 - q^2\right) + 2\mu k^2\left(1 - \frac{2sq}{k^2+s^2}\right)}{q\left(1 - \frac{2k}{k^2+s^2}\right)}\right] \tag{B.5}$$

Equation (B.5) provides a link between the displacement (U_0) and the stress experienced by the probe wave ($\sigma_{xx|z=0}$).

Appendix C

Calculation of uncertainty in stress

The partial differentials of $\sigma_{xx|z=0}$ are:

$$\frac{\partial \sigma_{xx|z=0}}{\partial A} = \left(\lambda\left(k^2 - q^2\right) + 2\mu k^2\left(1 - \frac{2sq}{k^2+s^2}\right)\right), \qquad \frac{\partial \sigma_{xx|z=0}}{\partial \lambda} = A\left(k^2 - q^2\right)$$

$$\frac{\partial \sigma_{xx|z=0}}{\partial k} = 2kA\left(\lambda + 2G\left(1 - \frac{2qs^3}{\left(k^2+s^2\right)^2}\right)\right), \qquad \frac{\partial \sigma_{xx|z=0}}{\partial q} = -2A\left(\lambda q - \frac{2Gsk^2}{k^2+s^2}\right)$$

$$\frac{\partial \sigma_{xx|z=0}}{\partial G} = 2Ak^2\left(1 - \frac{2qs}{k^2+s^2}\right), \qquad \frac{\partial \sigma_{xx|z=0}}{\partial s} = 4GqAk^2\left(\frac{k^2-s^2}{k^2+s^2}\right)$$

The uncertainty in each of the factors are:

$$\delta_A = \sqrt{\left(\delta U_0 \frac{\partial A}{\partial U_0}\right)^2 + \left(\delta q \frac{\partial A}{\partial q}\right)^2 + \left(\delta s \frac{\partial A}{\partial s}\right)^2 + \left(\delta k \frac{\partial A}{\partial k}\right)^2}$$

$$\delta_s = \sqrt{\left(\delta k \frac{\partial s}{\partial k}\right)^2 + \left(\delta k_t \frac{\partial s}{\partial k_t}\right)^2}$$

$$\delta_q = \sqrt{\left(\delta k \frac{\partial q}{\partial k}\right)^2 + \left(\delta k_l \frac{\partial q}{\partial k_l}\right)^2}$$

Calculating the uncertainty in λ is complexed as it is related to the Young's and

shear modulus (E,G) which are dependent. This dependence is accounted for when calculating the uncertainty in λ by the use of a covariance term (cov_{eg}), in this case equal to the Poisson's ratio:

$$\delta\lambda = \sqrt{\left(\delta E \frac{\partial\lambda}{\partial E}\right)^2 + \left(\delta G \frac{\partial\lambda}{\partial G}\right)^2 + 2\frac{\partial\lambda}{\partial E}\frac{\partial\lambda}{\partial G} cov_{EG}}$$

The partial derivatives for A are:

$$\frac{\partial A}{\partial U_0} = \frac{1}{q\left(1 - \frac{2k^2}{k^2+s^2}\right)}, \qquad \frac{\partial A}{\partial q} = \frac{-U_0}{q^2\left(1 - \frac{2k^2}{k^2+s^2}\right)}$$
$$\frac{\partial A}{\partial k} = \frac{U_0\left(\frac{4qks^2}{(k^2+s^2)^2}\right)}{q^2\left(1 - \frac{2k^2}{k^2+s^2}\right)^2}, \qquad \frac{\partial A}{\partial s} = \frac{U_0\left(\frac{4qsk^2}{(k^2+s^2)^2}\right)}{q^2\left(1 - \frac{2k^2}{k^2+s^2}\right)^2}$$

The partial derivatives for s and q are:

$$\frac{\partial s}{\partial k} = \frac{k}{s}, \qquad \frac{\partial q}{\partial k} = \frac{k}{q}$$
$$\frac{\partial s}{\partial k_s} = \frac{-k_s}{s}, \qquad \frac{\partial q}{\partial k_l} = \frac{-k_l}{q}$$

The partial derivatives for λ are:

$$\frac{\partial\lambda}{\partial E} = \frac{G^2}{(3G - E)^2}, \quad \frac{\partial\lambda}{\partial G} = \frac{(-6G + 4EG - E^2)}{(3G - E)^2}$$

Finally the uncertainty in the wave numbers are given by:

$$\delta_k = \sqrt{\left(-\frac{\delta vel \times \omega}{vel^2}\right)^2 + \left(\frac{\delta\omega}{vel}\right)^2}$$

$$\delta_{k_s} = \sqrt{\left(\delta\omega\frac{\partial k_s}{\partial\omega}\right)^2 + \left(\delta\rho\frac{\partial k_s}{\partial\rho}\right)^2 + \left(\delta G\frac{\partial k_s}{\partial G}\right)^2}$$

$$\delta_{k_l} = \sqrt{\left(\delta\omega\frac{\partial k_l}{\partial\omega}\right)^2 + \left(\delta\rho\frac{\partial k_l}{\partial\rho}\right)^2 + \left(\delta\lambda\frac{\partial k_l}{\partial\lambda}\right)^2 + \left(\delta G\frac{\partial k_l}{\partial G}\right)^2}$$

with the partial differentials for the wave numbers k_s and k_l being:

$$\frac{\partial k_s}{\partial\omega} = \sqrt{\frac{\rho}{G}}, \qquad \frac{\partial k_s}{\partial\rho} = \frac{\omega}{2G}\sqrt{\frac{G}{\rho}}, \qquad \frac{\partial k_s}{\partial G} = \frac{-\rho\omega}{2G^2}\sqrt{\frac{G}{\rho}}$$

$$\frac{\partial k_l}{\partial\omega} = \sqrt{\frac{\rho}{\lambda+2G}}, \qquad \frac{\partial k_l}{\partial\rho} = \frac{\omega}{2\left(\lambda+2G\right)}\sqrt{\frac{\lambda+2G}{\rho}}$$

$$\frac{\partial k_l}{\partial\lambda} = \frac{\omega\rho}{2\left(\lambda+2G\right)^2}\sqrt{\frac{\lambda+2G}{\rho}}, \frac{\partial k_l}{\partial G} = \frac{-\rho\omega}{\left(\lambda+2G\right)^2}\sqrt{\frac{\lambda+2G}{\rho}}$$

By substituting the appropriate uncertainties that were either measured or assumed as outlined above the uncertainty in the stress field can be determined.

Appendix D

Further fatigue sample results

D.1 Aluminium 01

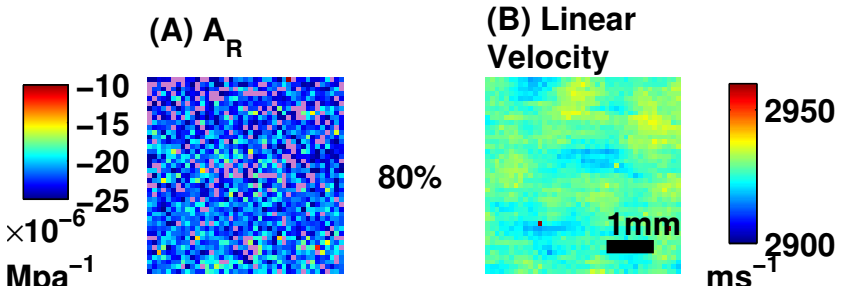

Figure D.1: Graph of aluminium 01 sample (A) squares acoustoelastic nonlinear response against fatigue. (B) squares velocity (SRAS) indicating the microstructure involved in the square.

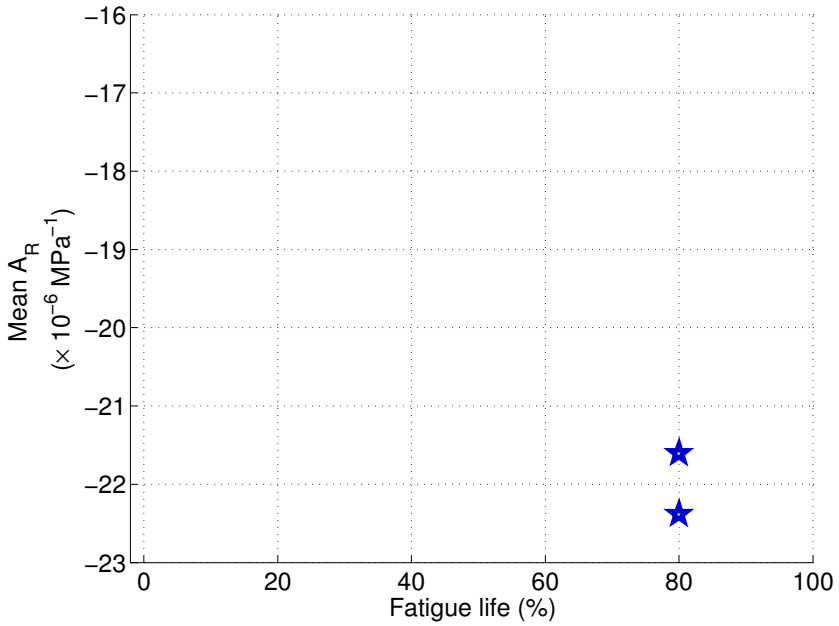

Figure D.2: Graph of aluminium 01 samples mean acousoelastic response against fatigue life.

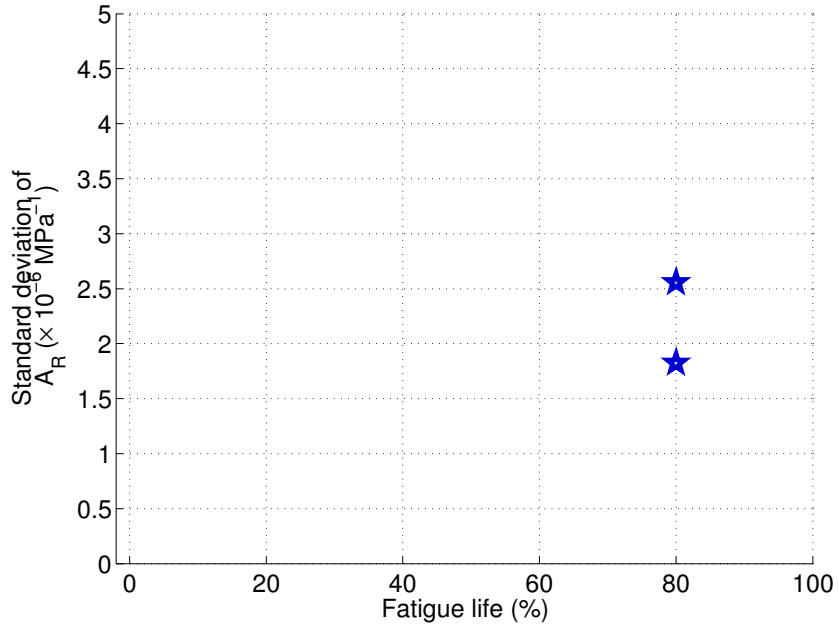

Figure D.3: Graph of aluminium 01 samples standard deviation of acousoelastic response against fatigue life.

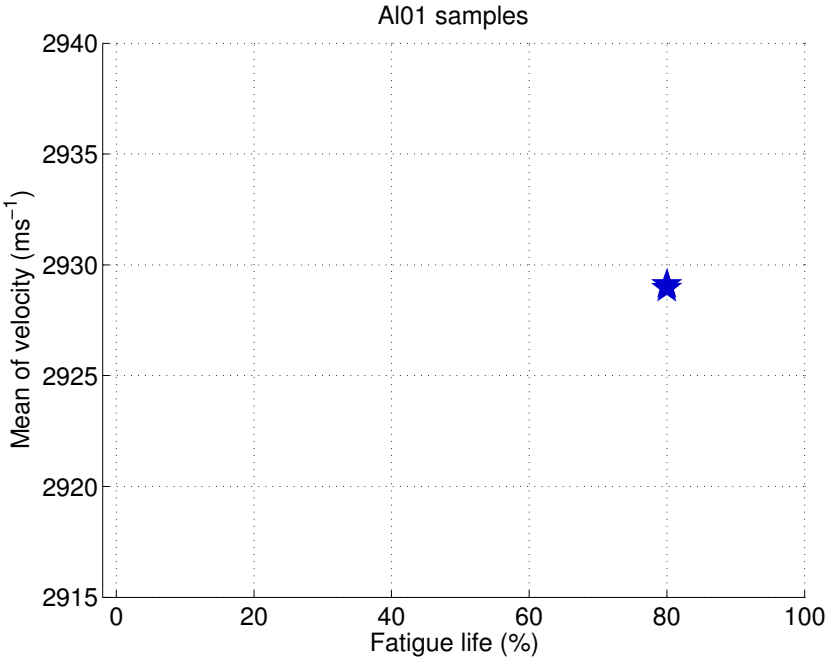

Figure D.4: Graph of the mean of the linear velocity of aluminium 01 sample against fatigue life.

D.2 Aluminium 02

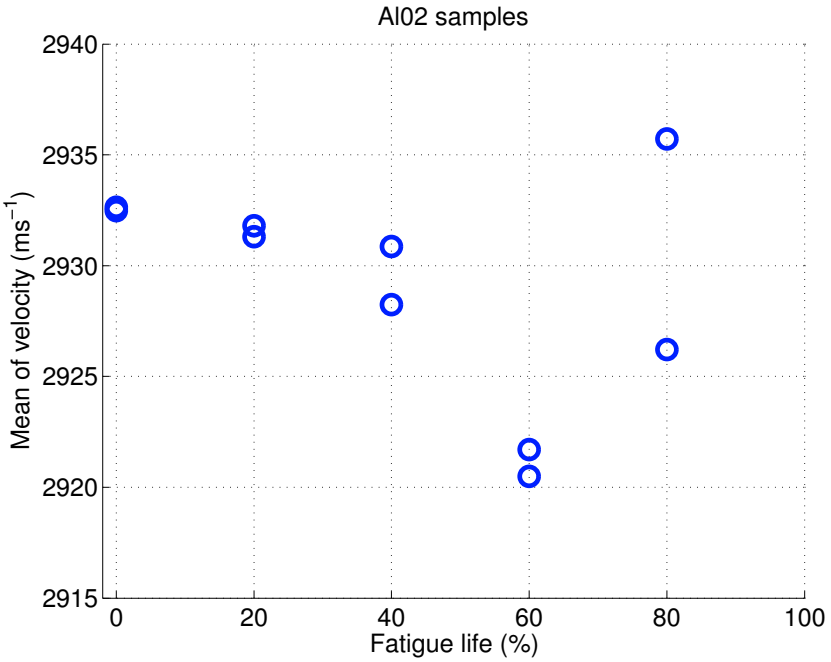

Figure D.5: Graph of the mean of the linear velocity of aluminium 02 sample against fatigue life.

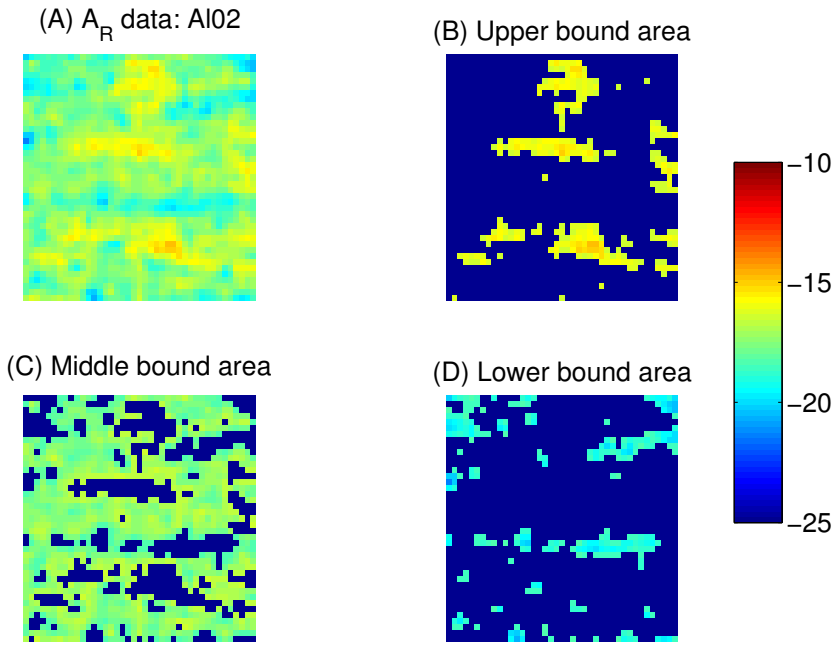

Figure D.6: Images of Aluminium 02's acoustoelasic response ($\times 10^{-6}$ MPa^{-1}) scan area being divided into segments of similar acoustelastic response, these are tracked throughout the fatigue life of the sample.

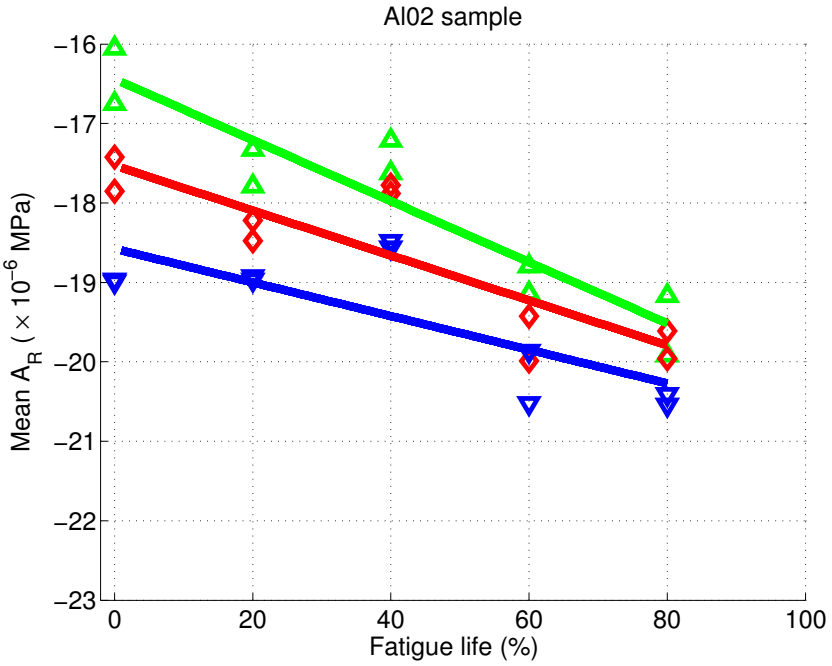

Figure D.7: Plots of mean value of the acoustoelastic response ($\times 10^{-6}$ MPa^{-1}) for sample aluminium 02 for each segment that is tracked through the samples fatigue life. The upper segment values are represented by $\bigtriangledown$, the mid segment values are represented by $\diamond$ and finally the lower bound segments are represented by $\bigtriangleup$. Each segment has a trend line (using a 1st order polynomial) fitted in the appropriate colour.

D.3 Aluminium 03

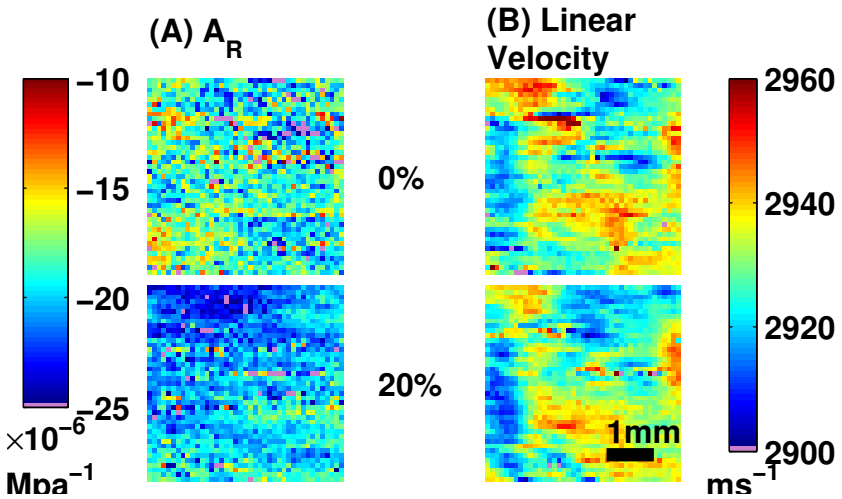

Figure D.8: Graph of aluminium 03 sample (A) squares acoustoelastic nonlinear response against fatigue. (B) squares velocity (SRAS) indicating the microstructure involved in the square.

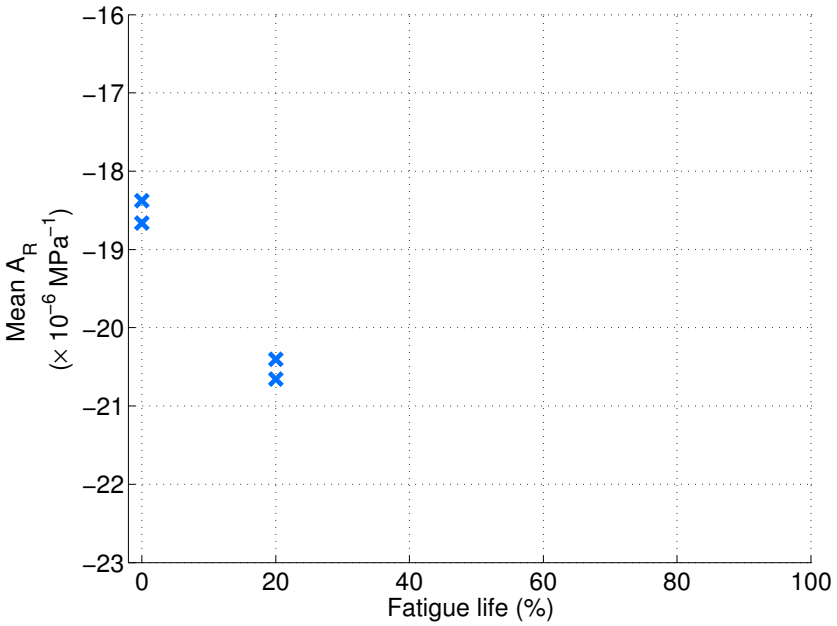

Figure D.9: Graph of aluminium 03 samples mean acousoelastic response against fatigue life.

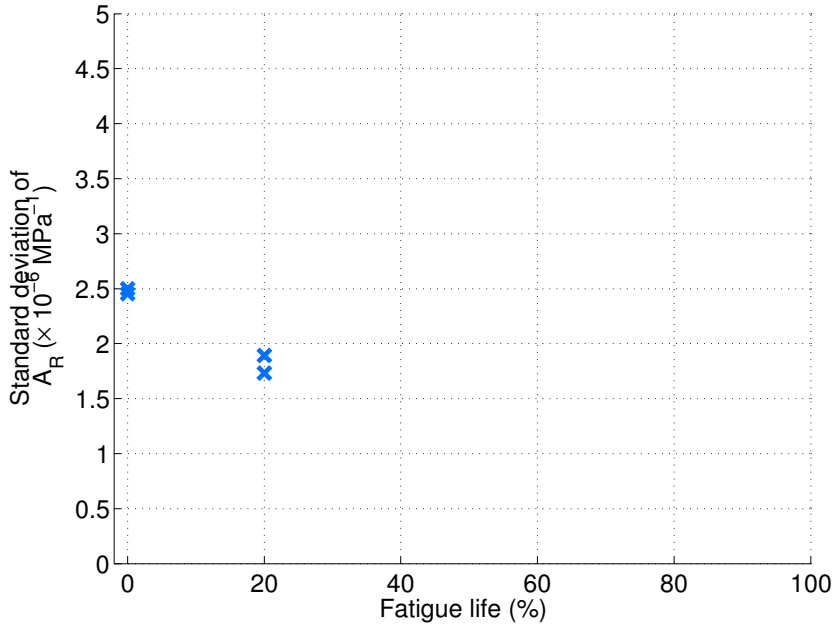

Figure D.10: Graph of aluminium 03 samples standard deviation of acousoelastic response against fatigue life.

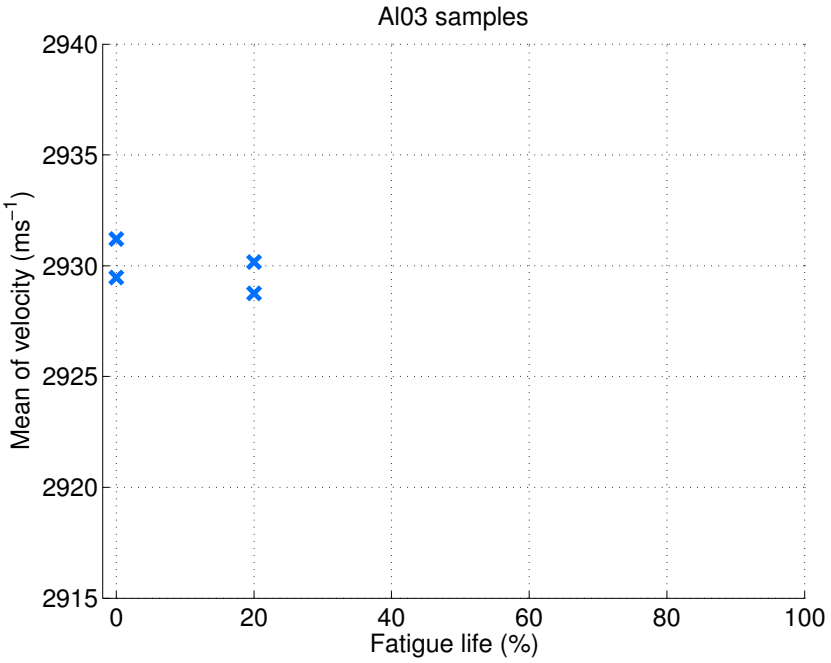

Figure D.11: Graph of the mean of the linear velocity of aluminium 03 sample against fatigue life.

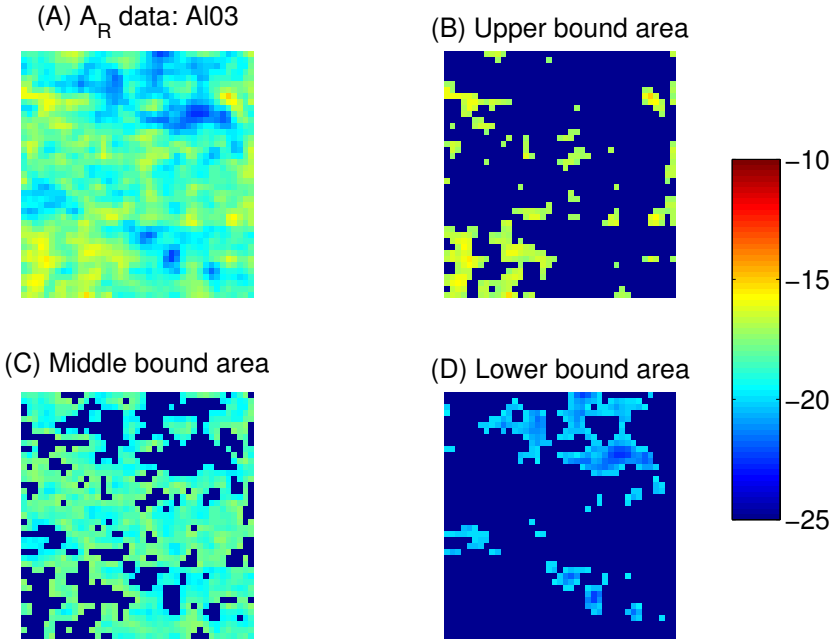

Figure D.12: Images of Aluminium 03's acoustoelasic response ($\times 10^{-6}$ MPa^{-1}) scan area being divided into segments of similar acoustelastic response, these are tracked throughout the fatigue life of the sample.

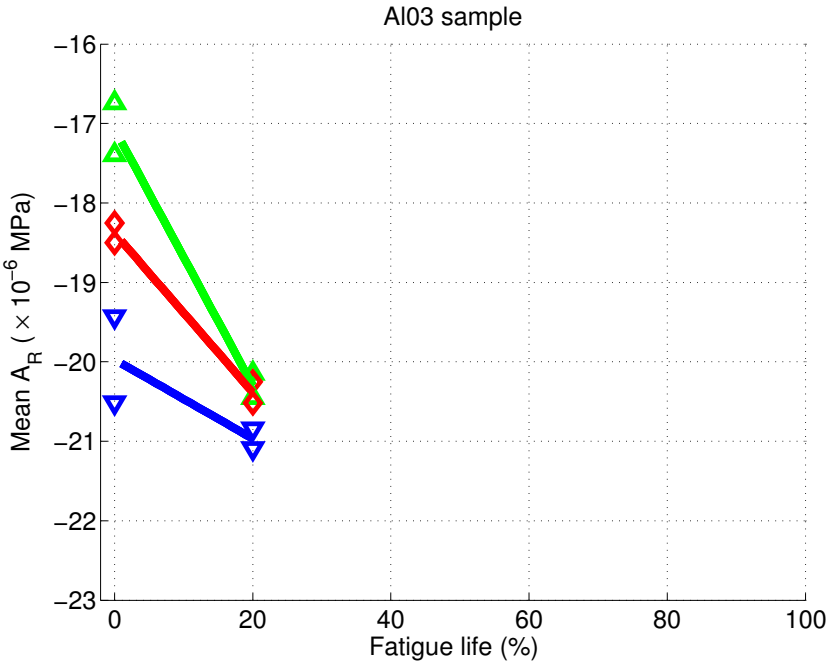

Figure D.13: Plots of mean value of the acoustoelastic response ($\times 10^{-6}$ MPa^{-1}) for sample aluminium 03 for each segment that is tracked through the samples fatigue life. The upper segment values are represented by $\bigtriangledown$, the mid segment values are represented by $\diamond$ and finally the lower bound segments are represented by $\bigtriangleup$. Each segment has a trend line (using a 1st order polynomial) fitted in the appropriate colour.

D.4 Aluminium 04

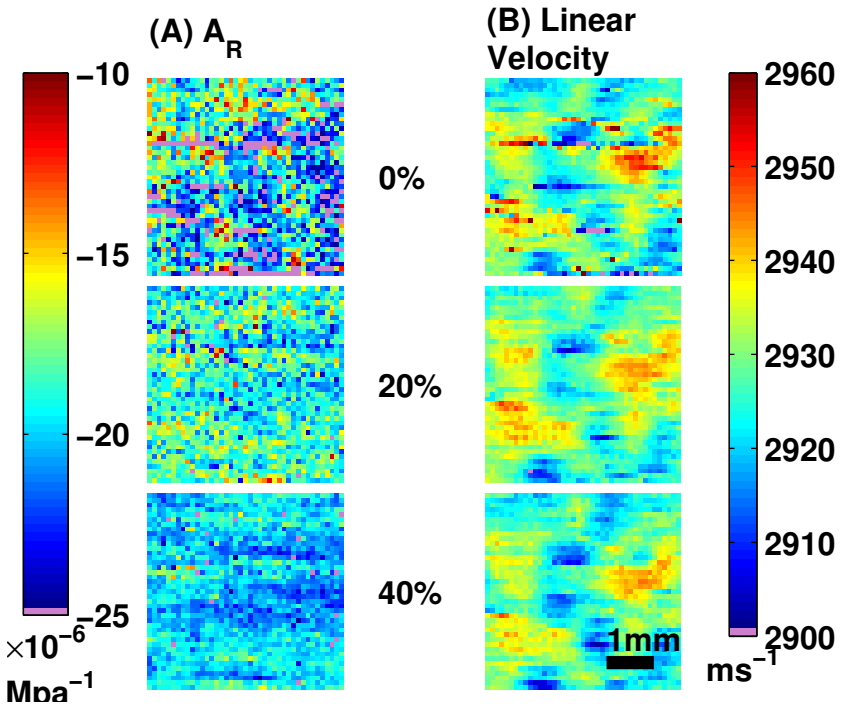

Figure D.14: Graph of aluminium 04 sample (A) squares acoustoelastic nonlinear response against fatigue. (B) squares velocity (SRAS) indicating the microstructure involved in the square.

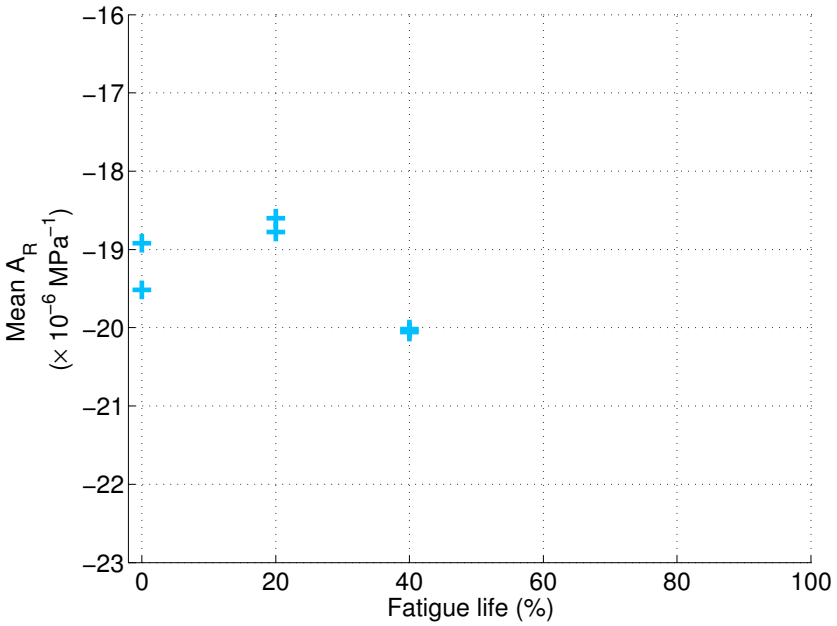

Figure D.15: Graph of aluminium 04 samples mean acousoelastic response against fatigue life.

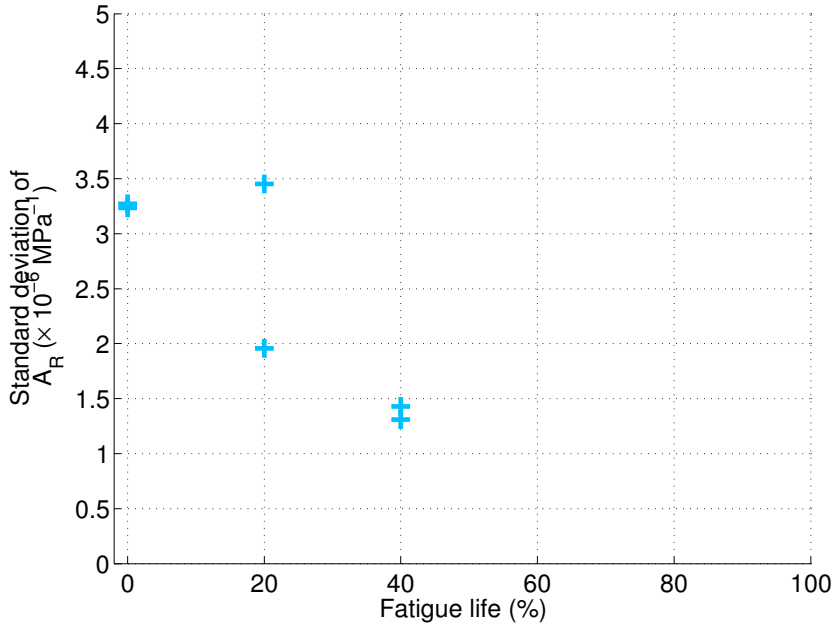

Figure D.16: Graph of aluminium 04 samples standard deviation of acousoelastic response against fatigue life.

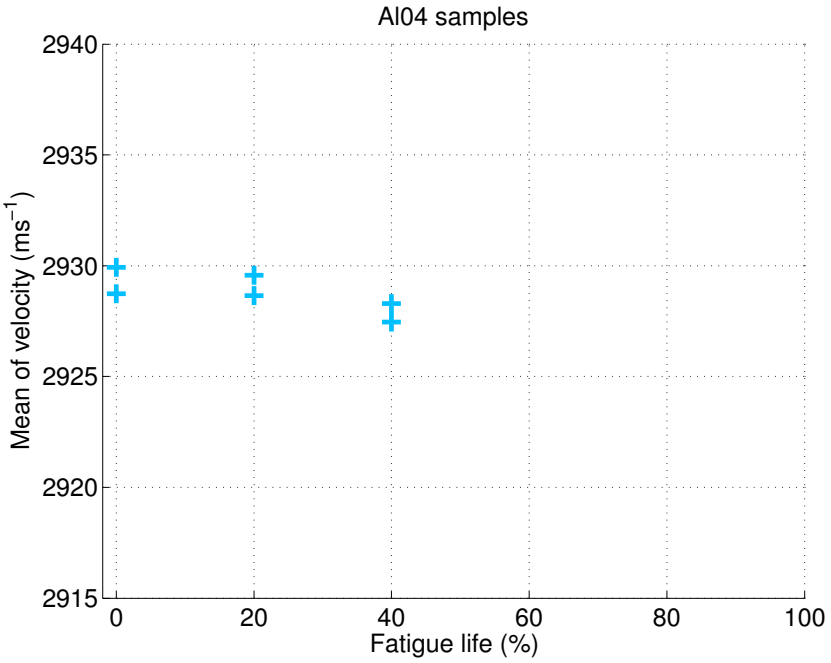

Figure D.17: Graph of the mean of the linear velocity of aluminium 04 sample against fatigue life.

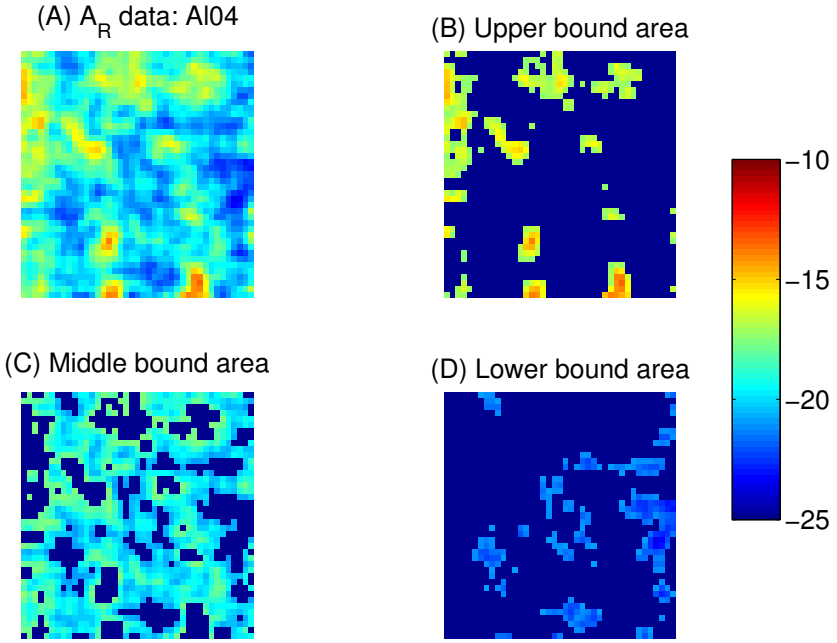

Figure D.18: Images of Aluminium 04's acoustoelasic response ($\times 10^{-6}$ MPa^{-1}) scan area being divided into segments of similar acoustelastic response, these are tracked throughout the fatigue life of the sample.

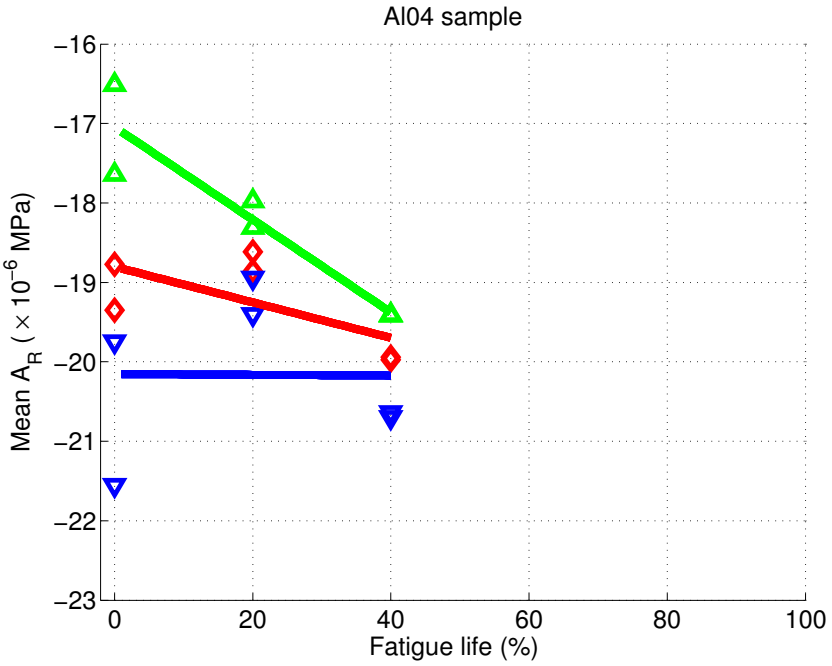

Figure D.19: Plots of mean value of the acoustoelastic response ($\times 10^{-6}$ MPa^{-1}) for sample aluminium 04 for each segment that is tracked through the samples fatigue life. The upper segment values are represented by $\bigtriangledown$, the mid segment values are represented by $\diamond$ and finally the lower bound segments are represented by $\bigtriangleup$. Each segment has a trend line (using a 1st order polynomial) fitted in the appropriate colour.

D.5 Aluminium 05

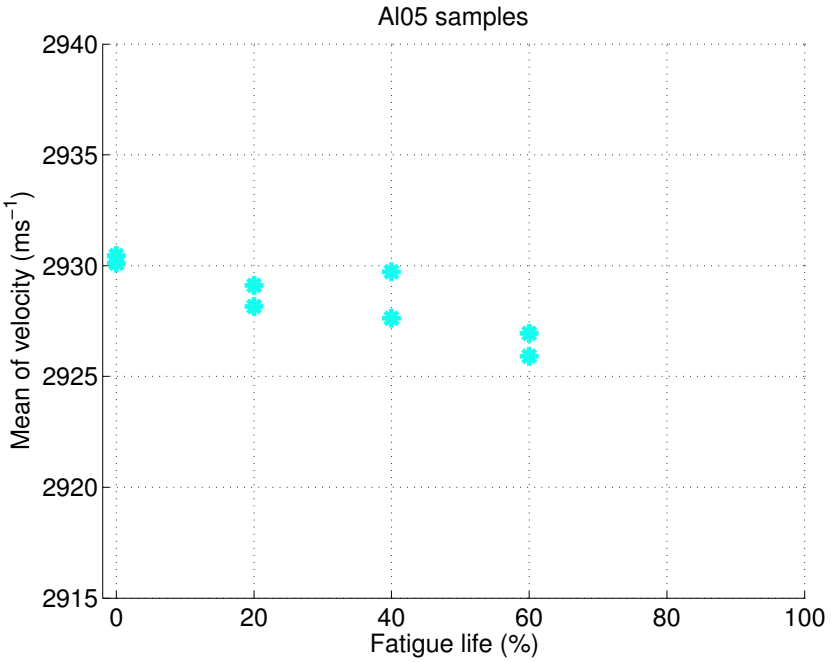

Figure D.20: Graph of the mean of the linear velocity of aluminium 05 sample against fatigue life.

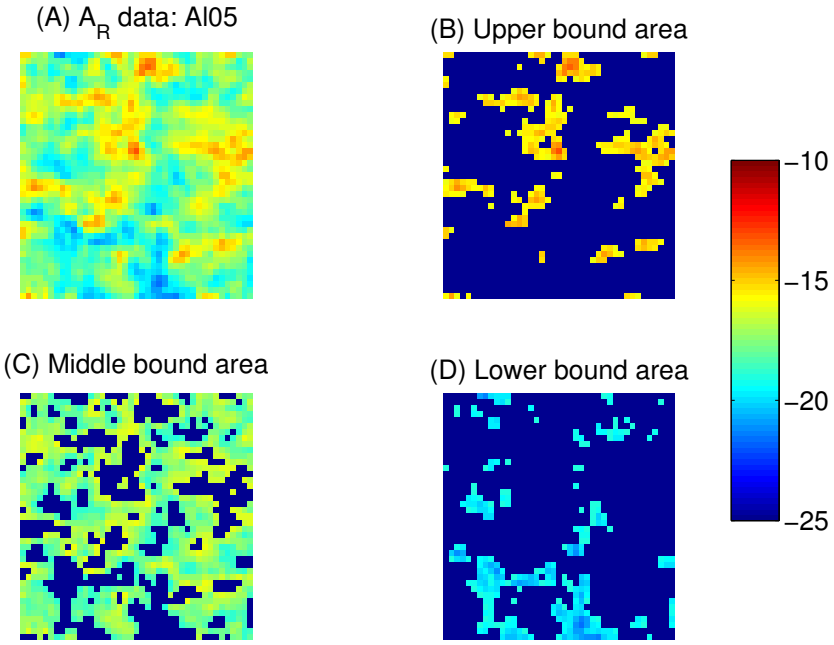

Figure D.21: Images of Aluminium 05's acoustoelasic response ($\times 10^{-6}$ MPa^{-1}) scan area being divided into segments of similar acoustelastic response, these are tracked throughout the fatigue life of the sample.

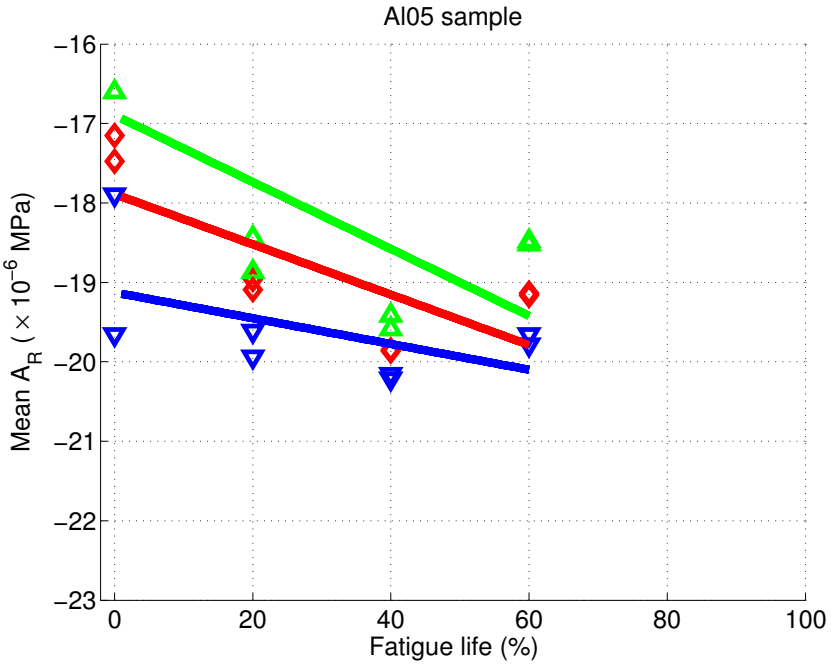

Figure D.22: Plots of mean value of the acoustoelastic response ($\times 10^{-6}$ MPa^{-1}) for sample aluminium 05 for each segment that is tracked through the samples fatigue life. The upper segment values are represented by $\bigtriangledown$, the mid segment values are represented by $\diamond$ and finally the lower bound segments are represented by $\bigtriangleup$. Each segment has a trend line (using a 1st order polynomial) fitted in the appropriate colour.

D.6 Aluminium 06

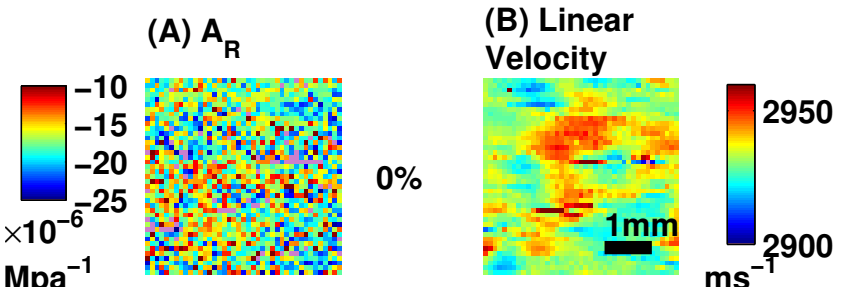

Figure D.23: Graph of aluminium 06 sample (A) squares acoustoelastic nonlinear response against fatigue. (B) squares velocity (SRAS) indicating the microstructure involved in the square.

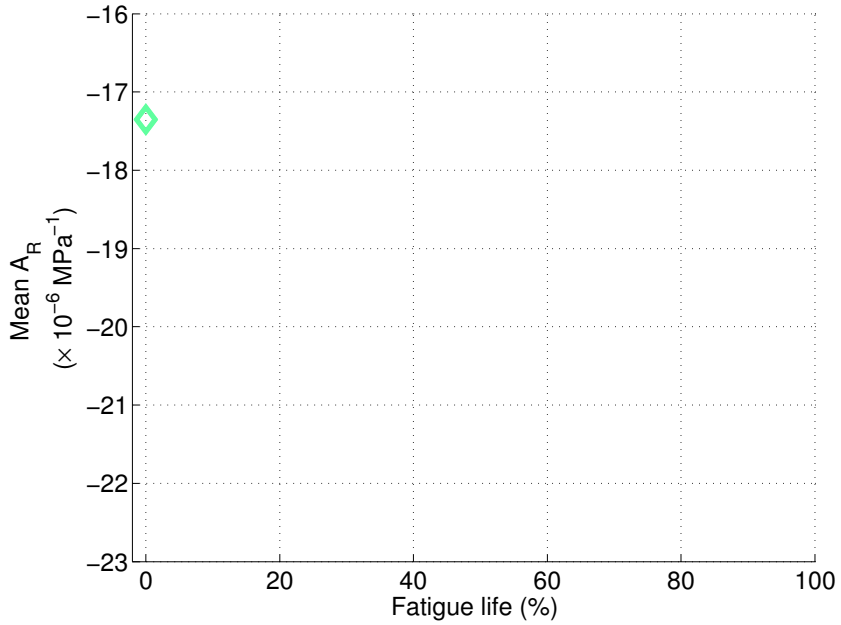

Figure D.24: Graph of aluminium 06 samples mean acousoelastic response against fatigue life.

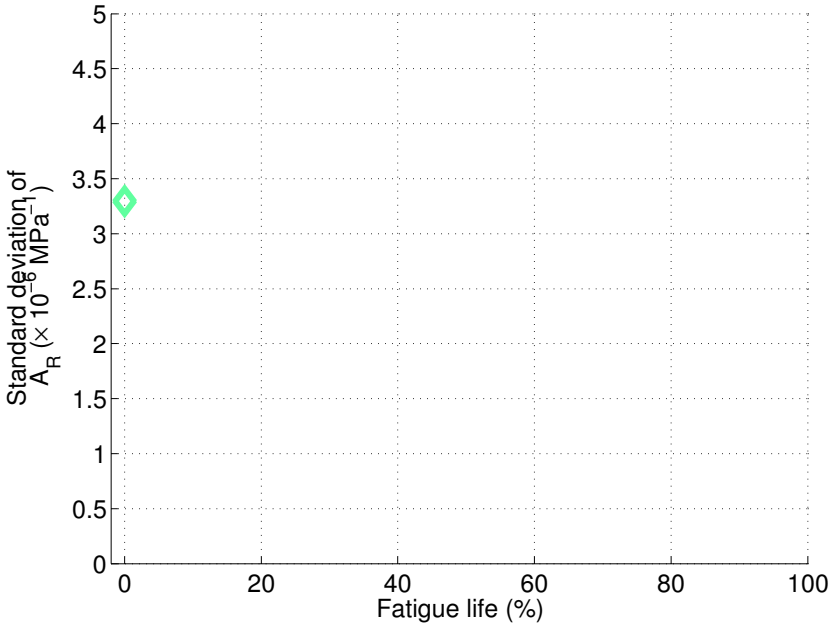

Figure D.25: Graph of aluminium 06 samples standard deviation of acousoelastic response against fatigue life.

D.7 Aluminium 07

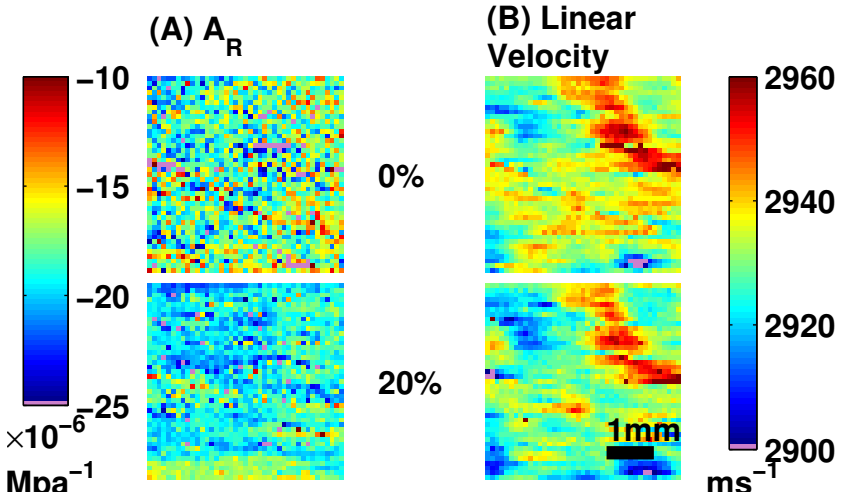

Figure D.26: Graph of aluminium 07 sample (A) squares acoustoelastic nonlinear response against fatigue. (B) squares velocity (SRAS) indicating the microstructure involved in the square.

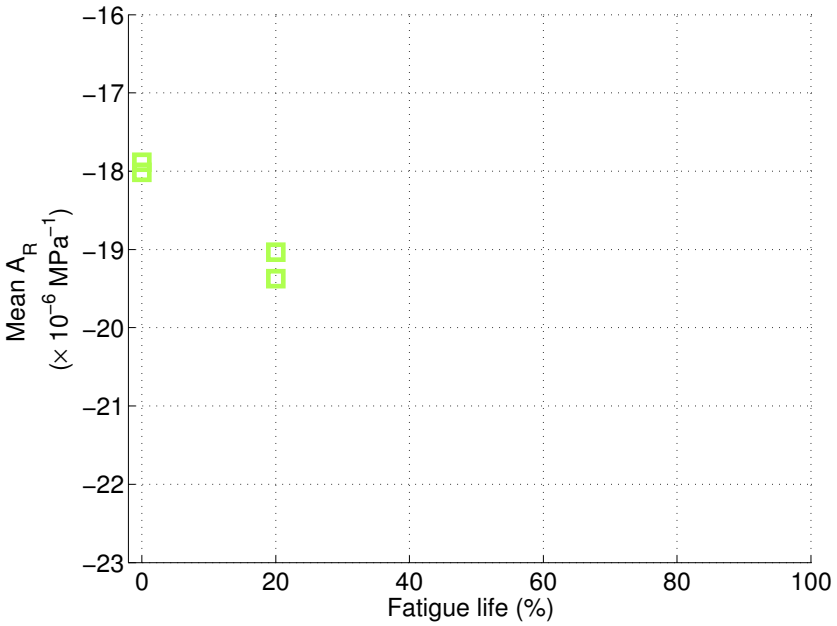

Figure D.27: Graph of aluminium 07 samples mean acousoelastic response against fatigue life.

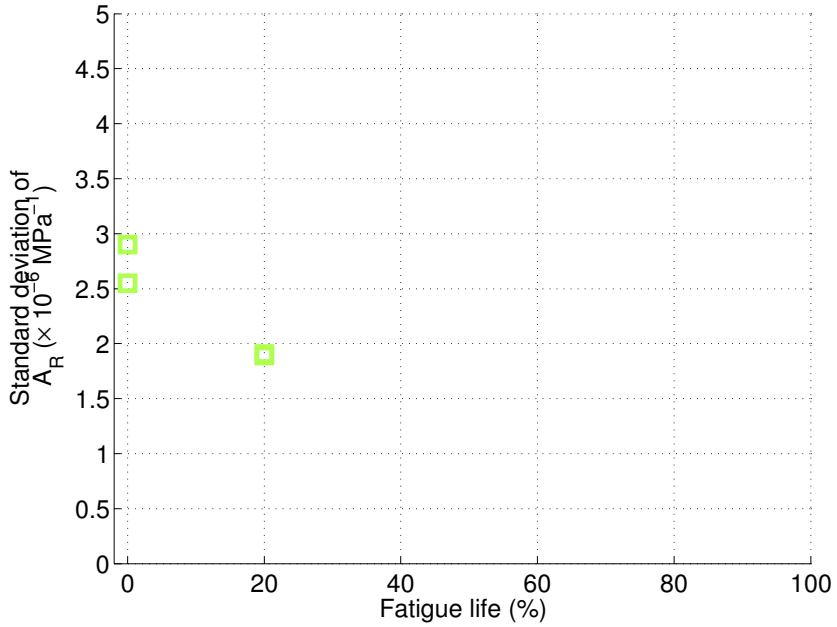

Figure D.28: Graph of aluminium 07 samples standard deviation of acousoelastic response against fatigue life.

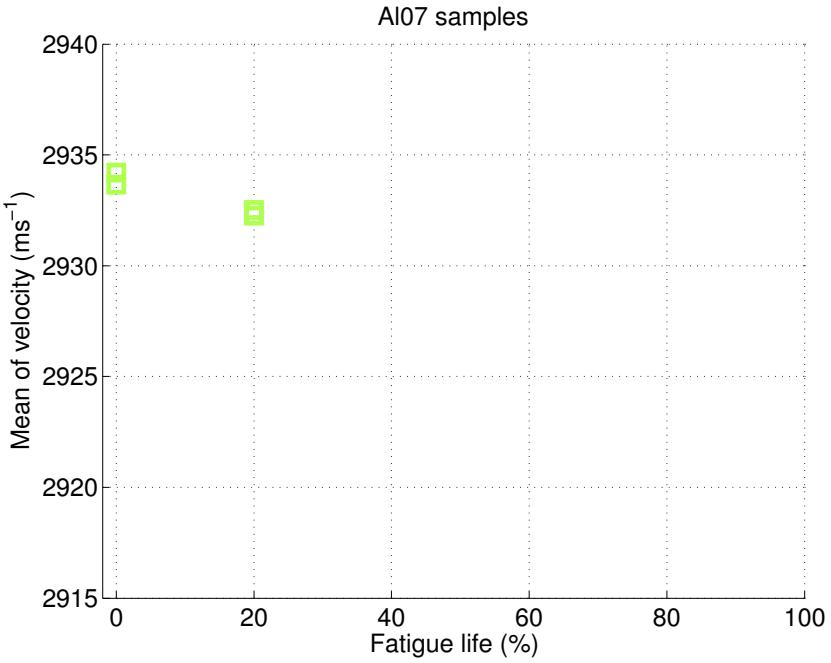

Figure D.29: Graph of the mean of the linear velocity of aluminium 07 sample against fatigue life.

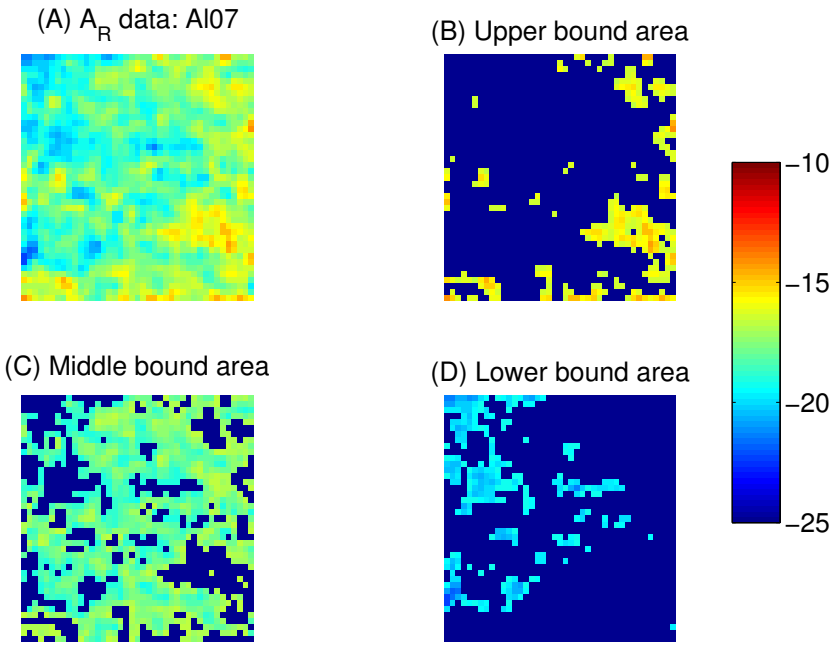

Figure D.30: Images of Aluminium 07's acoustoelasic response ($\times 10^{-6}$ MPa^{-1}) scan area being divided into segments of similar acoustelastic response, these are tracked throughout the fatigue life of the sample.

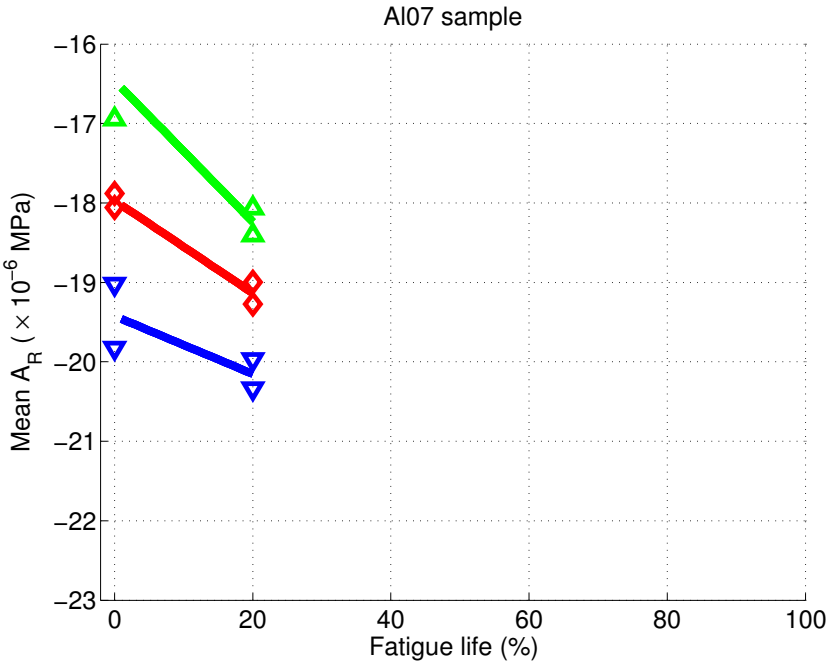

Figure D.31: Plots of mean value of the acoustoelastic response ($\times 10^{-6}$ MPa^{-1}) for sample aluminium 07 for each segment that is tracked through the samples fatigue life. The upper segment values are represented by $\bigtriangledown$, the mid segment values are represented by $\diamond$ and finally the lower bound segments are represented by $\bigtriangleup$. Each segment has a trend line (using a 1st order polynomial) fitted in the appropriate colour.

D.8 Aluminium 08

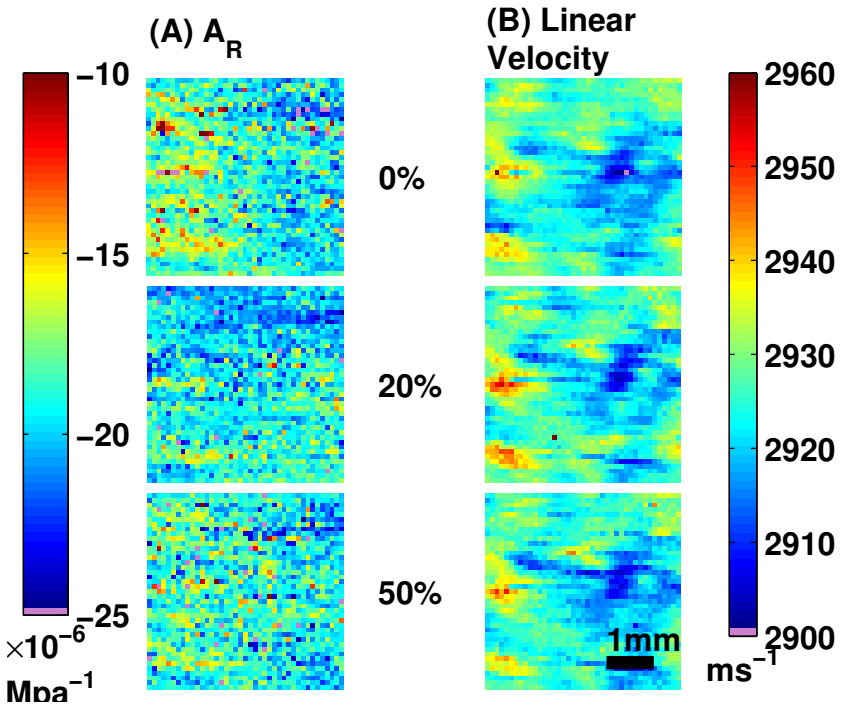

Figure D.32: Graph of aluminium 08 sample (A) squares acoustoelastic nonlinear response against fatigue. (B) squares velocity (SRAS) indicating the microstructure involved in the square.

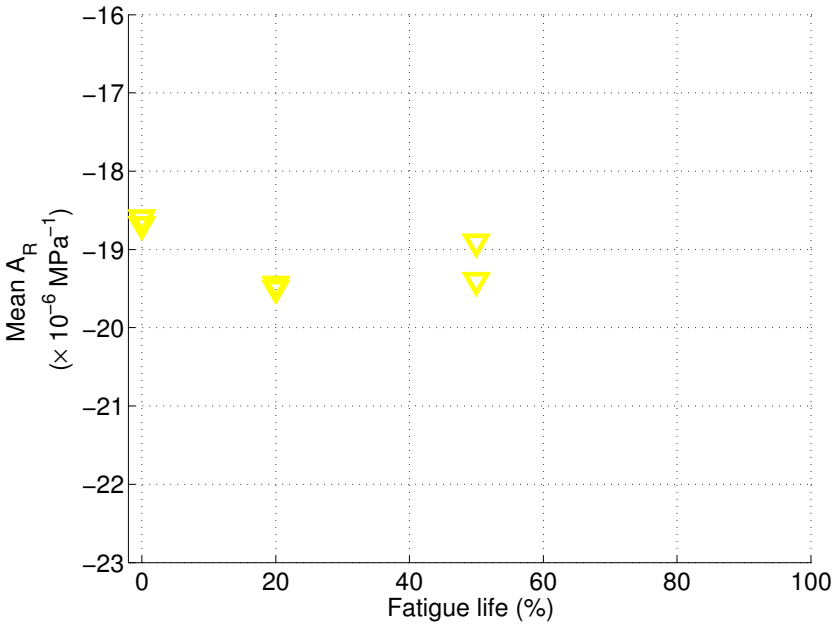

Figure D.33: Graph of aluminium 08 samples mean acousoelastic response against fatigue life.

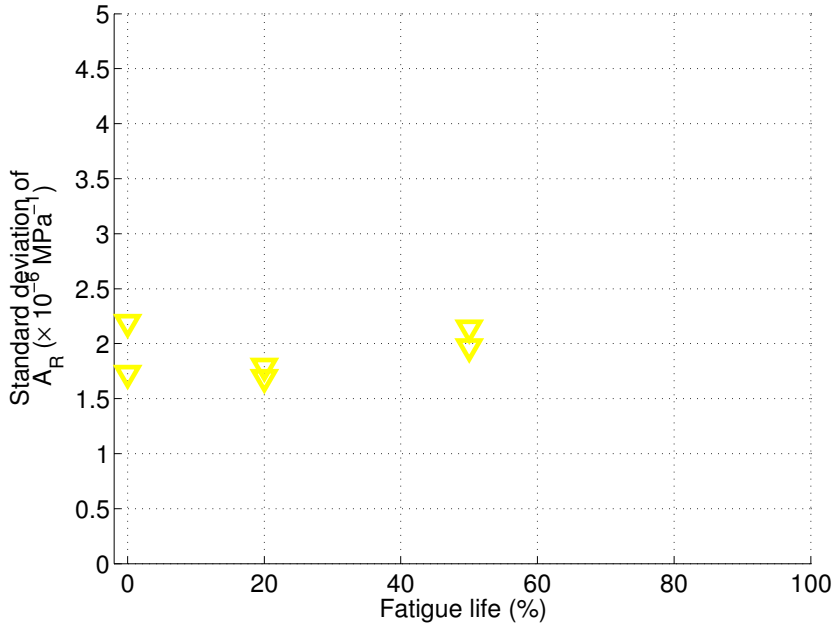

Figure D.34: Graph of aluminium 08 samples standard deviation of acousoelastic response against fatigue life.

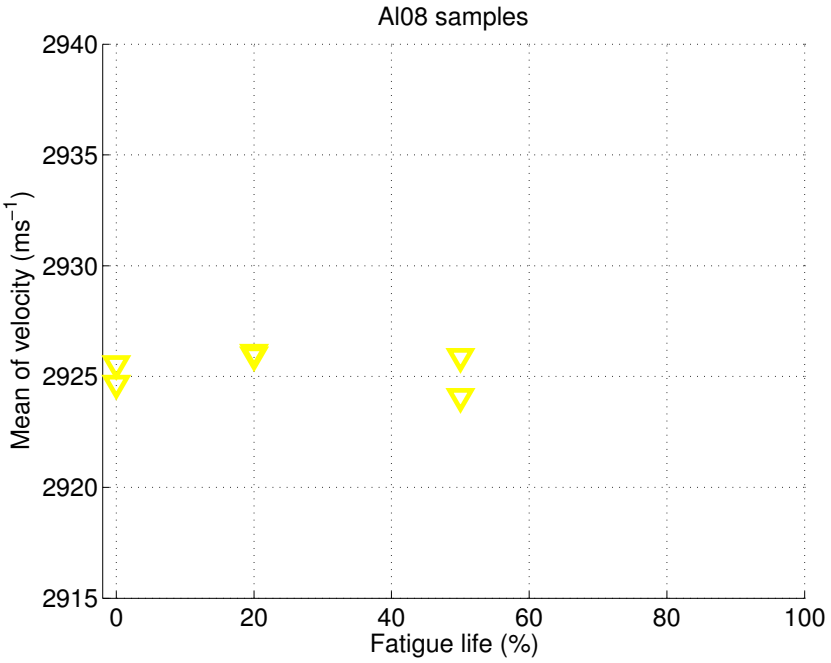

Figure D.35: Graph of the mean of the linear velocity of aluminium 08 sample against fatigue life.

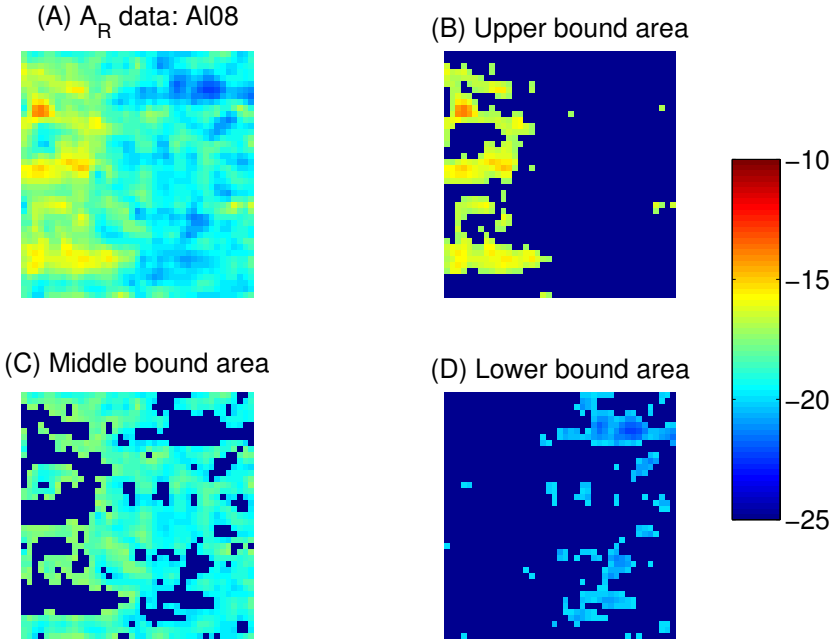

Figure D.36: Images of Aluminium 08's acoustoelasic response ($\times 10^{-6}$ MPa^{-1}) scan area being divided into segments of similar acoustelastic response, these are tracked throughout the fatigue life of the sample.

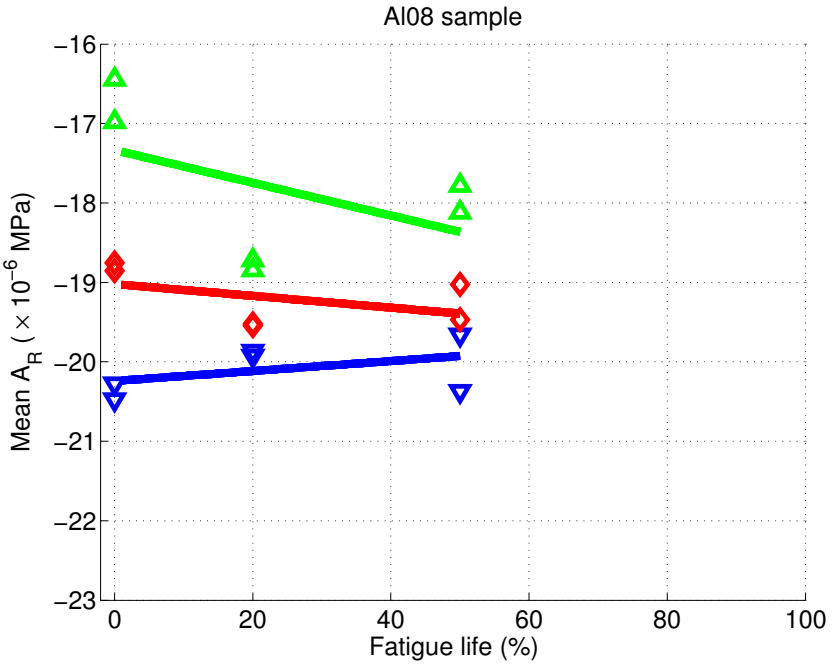

Figure D.37: Plots of mean value of the acoustoelastic response ($\times 10^{-6}$ MPa^{-1}) for sample aluminium 08 for each segment that is tracked through the samples fatigue life. The upper segment values are represented by $\bigtriangledown$, the mid segment values are represented by $\diamond$ and finally the lower bound segments are represented by $\bigtriangleup$. Each segment has a trend line (using a 1st order polynomial) fitted in the appropriate colour.

D.9 Aluminium 09

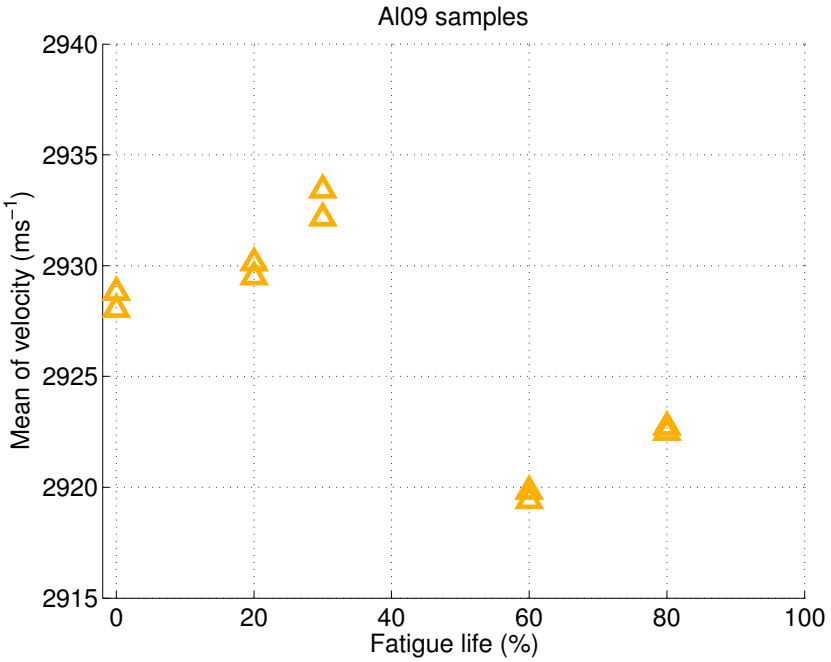

Figure D.38: Graph of the mean of the linear velocity of aluminium 09 sample against fatigue life.

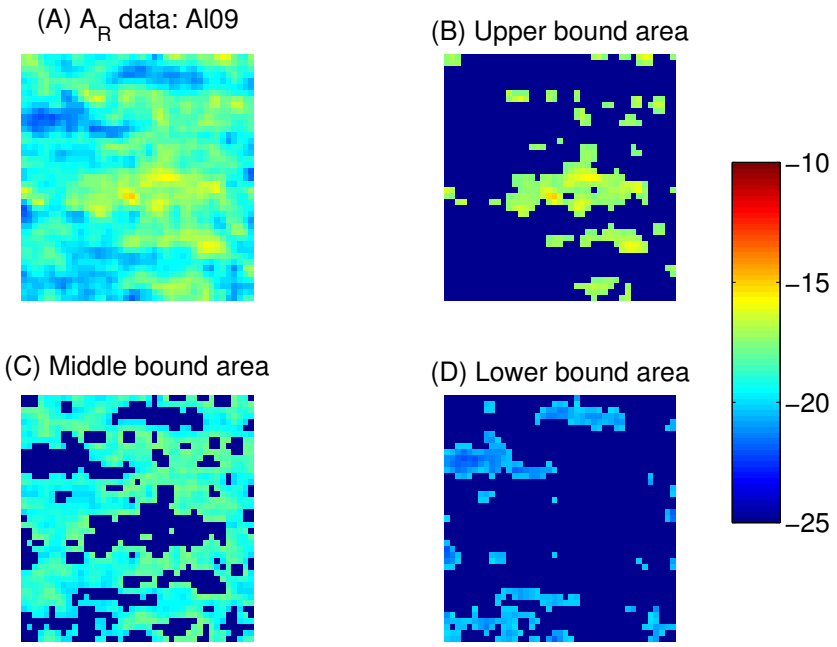

Figure D.39: Images of Aluminium 09's acoustoelasic response ($\times 10^{-6}$ MPa^{-1}) scan area being divided into segments of similar acoustelastic response, these are tracked throughout the fatigue life of the sample.

D.10 Aluminium 10

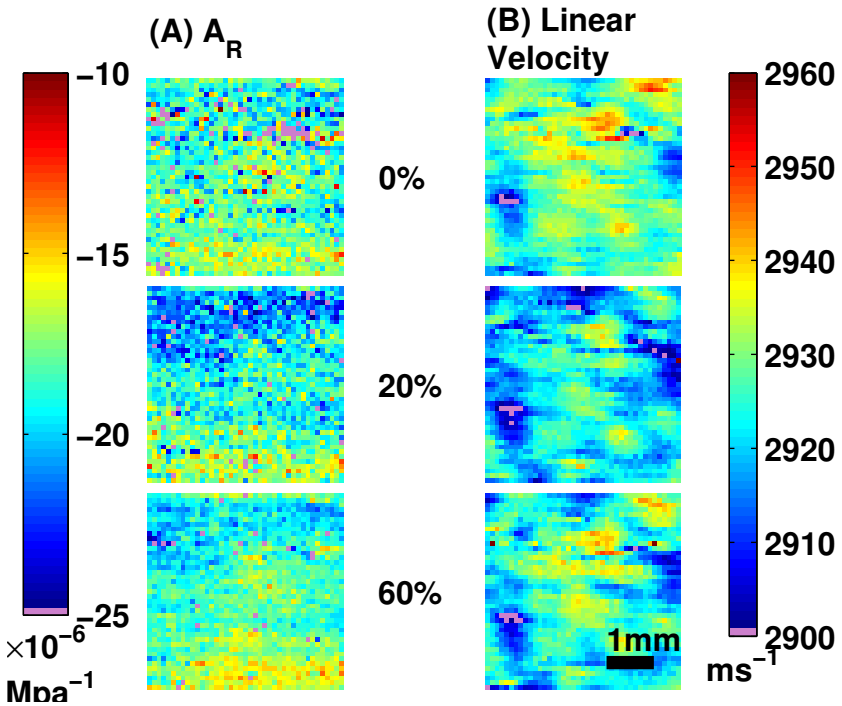

Figure D.40: Graph of aluminium 10 sample (A) squares acoustoelastic nonlinear response against fatigue. (B) squares velocity (SRAS) indicating the microstructure involved in the square.

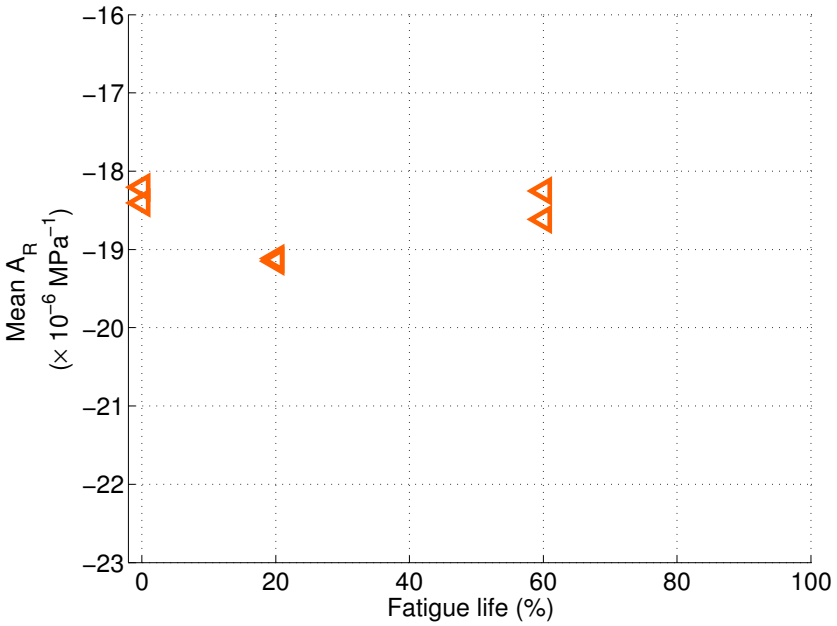

Figure D.41: Graph of aluminium 10 samples mean acousoelastic response against fatigue life.

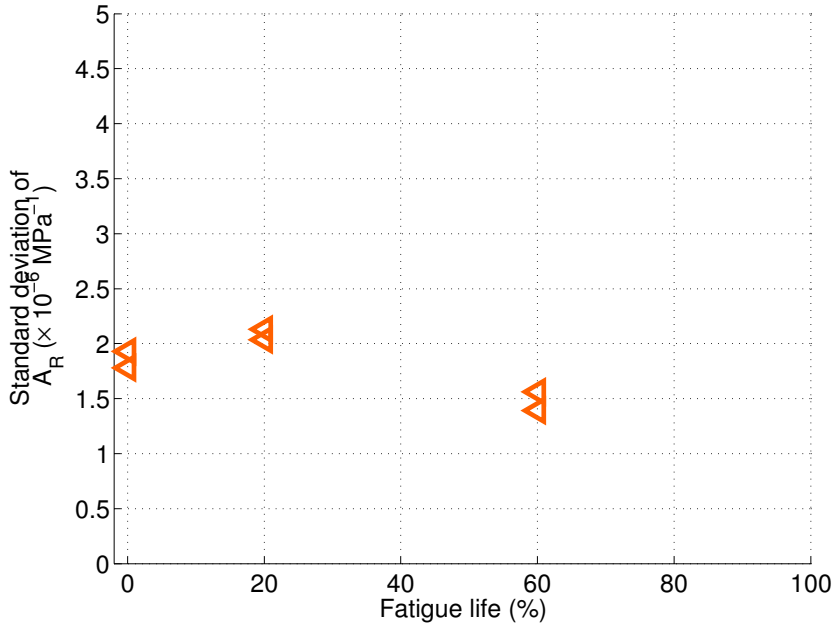

Figure D.42: Graph of aluminium 10 samples standard deviation of acousoelastic response against fatigue life.

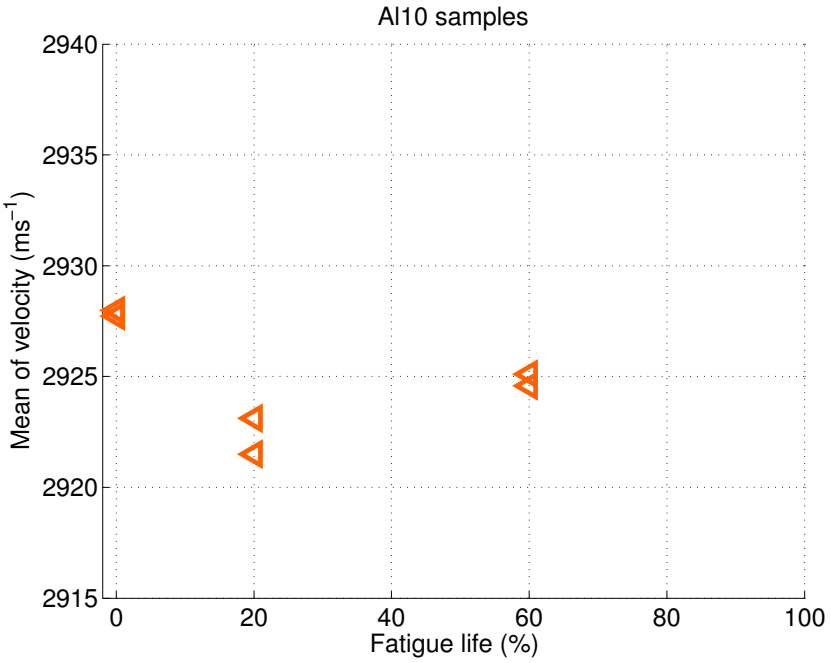

Figure D.43: Graph of the mean of the linear velocity of aluminium 10 sample against fatigue life.

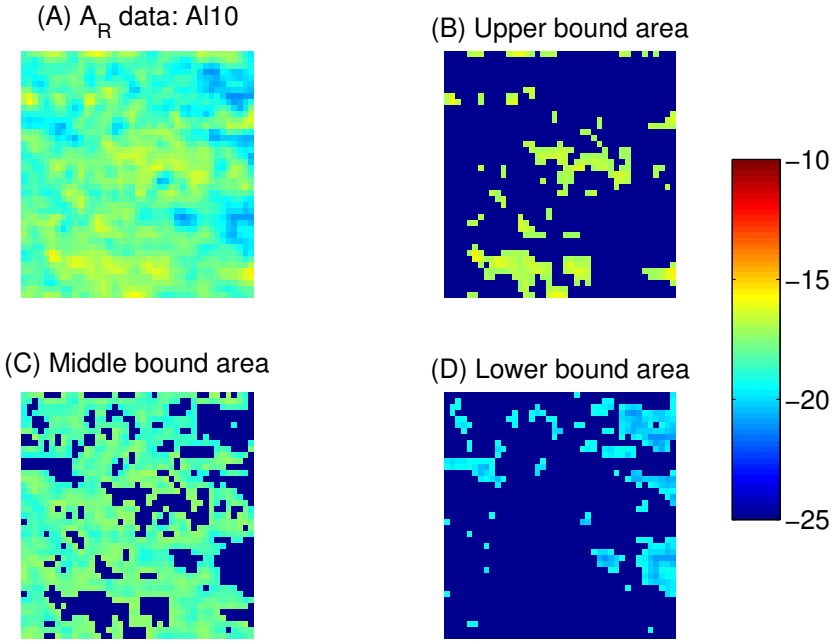

Figure D.44: Images of Aluminium 10's acoustoelasic response ($\times 10^{-6}$ MPa^{-1}) scan area being divided into segments of similar acoustelastic response, these are tracked throughout the fatigue life of the sample.

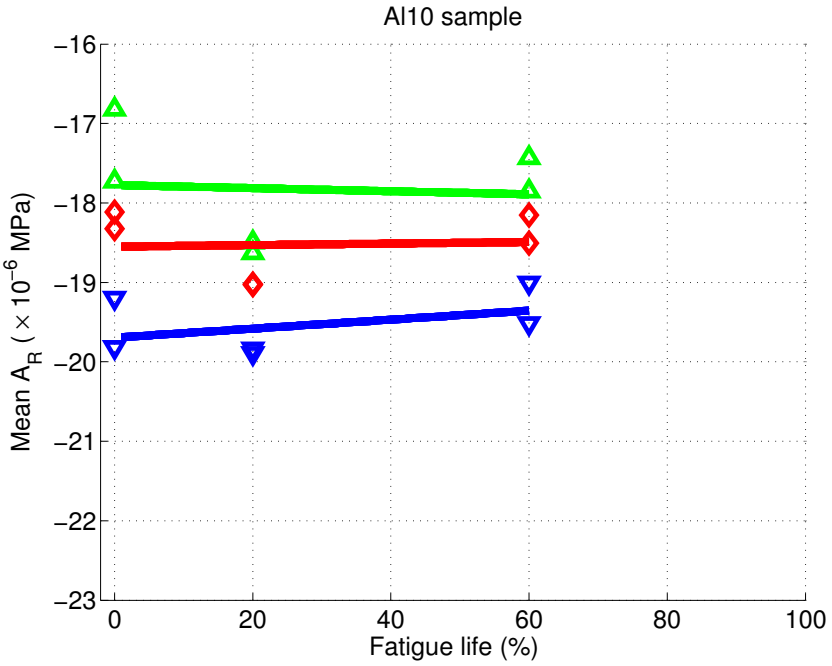

Figure D.45: Plots of mean value of the acoustoelastic response ($\times 10^{-6}$ MPa^{-1}) for sample aluminium 10 for each segment that is tracked through the samples fatigue life. The upper segment values are represented by $\bigtriangledown$, the mid segment values are represented by $\diamond$ and finally the lower bound segments are represented by $\bigtriangleup$. Each segment has a trend line (using a 1st order polynomial) fitted in the appropriate colour.

D.11 Aluminium 11

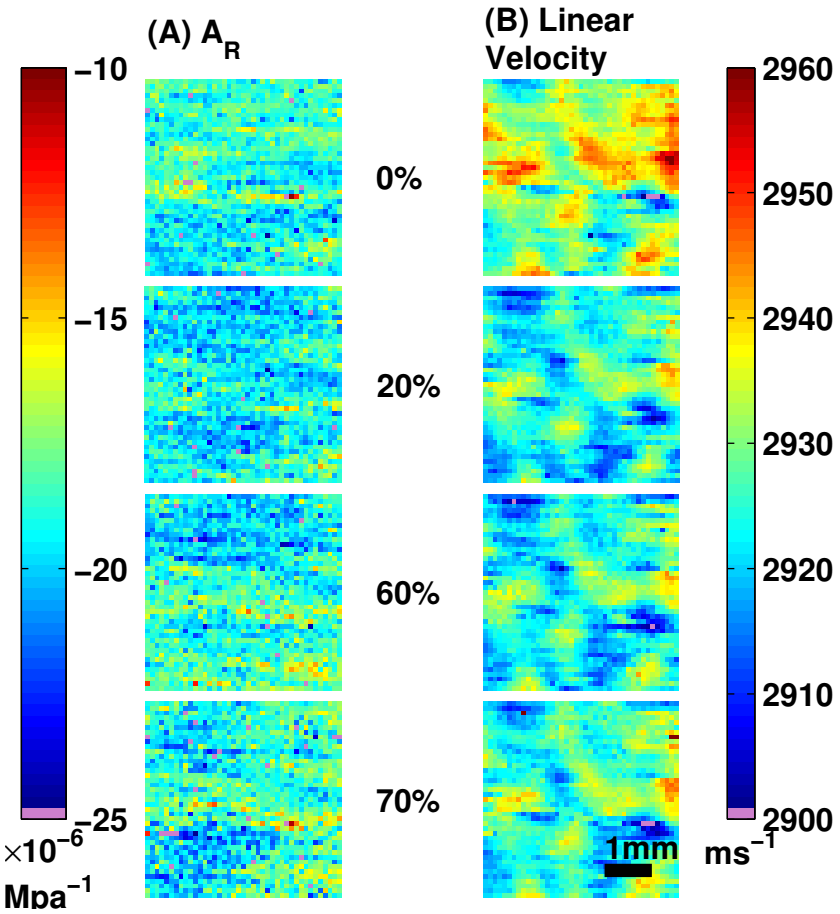

Figure D.46: Graph of aluminium 11 sample (A) squares acoustoelastic nonlinear response against fatigue. (B) squares velocity (SRAS) indicating the microstructure involved in the square.

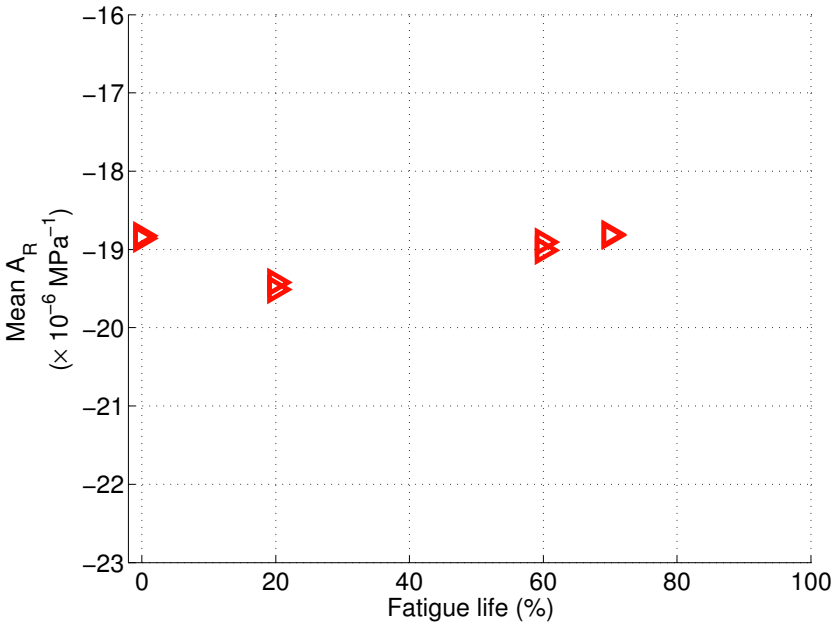

Figure D.47: Graph of aluminium 11 samples mean acousoelastic response against fatigue life.

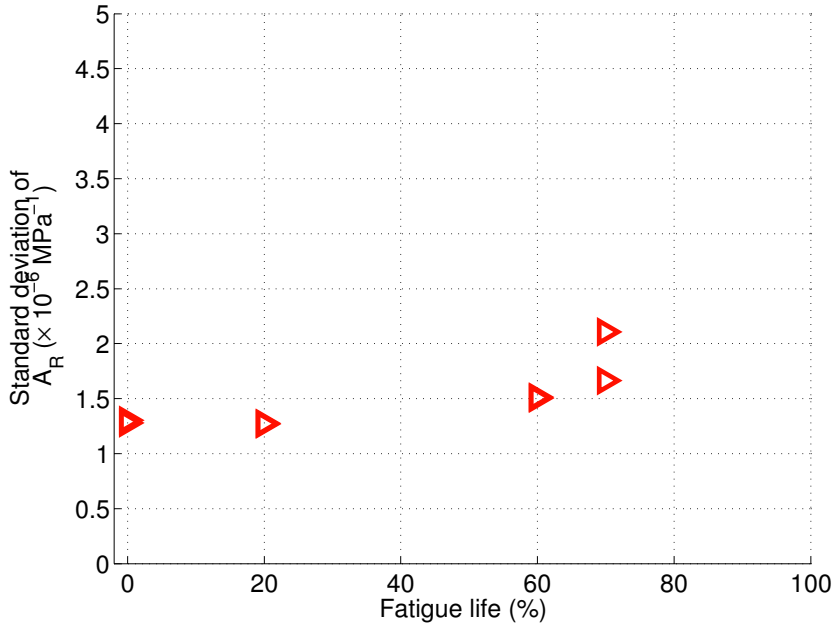

Figure D.48: Graph of aluminium 11 samples standard deviation of acousoelastic response against fatigue life.

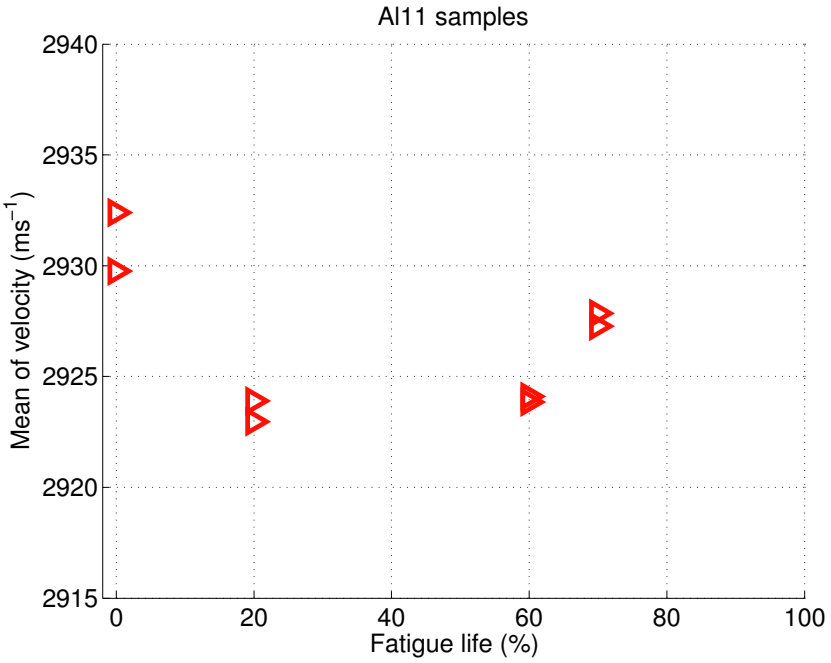

Figure D.49: Graph of the mean of the linear velocity of aluminium 11 sample against fatigue life.

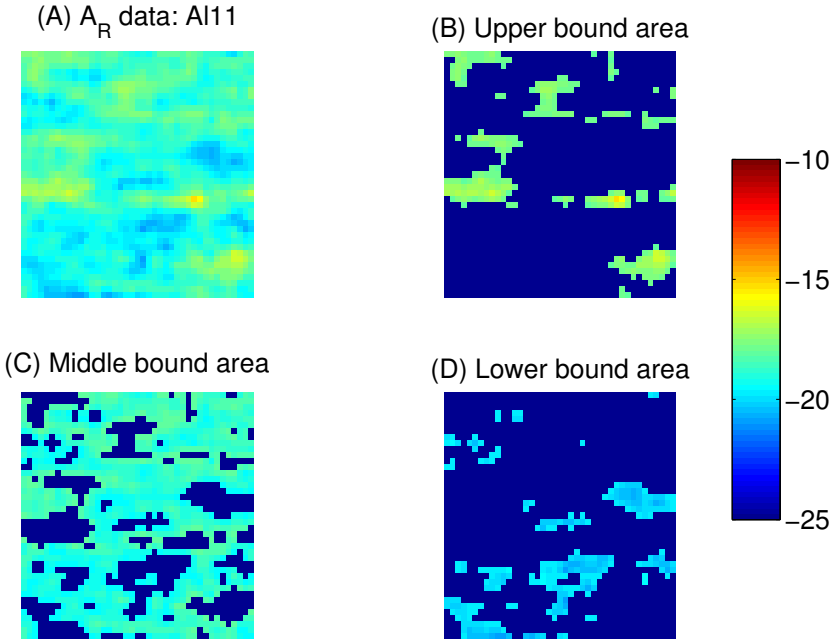

Figure D.50: Images of Aluminium 11's acoustoelasic response ($\times 10^{-6}$ MPa^{-1}) scan area being divided into segments of similar acoustelastic response, these are tracked throughout the fatigue life of the sample.

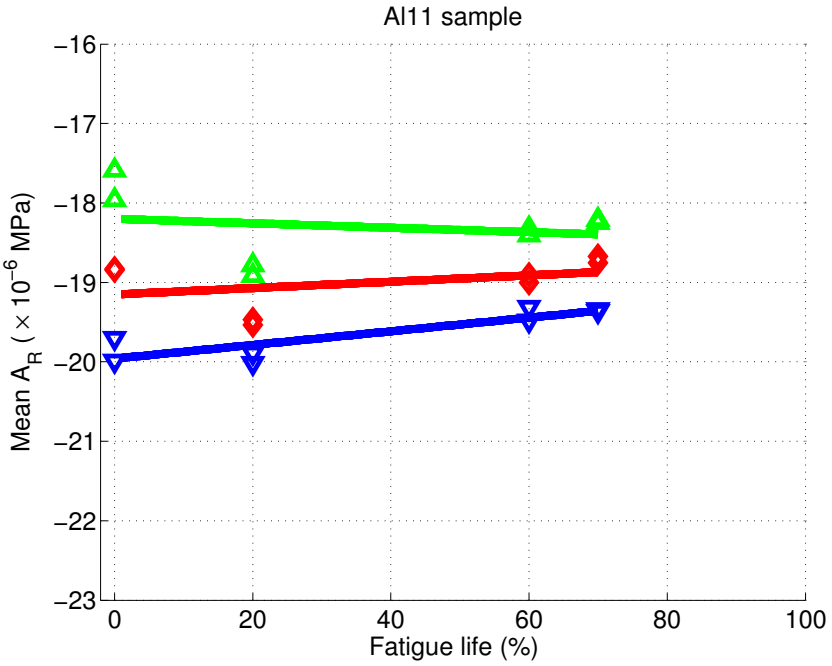

Figure D.51: Plots of mean value of the acoustoelastic response ($\times 10^{-6}$ MPa^{-1}) for sample aluminium 11 for each segment that is tracked through the samples fatigue life. The upper segment values are represented by $\bigtriangledown$, the mid segment values are represented by $\diamond$ and finally the lower bound segments are represented by $\bigtriangleup$. Each segment has a trend line (using a 1st order polynomial) fitted in the appropriate colour.

D.12 Aluminium 12

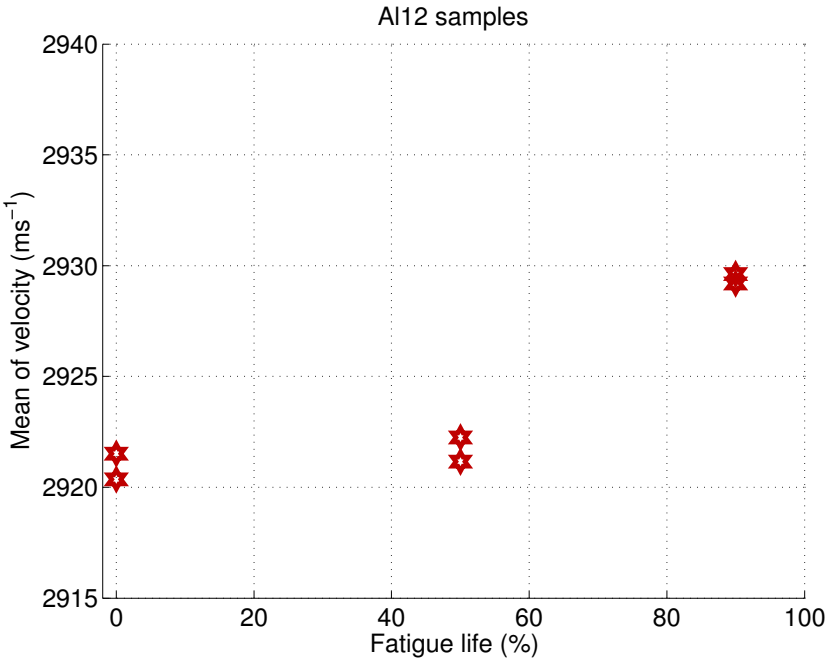

Figure D.52: Graph of the mean of the linear velocity of aluminium 12 sample against fatigue life.

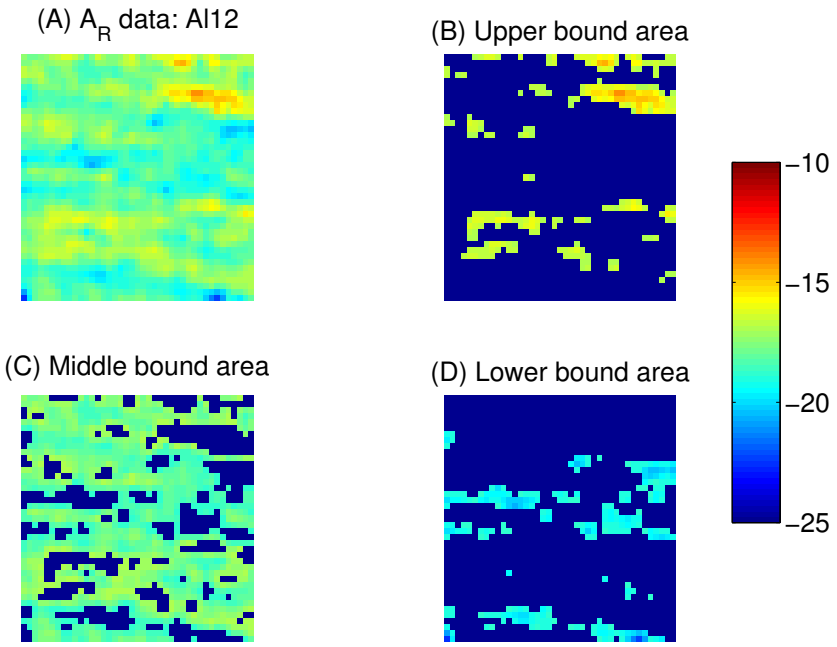

Figure D.53: Images of Aluminium 12's acoustoelasic response ($\times 10^{-6}$ MPa^{-1}) scan area being divided into segments of similar acoustelastic response, these are tracked throughout the fatigue life of the sample.

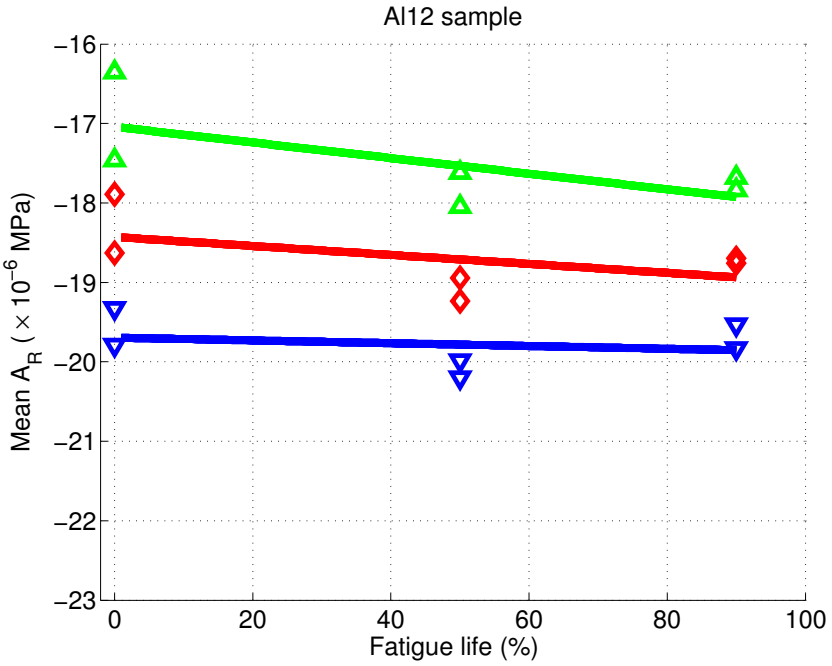

Figure D.54: Plots of mean value of the acoustoelastic response ($\times 10^{-6}$ MPa^{-1}) for sample aluminium 12 for each segment that is tracked through the samples fatigue life. The upper segment values are represented by $\bigtriangledown$, the mid segment values are represented by $\diamond$ and finally the lower bound segments are represented by $\bigtriangleup$. Each segment has a trend line (using a 1st order polynomial) fitted in the appropriate colour.

Bibliography

[1] P.Nagy, "Fatigue damage assessment by nonlinear ultrasonic materials characterization," *Ultrasonics*, vol. 36, pp. 375–381, 1998.

[2] K. E.-A. V. den Abeele, A. Sutin, J. Carmeliet, and P. Johnson, "Micro-damage diagnostics using nonlinear elastic wave spectroscopy (news)," *NDT& E International*, vol. 34, pp. 239–248, 2001.

[3] K.-Y. Jhang, "Applications of nonlinear ultrasonics to the nde of material degradation," *IEEE Transactions on Ultrasonics, Ferroelectrics and Frequency Control*, vol. 47, pp. 540–548, may 2000.

[4] I. Collison, *Measurement of material nonlinearity using laser ultrasound*. PhD thesis, University of Nottingham, July 2008.

[5] W. Yost and J. Cantrell, "The effects of fatigue on acoustic nonlinearity in aluminium alloys," *Ultrasonics symposium*, pp. 947–955, 1992.

[6] O. Buck, W. Morris, and J. M. Richardson, "Acoustic harmonic generation at unbonded interfaces and fatigue cracks," *Applied Physics Letters*, vol. 33, no. 5, pp. 371–373, 1978.

[7] M. F. Hamilton, Y. A. Ll'inskii, and E. A. Zabolotskaya, "Nonlinear surface acoustic waves in crystals," *Journal of Acoustic Society of America*, vol. 105, pp. 639–651, February 1999.

[8] A. Hikata and C. Elbaum, "Generation of ultrasonic second and third harmonics due to dislocations," *Physical Review*, vol. 144, pp. 469–477, April 1966.

[9] J. yeon Kim, J. Qu, L. J. Jacobs, J. W. Littles, and M. F. Savage, "Acoustic nonlinearity parameter due to microplasticity," *Journal of Nondestructive Evaluation*, vol. 25, pp. 29–37, March 2006.

[10] J. Cantrell, "Substructural organization,dislocation plasticity and harmonic generation in cyclically stressed wavy slip metals," in *Proceedings of the Royal Society A*, vol. 460, pp. 757–780, 2004.

[11] W. Yost, J. Cantrell, and J. Na, "Nonlinear ultrasonic pulsed measurements and applications to metal processing and fatigue," *Review of Progress in Quantitative Nondestructive Evaluation*, vol. 20, pp. 1268–1275, 2001.

[12] J. Cantrell and W. Yost, "Nonlinear ultrasonic characterization of fatigue microstructures," *International Journal of Fatigue*, vol. 23, pp. s487–s490, 2001.

[13] J. Blackshire, S. Sathish, J. Na, and J. Frouin, "Nonlinear laser ultrasonic measurements of localized fatigue damage," in *Review of Quantitative Nondestructive Evalutation*, vol. 22, pp. 1479–1488, 2003.

[14] J. Herrmann, J.-Y. Kim, L. J. Jacobs, J. Qu, J. W. Littles, and M. F. Savage, "Assessment of material damage in a nickel-base superalloy using nonlinear rayleigh surface waves," *Journal of Applied Physics*, vol. 99, pp. 1–8, 2006.

[15] K.-Y. Jhang and K.-C. kim, "Evaluation of material degradation using nonlinear acoustic effect," *Ultrasonics*, vol. 37, pp. 39–44, 1999.

[16] B. T. Reinhardt, M. Kropf, K. Boudraeu, M. J. Guers, and B. R. Tittmann, "Dislocation detection through harmonic generation," *Review of Quantative Nondestructive Evaluation*, vol. 29, pp. 1391–1396, 2010.

[17] J. yeon Kim, L. J. Jacobs, J. Qu, and J. W. Littles, "Experimental characterization of fatigue damage in a nickel-base superalloy using nonlinear ultrasonic waves," *Journal of Acoustic Society of America*, vol. 120, pp. 1266–1273, June 2006.

[18] A. J. Croxford, P. D. Wilcox, B. W. Drinkwater, and P. B. Nagy, "The use of non-collinear mixing for nonlinear ultrasonic detection of plasticity and fatigue," *JASA express letters*, vol. 126, pp. EL117–EL122, November 2009.

[19] B. O'Neill and R. G. Maev, "Acoustic-elastic measurement of the fatigue damage in waspaloy," *Research in Nondestructive Evaluation*, vol. 17, pp. 121–135, 2006.

[20] D. Donskoy, A. Sutin, and A. Ekimov, "Nonlinear acoustic interaction on contact interfaces and its use for nondestructive testing," *NDT&E International*, vol. 00, 2000.

[21] M. Ryles, F. H. Ngau, I. Mcdonald, and W. J. Staszewski, "Comparative study of nonlinear acoustic and lamb wave techniques for fatigue crack detection in metallic structures," *Fatigue and Fracture of Engineering Materials and Structures*, vol. 31, pp. 674–683, 2008.

[22] L. Straka, Y. Yagodzinskyy, M. Landa, and H. Hänninen, "Detection of structural damage of aluminium alloy 6082 using elastic wave modulation spectroscopy," *NDT&E International*, vol. 41, pp. 554–563, 2008.

[23] M. Meo, U. Polimeno, and G. Zumpano, "Detecting damage in composite material using nonlinear elastic wave spectroscopy methods," *Applied Composite Materials*, vol. 15, pp. 115–126, 2008.

[24] C. Bathias and A. Pineau, eds., *Fatigue of materials and structures*. 111 River Street, Hoboken, NJ 07030, USA: John Wiley & Sons, Inc, 2010.

[25] W. Schütz, "A history of fatigue," *Engineering Fracture Mechanics*, vol. 54, no. 2, pp. 263–300, 1996.

[26] M. A. Smith, "B.o.a.c. comet lost: Services suspended," *Flight and Aircraft Engineer*, vol. 65, p. 58, January 1954. URL: http://www.flightglobal.com/pdfarchive/view/1954/1954%20-%200130.html (Reviewed 17/01/2012).

[27] P. Withey, "Fatigue failure of the de havilland comet 1," *Engineering Failure Analysis*, vol. 4, no. 2, pp. 147–154, 1997.

[28] O. Buck, "Harmonic generation for measurement of internal stresses as produced by dislocations," *IEEE Transactions on Sonics and Ultrasonics*, vol. su-23, pp. 346–350, september 1976.

[29] P. Forsyth, "Some metallographic observations on the fatigue of metals," *Journal of the Institute of Metals*, vol. 80, p. 181, 1951.

[30] P. Forsyth, "Exudation of material form slip bands at the surface of fatigued crystals of an aluminium copper alloy," *Nature*, vol. 171, pp. 172–173, 1953.

[31] W. G. Moffat, G. W. Pearsall, and J. Wulf, *Structure and properties of materials*, vol. 1, ch. 6, pp. 122–147. John Wiley & Sons, Inc, 1964.

[32] D. Stobbe, "Acoustoelasticity in 7075-t651 aluminium and dependence of third order elastic constants on fatigue damage," Master's thesis, Mechanical Engineering Georgia Institute of Technology, August 2005.

[33] A. J. Stone, *The theory of intermolecular forces*. Oxford university press, Great clarendon Street, Oxford, OX2 6DP: Oxford University Press, 1996.

[34] R. Truell, C. Elbaum, and B. Chick, *Ultrasonic methods in solid state physics*, p. 43. 111 Fifth avenue, New york, New york, 10003: Academic Press Inc,, 1969.

[35] B. Raj, T. Jayakumar, and M. Thavasimuthu, *Practical non-destructive testing*. Woodhead Publishing, 2 ed., 2002.

[36] Y. Waseda, E. Matsubara, and K. Shinoda, *X-Ray diffraction crystallography : introduction, examples and solved problems*. Berlin, London: Springer, 2011.

[37] P. S. Pervéy, *Metals Handbook*, vol. 10, ch. X-ray diffraction residual stress techniques, pp. 380–392. Metals park: American Society for Metals, 1986.

[38] L. Botvina, I. Petrova, I. Gadolina, V. Levin, Y. A. Demina, A. Soldatenkov, and M. T'utin, "High-cycle fatigue failure of low-carbon steel after long-term ageing," *Inorganic Materials*, vol. 46, no. 14, pp. 1570–1577, 2010.

[39] R. Krause-Rehberg and H. S. Leiper, *Positron annihilation in semiconductors: defect studies*. Springer, 1999.

[40] D. Cook and Y. Berthelot, "Detection of small surface-breaking fatigue cracks in steel using scattering of rayleigh waves," *NDT&E International*, vol. 34, pp. 483–492, 2001.

[41] Q. Shan and R. Dewhurst, "Surfacebreaking fatigue crack detection using laser ultrasound," *Applied Physics Letters*, vol. 62, no. 21, pp. 2649–2651, 1993.

[42] M. G. Somekh, M. Liu, H. P. Ho, and C. W. See, "An accurate non-contact laser based system for surface wave velocity measurement," *Measurement Science and Technology*, vol. 6, pp. 1329–1337, 1995.

[43] G. R. Gerhart, "Rayleigh wave velocity for a stress-induced slightly anisotropic solid," *Journal of the Acoustical Society of America*, vol. 60, no. 5, pp. 1085–1088, 1976.

[44] M. Duquennoy, M. Ouaftouh, and M. Ourak, "Determination of stresses in aluminium alloy using optical detection of rayleigh waves," *Ultrasonics*, vol. 37, pp. 365–372, 1999.

[45] B. Mi, J. E. Michaels, and T. E. Michaels, "An ultrasonic method for dynamic monitoring of fatigue crack initiation and growth," *Jounal of Acoustic Society of America*, vol. 119, no. 1, pp. 74–84, 2006.

[46] P. Warren, C. Pecorari, O. Kolosov, S. Roberts, and G. Briggs, "Characterization of surface damage via surface acoustic waves," *Nanotechnology*, vol. 7, pp. 295–301, 1996.

[47] I. Pape, C. Lawrence, P. Warren, S. Roberts, G. Briggs, O. Kolosov, A. Hey, C. Paines, and B. Tanner, "Evaluation of polishing damage in alumina," *Philosophical Magazine*, vol. 80, no. 8, pp. 1913–1934, 2000.

[48] S. Sharples, M. Clark, and M. Somekh, "Fast noncontact imaging of material microstructure using local surface acoustic wave velocity mapping," *IEEE Ultrasonics Symposium*, pp. 886–889, 2005.

[49] M. Clark, S. D. Sharples, and M. Somekh, "Non-contact surface acoustic microscopy," *Measurement Science and Technology*, vol. 11, pp. 1792–1801, 2000.

[50] M. Clark, S. D. Sharples, and M. Somekh, "Fast all optical rayleigh wave microscope: Imaging on isotropic and anisotropic materials," *IEEE transactions on Ultrasonics, Ferroelectrics and Frequency Control*, vol. 47, no. 1, pp. 65–74, 1999.

[51] W. Li, S. Sharples, M. Clark, and M. Somekh, "Frequency spectrum spatially resolved acoustic spectroscopy for microstructure imaging," *JPCS*, Accepted 2010.

[52] P. Cawley and D. Alleyne, "The use of lamb waves for the long range inspection of large structures," *Ultrasonics*, vol. 34, pp. 287–290, 1996.

[53] T. Hayashi and K. Kawashima, "Multiple reflections of lamb waves at a de-lamination," *Ultrasonics*, vol. 40, pp. 193–197, 2002.

[54] J. Tian, U. Gabbert, H. Berger, and X. Su, "Lamb wave interaction with delaminations in cfrp laminates," *Computers, Materials and Continua*, vol. 1, no. 4, pp. 327–336, 2004.

[55] W. Staszewski, B. Lee, and R. Traynor, "Fatigue crack detection in metallic structures with lamb waves and 3d laser vibrometry," *Measurement Science and Technology*, vol. 18, pp. 727–7398, 2007.

[56] S. Grondel, C. Delebarre, J. Assaad, J.-P. Dupuis, and L. Reithler, "Fatigue crack monitoring of riveted aluminium strap joints by lamb wave analysis and acoustic emission measurement techniques," *NDT&E International*, vol. 35, pp. 137–146, 2002.

[57] L. Brehovskikh, *Waves in layered media*. Newyork: Academic Press, 1980.

[58] H. Kolsky, *Stress waves in solids*. Newyork: Dover, 1963.

[59] R. Truell, C. Elbaum, and B. Chick, *Ultrasonic methods in solid state physics*, ch. 2, pp. 77–89. 111 Fifth avenue, New york, New york, 10003: Academic Press Inc,, 1969.

[60] I. Oparina and L. Botvina, "Cumulative curves for size distribution of the number of defects at different stages of accumulating damages in conditions of fatigue and creep," *Doklady Physics*, vol. 48, no. 4, pp. 194–197, 2002.

[61] E. A. Zabolotskaya, "Nonlinear propagation of plane and circular rayleigh waves in isotropic solids," *Journal of Acoustic Society of America*, vol. 91, pp. 2569–2575, may 1992.

[62] M. F. Hamilton and D. T. Blackstock, *Nonlinear Acoustics*. 525 B Street, Suite 1900, San Diego, California, 92101-4495, USA: Academic Press, 1998.

[63] F. D. Murnaghan, "On the energy of deformation of an elastic solid," *Mathematics*, vol. 14, pp. 1928–1930, 1928.

[64] L. Landau, E. Lifshitz, A. Kosevich, and L. Pitaevskiĭ, *Theory of elasticity*. Theoretical Physics, Butterworth-Heinemann, 3 ed., 1986.

[65] G. Shui, J. Kim, Y. W. J.Qu, and L. Yacobs, "A new technique for measuring the acoustic nonlinearity of materials using rayleigh waves," *NDT&E International*, vol. 41, pp. 326–329, 2008.

[66] H. Ogi, M. Hirao, and S. Aoki, "Noncontact monitoring of surface-wave nonlinearity for predicting the remaining life of fatigued steels," *Journal of Applied Physics*, vol. 90, no. 1, pp. 438–442, 2001.

[67] V. J. Rao, E. Kannan, R. Prakash, and K. Balasubramaniam, "Fatigue damage characterization using surface acoustic wave nonlinearity in aluminium alloy aa7175-t7351," *Journal of Applied Physics*, vol. 104, p. 123508, 2008.

[68] G. E. Dace, R. B. Thompson, and O. Buck, "Measurement of the acoustic harmonic generation for materials characterization using contact transducers," in *Review of Progress in Quantitative Nondestructive Evaluation*, vol. 11B, pp. 2069–2076, 1991.

[69] I. Y. Solodov, "Ultrasonics of nonlinear contacts: propagation,reflection and nde- applications," *Ultrasonics*, vol. 36, pp. 383–390, 1998.

[70] X. Liu, J. Li, X. Gong, Z. Zhu, and D. Zhang, "Theoretical and experimental study of the third order nonlinearity parameter c/a for biological media," *Physica D: Nonlinear Phenomena*, vol. 228, pp. 172–178, april 2007.

[71] Y. Ohara, T. Mihara, and K. Yamanaka, "Effect of adhesion force between crack planes on subharmonic and dc reponses in nonlinear ultrasound," *Ultrasonics*, vol. 44, pp. 194–199, 2006.

[72] P. Li, W. P. Winfree, W. T. Yost, and J. H. Cantrell, "Observation of collinear beam-mixing by an amplitude modulated ultrasonic wave in a solid," *IEEE Ultrasonics symposium*, pp. 1152–1156, 1983.

[73] V. Zaitsev and P. Sas, "Nonlinear response of a weakly damage metal sample: A dissipative modulation mechanism of vibro-acoustic interaction," *Journal of Vibration Control*, vol. 6, pp. 803–822, 2000.

[74] V. V. Kazakov, A. Sutin, and P. A. Johnson, "Sensitive imaging of an elastic nonlinear wave-scattering source in a solid," *Applied Physics Letters*, vol. 81, no. 4, pp. 646–648, 2002.

[75] Z. Yan and P. B. Nagy, "Thermo-optical modulation for improved ultrasonic fatigue crack detection in ti-6al-4v," *NDT&E International*, vol. 33, pp. 213–223, 2000.

[76] Z. Yan and P. B. Nagy, "Thermo-optical modulation of ultrasonic surface waves for nde," *Ultrasonics*, vol. 40, pp. 689–696, 2002.

[77] C. Barrire and D. Royer, "Diffraction effects in the parametric interaction of acoustic waves: Application to measurements of the nonlinearity parameter b/a in liquids," *IEEE transactions on Ultrasonics, Ferroelectrics and Frequency Control*, vol. 48, pp. 1706–1714, November 2001.

[78] X. Jacob, C. Barrire, and D. Royer, "Acoustic nonlinearity parameter measurement in solids using the collinear mixing of elastic waves," *Applied Physics Letters*, vol. 82, no. 6, pp. 886–888, 2003.

[79] M. Vila, F. Vander-Meulen, S. Dos-Santos, L. Haumesser, and O. Bou-Matar, "Contact phase modulation method for acoustic nonlinear parameter measurement in solid," *Ultrasonics*, vol. 42, pp. 1061–1065, 2004.

[80] O. B. Matar, S. D. Santos, M. Vila, and F. V. Meulen, "Acoustic nonlinear parameter measurement in solid with a contact phase modulation method," *IEEE Ultrasonics symposium*, pp. 881–884, 2002.

[81] I. Collison, T. Stratoudaki, M. Clark, and M. Somekh, "Measurement of elastic nonlinearity using remote laser ultrasonics and cheap optical transducers and dual frequency surface acoustic waves.," *Ultrasonics*, vol. 48, pp. 471–477, 2008.

[82] T. Stratoudaki, I. Collison, R. Ellwood, S. Sharples, M. Clark, and M. Somekh, "Measurement of material nonlinearity using saw parametric interaction and laser ultrasonics.," *Journal of the Acoustic Society of America*, pp. 1721–1728, 2011.

[83] R. Ellwood, S. D. Sharples, T. Stratoudaki, M. Clark, and M. G. Somekh, "Investigation of the fatigue process using nonlinear ultrasond," *Journal of Physics: Conference Series*, vol. 278, no. 012013, pp. 1–4, 2011.

[84] M. Duquennoy, M. Ouaftouh, M. Ourak, and F. Jenot, "Theoretical determination of rayleigh wave acoustoelastic coefficients: comparison with experimental values," *Ultrasonics*, vol. 39, pp. 575–83, 2002.

[85] D. S. Hughes and J. L. Kelly, "Second-order elastic deformation of solids," *Physical Review*, vol. 92, no. 5, pp. 1145–1149, 1953.

[86] R. N. Thurston and K. Brugger, "Third-order elastic constants and the velocity of small amplitude elastic waves in homogeneously stressed media," *Physcial Review*, vol. 133, no. 6A, pp. A1604–A1610, 1964.

[87] M. Kato, T. Sato, and K. Ando, "Determination of the higher-order elastic compliance constants of metals from measurements of the dependence of ultrasound velocity on stress," *Journal of the Acoustic Society of America*, vol. 101, no. 4, pp. 2111–2121, 1997.

[88] R. E. Kumon and D. C. Hurley, "Effects of residual stress on the thin-film elastic moduli calculated from surface acoustic wave spectroscopy experiments," *Thin Solid Films*, vol. 484, pp. 251–256, 2005.

[89] V. I. Erofeev, V. A. Zaznobin, and R. V. Samokhvalov, "Determination of mechanical stresses in solids by acoustic method," *Acoustical Physics*, vol. 53, no. 5, pp. 546–552, 2007.

[90] S. Wormley, R. B. Thompson, G. A. Alers, R. Alers, and M. Warchol, "The influence of microstructure on the acoustoelastic measurement of stress in aluminium alloys," *Review of Quantitative Nondestructive Evaluation*, vol. 21, no. 1688-1695, 2002.

[91] G. L. Jones and D. R. Kobett, "Interaction of elastic waves in an isotropic solid," *Journal of the Acoustical Society of America*, vol. 35, no. 1, pp. 5–10, 1963.

[92] L. H. Taylor and F. R. Rollins, "Ultrasonic study of three-phonon interactions, i. theory," *The Physcial Review*, vol. 136, no. 3A, pp. A591–596, 1964.

[93] L. H. Taylor and F. R. Rollins, "Ultrasonic study of three-phonon interactions, ii. experimental results," *The Physcial Review*, vol. 136, no. 3A, pp. A597–601, 1964.

[94] E. Furgason and V. Newhouse, "Noncollinear three-phonon interactions in a multimode structure," *Journal of Applied Physics*, vol. 45, no. 5, pp. 1934–36, 1973.

[95] E. Furgason and V. Newhouse, "Convolution and correlation using nonlinear interactions of lamb waves," *IEEE Transactions on Sonics and Ultrasonics*, vol. su-20, no. 4, 1973.

[96] R. A. Guyer and P. a. Johnson, "Nonlinear mesoscopic elasticity: Evidence for a new class of materials," *Physics Today*, pp. 30–36, 1999.

[97] K. V. D. Abeele, S. D. Santos, T. Goursolle, and O. B. Matar, "Nonlinear and ultrasonic ndt of aeronautical components," in *Innovations in Nonlinear Acoustics: 17th International on Nonlinear Acoustics*, pp. 75–78, 2006.

[98] K. E.-A. V. den Abeele, P. Johnson, and A. Sutin, "Nonlinear elastic wave spectroscopy (news) techniques to discern material damage, part i: Nonlinear wave modulation spectroscopy (nwms)," *Review of Nondestructive Evaluation*, vol. 12, pp. 17–30, 2000.

[99] AZoM.com, "Piezoelectric material- an overview." `http://www.azom.com/article.aspx?ArticleID=81`. Visited January 2012.

[100] R. J. Dewhurst, C. E. Edwards, A. D. W. Mckie, and S. B. Palmer, "Comparative study of wide-band ultrasonic transducers," *Ultrasonics*, vol. 25, no. 6, pp. 315–321, 1987.

[101] S. Dixon and S. Palmer, "Wideband low frequency generation and detection of lamb and rayleigh waves using electromagnetic acoustic transducers (emats)," *Ultrasonics*, vol. 42, pp. 1129–1136, 2004.

[102] S. D. Sharples, *All-Optical Scanning Acoustic Microscope*. PhD thesis, The University of Nottingham, 2003.

[103] T. W. Murray, H. Tuovinen, and S. Krishnaswamy, "Adaptive optical array receivers for detection of surface acoustic waves," *Applied Optics*, vol. 39, no. 19, pp. 3276–3284, 2000.

[104] R. J. Dewhurst and Q. Shan, "Optical remoted measurement of ultrasound," *Measurement Science and Technology*, vol. 10, pp. R139–168, 1999.

[105] T. E. Blum, K. van Wijk, B. Pouet, and A. Wartelle, "Multicomponent wavefield characterization with a novel scanning laser interferometer," *Review of Scientific Instruments*, vol. 81, no. 073101, pp. 1–4, 2010.

[106] D. Royer and E. Dieulesaint, *Elastic waves in solids: Generation, acousto-optic interaction, applications*. Advanced texts in physics, Springer, 2000.

[107] C. Scruby and L. Drain, *Laser ultrasonics techniques and applications*. 335 East 45th street, New York, NY, 10017-3483, USA: Adam Hilger by IOP Publishing Ltd, 1990.

[108] S. Kenderian, B. B. Djordjevic, and R. E. Green, "Point and line source laser generation of ultrasound for inspection of internal and surface flaws in rail and structural materials," *Research in Nondestructive Evaluation*, vol. 13, pp. 189–200, 2001.

[109] P. A. Doyle and C. M. Scala, "Near-field ultrasonic rayleigh waves from a laser line source," *Ultrasonics*, vol. 34, pp. 1–8, 1996.

[110] F. L. di Scalea, T. P. Berndt, J. B. Spicer, and B. boro Djordjevic, "Remote laser generation of narrow-band surface waves through optical fibers," *IEEE Transactions on Ultrasonics, Ferroelectrics and Frequency Control*, vol. 46, no. 6, pp. 1551–1557, 1999.

[111] J. Huang, S. Krishnaswamy, and J. D. Achenbach, "Laser gneration of narrow-band surface waves," *Journal of Acoustic Society of America*, vol. 92, no. 5, pp. 2527–2531, 1992.

[112] M. Clark, F. Linnane, S. D. Sharples, and M. G. Somekh, "Frequency contol in laser ultrasound with computer generated holography," *Applied Physics Letters*, vol. 72, pp. 1963–1965, april 1998.

[113] M. Clark, S. D. Sharples, and M. G. Somekh, "Diffractive acoustic elements for laser ultrasonics," *Journal of Acoustic Society of America*, vol. 107, no. 6, pp. 3179–3185, 2000.

[114] S. D. Sharples, M. Clark, and M. Somekh, "Efficient and flexible laser ultrasound generation using spatial light modulators," *Electronic Letters*, vol. 37, no. 18, 2001.

[115] E. Hect, *Optics*. Addison Wesley Longman, New York, USA: Addison Wesley, 4 ed., 2002.

[116] C. Scruby and L. Drain, *Laser ultrasonics techniques and applications*. 335 East 45th street, New York, NY, 10017-3483, USA: Adam Hilger by IOP Publishing Ltd, 1990.

[117] Y.Lu and J. Michaels, "A methodology for structural health monitoring with diffuse ultrasonic waves in the presence of temperature variations," *Ultrasonics*, vol. 43, pp. 717–731, 2005.

[118] M. Nentwig, "Delay estimation by fft." `http://www.dsprelated.com/showarticle/26.php`. visited January 2012.

[119] I. Viktorov, *Physical properties of ultrasonic Rayleigh waves, Rayleigh and Lamb Waves*, pp. 1–7. New York: Plenum Press, 1967.

[120] G. Kaye, T. Laby, and editorial Committee, *Kay and Laby 5th edition Tables of physical and chemical constants*. Longman Singapore Publishers (Pte) Ltd, 1993.

[121] R. Hearmon, "The elastic constants of anisotropic materials," *Review of Modern Physics*, vol. 18, no. 3, pp. 409–440, 1946.

[122] V. Joshi, *Titanium alloys: an atlas of structures and fracture features*. CRC/Taylor & Francis, 2006.

[123] V. Kaajakari, "Calculating variation of material properties in anielastic material dependent on orientation." `http://www.kaajakari.net/~ville/research/tutorials/tutorials.shtml`, September 2011. Visited September 2011.

[124] R. Truell, C. Elbaum, and B. Chick, *Ultrasonic methods in solid state physics*, ch. 3, p. 194. 111 Fifth avenue, New york, New york, 10003: Academic Press Inc,, 1969.

[125] R. B. Thompson, O. Buck, and D. O. Thompson, "Higher harmonics of finite amplitude ultrasonic waves in solids," *Jounal of Acoustic Society of America*, vol. 59, no. 5, pp. 1087–1094, 1976.

[126] H. Kuhn and D. Medlin, eds., *Mechanical testing and evaluation*, vol. 8 of *ASM handbook*, ch. Reference information, p. 936. ASM International, Materials Park Ohio 44073-0002: ASM international, October 2000.

[127] W. Li, *Laser ultrasonic method for determination of crystallographic orientation of large grain metals by spatially resolved acoustic spectroscopy (SRAS)*. PhD thesis, University of Nottingham, 2012.

[128] W. W. L. Morris, O. Buck, and R. V. Inman, "Acoutic harmonic generation due to fatigue damage in high-strength aluminium," *Journal of Applied Physics*, vol. 50, pp. 6737–6741, November 1979.

[129] K. Salama and G. Alers, "Third-order elastic constants of copper at low temperature," *Physical Review*, vol. 161, no. 3, pp. 673–680, 1967.

[130] V. J. S. Narayana, K. Balasubramaniam, and R. V. Prakash, "Detection and prediction of creep-damage of copper using nonlinear acoustic techniques," in *Review of Quantitative Nondestructive Evaluation* (D. O. Thompson and D. E. Chimenti, eds.), vol. 29, American Institute of Physics, 2010.

[131] S. Baby, B. N. Kowmudi, C. M. Omprakash, D. V. V.Satyanarayana, K. Balasubramaniam, and V. Kumar, "Creep damage assessment in titanium alloy using a nonlinear ultrasonic techniques," *Scripta Materials*, vol. 59, pp. 818–821, 2008.

[132] T. Ohtani, H. Ogi, and M. Hirao, "Noncontact evaluation of surface-wave nonlinearity for creep damage in cr-mo-v steel," *Japanese Journal of Applied Physics*, vol. 48, pp. 07GD02:1–6, 2009.

[133] M. Liu, J.-Y. Kim, L. Jacobs, and J. Qu, "Experimental study of nonlinear rayleigh wave propagation in shot peened aluminium plates- feasibility of measuring residual stress," *NDT&E International*, vol. 44, pp. 67–74, 2011.